



Enhancing the energy storage capability of electric domestic hot water tanks

by

Peter M. Armstrong

A thesis submitted in part fulfilment of the requirements for the degree of

Doctor of Philosophy (D.Phil)

Department of Engineering Science

Oxford University

30th of November 2015

This thesis describes work undertaken by the author. To the best of the author's knowledge the work is original. Where the work of others has been used, appropriate reference has been made. Parts of the work have been presented at conferences and in journal papers. These have also been referenced.

ABSTRACT

Electric hot water tanks play a pivotal role as demand response assets within the UK's energy system by storing heat when energy is inexpensive and delivering domestic hot water when it is required. This role will become increasingly important if non-dispatchable renewable energy sources are to play a bigger part in the energy mix.

Historically, the design standards relating to hot water tanks have focused primarily on minimising heat losses. However, in addition to preserving energy, a hot water tank should preserve the availability of heat above a useful temperature for as long as possible to avoid energy usage during peak times when it is costly or carbon intensive. To do this, thermal stratification within hot water tanks must be promoted. Unfortunately, thermal stratification leads to conditions that are conducive to bacterial growth due to the hospitable temperatures that arise during operation. For this reason, question marks have arisen over the extent to which more flexible control strategies, designed to allow for increasing penetrations of intermittent renewable energy sources, might lead to the growth of pathogenic bacteria within hot water tanks. The objective of the work discussed in this thesis was to understand the extent to which there is a conflict between thermal stratification and bacterial growth in practice, whether this conflict can be resolved and the potential implications for electric hot water tanks operating on a time of use tariff.

A small field study demonstrated that there is prolific bacterial growth within conventional electric cylinders and that this can be attributed to thermal stratification with a confidence of ($P < 0.01$). Fitting a de-stratification pump, to enhance sanitary performance, resulted in a 19% decrease in the recovery of useable hot water above 43°C. Given that the tanks tested during the field study were made of copper, the consequences of alternative material choices on thermal performance were explored. It was found that the rate of useable hot water loss, due to de-stratification associated with thermal diffusion across the thermocline, could be reduced by a factor of 2.7 by making the tank liner wall from stainless steel instead of copper. Further numerical work indicated that this improvement in stratifying performance was most significant for small tanks with high aspect ratios.

In addition to de-stratification that arises due to vertical conduction, de-stratification due to inlet mixing was reduced by up to 30% by installing a spiral diffuser into the base of a test cylinder. In addition, by lowering the immersion heating element to ensure there is sufficient heat transfer to the base of the cylinder, sterilising temperatures could be attained throughout the stored volume of water in the tank during heating. This showed that the conflict between thermal and sanitary performance within electric tanks could potentially be resolved.

A bespoke tank, made from stainless steel and fitted with a diffuser, was built and subjected to typical draw cycles that reflect real world operation. These tests showed that more useable hot water could be delivered in comparison to a commercial off the shelf copper tank and consequently the utilisation of the Economy 7 time of use tariff would be enhanced.

ACKNOWLEDGEMENTS

I'd like to acknowledge the support from my supervisor, Professor Malcolm McCulloch. Malcolm gave me the freedom to pursue my research wherever it led and provided invaluable feedback over the course of my four and a half years at Oxford. I am also grateful to the Engineering and Physical Sciences Research Council for the funding that enabled me to undertake this research.

I must also acknowledge the unstinting support that I have had from Mark Smith at Newark Copper Cylinders Limited. Mark allowed me to visit his factory frequently and built several test tanks in support of this work.

TABLE OF CONTENTS

Abstract.....	3
Acknowledgements.....	4
Nomenclature.....	9
Table of figures.....	12
Table of Tables.....	16
1. Introduction.....	17
1.1 The environmental context.....	18
1.2 Historic demand response measures applied to domestic water tanks in the UK.....	20
1.3 The changing nature of power systems and how this will affect the control of hot water tanks in future	23
1.3.1 The transition from a centralised to distributed power system.....	23
1.3.2 Potential future for hot water tanks.....	23
1.3.3 The implications that hot water control strategies might have on bacterial growth.....	25
1.4 System topologies.....	26
1.4.1 An overview of common system topologies.....	26
1.4.2 Thermal stores versus conventional hot water tanks.....	28
1.5 Thermal stratification in hot water tanks.....	30
1.5.1 Transition in emphasis from heat losses to thermal stratification.....	30
1.5.2 Quantifying the benefit of thermal stratification.....	30
1.5.3 Sources of de-stratification.....	32
1.6 Research objectives, roadmap and novel contributions.....	33
2. A Review of thermal modelling techniques.....	36
2.1 Introduction.....	36
2.2 Thermal metrics used to assess operational performance of hot water tanks.....	37
2.3 Important dimensionless numbers associated with hot water tank design and operation.....	41
2.4 Approximation of thermal stratification using one dimensional models.....	45
2.4.1 Analytical approach.....	45
2.4.2 One dimensional numerical models.....	47
2.5 Computational fluid dynamics (CFD).....	54
2.5.1 The governing equations.....	55
2.6 Experimental test rig.....	64
2.6.1 Test rig overview.....	64
2.6.2 Flowrate measurement and control.....	66
2.6.3 Water temperature measurements.....	68
2.6.4 Error analysis.....	70
2.7 Model overview.....	71

3.	Bacterial growth within hot water tanks	72
3.1	Introduction	72
3.2	Discussion of bacterial growth in the literature	73
3.3	Field study of student apartments	74
3.3.1	Retrofit of temperature sensor arrays	74
3.3.2	Bacterial sample analysis	77
3.4	Field study results	79
3.4.1	Temperature readings	79
3.4.2	Bacterial Sample Results	82
3.5	Laboratory testing of student tank	84
3.5.1	Retrofit of de-stratification pump	84
3.5.2	Laboratory results	86
3.6	Summary	87
4	The influence of wall material specification on static mode performance	88
4.1	Introduction	88
4.2	Wall material selection criteria	89
4.2.1	Material cost	89
4.2.2	Compatibility with potable water	89
4.2.3	Mechanical properties	89
4.2.4	Thermal performance	91
4.2.5	Summary table	91
4.3	Experimental model	92
4.3.1	Experimental test set-up and procedure	92
4.3.2	Error analysis	94
4.4	Numerical model	95
4.4.1	Numerical approaches to static mode de-stratification	95
4.4.2	Application of a 2 dimensional axisymmetric model	96
4.5	Results	97
4.5.1	Experimental results	97
4.5.2	CFD results	99
4.5.3	Exploration of different aspect ratios and cylinder volumes	106
4.6	Discussion and conclusions	109
5.	Addressing dynamic losses and bacterial growth through application of a spiral inlet diffuser..	112
5.1	Chapter introduction and roadmap	112
5.2	Diffuser design	113
5.3	Diffuser thermal model	115
5.3.1	Model description	115
5.3.2	Model and experimental results	120

5.4	Specifying the diffuser outlet holes using a one dimensional flow model	122
5.5	CFD model	126
5.6	Experimental test	129
5.6.1	Description of test procedure	129
5.6.2	Experimental errors and uncertainties	129
5.7	Results	131
5.7.1	Experimental and numerical results	131
5.7.2	Insights from CFD scalar fields	136
5.7.3	Exploration of larger tank diameters	137
5.8	Summary	143
6	How does enhanced static and dynamic performance improve storage of service?	145
6.1	Chapter roadmap	145
6.2	Experimental test configuration and procedure	146
6.2.1	Test rig configuration	146
6.2.2	Test procedure	146
6.3	Results	148
6.3.1	ASHRAE test	148
6.3.2	Burch & Thornton Test	150
6.3.3	Volumetric performance	152
6.4	Summary	153
7	Conclusions and Further Work	154
7.1	Thesis output against research objectives	154
7.1.1	To what extent does thermal stratification affect the performance of real systems and is it responsible for bacterial growth? (Chapter 3)	154
7.1.2	To what extent does the material selection associated with the tank wall influence static mode de-stratification? (Chapter 4)	155
7.1.3	How can dynamic mode de-stratification and bacterial growth be inhibited by the inclusion of a diffuser? (Chapter 5)	156
7.1.4	How much hot water can a tank deliver on an off-peak tariff against typical demand profiles and can this be improved? (Chapter 6)	157
7.2	Further work	158
7.2.1	Exploration of the implications of research findings within a real world context	158
7.2.2	Exploration of the benefits that higher performing tanks might bring under flexible control strategies	161
7.2.3	Exploration of the benefits that enhanced stratification brings to other tank topologies	162
7.2.4	Undertake more research into ways in which the diffuser design could be further optimised	163
7.2.5	The implications of reduced dynamic mode de-stratification on the accuracy of one dimensional multi-node models	163
	References	164
A.	Appendix	176

A.1 Thermal stores versus conventional hot water tanks.....	176
A.2 Test rig details.....	178
A.3 Flow draw cycles	182

NOMENCLATURE

<i>Symbol</i>	<i>Units</i>	<i>Descriptions</i>
t	seconds	Elapsed time
T_h	°C	Tank outlet temperature
T_{init}	°C	The initial temperature of a fully heated and fully mixed tank of water
T_m	°C	The temperature of the cold inlet mains water supply feeding a tank
m_T	kg	The mass of water stored within a tank
\dot{m}	kg	The mass flow rate of water flowing through a tank
$T(x)$	°C	Vertical temperature distribution within a tank
T_u	°C	Useable temperature threshold
η_d	NA	Discharge efficiency of a tank
Q_d	Joules	The quantity of energy discharged from a tank
Q_0	Joules	The initial quantity of energy stored with a tank
C_p	J/kg°C	Specific heat capacity
T_a	°C	Ambient temperature of environment
H	m	Height of tank from bottom to outlet
E_x	Joules	Exergy
E_{xd}	Joules	Exergy discharged
E_{xsoc}	Joules	Exergetic state of charge
η_{ex}	NA	Exergetic efficiency
V_u	Litres	Useable volume of water delivered at T_u
V_{usoc}	Litres	State of charge of a tank in terms of useable volume
η_{vu}	NA	Volumetric efficiency of a hot water tank (useable volume delivered from an initial state of charge)
Re	NA	Reynolds number
ρ	kg/m ³	Density
U	m/s	Mean velocity
u'	m/s	Fluctuating velocity
v	m/s	Vertical flow velocity through a hot water tank
L	m	Characteristic length scale
μ	Ns/m ²	Dynamic viscosity
AR	NA	Aspect ratio of a tank (height over diameter)
D	m	Diameter of hot water tank cylinder

A	m^2	Tank cross sectional area
A_s	m^2	Tank surface area, used for computing heat losses
N_u	NA	Nusselt number
h	W/m^2K	Heat transfer coefficient
k_f	W/mK	Fluid thermal conductivity
R_a	NA	Rayleigh
G_r	NA	Grashoff number
P_r	NA	Prandtl number
γ	m^2/s	Kinematic viscosity
R_i	NA	Richardson number
g	m/s^2	Gravitational acceleration
v_s	m/s	Mean inlet velocity for a domestic hot water tank
T_{top}	$^{\circ}C$	Temperature at the very top of a hot water tank
T_{bottom}	$^{\circ}C$	Temperature at the very bottom of a hot water tank
F_o	NA	Fourier number
T_{me}^i	$^{\circ}C$	A measured temperature value
Q_E	Watts	Electrical power going into a heating element
T_h	$^{\circ}C$	Homogenous temperature in a mixed tank
C_T	£	Total cost of energy
$C(t)$	£	Cost of energy over time
\mathbf{V}	m/s	Velocity vector
∇	NA	Divergence operator
τ	N	Viscous shear stress
p	Pascals	Pressure
S_M	N	Body force on a finite element
g'	m/s^2	Boussinesq gravitational term to account for thermal stratification in a CFD simulation that assumes an incompressible flow
S_i	Joules	Energy source term
Φ	Joules	Viscous dissipation term
σ_h	Pascals	Hoop stresses within a cylinder wall
σ_l	Pascals	Longitudinal stresses within a cylinder wall
σ_{VM}	Pascals	Von mises stresses within a cylinder wall
T	m	Tank liner wall thickness
x_d	m	x coordinate associated with diffuser spiral path

y_d	m	Y coordinate associated with diffuser spiral path
Γ	NA	Pseudo time variable used to plot diffuser spiral
θ	Radians	Initial diffuser spiral wall offset angle

<i>Acronyms and terminology</i>	<i>Description</i>
DHW	Domestic hot water
TRNSYS	TraNSYient SYtem Simulation
CFD	Computational Fluid Dynamics
DNS	Direct Numerical Simulation
RES	Renewable Energy Sources
DSM	Demand Side Management
Useable volume	The amount of water that can be mixed from the outlet of a tank to a useable temperature, T_u , assumed to be 43°C throughout this thesis.

TABLE OF FIGURES

Figure 1-1 The breakdown of emission sources by sector. Data sourced from [13].....	19
Figure 1-2 Demand and renewable generation profile of electricity on July 1st 2015 (sourced from National Grid [31]) against a typical demand profile associated with domestic hot water [32]	21
Figure 1-3 Top: Carbon intensity of electricity in the UK during 2015, data sourced from [33]. (Bottom left) resolution of carbon intensity on 1st of February. (Bottom right) resolution of carbon intensity on 1st of July. .	21
Figure 1-4 UK national system buy price and generation imbalance during April 26th 2013 [33]	24
Figure 1-5 Hot water system topologies tree [56]	26
Figure 1-6 Illustration of a conventional direct electric hot water tank connected in a vented and unvented configuration.....	27
Figure 1-7 Selection of common hot water tank topologies that are produced by partner manufacturer (schematics provided by Newark Copper Cylinder Limited, redrawn by author in this figure).....	27
Figure 1-8 Relationship between exchanger coil length, associated cost and thermal store operating temperature compared to conventional hot water tank	29
Figure 1-9 outlet temperature of a mixed versus stratified 200 litre tank where flow rate is 15lpm and inlet temperature is 20°C against the sterilising threshold for <i>Legionella</i> and comfort threshold for human skin	31
Figure 1-10 Illustration of mechanisms associated with destratification within a conventional tanks	32
Figure 1-11 Illustration of how thesis chapters relate to the physical layout of a conventional electric hot water tank	35
Figure 2-1 System diagram illustrating salient features of domestic hot water tank delivering hot water to a user	37
Figure 2-2 Reynolds Experimental Apparatus to Visualise Streamlines in Flow Through A Glass Pipe. drawings collected and annotated from original paper [84]	41
Figure 2-3 Illustration of pipe velocity profile for laminar and turbulent flow (see Street et al [87])	42
Figure 2-4 Vertical temperature measurements and imposed error to compare performance of hypothesis function versus spline fits	47
Figure 2-5 Energy balance around node within nodal model	49
Figure 2-6 Illustration of mixing procedure applied to thermal input to one node within a timestep.....	50
Figure 2-7 Influence of number of nodes on simulation of a draw event from a 76 litre tank at 15lpm.	50
Figure 2-8 Vertical temperature distribution within 120 litre hot water tank simulated using multi-nodal model	53
Figure 2-9 Comparison of mixed, perfect stratification and multi-node models	54
Figure 2-10 Different models of flow and how they give rise to different forms of the continuity equation. This figure is a simplified version of a diagram presented in [117]	55
Figure 2-11 Illustration of forces acting on a fluid element which gives rise to the momentum equation	57
Figure 2-12 Illustration of a point velocity measurement within a turbulent flow based on an illustration in [124]	59
Figure 2-13 Workflow associated with CFD analysis described in this thesis	63
Figure 2-14 Schematic layout of tank test rig	64

Figure 2-15 Photograph of test rig.....	65
Figure 2-16 Photograph showing inside of rig control cabinet.....	65
Figure 2-17 Sump draw test showing linearity and repeatability of measurement.....	67
Figure 2-18 Thermocouple immersed into stream within pipe.....	68
Figure 2-19 Thermocouple arrangement for insertion into tank wall.....	68
Figure 2-20 British Standard test tank with array of thermocouple probes fitted.....	69
Figure 3-1 Qualitative illustration of <i>Legionella</i> growth rate against temperature, adapted from [145].....	73
Figure 3-2 Illustration of extruded cut applied to tank solid model to deduce isochoric volume intervals.....	75
Figure 3-3 Schematic Illustrating Sensor Arrangement.....	76
Figure 3-4 Raspberry PI with ADC expansion module.....	76
Figure 3-5 Photographs showing (left) hot water tank with sensors fixed to outer surface and raspberry pi powered up to verify operation (middle) close up of sensor arrangement fastened to tank wall outer surface. (Right) tank with sensors in place and insulation replaced with expanding foam held by polythene sheeting.....	77
Figure 3-6 Cross section of sample scoop arrangement inserted into hot water tank.....	77
Figure 3-7 (Left) Meg Uaipatanakul from the Oxford Microbiology Research Group taking samples from bottom of tank using sample probe (right) endoscope camera inserted to take images of bottom of tank.....	78
Figure 3-8 (left) image of bottom of tank (right) temperature data logger fitted to record temperature profiles over time.....	78
Figure 3-9 Temperature traces over two week period at flat c.....	80
Figure 3-10 Average mean, minimum and maximum temperatures recorded across all successfully logged tanks at each sensor location with bars showing standard deviation across tanks.....	81
Figure 3-11 Temperatures at the top and bottom of tanks k to p during reconnection to mains power supply....	81
Figure 3-12 Bacterial counts in tank water and sediment samples before heating.....	82
Figure 3-13 Bacterial counts in tank water and sediment samples after heating.....	82
Figure 3-14 Schematic of test rig for testing influence of de-stratification pump on the dynamic performance of a BS 7 tank.....	84
Figure 3-15 Photograph of tank from flat a retrofitted with destratification pump.....	85
Figure 3-16 Fluctuation of mains voltage within lab over the course of 24 hours.....	85
Figure 3-17 experimental comparison of tank output from initial 4.62kWh charge.....	86
Figure 4-1 (Left) photograph of the stainless and (centre) copper test tanks prior to insulation (right).....	93
Figure 4-2 Schematic showing (left) stainless test tank assembly and (right) copper BS1 test tank assembly....	93
Figure 4-3 Application of 2d axisymmetric CFD model to stainless test tank geometry.....	96
Figure 4-4 Experimental results: (a) vertical temperature distribution over time for the copper tank, (b) vertical temperature distribution over time for the stainless tank, (c), change in useable volume over time for both copper and stainless tanks where +E and -E denote values associated with maximum error (d) changing internal energy and energy for both the copper and stainless tanks.....	98
Figure 4-5: Evolution of vertical temperature distribution from initial condition after, 5 and 10 hours against CFD model for the stainless test tank. (HL) = model where heat losses to ambient are included, (A) shows CFD model output for adiabatic system.....	99
Figure 4-6 Evolving temperature field against CFD simulation for copper tank.....	100

Figure 4-7 Temperature and velocity fields around thermocline for copper (left) and stainless (right) walled 350mm diameter tanksnn.....	100
Figure 4-8: (Left) heat engine analogy for natural convection presented in [183] (right) twin heat engine analogy applied to a conductive wall within a stratified fluid.....	101
Figure 4-9 Simulated radial heat flux exchange between wall and water for stainless and copper 1mm walls with thermocline gradient of 400K/m.....	102
Figure 4-10 Simulated local heat transfer coefficient for 1mm copper wall alongside averaged analytical flat plate correlations based on mean wall water temperature difference.	103
Figure 4-11 Simulated and measured useable volume loss curves for stainless, copper and polyethylene materials.	105
Figure 4-12 Sizes of 83 hot water tanks manufactured in the UK according to volume and aspect ratio against simulation points (data from Newark Copper Cylinder ltd)	106
Figure 4-13 Cylinder sizes used for static mode de-stratification simulations against dimensions of a typical adult male for references	107
Figure 4-14 Changes in useable volume against aspect ratio for different stainless and copper walled tanks at 74, 210 and 450 litres.	108
Figure 4-15 Changing state of charge of tank against aspect ratio after 4 hours for 74, 210 and 450 litre volumes in stainless and copper.....	109
Figure 5-1 (Left) Hot water test tank assembly (shown without flange bolts for clarity), (right) bottom view of hot water test tank showing diffuser assembly	113
Figure 5-2 Application of multi node model which treats wall and water volumes separately	115
Figure 5-3 Simulation of temperature distribution through diffuser for a 3 turn spiral with 20 nodes applied to represent diffuser geometry assuming initial ambient temperature of 13°C.....	121
Figure 5-4 Hole locations and numbering scheme (left) related to an analytical flow distribution model (right)	122
Figure 5-5 Loss coefficients associated with duct bends, image sourced from [190].....	123
Figure 5-6 Algorithmic procedure to solve for flow rates throughout the diffuser.....	124
Figure 5-7 Hole sizes and flow distributions for the constant and tapered arrangements.....	125
Figure 5-8 (Left) constant hole arrangement (right) tapered hole arrangement.....	125
Figure 5-9 (left) photo showing isometric view of diffuser, (right) photo showing underside view of diffuser in tank assembly	125
Figure 5-10 (left) side view of tank showing application of mesh refinement zones to capture inlet and outlet pipes along with diffuser geometry (right) close up view of inlet pipe showing application of prism layer meshing to wall boundary	127
Figure 5-11 Isometric view of tank (left) and close up showing diffuser geometry (right)	127
Figure 5-12 Mesh applied to empty tank	127
Figure 5-13 Magnitude of a selection of numerical residuals over time.....	128
Figure 5-14 Y+ values plotted for wall boundary surface nodes to ensure that turbulence wall models are applied	128
Figure 5-15 Stainless steel test tank before insulation was applied	129
Figure 5-16 Outlet/inlet temperature traces for three draw tests showing consistency of experiments	130

Figure 5-17 Draw event test results against CFD simulations for diffuser with constant holes compared to the no diffuser case.....	132
Figure 5-18 Volumetric efficiency as a function of flow rate for the diffuser and no diffuser cases assuming a usable temperature threshold of 43°C.....	132
Figure 5-19 Discharge efficiency as a function of flow rate for the diffuser and no diffuser cases assuming a threshold temperature of 48°C (outlet temperature -20%).....	133
Figure 5-20 Exergetic efficiency as a function of flow rate for the diffuser and no diffuser cases	133
Figure 5-21 Volumetric efficiency of the optimised (tapered hole) versus non-optimised (constant hole) diffuser arrangements against flow rate	134
Figure 5-22 Discharge efficiency of the optimised (tapered hole) versus non-optimised (constant hole) diffuser arrangements against flow rate	134
Figure 5-23 Exergetic efficiency of the optimised (tapered hole) versus non-optimised (constant hole) diffuser arrangements against flow rate	135
Figure 5-24 Isometric view of scalar field over the course of 36 seconds showing progression of cold inlet through diffuser spiral channel	137
Figure 5-25 Hot water tank sections explored to understand the influence that tank diameter would have on the performance of a diffuser.....	138
Figure 5-26 Temperature distribution within tank after 15 litre draw events from 300mm diameter tank.....	139
Figure 5-27 Temperature distribution within tank after 15 litre draw events from 450mm diameter tank.....	139
Figure 5-28 Temperature distribution within tank after 15 litre draw events from 600mm diameter tank.....	139
Figure 5-29 Loss of useable volume against the Richardson number for each tank section.....	140
Figure 5-30 Loss of useable volume against the Richardson number for each tank section.....	140
Figure 6-1 Test tanks 1 and 2 without insulation.....	146
Figure 6-2 Intermittant draw cycle provided by [79].....	147
Figure 6-3 Temperature traces produced by test rig during ASHRAE draw test.....	148
Figure 6-4 Internal temperatures within test tanks (top) tank 1, stainless with diffuser, (bottom) tank 2, copper without diffuser (ASHRAE test)	149
Figure 6-5 Useable volume extracted over time for tank 1 and tank 2 during ASHRAE test	150
Figure 6-6 Temperature traces produced by test rig during Burch & Thornton test.....	150
Figure 6-7 Internal temperatures within test tanks (top) tank 1, stainless with diffuser, (bottom) tank 2, copper without diffuser (Burch & Thornton test).....	151
Figure 6-8 Useable volume over time for tank 1 and tank 2 during Burch & Thornton draw test	152
Figure 7-1 Integration of diffuser assembly into manufacturer’s hot water tank range. (Left) isometric transparent solid model view of tank without insulation. (Centre) semi transparent line drawing showing castleated wall/plate assembly. (Right) photograph showing underside of manufacturing prototype diffuser assembly	159
Figure 7-2 (Left) stainless tanks and diffusers prior to insulation, (right) stainless tanks insulated and cased ..	159
Figure 7-3 Volumetric efficiency of tank with a diffuser and flow path entering in at the bottom of the tank against performance of the same cylinder with conventional inlet and heating element scheme.	160
Figure 7-4 Comparison of conventional 166 litre tank to a 130 litre tank with diffuser in two different dwellings with two occupants both operating on an Economy 7 tariff	161
Figure 7-5 Temperature distribution within test cylinders during ASHRAE draw cycle at 10lpm	162

Figure A-1 Relationship between exchanger coil length, associated cost and thermal store operating temperature compared to conventional hot water tank	177
Figure A-2 Schematic layout of test rig used for reference with Table A.1	178
Figure A-3 High level electrical layout of rig control cabinet	178
Figure A-4 Thermocouple calibration system	181

TABLE OF TABLES

Table 2-1 Overview of model types along with their associated advantages and disadvantages	71
Table 3-1 Details of inhabited flats sampled along with bacterial counts for bottom and top tank water samples	83
Table 4-1 Materials and their associated parameters considered in this chapter	91
Table 4-2 Cost of wall materials against operating pressure for a 144 litre cylindrical tank.....	92
Table 4-3 Specifications of CFD platform used to conduct simulations	97
Table 4-4 Thermal gradients measured and sourced from the literature.....	103
Table 4-5 Simulated and measured rates of useable volume and exergy loss within test tanks for different wall materials and thicknesses.....	105
Table 5-1 parameters used to run diffuser thermal model	120
Table 5-2 Repetition of draw tests to assess consistency of measurements.....	130
Table 5-3 Measurement parameters and associated error estimates	131
Table 5-4 Evolution of temperature distribution within tank for no diffuser (top) and constant hole diffuser case for a flow rate of 15lpm drawn over 96 seconds	136
Table 5-5 Evolution of inlet plume within 300 and 600mm cylinder sections at 5lpm and 15lpm where there was no diffuser.....	142
Table 6-1 Performance of tank 1 and tank 2 in terms of volumetric efficiency against ASHRAE and Burch & Thornton draw cycle tests.....	152
Table A-1 Inventory of electrical and mechanical components used on test rig	179
Table A-2 Calibration results for 16 thermocouples.....	181
Table A-3 ASHRAE draw cycle events	182
Table A-4 Burch & Thornton draw cycle events.....	183

1. INTRODUCTION

This thesis explores the question: *how can conventional electric hot water tanks be improved so that they function as effective demand response assets within the UK's electrical power system?*

This introductory chapter sets out the main themes that are embedded within the above question along with the research objectives that arise from them.

Section 1.1 begins with a discussion of the environmental context which motivates this research and explains the future transition from gas fired to electrified domestic hot water systems that is anticipated. The way in which fleets of electric hot water systems are presently controlled, within the UK's existing electricity system, is described in section 1.2 along with the opportunity to use electricity when the price and carbon intensity is low under an Economy 7 tariff. Whilst the Economy 7 tariff has worked well for nearly 40 years, section 1.3 discusses the change that the electricity system is undergoing and the potential need to apply more flexible control strategies to fleets of hot water tanks in future. The potential consequences of such measures on bacterial growth within conventional hot water tanks is discussed. The reason for focussing on conventional electric tanks, given the range of other system topologies that are available, is provided in section 1.4. Common to all tank topologies, is the role that thermal stratification plays in ensuring that thermal performance is maximised, a theme explored in section 1.5. Over the course of sections 1.1 to 1.5, a number of gaps in the literature are identified, these are distilled into a series of research objectives in section 1.6 which also provides details of the thesis roadmap and novel contributions that have been made.

1.1 THE ENVIRONMENTAL CONTEXT

“An inefficient virus kills its host. A clever virus stays with it” – James Lovelock

The Anthropocene is having an impact on the Earth’s geology and climate at a scale and speed which is rivalled perhaps only by asteroid impacts and large tectonic events [1]. Whilst there are many different threats to human life on Earth [2], anthropogenic climate change is a serious one given a human population, with an increasing appetite for energy, that looks set to rise from around 7 billion as of 2015 to somewhere between eight and ten billion by 2050 according to the Intergovernmental Panel on Climate Change (IPCC) [3].

In their summary for policy makers, the IPCC noted that anthropogenic sources of CO₂ need to be curtailed such that a cumulative release of between 2550 Giga-tonnes and 3150 Giga-tonnes of CO₂ is avoided to prevent a 2°C rise in average temperature relative to the late 19th Century [4]. A rise of 2°C or less by 2100 is generally accepted to be a manageable state of affairs with potential pressures on food security, catastrophic sea-level rises and extinction of vulnerable species becoming a prospect as this threshold is exceeded. Of this budget, 1900 Giga-tonnes has already been spent as of 2014 [4]. In 2013 the rate of CO₂ production was 35 Giga-tonnes/year which means that as of 2015, the remaining budget will be consumed in less than 30 years assuming the population stays fixed and technology doesn’t change [5].

It is possible that a 2°C rise could be avoided by altering the Earth’s radiative heat balance through geo-engineering, a strategy referred to as Solar Radiation Management (SRM). This approach has gained prominence through the work of Salter et al who propose the development of marine vessels that seed reflective clouds [6]. However, in a recent assessment of geo-engineering, it was concluded that: *“SRM will not provide an easy way out of the climate problem”* due to the uncertainty surrounding potential side effects [7]. Consequently a de-facto moratorium on anything other than small scale experiments is in effect until the risks are better understood [8]. Moreover, SRM will not address the increasing acidification of the ocean that results from CO₂ emissions which pose a serious threat to the world’s coral reefs and other marine life [9]. An alternative tact is to consider Carbon Capture and Storage or utilisation (CCS and CCU) where CO₂ emissions are pumped into aquifers or converted into liquid fuels such as biodiesel respectively. However, such technologies are expected to take until well into the 2020s before they are sufficiently mature for deployment; by which time some of the irreversible effects of climate change may already be upon us [10]. Other carbon sequestering approaches, such as seeding oceans with iron to enable carbon consuming plumes of plankton to flourish [11] or changing soil handling practices in agriculture [12], have yet to be proven at scale.

Given the geopolitical challenges around SRM, along with the technical and scaling hurdles facing CCS, much emphasis has been placed on reducing the carbon emissions associated with human activities. Figure 1-1 shows a breakdown of anthropogenic emissions according to source type [13]:

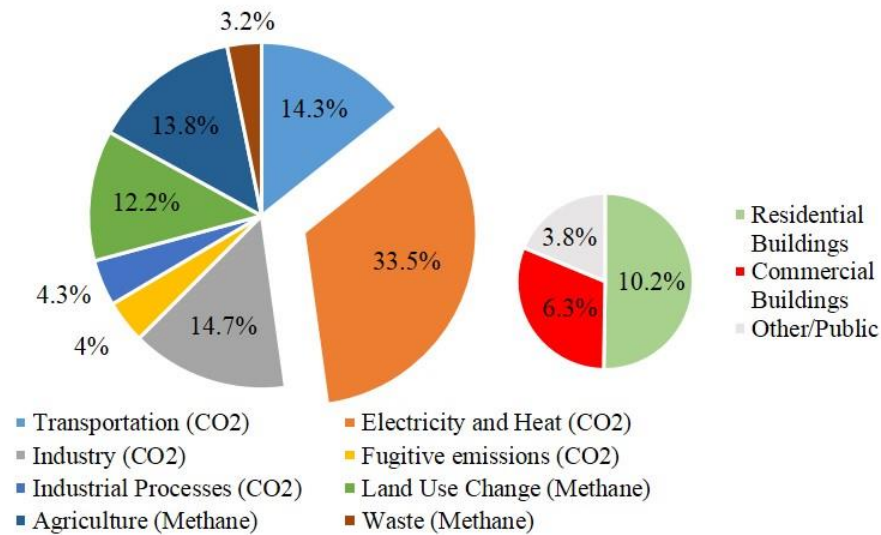


Figure 1-1 The breakdown of emission sources by sector. Data sourced from [13]

Over one third of all greenhouse gas emissions are associated with electricity and heat provision within buildings of which over half is produced by residential buildings. Within residential buildings, domestic hot water usage is responsible for somewhere between 17% and 39% in countries such as the UK [14] and South Africa [15] respectively. By extrapolating these figures, we can estimate that domestic hot water consumption is responsible for somewhere between 1.7% and 4% of all global emissions, a figure comparable to aviation which accounts for between 1% and 2% [16]. These figures are likely to increase in relative terms as building insulation standards and air handling services improve [17].

Within the UK, natural gas presently delivers approximately 81% of domestic heating demands [18]. The reasons include:

1. Household gas provision is at present considerably cheaper than electricity, retailing at 3.5 pence per kWh compared to 13.8 pence per kWh [19]
2. In comparison with other fuels, natural gas is clean burning with a carbon intensity of 0.16kg of CO₂/kWh of heat versus 0.29kg of CO₂/kWh for coal [20].
3. There was a strategic shift from coal to natural gas in the UK during the 1980s, motivated in part by an industrial relations stand-off between the National Union of Mineworkers and the Conservative government of the time [21]

However, given the imperatives to decarbonise our energy infrastructure, it is anticipated that the UK gas network will have to be shut down entirely by 2050 [22]. If this occurs, it is likely that there'll be an increase in the electrification of domestic hot water production from a present situation in which 10% of all residential hot water systems rely on an electric heating element within the UK [23].

Given the significant contribution to energy consumption associated with domestic hot water production, along with the trajectory of our environmental and political climate, it is interesting to consider the extent to which carbon reductions can be achieved through improvements in the performance and operation of conventional domestic hot water tanks.

1.2 HISTORIC DEMAND RESPONSE MEASURES APPLIED TO DOMESTIC WATER TANKS IN THE UK

In the UK, much of today's electrical infrastructure was commissioned and built under a state monopoly which was established as a result of the 1947 Electricity Act; an act which nationalised electricity production in the wake of the Second World War [24]. Prior to 1947, electricity provision was sporadic and chaotic. For instance, in London at the time, approximately 50 islanded power systems ran at ten different frequencies and 20 different voltages with a mixture of schemes operating on DC and AC on different numbers of phases [25]. However from 1947, nationalisation brought about the imposition of design standards which, along with the establishment of the National Grid, facilitated the bulk transmission of power from centralised generation facilities at high voltage to homes via low voltage distribution networks using Tesla's now ubiquitous three phase AC arrangement [26].

The stability of such large interconnected power systems relies on the synchronous operation of many rotating generators whose collective output must track changes in demand at all times [27]. This has been achieved historically using a mixed portfolio of generation assets, from relatively fast and responsive hydro-electric and small gas turbine driven units, to large baseload thermal plant that operates continuously with relatively high efficiency.

To ensure that baseload plant is utilised effectively, system operators charge pumped hydro storage facilities with surplus generation capacity during the night and discharge them during periods of peak demand [28]. In addition to this, a radio controlled domestic relay system was introduced from 1978 to coordinate the operation of electric heating loads, including domestic hot water tanks, under a tariff called 'Economy 7' [29]. Under this scheme the price of electricity goes low for seven hours at night (typically 24:00 to 07:00) whilst the heating circuits are energised [30]. The transition times associated with the Economy 7 scheme, along with the UK's national electricity and typical hot water demand profiles, are shown on Figure 1-2:

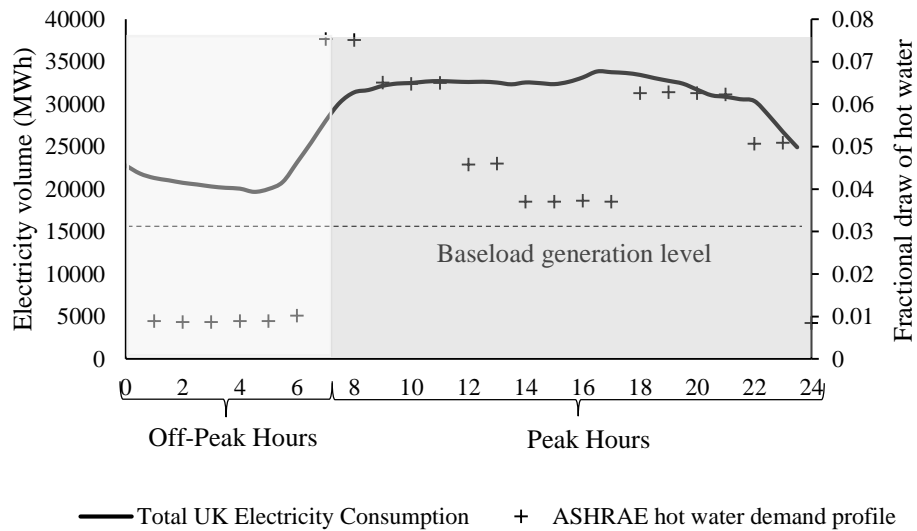


Figure 1-2 Demand and renewable generation profile of electricity on July 1st 2015 (sourced from National Grid [31]) against a typical demand profile associated with domestic hot water [32]

Boait et al asserts that the carbon intensity associated with electricity production during off-peak hours is lower than peak electricity [17]. It is interesting to examine this claim against the latest figures for the UK, shown on Figure 1-3 (sourced from Elexon on behalf of National Grid) [33]:

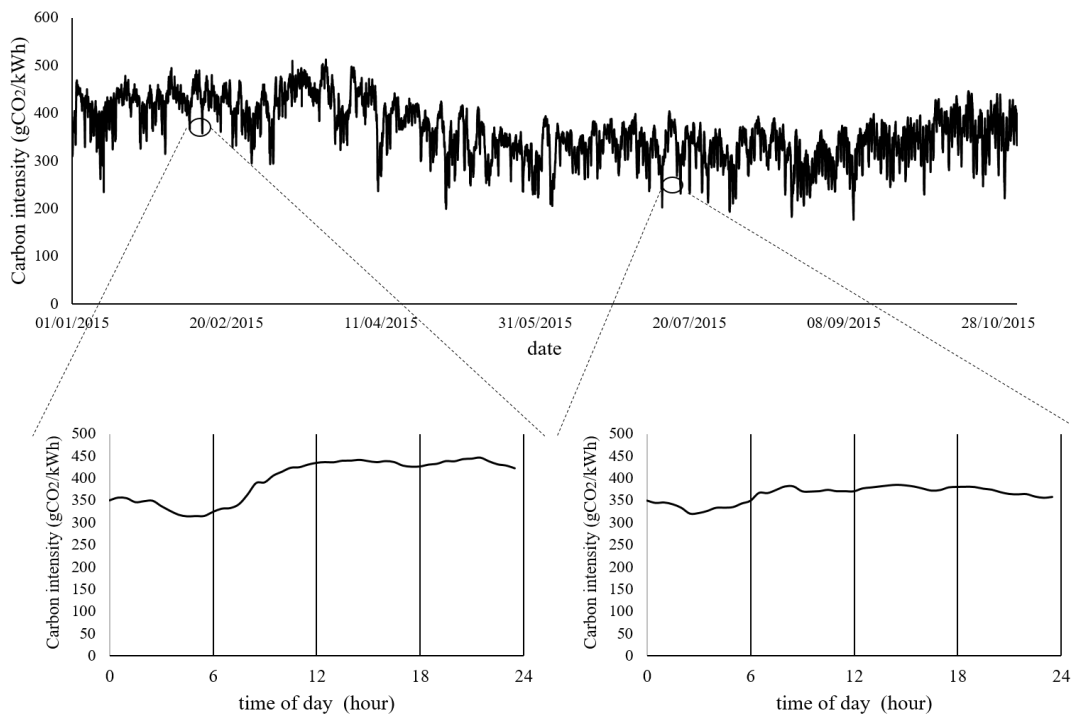


Figure 1-3 Top: Carbon intensity of electricity in the UK during 2015, data sourced from [33]. (Bottom left) resolution of carbon intensity on 1st of February. (Bottom right) resolution of carbon intensity on 1st of July.

The carbon intensity of electricity production appears to be higher during the winter months than summer during which the variation is less pronounced throughout the day. For instance, on the 1st of February 2015, the lowest intensity was 315gCO₂/kWh at 04:30, a figure which climbed 42% to 447gCO₂/kWh at 21:30. However, on July 1st, the variation is less intense with a change of 20% from 321gCO₂/kWh to 386gCO₂/kWh at 02:30 and 14:30 respectively. Over the course of an Economy 7 tariff period, the average carbon intensity associated with off-peak hours is 28% and 10% lower than the averages throughout the rest of the day for the 1st of February and 1st of July respectively. In addition to carbon intensity, the tariff price during off-peak hours is significantly lower at 7p/kWh versus 18p/kWh during peak hours [34].

Given the continuing variability of carbon intensity and price for the UK's electricity throughout the day, it is interesting to ask: *how effective is a conventional electric hot water tank at providing a continuous, useable supply of hot water from an initial charge that is delivered during off-peak hours and can this be improved?* Whilst the timing of off-peak hours during existing tariffs such as Economy 7 are fairly static, this might change as the UK's electricity system evolves to accommodate more renewable energy sources in future.

1.3 THE CHANGING NATURE OF POWER SYSTEMS AND HOW THIS WILL AFFECT THE CONTROL OF HOT WATER TANKS IN FUTURE¹

1.3.1 THE TRANSITION FROM A CENTRALISED TO DISTRIBUTED POWER SYSTEM

Since the 1989 electricity act, which ushered in the privatisation of the power infrastructure [35], the UK's electricity system has begun to change in composition. A similar picture is emerging across Europe, and other advanced economies with the advent of smaller embedded generation facilities, including a growing demand for renewable energy sources such as off-shore wind and roof-top photovoltaics. This, along with the imposition of carbon taxes on heavily polluting facilities such as lignite coal power stations, is beginning to challenge the centralised model of power generation, transmission and distribution which dominated the 20th century [36].

In spite of these changes, there is a great deal of uncertainty surrounding the extent to which large centralised facilities will continue to play a role in the UK's electricity system. This uncertainty stems in part from the advent of shale gas, with an indigenous resource that could supply the UK for 470 years[37], along with the start of construction work on Hinkley Point C, a nuclear facility which could generate up to 7% of the UK's electricity consumption [38].

However, in parts of the UK, such as Cornwall, power networks are encountering capacity limits due to large surpluses of renewable power production to the extent that limits on renewable integration are being encountered [39]. In addition to this problem, the migration away from large synchronous machines, and their associated inertia, is leading to increasing challenges around the stability of the power system and its response to transient events such as faults or plant outages [40].

1.3.2 POTENTIAL FUTURE FOR HOT WATER TANKS

To ameliorate these problems there has been recent emphasis on the role that domestic energy storage technologies, such as batteries, might play [41]. Significant improvements in the performance of battery chemistries has been achieved, notably the step change in performance from lead acid to lithium ion cells where energy densities have risen from 95Wh/L to 360Wh/L respectively [42]. This has culminated in the release of the *Tesla Power Wall*, a lithium ion based home battery system which can store up to 10kWh and deliver 3.3kW of power for a price of \$3000 [43]. However, banks of lithium ion cells are less stable in comparison to lead acid and require elaborate battery management systems to avoid catastrophic thermal runaway; a scenario which can result in spectacular explosions and lithium fires [44]. A complimentary approach to home batteries is to move towards a more flexible demand side management strategy for domestic hot water tanks. Storing service rather

¹ This section comprises of excerpts and data presented as part of a conference paper delivered by the author [97]

than energy in this manner could eliminate or significantly reduce the demands on a home battery system allowing for smaller units that are subjected to shallower charge cycles for increased reliability.

In comparison to batteries, tanks of heated water can store energy with a near indefinite cycle life, low environmental footprint and low cost. A 120 litre tank, purchased in the UK and heated from an initial temperature of 20°C to 60°C, represents a cost of approximately 50\$/kWh compared with 300\$/kWh [43] for a home lithium ion storage system. Hot water tanks also deliver the significant power requirements associated with power showers which increasingly are being installed in the UK [45]. The power delivery associated with a 17lpm power shower equates to 47.6kW, over ten times the power capacity of a *Tesla Power Wall*.

The distributed energy storage potential associated with electric hot water tanks in UK households is considerable. 55% of the 23 million homes throughout England make use of hot water tanks with 7.5% of households on an Economy 7 tariff and over 50% using a tank that is fired by gas with a back-up electric heating element [17]. Assuming a typical cylinder, sized at 120 litres and operating at 60°C[46], this equates to approximately 10GWh of energy storage potential for Economy 7 units alone, a capacity comparable to the UK’s largest pumped hydro facility, Dinorwig in Wales.

To put this into perspective we consider the UK energy balancing market, which is updated at half hourly intervals to tender for increases or reductions in generation depending on the balance between supply and demand. Figure 1-4 shows the system sell price and surplus of generation which occurred on the system throughout the 26th of April, 2013:

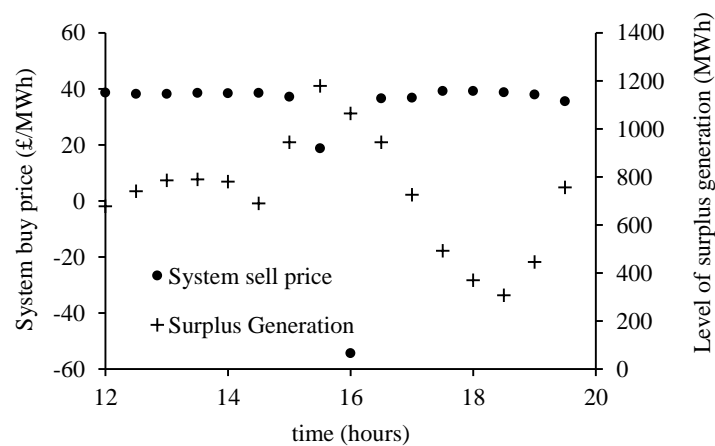


Figure 1-4 UK national system buy price and generation imbalance during April 26th 2013 [33]

At 16:00 hours, the surplus generation reached 1.06GWh for the trading period between 16:00 and 16:30 causing the system buy price to go negative at £-54.41/MWh. Under such circumstances, the system operator can demand for the curtailment of renewable energy sources, such as wind, causing much consternation in the popular press both in the UK and North America [47], [48]. However, in this particular instance, 1.06GWh of demand over a

half hour period would have equated to turning a typical 3kW immersion element on in 355,000 tanks which amounts to 3% of the entire UK fleet or 21% of those on an Economy 7 tariff. This idea is not exclusive to the UK. For instance, Atikol et al estimate that in North Cypress, demand side management strategies could potentially delay the procurement of peaking generation equipment, saving over ten million dollars in capital costs [49]. However, introducing such ideas to conventional hot water tanks would require a move away from the fixed time periods over which the Economy 7 tariff is designed to operate.

1.3.3 THE IMPLICATIONS THAT HOT WATER CONTROL STRATEGIES MIGHT HAVE ON BACTERIAL GROWTH

There are a number of demand response strategies which have been discussed in the literature. For instance Paull et al discuss the simulation of a control scheme whereby a single thermal mass is used to approximate the tank's energy content [50]. One concern associated with such approaches is that, unlike Economy 7 units, where the tank is scheduled to be fully heated throughout every evening unless overridden by the user, a flexible control strategy may lead to prolonged periods during which the tank is unheated. This observation led Paull et al to note that any demand response strategy should avoid '*the growth of unwanted and potentially dangerous bacteria*'. However, using a single thermal mass to describe the physics of a hot water tank fails to capture the real temperature distribution over time since in reality, thermal stratification prevails during operation, a topic discussed in section 1.5. Other approaches, including the application of fuzzy logic [51] and neural network based algorithms [52], assume the tank's state can be represented by a single temperature and ignores any operational constraints considering bacterial growth. More sophisticated approaches, which consider thermal stratification whilst alluding to bacterial growth, have been pursued by Lacroix [53] and Moreau [54], however neither of these papers make use of experimental data to quantify the extent to which bacterial growth is a problem in reality and there is a lack of resolution of the temperature distribution throughout the systems they simulate which might otherwise allow for a prediction of whether a problem is likely.

Interestingly, Alary et al took bacterial growth samples from 211 Canadian hot water systems back in 1991[55]. They found that there was a strong link between whether a tank was electrically heated against the risk of contamination with 39% of electric tanks yielding a positive result for *Legionella*. At the time it was suggested that the positioning of the heating element might be responsible, leading to inadequate operating temperatures, however no temperature measurements were taken from the cylinders during operation and so this hypothesis was not proved.

Given that bacterial growth is highly sensitive to temperature, along with the role that more flexible control strategies might play to improve the stability of our power system in future, understanding the extent to which bacteria grows within real electric hot water tanks during operation is a key question to address. Answering this question demands an understanding of the system topologies that are installed throughout the UK.

1.4 SYSTEM TOPOLOGIES

The preceding sections outlined the rationale for exploring the performance of electric hot water tanks along with the potential issues around bacterial growth. This section provides an overview of the types of hot water tank which operate within the UK before explaining why the emphasis in this research is on electrically heated direct systems in spite of the claims that an alternative topology, the thermal store, delivers higher sanitary performance.

1.4.1 AN OVERVIEW OF COMMON SYSTEM TOPOLOGIES

Figure 1-5 provides a system topologies tree which highlights the key features that differentiate the majority of systems available on the market:

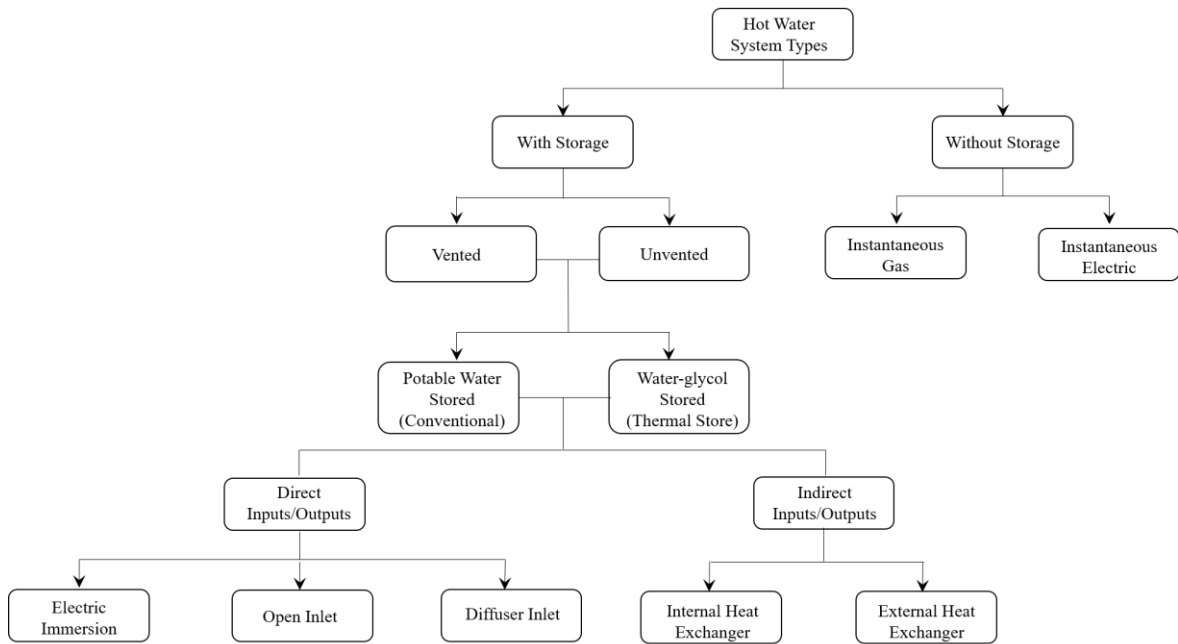


Figure 1-5 Hot water system topologies tree [56]

Domestic Hot Water (DHW) systems can be divided according to whether they incorporate a hot water tank or not. Systems without any storage typically use an instantaneous gas or electric heating arrangement. Whilst such systems constitute approximately half of the UK domestic fleet [17], they are outside of the scope of this thesis. For systems making use of a tank, the hot water can be stored with a working head above atmosphere, referred to as vented, or under mains pressure, referred to as unvented. In mains pressurised systems, an expansion vessel is used to accommodate the water as it expands due to its rising temperature whereas vented systems are arranged to discharge expanded water into their respective header tank. These two arrangements are illustrated by Figure 1-6 with vented and unvented systems shown on the left and right hand sides respectively.

The advantage of unvented systems is that hot water is delivered at mains pressure whereas vented systems are limited by the head that the building's height permits. Furthermore, heat losses are reportedly lower in unvented systems compared to vented units which discharge vapour into the atmosphere. Vented systems were installed

exclusively throughout the UK until 1986 when regulations were amended to allow unvented units to be sold [57], however both types are still available. Unvented units have to be made of a thicker grade of metal to withstand mains water operating pressures and also require additional safety features such as a Temperature & Pressure (T&P) relief valves along with a gas filled expansion vessel [58]; consequently, where cost is of concern, vented systems are still installed.

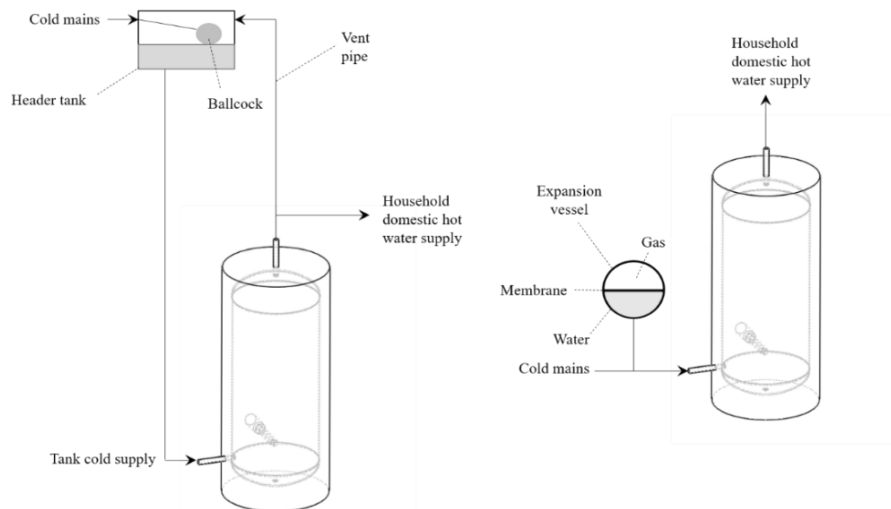


Figure 1-6 Illustration of a conventional direct electric hot water tank connected in a vented and unvented configuration

Figure 1-7 shows five permutations of hot water tank which are commonly found in the UK and manufactured by Newark Copper Cylinder Limited, a company who produced bespoke hot water tanks in support of the research detailed throughout this thesis:

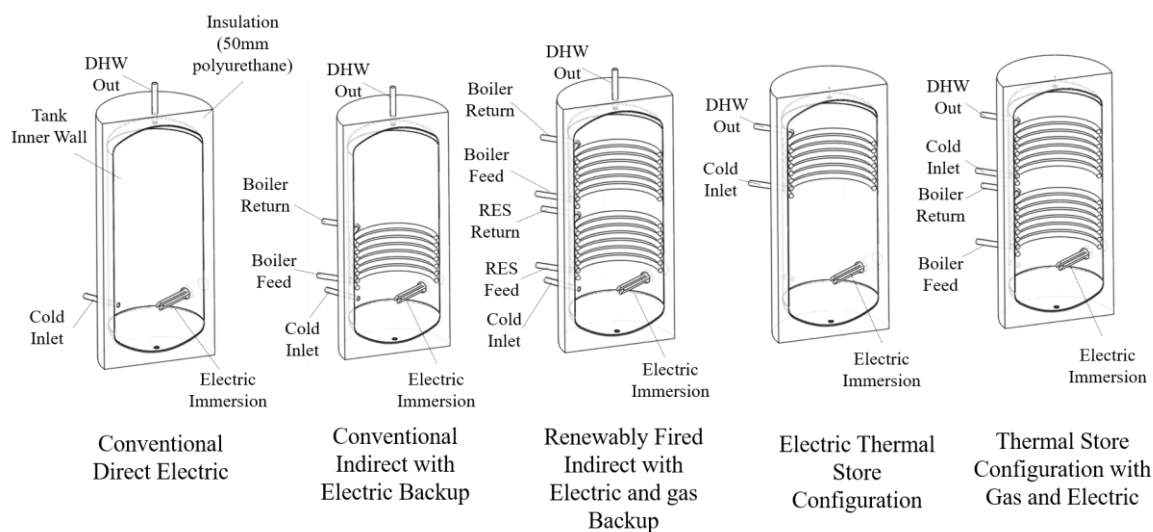


Figure 1-7 Selection of common hot water tank topologies that are produced by partner manufacturer (schematics provided by Newark Copper Cylinder Limited, redrawn by author in this figure)

The focus of this research is on the conventional direct electric system depicted on the far left. However the research findings also apply to conventional systems where heating is provided indirectly by gas or Renewable Energy Sources (RES) via helical coils or plate heat exchangers from heat pumps, solar thermal collectors or biomass boilers.

1.4.2 THERMAL STORES VERSUS CONVENTIONAL HOT WATER TANKS

A further distinction can be made between conventional and thermal store configurations. A conventional tank holds potable water inside which is replenished from the cold inlet as it is drawn from a hot outlet on the top, as is the case for the first three tanks from the left on Figure 1-7. A thermal store, on the other hand, holds a fluid such as a glycol mix [56] which transfers heat to a potable supply via a heat exchanger, typically a helical coiled tube inside the tank made of copper or stainless [59]. Thermal store topologies are advantageous in that they are able to supply hot water at mains pressure without requiring a pressurised hot water tank with the associated wall thickness and safety features that are necessary. It is also claimed that thermal stores are less prone to bacterial contamination since there isn't a large body of stagnant potable water being stored as is the case with conventional systems. This claim is asserted by sales brochures published by industry, for instance:

“The key advantage of a thermal store is that a large volume of potable mains water is not standing still. Because it's constantly flowing, there is little chance of bacterial growth in the hot water system.” [60]

Whether the above claim is true or not, thermal stores come with the disadvantage that they suffer from greater standing heat losses due to the heat transfer penalty associated with the internal heat exchanger. We can illustrate this penalty by analysing the heat transfer performance within a thermal store by applying the logarithmic mean temperature difference method outlined in [61] and detailed in Appendix A.1. The method is used in industry and is recommended by the technical datasheet describing a common finned copper heat exchanger, the Wieland WR18W series, that is used by Newark Copper Cylinder [59]. By applying the procedure, it is possible to estimate the required store operating temperature needed to deliver 15lpm of water at 60°C from a fully charged thermal store for a given length of helical coil. Figure 1-8 shows the relationship between the coil length, store temperature and resulting heat losses assuming a 200 litre, cylindrical tank with a diameter of 450mm and 50mm of polyurethane insulation with a thermal conductivity of 0.03W/mK where the mains inlet temperature and ambient temperature is at 20°C. The figure is also annotated to show the cost of the coil, assuming a market price of 5\$/kg of copper [62] along with the losses that would result from a conventional cylinder where the temperature of the stored water is 60°C.

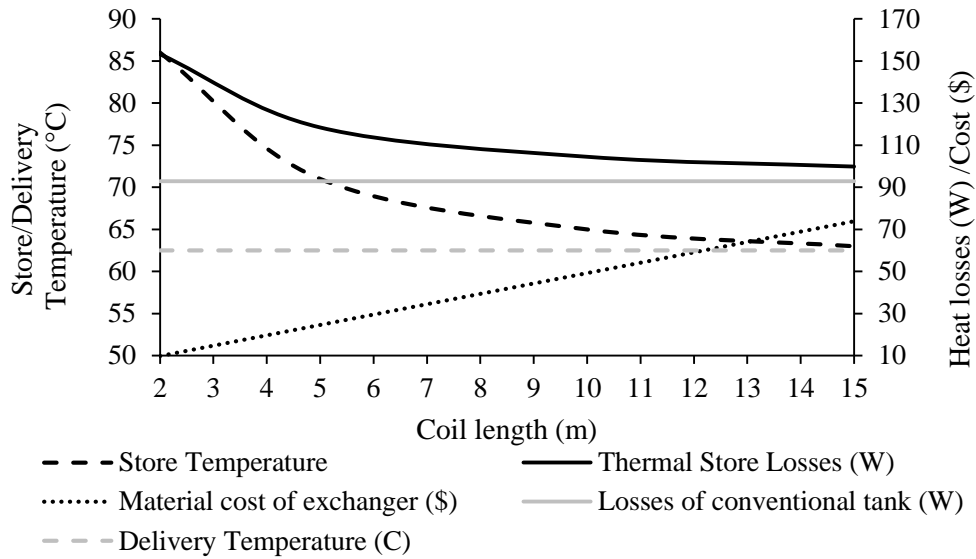


Figure 1-8 Relationship between exchanger coil length, associated cost and thermal store operating temperature compared to conventional hot water tank

There is a clear trade-off between the cost of the heat exchanger, which increases with the length of the coil, against the heat losses which rise with the required operating temperature to ensure that water is delivered at 60°C. At 2 meters in length, the cost of the exchanger is 10\$ but the heat losses are 65% greater than a conventional cylinder at 153 Watts. Increasing the length of the coil to 8m reduces the losses such that they are only 6% greater, however the cost has increased four-fold to 40\$. In addition to cost and heat losses, the helical coil incurs a pressure drop which increases with its length meaning that flow rates will be lower in comparison to a conventional, unvented system.

The model above only compared the performance of two fully charged hot water tank topologies during the first moments that hot water is drawn from them. In practice, as energy is withdrawn from either topology of hot water tank, the water within it will begin to stratify, the subject of the following section.

1.5 THERMAL STRATIFICATION IN HOT WATER TANKS

Whilst the analysis in the preceding section illustrates the costs incurred by having an isolating heat exchanger within a thermal store, for both thermal stores and conventional tanks, the overall performance is affected significantly by the extent to which thermal stratification prevails during operation.

1.5.1 TRANSITION IN EMPHASIS FROM HEAT LOSSES TO THERMAL STRATIFICATION

In spite of the importance of thermal stratification, discussed later in this section, regulatory measures on the performance of hot water tanks have historically focused almost entirely on reducing heat losses, for instance the UK's Part L building code mandated that allowable heat losses from electric hot water tanks in 2011 [63] were to be 11% lower than in 2008 [64]. This has been achieved largely by increasing the thickness of polyurethane tank insulation from 25mm or less in 1978 to over 50mm beyond 2008. As the thickness increases further, diminishing returns set in and the physical constraints associated with door frame and cupboard sizes are encountered. This led the Department of Energy and Climate Change to note in 2011 that: *'the potential for improving tank insulation is in decline'* [14]. Given the limits on performance that can be achieved through thermal insulation alone, most recent academic research on hot water tank performance has been focused on the influence of thermal stratification.

1.5.2 QUANTIFYING THE BENEFIT OF THERMAL STRATIFICATION

Thermal stratification arises due to water's inverse relationship between density and temperature. The process gives rise to buoyancy forces which can maintain a remarkably stable segregation between hot and cold water volumes [65]. Figure 1-10 shows a cross section through a hot water tank as water is being drawn from the top and replenished from the bottom, a so called 'draw event'. Ideally, the cold water entering the bottom would displace the hot water out the top without mixing. In this case, assuming that there are no heat losses, the outlet temperature could be described by the following function:

$$T_h(t) = \begin{cases} T_{init} & \text{for } 0 < t < \frac{m_T}{\dot{m}} \\ T_m & \text{for } t > \frac{m_T}{\dot{m}} \end{cases} \quad (1-1) \quad \left| \begin{array}{l} \text{Outlet temperature of an} \\ \text{adiabatic and perfectly} \\ \text{stratified tank} \end{array} \right.$$

Where: m_T is the mass of water within the tank, the initial homogenous temperature throughout the tank is T_{init} , and time is denoted by t . In the worst case scenario, the cold mains would mix with the water stored throughout the tank in which case the outlet temperature would vary according to (1-2):

$$T_h(t) = T_m + [T_{init} - T_m]e^{-\frac{\dot{m}}{mT}t} \quad (1-2)$$

Outlet temperature of a perfectly mixed tank

It is instructive to compare the output of Equations (1-1) and (1-2) for a 200 litre conventional tank initially charged at 60°C being discharged by incoming cold water at 15lpm and at 20°C:

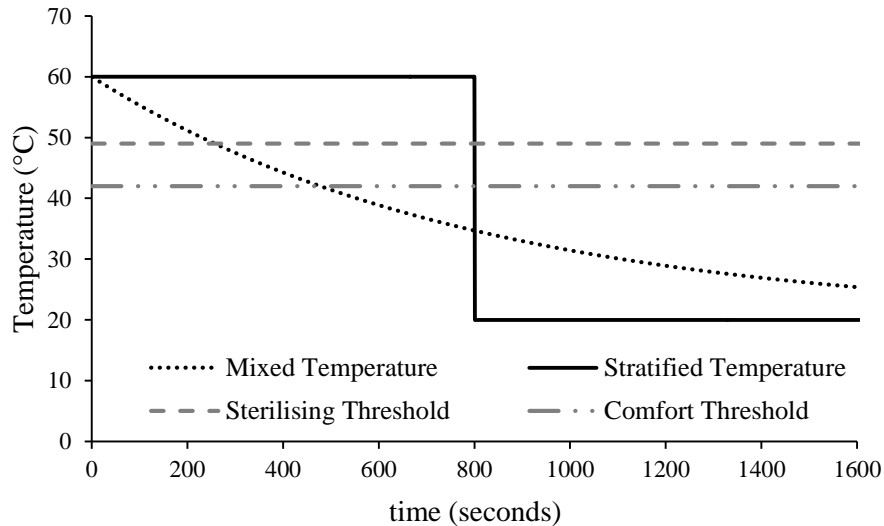


Figure 1-9 outlet temperature of a mixed versus stratified 200 litre tank where flow rate is 15lpm and inlet temperature is 20°C against the sterilising threshold for *Legionella* and comfort threshold for human skin

Figure 1-9 shows the outlet temperature from both the mixed and perfectly stratified cases. For the mixed case, the outlet temperature begins falling immediately, dropping beneath the sterilising threshold for *Legionella* [66] by 258 seconds and the threshold for human comfort [67] by 443 seconds. On the other hand, the perfectly stratified system produces water at 60°C continuously for 800 seconds until the cold mains water has completely displaced all of the hot water that was initially stored.

The above analysis clearly shows how a perfectly stratified tank is capable of delivering useful hot water for longer than a fully mixed system from the same initial state of charge. This is important for an Economy 7 tariff, discussed in section 1.2, where the objective is for the tank to deliver water that is hot enough throughout peak hours to avoid energy being bought when the price and carbon intensity of electricity is high. It is interesting to note that the volumetric output above a useable threshold of 43°C from the 200 litre mixed case could have been matched by a 113 litre, perfectly stratified tank. This would enable the tank to be reduced in size by 44% leading to a significant reduction in heat losses as a result of the lower surface area with scope to increase thermal insulation further to compound the benefit.

Thermal stratification will also enhance the performance of indirect heat exchangers in the bottom of the tank due to the greater temperature gradient between the water sitting in the cylinder and the water flowing through the exchanger coil; a particularly important consideration for heat pumps where the coefficient of performance is sensitive to temperature [68].

1.5.3 SOURCES OF DE-STRATIFICATION

In practice, a real hot water tank will operate between the two extremes of fully mixed and perfectly stratified operation. The extent to which the system is biased to one case or the other will depend on the extent to which de-stratification occurs. Figure 1-10 illustrates a stratified temperature distribution within a tank during a draw event along with the primary sources of de-stratification:

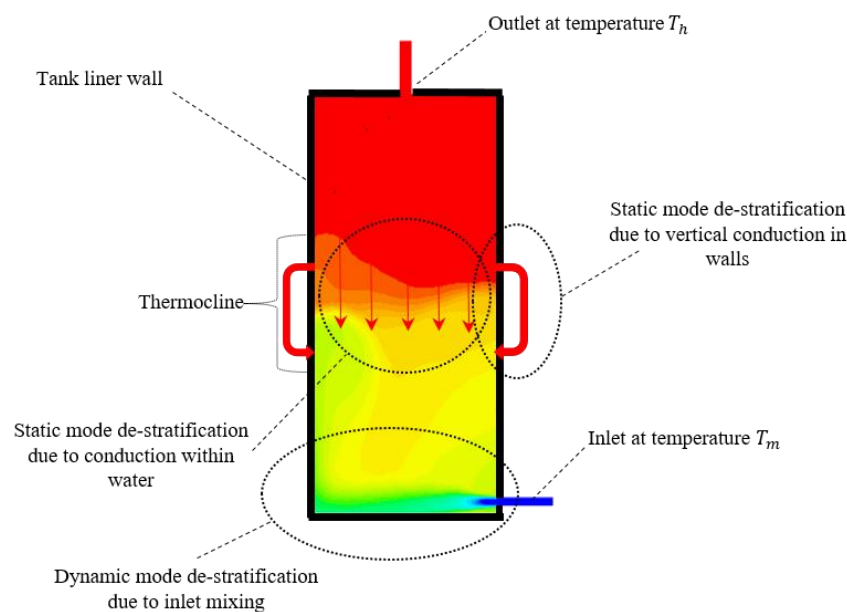


Figure 1-10 Illustration of mechanisms associated with destratification within a conventional tanks

There are two primary sources of de-stratification, static mode and dynamic mode. Static mode de-stratification is caused by thermal conduction through the stored water and the metallic tank lining wall. In chapter 4, the influence of the tank wall on rates of static mode de-stratification are explored in detail. Dynamic mode de-stratification arises due to mixing between the cold plume emerging from the tank inlet and the stored hot water within the tank. This phenomena, along with an inlet diffuser to mitigate it, is discussed in chapter 5.

Given the important role that thermal stratification plays in delivering thermal performance, it is important to understand how well real systems stratify during operation. It is also interesting to explore whether within conventional cylinders, where the potable water is heated and used directly, conditions become conducive towards bacterial growth as a result of thermal stratification, a theme explored in chapter 3.

1.6 RESEARCH OBJECTIVES, ROADMAP AND NOVEL CONTRIBUTIONS

The preceding sections outlined the role that a conventional tank plays in absorbing energy when it is available at low cost with a low carbon intensity. The ability to do this depends on the extent to which the system will remain thermally stratified during operation. If systems are to exploit thermal stratification, without the penalties associated with a heat exchanger, there is a risk that bacteria might flourish in the system due to the temperature gradient between the cold inlet and hot water that prevails. This is a problem of particular concern if tanks are to be controlled more flexibly to accommodate renewable energy sources in future.

To obtain a better understanding of the above dilemma, a series of experimental and numerical research activities were pursued with a view to answering the following questions:

1. *‘To what extent does thermal stratification affect the performance of real systems and is it responsible for bacterial growth in real hot water tanks?’*

In order to answer this question, a definition of thermal performance is required. Chapter 2 explores a number of metrics which quantify thermal performance and introduces the idea of ‘useable volume’ which defines the amount of water that can be delivered from a hot water tank at a useable temperature. Quantifying thermal performance metrics requires the development of numerical and experimental models which are also described from simple dimensionless parameters through to more elaborate Computational Fluid Dynamic (CFD) simulations. At the end of chapter 2, an experimental test rig, developed to test off-the-shelf hot water tanks against alternative designs, is discussed.

Once the metrics, models and test methodology have been detailed, chapter 3 discusses a field study in which 10 conventional electric hot water tanks, operating on an Economy 7 tariff, were monitored in situ with one unit being removed and tested in the laboratory. The details of bacterial samples, taken to establish the extent to which thermal stratification might be responsible for bacterial growth, are given. The chapter also discusses how a de-stratification pump, retrofitted to one of the tanks to improve sanitary performance, affects the thermal performance of the system during a draw test.

The key research contribution, highlighted in chapter 3, is the discovery that conventional electric tanks in the UK provide conditions suitable for bacterial growth due to the fact that the heating element is too far from the base of the cylinder. Furthermore, retrofitting a de-stratification pump to enhance sanitary performance, has an adverse effect on the thermal performance of the system during a draw event.

2. *To what extent does the material selection associated with the tank wall influence static mode de-stratification?*

In chapter 3, it is found that bacterial growth is prolific in spite of the fact that the tank liner walls were made from copper, a material which is perceived as a biocide. Consequently, chapter 4 explores the potential influence that alternative wall materials and thicknesses might have on the static mode performance. An experimentally validated CFD model is used to demonstrate the advantages of using stainless steel instead of copper and quantifies this advantage over the range of tank geometries encountered in the UK market.

The key contribution from chapter 4 is the finding that a tank made of stainless significantly improves static mode performance to the extent that the rate of useable volume loss can be reduced by a factor of 2.7. A counter rotating vortex system was also observed during simulation which results from vertical heat transfer through a wall next to a thermocline.

3. *How can dynamic mode de-stratification and bacterial growth be inhibited by the inclusion of a diffuser?*

In chapter 3, it is noted that the dynamic mode performance of the tank is severely reduced by the operation of a de-stratification pump. In chapter 5, a spiral diffuser arrangement is introduced which is designed to reduce inlet mixing and conduct heat all the way to the base of the cylinder so that sterilising temperatures are attained at the base of the tank during an Economy 7 warm up period.

The key contribution from chapter 5 is numerical resolution of the inlet plume colliding with the side wall within a cylindrical hot water tank. Another contribution is the finding that the diffuser outlet hole sizing scheme plays a relatively insignificant role and that the main function of the diffuser is to contain the inlet plume that would otherwise cause a high degree of mixing. The chapter also describes a parametric study which shows that inclusion of a diffuser within a range of tank sizes and across a range of flow rates, typical of domestic systems, has a significant effect on the dynamic performance of the tank.

4. *How much hot water can a tank deliver on an off-peak tariff against typical demand profiles and can this be improved?*

Whilst chapters 4 and 5 indicate that choosing stainless steel over copper and fitting a diffuser will enhance static and dynamic modes of operation respectively, chapter 6 explores whether combining these two features makes a significant difference to the overall thermal performance of the tank when operating on an Economy 7 tariff. Draw events through a diffuser will inevitably result in a steeper temperature gradient throughout the stored hot water, this steeper temperature gradient will result in an increased rate of static mode de-stratification, an observation which begs the question: *'to what extent does the enhancement of dynamic mode*

performance, brought about by the inclusion of a diffuser, get eroded by a greater rate of static mode de-stratification that arises over a typical draw cycle?’

The key contribution from chapter 6 is the answer to the above question: ‘For a typical domestic draw cycle, a tank with stainless walls and a diffuser will out-perform a conventional copper tank with no diffuser, yielding more useful hot water over the course of the day when starting from the same initial state of charge.’

Once the themes outlined by questions 1 to 4 have been addressed, chapter 7 concludes with an overview of the research outcomes before detailing areas of further work that should, and in some cases currently is, being pursued.

Figure 1-11 shows a section view through a conventional hot water tank which is illustrated to show how the themes addressed throughout the thesis chapters relate to its physical layout:

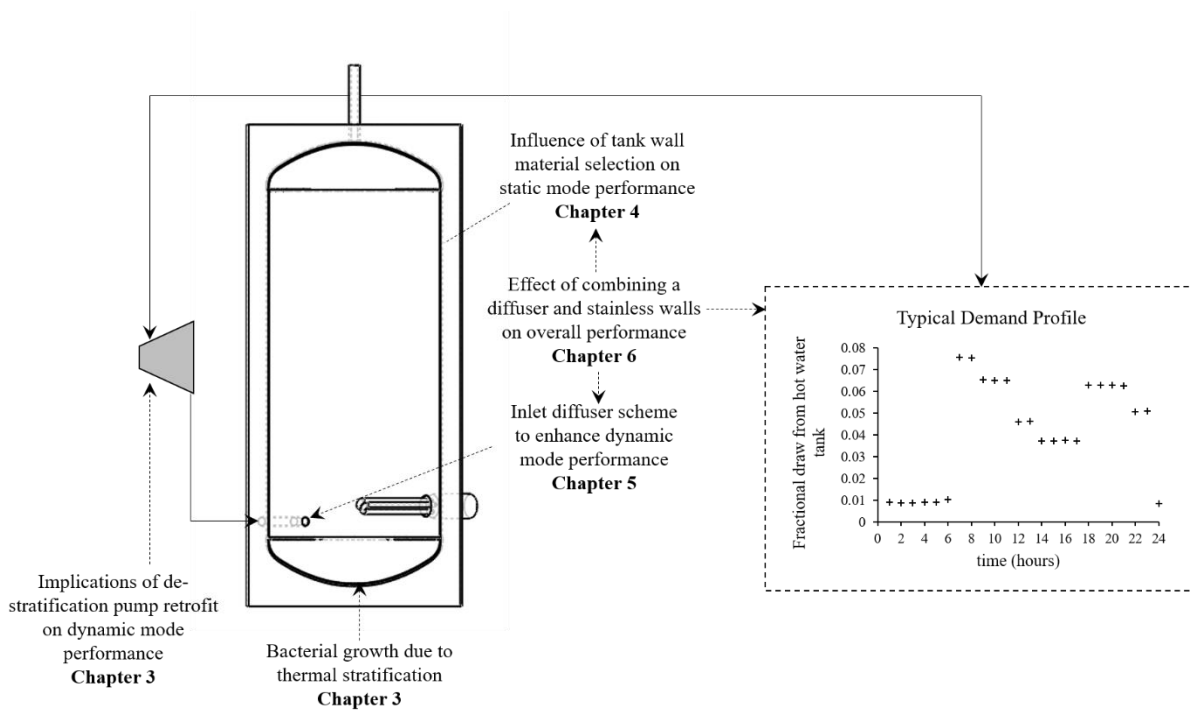


Figure 1-11 Illustration of how thesis chapters relate to the physical layout of a conventional electric hot water tank

2. A REVIEW OF THERMAL MODELLING TECHNIQUES

“All models are wrong, but some models are useful” – George E. P. Box

2.1 INTRODUCTION

If hot water tanks are to operate effectively as demand side management assets, it is important that they retain a useable supply of hot water over time during periods where energy is either expensive or unavailable.

In order to understand how the availability of hot water within a tank changes according to design and operating conditions, we need a combination of analytical, numerical and experimental models. These models are used to explore questions in later chapters such as: *‘how does the material used in the tank’s inner wall affect thermal performance?’* and *‘to what extent does inlet mixing affect the availability of hot water during a draw event?’*

To answer such questions with the data produced by these models, section 2.2 begins with a discussion of the metrics that will be used to evaluate thermal performance. All of the metrics will be associated with either a vertical temperature distribution throughout the tank, or an outlet temperature and its dependence on time for a given set of operating conditions such as flow rate, inlet temperature etc.

Predicting these temperature distributions, and how they change over time, will require numerical models. Before discussing numerical models, section 2.3 provides a presentation of dimensionless numbers that have been formulated to provide insight into the key geometric and operating considerations which have been identified in the literature.

Once an understanding of tank geometry and its influence on performance has been developed, we move on to consider numerical models in order of increasing complexity. One dimensional stratification models, discussed in section 2.4, allow for analysis of a tank over long timescales within a simulation of an energy system. However, such models fail to capture small scale phenomenon such as mixing between volumes of cold and hot water around the tank’s inlet during operation, therefore, section 2.5 introduces the theory behind Computational Fluid Dynamics (CFD). This thesis makes use of both 2 dimensional and 3 dimensional CFD models for simulation in later chapters and so these are discussed in sections 2.5.2 and 2.5.3 respectively. Ultimately, the fidelity of all models must be tested against experiment. A test rig, developed for the purposes of this project, is presented in section 2.6. This test rig is used to explore hypothesis and insights that have been gained through the numerical methods discussed earlier. Ultimately the criteria for a good model is the balance it strikes between its accuracy, the insights it reveals and its computational efficiency. Section 2.7 presents an overview of the models discussed in this chapter along with a justification for why the work described in this thesis for the most part relies on a mixture of CFD and experimental modelling.

2.2 THERMAL METRICS USED TO ASSESS OPERATIONAL PERFORMANCE OF HOT WATER TANKS

Before delving into the analysis that will be used to quantify the performance of hot water tanks, it is helpful to begin by considering the following system diagram.

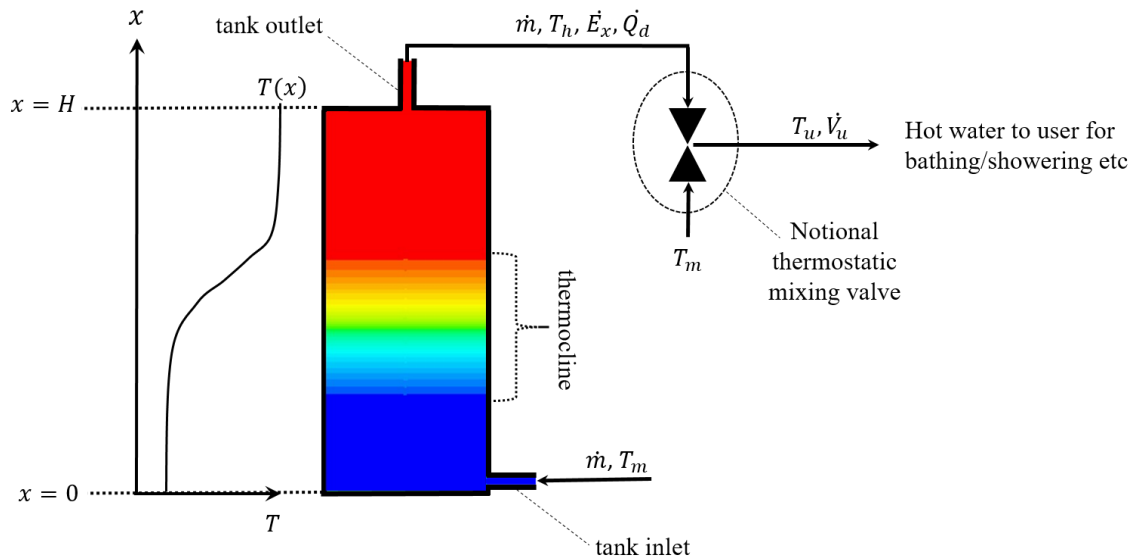


Figure 2-1 System diagram illustrating salient features of domestic hot water tank delivering hot water to a user

A cylindrical hot water tank with height, H and temperature distribution, $T(x)$ delivers hot water from its outlet at temperature T_h with a mass flow rate of \dot{m} kg/sec. The distribution, $T(x)$, is characterised by the presence of a thermocline which is a sudden transition in temperature associated with natural stratification [65]. Water flowing from the outlet at temperature, T_h , is mixed to a useable temperature, T_u with mains water at temperature T_m . This is achieved in practice either by using a thermostatic mixing valve or by the user of the system manually mixing water with a cold and hot tap.

To quantify the performance of the system depicted in Figure 2-1, some comparison must be made between the thermal energy that is extracted over time relative to the tank's initial state of charge. A number of approaches have been taken in the literature, these can generally be separated into *First* and *Second Law* approaches.

An example of a *First Law* approach is the discharge efficiency ratio formulated by Abdolyt et al [69]. The ratio is defined as follows:

$$\eta_d = \frac{Q_d}{Q_0} \quad (2-1) \quad \left| \begin{array}{l} \text{The discharge efficiency} \\ \text{from a hot water tank} \end{array} \right.$$

Where Q_d is the quantity of energy extracted from the tank and Q_0 is the initial quantity of energy stored within the tank. Due to the conservation of energy principle, η_d is always less than one due to standing heat losses from the tank's walls. In addition to this, a threshold was applied to Q_d such that all heat dispatched at a temperature less than 10% of the initial value for the outlet temperature, T_h , is ignored; in later experiments a figure of 20% was selected [69]. Later work applied a constant temperature as a threshold for domestic applications, for instance Castell et al who specify a value of 45°C [70]. Q_d can be calculated by considering the energy flux from the tank, \dot{Q}_d , over time, t :

$$Q_d = \int_0^t \dot{Q}_d dt \quad (2-2) \quad \left| \begin{array}{l} \text{Energy discharged from} \\ \text{a tank over time} \end{array} \right.$$

Where:

$$\dot{Q}_d = \dot{m}C_p[T_h - T_m] \quad (2-3) \quad \left| \begin{array}{l} \text{Definition of energy flux} \\ \text{from tank outlet} \end{array} \right.$$

For a given outlet mass flow rate \dot{m} , and heat capacity, C_p . Note that whilst computing (2-3), the change of tank outlet, mains inlet and ambient temperatures over time: $T_h(t)$, $T_m(t)$ and $T_a(t)$, are tracked. The initial state of charge of the tank can be determined by computing:

$$Q_o = \int_0^H m_T C_p (T(x) - T_m) dx \quad (2-4) \quad \left| \begin{array}{l} \text{Computing the energetic} \\ \text{state of charge of a tank} \end{array} \right.$$

Where H is the height of the tank and $T(x)$ is the vertical temperature distribution between heights $x = 0$ at the bottom of the tank and $x = H$ with the total mass of stored water being m_T . It is assumed in later chapters that the heat capacity of water is independent of temperature for domestic applications which is justified on the basis that C_p changes by just under 1% between temperatures of 25°C and 100°C [68].

When Abdolyt and Castell apply thresholds to the energy that is accounted for during discharge, they are recognising the fact that the value of energy is determined by the temperature at which it is dispatched. *Second Law* approaches consider this explicitly by the application of exergy analysis to thermal stores, an approach advocated by Dincer et al [71]. The formal definition of exergy is the maximum amount of useful work that can

be extracted from a unit of energy within its environment [72]. Exergy analysis is perhaps most commonly associated with the evaluation and design of thermal power plant and internal combustion engines [73]; however, there have been numerous applications of exergy analysis to domestic energy storage systems [74]–[76]. The rate of exergy drawn from a tank is calculated by multiplying the heat flux from the tank by the Carnot efficiency associated with its temperature:

$$\dot{E}_x = \dot{Q}_d \left[1 - \frac{T_h}{T_a} \right] \quad (2-5) \quad \left| \begin{array}{l} \text{Definition of exergy} \\ \text{flow rate from a hot} \\ \text{water tank} \end{array} \right.$$

Where: T_a is the temperature of the environment into which the heat is discharged. If we consider a draw event from the outlet of a tank, occurring over time t , then the total quantity of exergy extracted can be computed:

$$E_{xd} = \int_0^t \dot{E}_x dt \quad (2-6) \quad \left| \begin{array}{l} \text{Total exergy yielded} \\ \text{from a draw event} \end{array} \right.$$

Rosen et al considered the state of charge of the tank in terms of exergy [77], for a given instance in time this can be defined as:

$$E_{xsoc} = \int_0^H m_T C_p (T(x) - T_m) \left[1 - \frac{T(x)}{T_c} \right] dx \quad (2-7) \quad \left| \begin{array}{l} \text{State of charge of a tank} \\ \text{in terms of exergy} \end{array} \right.$$

In practice, the exergy within the tank at a given time instance will always exceed what is extracted by all subsequent draw events, assuming that no thermal energy is added, since $T_h(x)$ will be affected by both static and dynamic modes of de-stratification during operation. The overall exergetic efficiency of a hot water tank can now be expressed as:

$$\eta_{ex} = \frac{1}{E_{xsoci}} \sum_{n=1}^{n=N} E_{xdn} \quad (2-8) \quad \left| \begin{array}{l} \text{Definition of exergetic} \\ \text{efficiency of a hot water} \\ \text{tank} \end{array} \right.$$

Where designator n is used to signify one of a number of N draw events occurring from an initial state of charge, E_{xsoci} to the point at which the tank is fully discharged by the N^{th} draw event.

Whilst exergy analysis is undoubtedly important in determining the amount of mechanical work that can be extracted from a store of thermal energy, it is questionable whether this metric makes sense for a domestic hot water tank providing heat for bathing and cleaning activities. Consequently, in addition to the discharge ratio and

exergetic efficiency, this thesis will emphasis an alternative parameter referred to here as useable volume, V_u which was introduced into the literature in [78].

We define the useable volume as: *the quantity of water that can be delivered at a useful operating temperature*. The operating temperature will depend on the final application associated with a given draw event. The National Renewable Energy Laboratory (NREL) in the United States makes a distinction between tempered and un-tempered draw events from hot water tanks [79]. A tempered draw event occurs where cold water is mixed with the stream from the tank outlet until the user has a quantity of water delivered at a comfortable temperature, for instance a warm shower. An un-tempered draw event is delivered to appliances such as dishwashers and washing machines which draw a fixed quantity of hot water regardless of temperature. In the UK, modern washing machines and dishwasher equipment are rarely sold with a hot connection with water being heated instantaneously within the appliance itself instead [80], [81]; therefore, un-tempered draw events from UK domestic hot water tanks are uncommon and so will not be considered in this thesis.

The rate of useable volume yielded from the outlet stream of a hot water tank is defined as:

$$\dot{V}_u = \dot{m} \left[1 + \frac{T_h - T_u}{T_u - T_m} \right] \quad (2-9) \quad \left| \begin{array}{l} \text{Flow of useable volume} \\ \text{from tank outlet} \end{array} \right.$$

For domestic applications, the UK Care Association recommends that T_u is limited to between 41°C to 44°C depending on whether the application is bathing or showering [67] to avoid scalding. Throughout this thesis a value of 43°C is assumed since this is the maximum temperature output that *Bristan Ltd*, a leading plumbing component manufacturer, set for their bath/shower thermostatic mixing valves [82].

In a similar manner to equations (2-2) and (2-6), we can compute the total quantity of useable volume extracted from a draw event over a given period of time:

$$V_u = \int_0^t \dot{m} \left[1 + \frac{T_h(t) - T_u}{T_u - T_m} \right] dt \quad (2-10) \quad \left| \begin{array}{l} \text{Useable volume} \\ \text{yielded from a draw} \\ \text{event} \end{array} \right.$$

Along with the potential useable volume stored within a tank for a given vertical temperature distribution, $T(x)$:

$$V_{usoc} = \int_0^H m_T \left[1 + \frac{T(x) - T_u}{T_u - T_m} \right] dx \quad (2-11) \quad \left| \begin{array}{l} \text{Tank state of charge in} \\ \text{terms of useable} \\ \text{volume} \end{array} \right.$$

Using (2-10) and (2-11), we can evaluate the volumetric performance of a hot water tank in a similar manner to the exergetic efficiency described by (2-8):

$$\eta_{vu} = \frac{1}{V_{usoci}} \sum_{n=1}^{n=N} V_{u_n} \quad (2-12) \quad \left. \begin{array}{l} \text{Definition of} \\ \text{volumetric efficiency} \\ \text{of a hot water tank} \end{array} \right\}$$

In later chapters, the performance of hot water tanks that are subject to simulation and test will be evaluated in terms of η_d , η_{ex} and η_{vu} . This will allow for a fuller discussion of the implications associated with the use of such metrics when comparing the performance of different systems.

2.3 IMPORTANT DIMENSIONLESS NUMBERS ASSOCIATED WITH HOT WATER TANK DESIGN AND OPERATION

Dimensionless numbers provide a concise way of describing physical phenomena which can occur across a broad class of problems. Dimensionless groups of numbers can be formulated using the Buckingham Pi method [83], from which the most relevant parameters can be identified empirically through experiment or observation. Perhaps the most famous example is the Reynolds number, formulated by Osborne Reynolds to provide physical insights into pipe flow [84]:

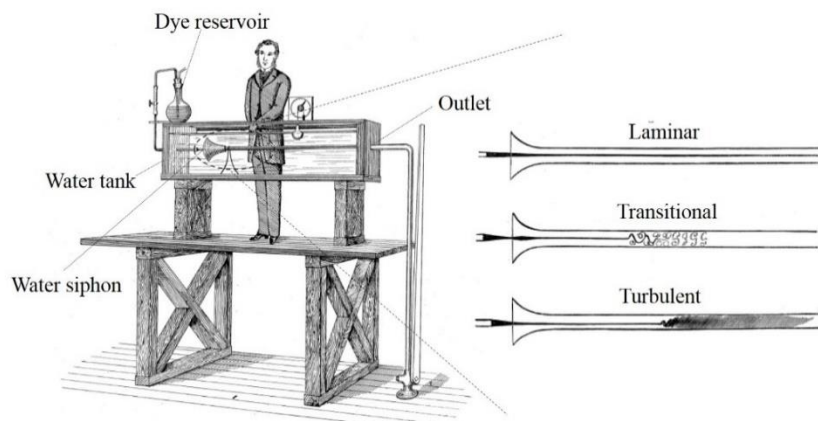


Figure 2-2 Reynolds Experimental Apparatus to Visualise Streamlines in Flow Through A Glass Pipe. drawings collected and annotated from original paper [84]

Figure 2-2 shows the apparatus originally used by Reynolds to visualise a dyed streamline as it progresses in water down the length of a glass pipe, illuminated by an electric spark. By adjusting a valve beyond the tank's outlet, the water flow velocity was controlled, a siphon at the pipe's inlet draws the water past the outlet of a small jet through which the dye is pulled. Reynolds observed that at very low flow rates, the dye would travel down a perfectly straight line. As the flow rate increased, the streamline would gradually wiggle before breaking up into alternating eddies. At higher flow rates, the streamline would breakdown to the point that the dye was fully mixed

with the flowing water. These three scenarios are referred to as laminar, transitional and turbulent flow regimes respectively [85].

The Reynolds number can be used to determine the approximate point at which the flow regime transitions from laminar to turbulence and is defined as:

$$Re = \frac{\rho UL}{\mu} \quad (2-13) \quad \left. \begin{array}{l} \text{Definition of the Reynolds} \\ \text{number} \end{array} \right\}$$

Where ρ is the fluid's density and μ is dynamic viscosity. L is a characteristic length scale, for instance the axial length down a pipe to define the onset of turbulence within the boundary layer or the diameter of a cylinder to characterise the onset of Von Karmen Street vortices[86], and U is the mean flow velocity. The Reynolds number also describes the onset of turbulence within surface boundary layers which results in a sudden increase in the local heat transfer coefficient along with the progression towards a turbulent plug velocity profile from a laminar to a parabolic profile as illustrated by Figure 2-3:

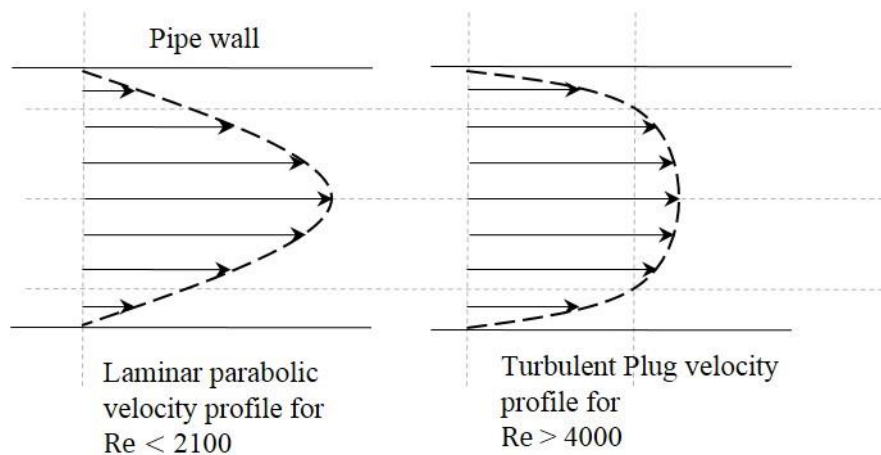


Figure 2-3 Illustration of pipe velocity profile for laminar and turbulent flow (see Street et al [87])

In chapter 5, where three dimensional CFD simulations were conducted, the cold inlet pipe length was selected such that a fully turbulent velocity profile was established before the inlet plume entered the tank.

The stratifying performance of cylindrical hot water vessels has been associated with their aspect ratio, which is defined by the tank's height over its diameter [70]:

$$AR = H/D \quad (2-14) \quad \left. \begin{array}{l} \text{Definition of a tank's} \\ \text{aspect ratio} \end{array} \right\}$$

Where H is the tank's height whilst D is the diameter. As the aspect ratio increases, the extent to which a stratified temperature distribution prevails over time is enhanced; however, the tank's surface area relative to its stored volume also rises leading to higher standing heat losses. Discussions in the literature have suggested that an aspect ratio of between 3 and 4 provides a good compromise between stratification and heat losses [88], [89]. However, the experimental evidence in the work undertaken by both Lavan et al in [88] and Khalifa et al more recently [90], involved tanks that had no thermal insulation. In chapter 4, the influence of aspect ratio with modern insulation parameters is explored using a 2d CFD axisymmetric model. The model accounts for the conjugate heat transfer which occurs between the water volume and metallic lining wall within the tank which is associated with the Nusselt number, a parameter that expresses the ratio of convective to conductive heat transfer [91]:

$$N_u = \frac{hL}{k_f} \quad (2-15) \quad \left| \begin{array}{l} \text{Definition of the Nusselt} \\ \text{number} \end{array} \right.$$

Where h is the heat transfer coefficient, L is a characteristic length scale and k_f is the thermal conductivity of the fluid. Determining values of h analytically has been achieved for vertical plates immersed in a fluid [92] by applying the simplifying assumptions associated with Prandtl's boundary layer theory [93]. The range of values for which analytical predictions for h are valid is determined by the Rayleigh number which is used to determine the transition point from conductive to convective modes of heat transfer around a surface which occurs as the local temperature gradient increases [91]:

$$R_a = G_r P_r \quad (2-16) \quad \left| \begin{array}{l} \text{Definition of the Rayleigh} \\ \text{number} \end{array} \right.$$

Where P_r , the Prandtl number, is given by [83]:

$$P_r = \frac{C_p \mu}{k_f} \quad (2-17) \quad \left| \begin{array}{l} \text{Definition of the Prandtl} \\ \text{number} \end{array} \right.$$

The Grashoff number, G_r is expressed as [70]:

$$G_r = \frac{g\beta(T_{top} - T_{bottom})H^3}{\nu^2} \quad (2-18) \quad \left| \begin{array}{l} \text{Definition of the} \\ \text{Grashoff number} \end{array} \right.$$

Where: ν is kinematic viscosity, g is acceleration due to gravity, β is the thermal expansion coefficient of water, $T_{top} - T_{bottom}$ are the temperatures at the top and bottom of the tank and ν is the kinematic viscosity.

In addition to characterising static mode de-stratification over time, through consideration of a tank's aspect ratio and the conjugate heat transfer between the water and wall volumes, the amount of dynamic mode de-stratification, or mixing that occurs due to a draw event, has been associated with the Richardson number. The Richardson number expresses the ratio of potential energy within a stratified temperature distribution over the kinetic energy possessed by the inlet flow stream [94], [95].

$$R_i = \frac{g\beta H(T_{top} - T_{bottom})}{v_s^2} \quad (2-19) \quad \left| \begin{array}{l} \text{Definition of the} \\ \text{Richardson number} \end{array} \right.$$

Where V_s is the mean inlet flow velocity. The Richardson number is closely related to the Reynolds number and Grashoff number [70], and can be expressed as $R_i = G_r \cdot R_e^{-2}$.

If we consider a tank heated to a homogenous temperature, under ideal circumstances, as cold inlet water is admitted, a steep thermocline is established segregating the thermal energy into a nearly discrete zone of hot water sitting on top of cold inlet water. As the inlet flow velocity increases, the momentum of the inlet jet overwhelms the buoyancy forces which maintain thermal stratification; consequently the jet impinges on the thermocline causing entrainment of hot water into the cold zone. This process results in mixing leading to a consequent destruction of exergy and useable volume. In experimental work, conducted by Cole et al, it was found that mixing within the tank became prevalent for Richardson numbers less than 0.25 [94]. A qualitative feel for the entrainment that arises as a vertical jet impinges on a thermocline was provided by time-lapse photographs which showed increasing entrainment at lower Richardson numbers [23]. However, in [96], the Richardson number is referred to merely as a 'correlating parameter' whilst Castell et al concluded in their work that the "*Richardson number represents qualitatively the stratification in a tank, but not quantitatively*" [70]. In chapter 5 it is demonstrated that by adding an inlet diffuser, the dependence of inlet mixing on flow rate is substantially eliminated and consequently the application of the Richardson number is no longer relevant.

2.4 APPROXIMATION OF THERMAL STRATIFICATION USING ONE

DIMENSIONAL MODELS

Whilst dimensionless parameters provide useful insights into processes such as mixing and local heat transfer, to understand how a hot water tank behaves over time for a given draw cycle and set of thermal inputs, thermal stratification models, which provide resolution of the vertical temperature distribution, $T(x)$, over time, need to be formulated. The one-dimensional approaches, described in this section, greatly reduce computational expense to the point where it is feasible to simulate over timescales of many days and explore the implications of different demand side control strategies [54].

2.4.1 ANALYTICAL APPROACH

Cole et al presented the following coupled heat equation describing the interaction between the tank liner wall and water volumes [94]:

$$\begin{aligned} k_1 A_1 \frac{\partial^2 T_1}{\partial x^2} - \rho_1 C_{p1} A_1 v - \rho_1 C_{p1} A_1 \frac{\partial T_1}{\partial t} &= -h(x)l(T_2 - T_1) \\ k_2 A_2 \frac{\partial^2 T_2}{\partial x^2} - \rho_2 C_{p2} A_2 \frac{\partial T_2}{\partial t} &= h(x)l(T_2 - T_1) \end{aligned} \quad (2-20)$$

Coupled heat equation
describing thermal
exchange between tank
water and wall volumes

Where: subscripts 1 and 2 refer to water and wall properties respectively, C_p is the specific heat capacity, ρ is material density, k is thermal conductivity, T_1 and T_2 stand for temperatures as a function of position x for both the water and wall volumes, A is the cross sectional area, v is the average vertical flow velocity through the tank which is zero for static mode operation, x is the vertical position as shown in Figure 2-1 and l is the tank circumference.

Of particular interest is the parameter $h(x)$ which denotes the local film heat transfer coefficient between the wall and water. Cole et al were unable to derive solutions for (2-20); however an analytical solution with empirical coefficients was derived on the assumption that vertical conduction through the wall was negligible ($k_2 = 0$). However, both numerical and experimental work, discussed in chapter 4, demonstrates that vertical conduction through the wall has a highly significant influence on the rate of static mode de-stratification within the tank. However, by making $h(x) = 0$, Cole et al derived the following analytical solution to (2-20):

$$\frac{T(x) - T_m}{T_{init} - T_m} = \frac{1}{2} \left[1 + \operatorname{erf} \left(\frac{\frac{x}{H} - \frac{t}{t^*}}{2\sqrt{F_0} \sqrt{\frac{t}{t^*}}} \right) \right] \quad (2-21)$$

Analytical solution to
(2-20) where effects of
tank wall are neglected

Where T_{init} is the initial temperature throughout the tank at $t = 0$, t^* is a dimensionless time constant and F_o is the Fourier number.

Whilst (2-21) is limited in that it requires that $T(x)$ is constant for all x at $t = 0$, it is useful as the basis of an interpolant function to reduce the sensitivity of $T(x)$ estimates to individual vertical temperature sensor errors. These errors can corrupt the function used to interpolate between measurements as shown in Figure 2-4 [97]. By re-arranging (2-21), and assuming that the temperature distribution observed through measurement is a snapshot from a previous state in time, we can modify the equation to include variables: a , b and c :

$$T(x) = \frac{T_s - T_m}{2} \left[1 + \operatorname{erf} \left(\frac{\frac{x}{L} - a}{b} \right) \right] + T_m + c \quad (2-22)$$

Hypothesis function to provide a robust estimate of tank state of charge

(2-22) is used as a hypothesis function where parameters a , b and c are chosen such that the following cost function described by (2-23) is minimized [98], [99]:

$$J(a, b, c) = \frac{1}{2m} \sum_{i=1}^8 (T(x)^i - T_{me}^i)^2 \quad (2-23)$$

Cost function minimised to fit (22) to data

Where T_{me}^i is the measured data point and $T(x)^i$ is the interpolation value at measurement point i .

An alternative approach to interpolating between temperature measurements is through application of a cubic equation where splines are fitted such that the first and second derivative of the curve at either side of each sample point is equivalent [100].

Figure 2-4 shows $T(x)$ at a particular instant during testing that was undertaken during experimental work detailed in chapter 4. A 10% error was deliberately imposed on T_5 to compare the performance of hypothesis (2-24) and cubic interpolation methods. Whilst the splines are forced through every point, the hypothesis function is weighted by all measurements and so is less influenced by a single measurement error. Against the initial error free measurement, we get a deviation of $R^2 = 0.978$ compared to $R^2 = 0.993$ for the spline and analytical methods respectively.

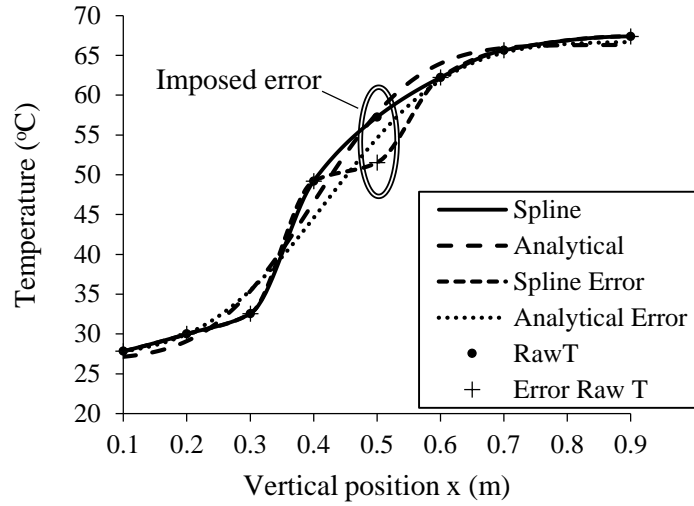


Figure 2-4 Vertical temperature measurements and imposed error to compare performance of hypothesis function versus spline fits

Later chapters of this thesis make use of the above approach when computing estimates of Q_o , E_{xsoc} and V_{usoc} .

2.4.2 ONE DIMENSIONAL NUMERICAL MODELS

Whilst section 2.4.1 showed that analytical solutions to the heat equations can be useful as interpolants for $T(x)$, for the purposes of determining the state of charge within a water tank, they are not suitable for simulating hot water tanks with different draw cycles and thermal inputs. This is due to the inflexibility of the boundary conditions that have to be imposed on (2-20) to allow for a solution to be derived. This section discusses a more flexible class of numerical models, in particular, the multi-node model discussed in 2.4.2.4 which has been used most extensively in the literature.

2.4.2.1 MIXED TANK MODEL

The simplest approach to simulating a hot water tank is to ignore thermal stratification altogether and assume that the tank is fully mixed at all times, as illustrated by equation (1-2) in section 1.5.2. To simulate the changing tank temperature over time, with varying thermal inputs, the following equation can be formulated:

$$m_T C_p \frac{dT_h}{dt} = \dot{m}(t) C_p [T_m - T_h] + h A_s [T_a - T_h] + Q_E \quad (2-24) \quad \left. \begin{array}{l} \text{Equation describing} \\ \text{Mixed tank model} \end{array} \right\}$$

Where the tank is at a homogenous temperature T_h , loses heat across a surface area A_s and has a thermal input Q_E . This approach has been taken to evaluate a demand side management control strategy by Paull et al [50]. However by ignoring thermal stratification, the mixed tank model provides a worst case scenario in terms of energy tariff utilisation, as will be demonstrated in section 2.4.2.5.

2.4.2.2 IDEAL STRATIFICATION MODEL

As discussed in section 1.5.2, the ideal performance of a tank would be where there is a perfect thermocline providing an instantaneous transition between the stored hot water and cold inlet water as illustrated by equation (1-1) section 1.5.2. In order to simulate the response of such a system over time, the mass of hot water stored in the tank, m_T , must be allowed to vary depending on whether cold water or thermal energy is admitted along with any heat losses to ambient:

$$m_T = \int_0^t \frac{Q_E(t) + hA_s \frac{m_T}{m_0} [T_a - T_s]}{C_p(T_s - T_m)} - \dot{m}(t) dt \quad (2-25)$$

Variable mass balance
associated with perfectly
stratified hot water tank

Where the initial volume of a fully heated tank is $m_T = m_0$.

2.4.2.3 PLUG FLOW MODEL

An elaboration of the ideal stratification model is a numerical scheme described by Cohen [96] called the ‘plug-flow model’. In this scheme, the tank is divided into segments with an associated temperature which approximates $T(x)$. At each time step, an energy balance is performed which accounts for any thermal input coming into the top of the tank from a source such as a solar collector or cold water admitted to the bottom of the tank, the corresponding top and bottom segments are re-sized at the end of the time-step and the net-change results in a corresponding shift of the thermocline region. The assumption that the temperature distribution moves in-tact is why the term ‘plug-flow’ is invoked.

2.4.2.4 MULTI NODE MODELS

In reality the performance of a tank will not be as bad as suggested by a fully mixed model nor as good as the ideal case. Whilst the plug flow model is an approximation between these two extremes, it assumes a fixed thermocline shape whereas in practice this may change over time due to vertical conduction or inlet mixing. Multi node models, such as those produced for the TRaNsient SYstem Simulation (TRNSYS) modelling environment, developed by the University of Wisconsin [101], are therefore widely used in the literature.

Figure 2-5 illustrates the energy balance performed around each vertical node used to represent the water volume within the tank:

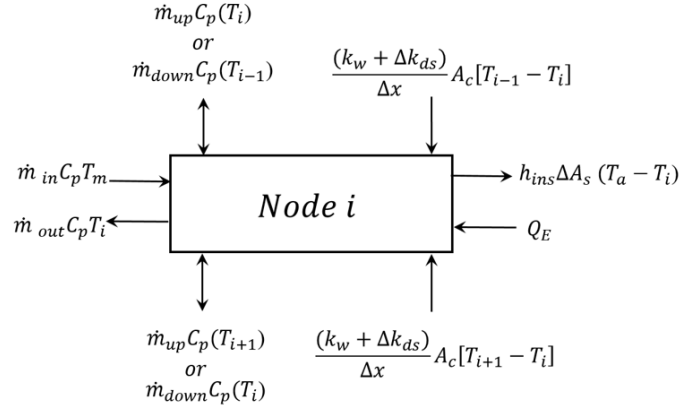


Figure 2-5 Energy balance around node within nodal model

Where k_w is the thermal conductivity of water. By assuming that the wall and water volumes are at the same temperature at each node, the model introduces Δk_{ds} , an additional conductivity term which accounts for de-stratification related to the tank wall. This term is determined empirically since in practice, convection currents around the inner wall surface add an additional convective heat transfer process [101], a topic discussed in more detail throughout chapter 4. Δx is the spatial step size along the vertical extent of the tank, \dot{m}_{up} and \dot{m}_{down} are mass flow rates due to inlets and outlets above and below node i whilst \dot{m}_{in} and \dot{m}_{out} denote mass flow rates directly into or out of node i , h_{ins} is the heat transfer coefficient associated with insulation applied over the node's surface area ΔA_s . With reference to Figure 2-5, a heat balance can be performed for each node such that:

$$\begin{aligned}
 \Delta m C_p \frac{dT_i}{dt} = & \dot{m}_{up \text{ or } down} C_p (T_{i+1}) + \dot{m}_{up \text{ or } down} C_p (T_{i-1}) \\
 & + \frac{(k_w + \Delta k_{ds})}{\Delta x} A_c [T_{i-1} - T_i] \\
 & + \frac{(k_w + \Delta k_{ds})}{\Delta x} A_c [T_{i+1} - T_i] + h_{ins} \Delta A_s (T_a - T_i) \\
 & + \dot{m}_{in}
 \end{aligned}
 \tag{2-26}$$

Energy balance performed around node in multi node model

To account for thermal stratification, multi-node models make use of a mixing algorithm [102]. At each time-step, the energy balance described by (2-26) is performed for all nodes. The temperature of nodes that are in receipt of a net thermal input, perhaps due to Q_E , might have risen to the point where $T_i > T_{i-1}$; or in other words, the temperature of a node may exceed that of the node above it resulting in a so called temperature inversion. On detecting a temperature inversion, the mixing algorithm combines nodes i and $i - 1$ such that they assume the same mixed temperature. If the two nodes, i and $i - 1$, exceed the temperature of $i - 2$, then the temperatures of all three nodes will be combined and so on until all temperature inversions have been removed. The mixing algorithm assumes that there is no vertical mixing beyond adjacent nodes where temperature inversions arise, this assumption was tested numerically by the team behind the TRNSYS commercial range of one-dimensional models

in [102] with reference to the theory of vertical plume entrainment provided in [103]. The procedure is illustrated in Figure 2-6:

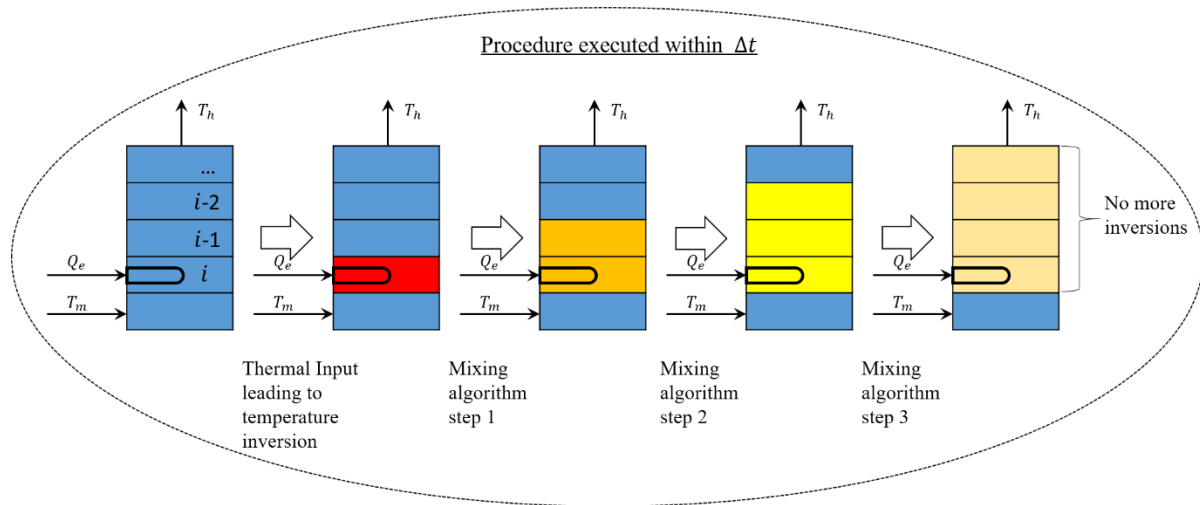


Figure 2-6 Illustration of mixing procedure applied to thermal input to one node within a timestep

A feature of the multi-node models is that the user is driven to select the appropriate number of nodes that best reflects the degree of stratification associated with the system modelled [101]; with 1 node representing a fully mixed state [104]. Lacroix et al [53] validated a tank model which was discretised into 20 nodes whereas Jordan et al [105] opted for 100 nodes for their simulation. Figure 2-7 illustrates the effect that the number of nodes has on the degree of dynamic de-stratification that arises during a simulated draw event:

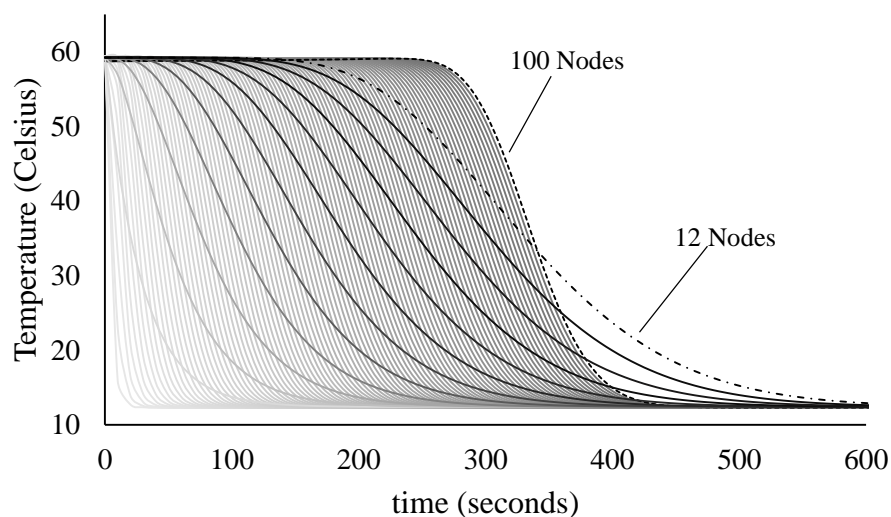


Figure 2-7 Influence of number of nodes on simulation of a draw event from a 76 litre tank at 15lpm.

The traces with a lighter colour refer to nodes towards the bottom of the tank whilst the solid black dashed line shows the temperature of the tank's top node, corresponding to the tank's outlet. Where 12 nodes have been used,

the outlet temperature begins to drop beneath 20% of its initial value at around 210 seconds, this increases to 310 seconds for the 100 node simulation. Whilst the total energy extracted from the two tank simulations after 600 seconds is the same, quantities of recovered useable volume and exergy are significantly greater for the 100 node case due to the greater degree of stratification occurring throughout the simulation.

Figure 2-7 illustrates the way in which numerical diffusion, which is an artefact of the truncation error associated with the finite difference approximation of (2-26) [106], influences the degree of dynamic mode de-stratification which is simulated. Equation (2-26) can be solved using a number of finite difference schemes. The time step size associated with any scheme will trade-off *truncation* errors (neglected terms in the Taylor series which increase with larger deltas) against *round-off* errors (neglected decimal points due to the finite word length possessed by a computer) [106]. The mathematical description of the TRNSYS model [101] references the embedded Crank Nicholson solver, described in [102]. This solver generates an internal time step based on the critical Euler criterion [107]. The user programming the TRNSYS model therefore only has a choice on the spatial time-step, Δx which is the prime source of numerical diffusion. However, there is little detailed discussion in the literature on the importance of numerical diffusion within TRNSYS multimode models. Whilst TRNSYS models are used in simulations by: Lacroix et al [53], Spur et al [108] and Buonomano et al [109], none of the authors make reference to numerical diffusion and how it affects the dynamic mode performance of the simulation. Jorden et al did acknowledge numerical diffusion briefly in their paper when they stated:

'Heat transport within the tank volume is modelled due to numerical diffusion, to be controlled by the number of storage layers chosen for each tank with parameter identification methods [105]'

However there is no detail on how they related inlet mixing to the number of nodes they selected for their model. Whilst using numerical diffusion to capture dynamic de-stratification might work for a given flow rate and inlet configuration, in practice there may be a variety of draw events demanded at different flow rates. Given the significance that flow rate has on inlet mixing within conventional tanks, discussed in chapter 5, it is questionable the extent to which multi-mode models can accurately simulate real world draw cycles.

2.4.2.5 COMPARISON OF ONE DIMENSIONAL MODELS

This section evaluates the models described throughout this section by simulating a tank operating according to an Economy 10 tariff [110] and ASHRAE hourly draw cycle as illustrated in Figure 1-2 from chapter 1 section 1.2. A conventional direct electric hot water tank, as depicted by Figure 2-1, is assumed. A single heating element in the bottom of the tank injects Q_E into the bottom of the tank under the following circumstances:

$$Q_E = \begin{cases} 3kW, & t_{opn} < t < t_{pn} \text{ AND } T(0) < 60^\circ\text{C} \\ 3kW, & T_h < 50^\circ\text{C until } T(0) = 60^\circ\text{C} \\ 0kW, & T_h > 50^\circ\text{C AND } t_{pn} < t < t_{opn} \end{cases} \quad (2-27)$$

Logic dictating when heating element is fired within simulated hot water tank

The heating element is fired whenever the temperature at the outlet, T_h is beneath 60°C and the simulated time is between the transition times for off-peak and on peak pricing designated as t_{opn} and t_{pn} respectively. This reflects the typical installation scheme associated with both Economy 7 and 10 tariffs within UK households where connections to heating elements are connected by a timed relay with a mechanical thermostat set to open when the temperature rises above 60°C . Outside of the tariff transition times, the heating element is also fired when the outlet temperature, T_h drops below 50°C , this reflects guidelines provided by the UK health and safety executive that hot water taps should attain a temperature of 50°C within one minute [111], in practice, there'll be a temperature drop between the tank and the taps due to the intermediary pipework, however in this analysis pipework losses are neglected.

The cost of energy is computed over time according to:

$$C_T = \int_{t_{start}}^t C(t) dt \quad (2-28)$$

Cumulative cost of electricity over time

Where t_{start} designates the time at which the cost starts to be accounted for, in this case $t_{start} = 24\text{hours}$ to allow the simulation to reach steady state before computing the daily cost thereafter.

$$C(t) = \begin{cases} \text{Peak Price,} & t_{pn} < t < t_{opn} \\ \text{Off Peak Price,} & t_{opn} < t < t_{pn} \end{cases} \quad (2-29)$$

Electricity cost as a function of time

The price switches between 7.9p/kWh and 19p/kWh for off-peak and peak hours respectively [30].

We apply the ASHRAE draw cycle [32] and cost function shown above to the multi-node model discussed in the previous section parameterised for a 120 litre hot water tank with a 1mm thick stainless steel wall with a height of 0.755 meters and a diameter of 0.45 meters. We assume that 120 litres of hot water are consumed over the course of 24 hours and by computing (2-26) across 50 nodes, we can resolve $T(x)$ at each instant in time. It is further assumed that a 50mm layer of polyethylene insulation, with a thermal conductivity of 0.028W/mK [112], is applied to the outside surface of the tank we arrive at the following temperature distribution over time throughout the tank:

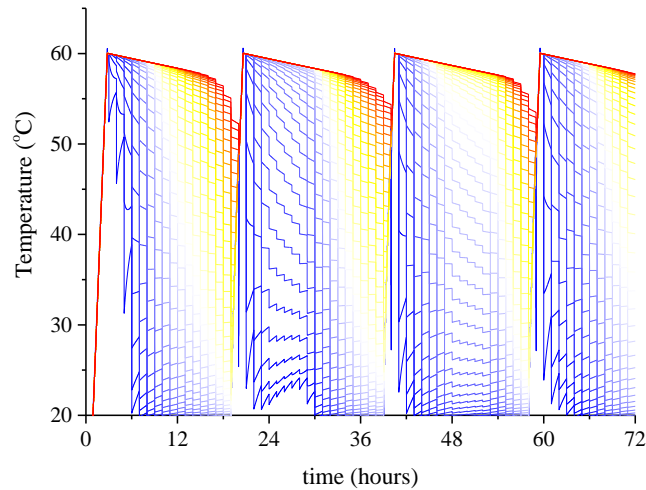


Figure 2-8 Vertical temperature distribution within 120 litre hot water tank simulated using multi-nodal model

The traces for each node are shown in Figure 2-8 with shading applied so that towards the red end of the spectrum we approach the top of the tank, T_h with the darkest blue associated with $T(0)$. The simulation ran for 72 hours with C_T being computed from 24 to 72 hours to reflect the steady state operating conditions. At the beginning of each hour, a fractional draw is implemented at a flow rate of 10 litres per minute, an associated step change in temperature distribution can be observed. Initially, the lowest (bluest) nodes change temperature most rapidly with the top nodes exhibiting a relatively flat response in temperature until the tank is close to being fully discharged; this reflects the behaviour of a real tank as the thermocline moves upwards as cold water is drawn into the bottom inlet. As discussed in the previous section, the number of nodes selected will determine the extent to which inlet mixing will occur, however an arbitrary selection of 50 nodes is used in this example since it is within the range of node numbers used in the literature [53], [105].

Figure 2-9 shows the output of the multi-node model against the two extremes associated with the mixed and perfectly stratified hot water tank models. The first thing to note is that the perfectly stratified model predicts that the outlet temperature stays constant at 60°C, reflecting the fact that the water tank is sized adequately to service the volume associated with all draw events that occur between the off-peak tariff periods during which the tank is recharged. The mixed and multi-node models exhibit a noticeable decrease in outlet temperature during operation. In the case of the fully mixed tank, the outlet temperature drops more rapidly resulting in frequent instances where $T_h < 50^\circ\text{C}$. These instances trigger the heating element to turn on according to (2-27). However, the outlet temperature, as predicted by the multi-node model, never drops below the 50°C threshold and therefore heating events occur only during periods where the off-peak tariff applies. Computing (2-28) from 24-72 hours yields costs of 74.5p/day, 60.9p/day and 39.7p/day for the mixed, multi-node and perfectly stratified models respectively.

The mixed and perfect stratification models took less than one second to simulate whereas the multimode model took 320 seconds on an Intel I7 2.4GHz processor. This is orders of magnitude faster than a full 3d CFD model, which in chapter 5, took one day to simulate a 1000 second draw event.

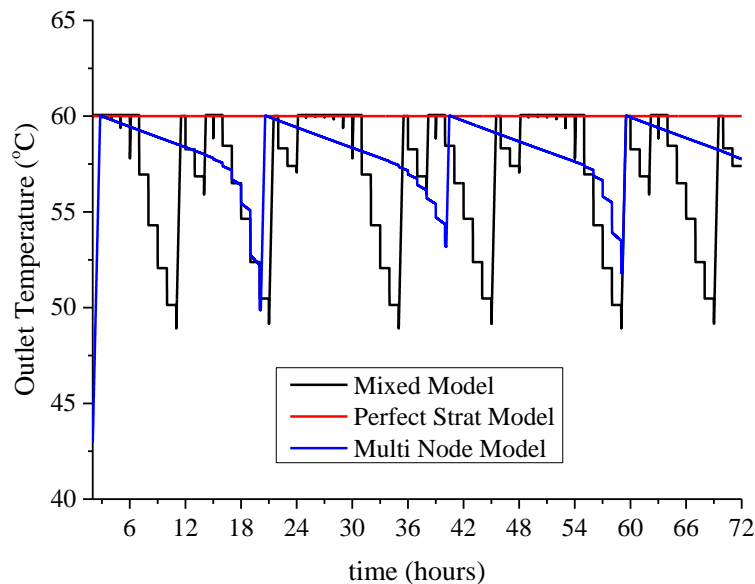


Figure 2-9 Comparison of mixed, perfect stratification and multi-node models

The results illustrate the wide difference in outlet temperature profile and cost predicted by the mixed, stratified and multimodal models. Whilst the multi-node model does provide a balance between the two extreme predictions associated with the best and worst case scenarios, the difficulty in linking numerical diffusion to inlet mixing in a rigorous way, across a range of flow rates, meant that more emphasis was placed on experimental and CFD models for the purpose of this thesis.

2.5 COMPUTATIONAL FLUID DYNAMICS (CFD)

Computational Fluid Dynamics (CFD) involves the discretization of the governing equations associated with a finite volume of fluid, these equations amount to statements of the conservation laws of physics: mass, energy and momentum [113]. CgcFD is widely used as a tool for understanding stratified hot water tanks in both dynamic and static modes of operation. For instance Altuntop et al, using a 3d CFD model, found that the presence of obstacles within the tank, such as baffle plates, led to an improvement in dynamic mode performance during operation [114]. Ievers et al [115] applied CFD to reveal a correlation between aspect ratio and static mode performance and in addition, showed that there was reduced mixing associated with mass flow from the inlet during charging at higher aspect ratios, compounding the benefits that a high aspect ratio brings in terms of reduced rates of dynamic mode de-stratification. In later chapters, this thesis makes use of both axi-symmetric 2d and 3d CFD simulations to shed light on static and dynamic modes of operation respectively.

This section goes into the theory behind CFD, the equations throughout are referenced from Versteeg et al [113] unless stated otherwise.

2.5.1 THE GOVERNING EQUATIONS

The governing equations, as used by commercial CFD packages, can be formulated via a number of different models of flow. Each model of flow gives rise to a different form in which the governing equation is stated, as illustrated by Figure 2-10 for the continuity equation which shows the fixed infinitesimal fluid element approach, (a), alongside the moving infinitesimal fluid element, (b), and finite control volume, (c). For the purposes of understanding physically what is going on, the particular form that the governing equation takes is largely irrelevant, indeed Anderson demonstrates the equivalence of different forms but discusses why the integral forms are more robust in the face of discontinuities that can be encountered in certain simulations within compressible flow fields [116]. For the purposes of this thesis however, these considerations will not apply.

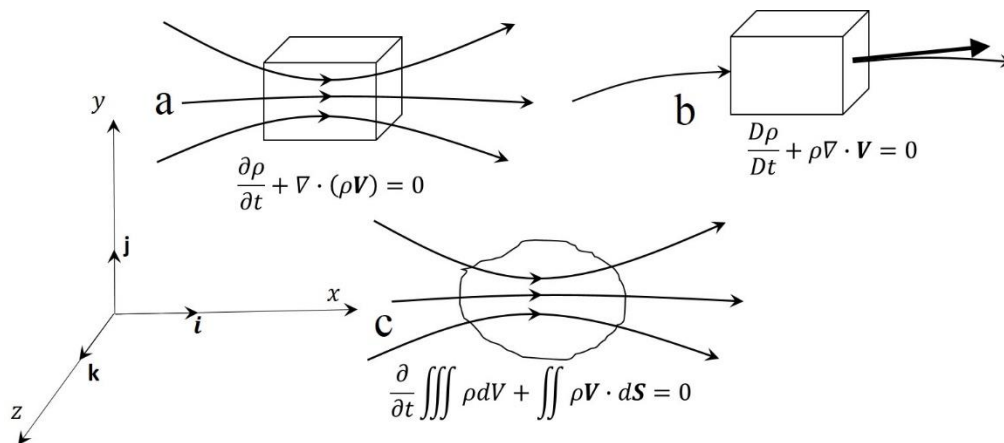


Figure 2-10 Different models of flow and how they give rise to different forms of the continuity equation. This figure is a simplified version of a diagram presented in [117]

2.5.1.1 CONSERVATION OF MASS

We begin by considering the conservation of mass principle which expresses the physical rule that any net flow of mass into a control volume must be balanced by the change in mass at each instant in time. By applying this principle to a point in Cartesian co-ordinates, for a compressible fluid, we arrive at the continuity equation:

$$\frac{\partial \rho}{\partial t} + \nabla \cdot (\rho \mathbf{V}) = 0 \quad (2-30) \quad \left. \begin{array}{l} \text{The continuity equation} \\ \text{in differential form} \end{array} \right\}$$

Where ρ is density, $\mathbf{V} = u\mathbf{i} + v\mathbf{j} + w\mathbf{k}$ is the velocity vector and ∇ denotes the divergence operator, $\nabla = \mathbf{i} \frac{\partial}{\partial x} + \mathbf{j} \frac{\partial}{\partial y} + \mathbf{k} \frac{\partial}{\partial z}$. The first term denotes the local change in density per unit volume whilst the second term, often

referred to as the convective term, expresses the net out-flow of mass across the boundaries of the element illustrated by Figure 2-10 a. For incompressible flow, the density is constant and the continuity equation reduces to:

$$\nabla \cdot \mathbf{V} = 0 \quad (2-31) \quad \left| \begin{array}{l} \text{The continuity equation} \\ \text{for incompressible flow} \end{array} \right.$$

Since the process of thermal stratification is driven by changes in density due to temperature variations, one might think that (2-31) is unsuitable due to the assumption of constant density. In practice, when simulating thermal stratification, it is more computationally expedient to assume that the flow is incompressible and to capture the effect of temperature related changes in local density by applying the Boussinesq approximation to the momentum equation instead. This is discussed in section 2.5.1.2 where an additional gravitational term is added to the momentum equation to account for the buoyancy forces associated with a non-uniform density [118]. Note the Boussinesq approximation of thermal stratification is not to be confused with Boussinesq's approximation of turbulence which is discussed in Section 2.5.1.4 and unfortunately shares the same name in the literature.

2.5.1.2 CONSERVATION OF MOMENTUM

The conservation of momentum principle reflects Newton's second law by stating that the rate of increase of momentum associated with a fluid element is equal to the total net force exerted by the surrounding boundary and body forces. Figure 2-11 illustrates an element of fluid traveling through space along with the body forces it encounters. One of the body forces is viscous shear which, for a Newtonian fluid, is proportional to the rate of change of the element's velocity in space [119]:

$$\tau_x = \mu \frac{du}{dx} \quad (2-32) \quad \left| \begin{array}{l} \text{Shear force due to} \\ \text{viscosity in x direction} \end{array} \right.$$

Where τ_x is the x-component of shear associated with velocity u and viscosity μ . The fluid element will also encounter forces due to the pressure gradient it encounters along with body forces such as gravitational, magnetic or buoyancy terms. The body force terms can all be considered to act on the element's centroid and are grouped and denoted collectively as S_M .

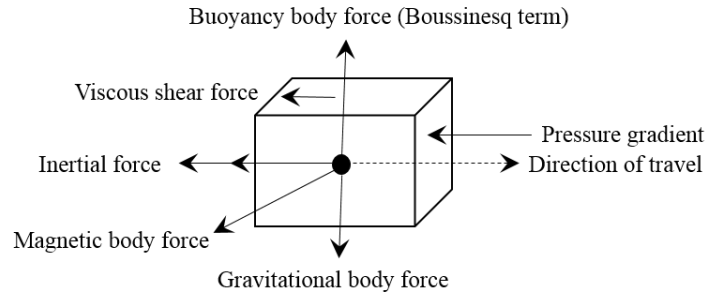


Figure 2-11 Illustration of forces acting on a fluid element which gives rise to the momentum equation

By equating all of the forces associated with the momentum equation to the inertial response due to acceleration in each co-ordinate, we can state the Navier Stokes equations as follows:

$$\begin{aligned}
 \rho \frac{Du}{Dt} &= -\frac{\partial p}{\partial x} + \nabla \cdot (\mu \nabla u) + S_{Mx} \\
 \rho \frac{Dv}{Dt} &= -\frac{\partial p}{\partial y} + \nabla \cdot (\mu \nabla v) + S_{My} \\
 \rho \frac{Dw}{Dt} &= -\frac{\partial p}{\partial z} + \nabla \cdot (\mu \nabla w) + S_{Mz}
 \end{aligned}
 \tag{2-33}$$

Inertial terms
Pressure gradients
Viscous shear forces
Body forces

The Navier Stokes Equations in cartesian coordinates for a Newtonian fluid as presented by Versteeg et al [120]

As discussed in section 2.5.1.1, when simulating a thermally stratified fluid field, it is convenient to assume that the fluid is incompressible and to adjust the constant of gravity as it appears within the body force terms as follows:

$$g' = g \frac{\rho_o - \rho}{\rho_o}
 \tag{2-34}$$

Adjustment of gravitational term to reflect change in density

Where g' is the adjusted gravitational constant for reference gravitational constant g associated with a reference density ρ_o . The actual density ρ is a function of temperature and can be deduced from a look up table of fluid properties, for example see Douglas et al [121].

2.5.1.3 CONSERVATION OF ENERGY

In order to simulate thermal stratification, the internal energy, E_i , and associated temperature of a fluid element must be tracked. This is achieved via application of the first law of thermodynamics, namely the conservation of energy principle. By applying this principle to a control volume we arrive at the energy equation, which for an incompressible flow can be expressed as:

$$\underbrace{\rho \frac{DE_i}{Dt}}_{\text{Internal Energy}} = \underbrace{k\nabla^2 T}_{\text{Thermal diffusion}} + \underbrace{\Phi}_{\text{Viscous dissipation}} + \underbrace{S_i}_{\text{Energy Source term}} \quad (2-35) \quad \left. \vphantom{\rho \frac{DE_i}{Dt}} \right\} \text{Conservation of energy}$$

On the left hand side, the change in internal energy associated with the fluid element, is tracked and equated to the thermal diffusion and viscous dissipation across the element's boundary surfaces. The viscous dissipation term, Φ , for an incompressible flow, is expressed as:

$$\Phi = \mu \left\{ 2 \left[\left(\frac{\partial u}{\partial x} \right)^2 + \left(\frac{\partial v}{\partial y} \right)^2 + \left(\frac{\partial w}{\partial z} \right)^2 \right] + \left(\frac{\partial u}{\partial y} + \frac{\partial v}{\partial x} \right)^2 + \left(\frac{\partial u}{\partial z} + \frac{\partial w}{\partial x} \right)^2 + \left(\frac{\partial v}{\partial z} + \frac{\partial w}{\partial y} \right)^2 \right\} \quad (2-36) \quad \left. \vphantom{\Phi} \right\} \begin{array}{l} \text{Dissipation due to shear} \\ \text{stresses across fluid} \\ \text{element's boundary} \\ \text{surfaces} \end{array}$$

2.5.1.4 TURBULENCE MODELLING

Turbulence, where the motion of a fluid breaks down into a chaotic assortment of eddies occurring randomly over a wide range of length and time scales, is a ubiquitous phenomenon which greatly increases the diffusion of thermal energy within the flow. During turbulence, kinetic energy cascades from large eddies to smaller ones until, at the smallest length scales, the energy is dissipated by viscosity; this so called energy cascade is captured eloquently in the following poem:

*“Big whorls have little whorls
Which feed on their velocity
And little whorls have lesser whorls
And so on to viscosity”*

- Lewis F. Richardson [122]

This phenomena could be captured directly by simulating the governing equations using a very fine grid, referred to as Direct Numerical Simulation (DNS). However, the effect of viscous dissipation only becomes prevalent at very low Reynolds numbers ($Re \approx 1$) which applies only to eddies at very small length scales. For instance, Davidson demonstrates that to apply DNS of turbulence to a 100m high chimney with a 0.3m long wake; eddies of the order of 0.1mm would have to be resolved [123].

To avoid the computational expense associated with DNS of turbulence, Reynolds introduced the idea of separating the flow variables into a mean and fluctuating component [85] as illustrated by Figure 2-12. In the case of the x-direction:

$$u = U + u'(t)$$

(2-37) | Splitting of flow variable into mean and fluctuating components

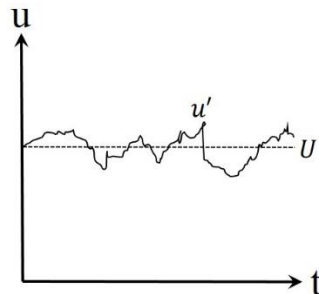


Figure 2-12 Illustration of a point velocity measurement within a turbulent flow based on an illustration in [124]

Substituting (2-37) for velocity in the momentum equation leads to the Reynolds Averaged Navier Stokes (or RANs) equations which for the x-co-ordinate can be expressed as:

$$\frac{\partial(\rho U)}{\partial t} + \nabla(UV) = -\frac{1}{\rho} \frac{\partial P}{\partial x} + \nabla \cdot (\mu \nabla V) + \underbrace{\left[-\frac{\partial \overline{\rho u'^2}}{\partial x} - \frac{\partial \overline{\rho u'v'}}{\partial y} - \frac{\partial \overline{\rho u'w'}}{\partial z} \right]}_{\text{Reynold's stresses introduced by time averaging NS equations}} + S_{Mx}$$

(2-38) | Reynold's averaged momentum equation in the x-direction with Reynold's stresses highlighted in green

Reynold's stresses introduced by time averaging NS equations

Additional terms, referred to as Reynold's stresses, have been introduced and are annotated on (2-38). Buchhave et al demonstrated that Reynold's stresses can be measured locally using laser doppler anemometry and that they usually greatly exceed viscous stresses in turbulent flow [125].

When time averaging the governing equations, additional terms also appear in the energy equation. These give rise to extra transport terms which lead to an increase in the rate of diffusion of heat throughout the flow.

Whilst the RANS equations provide an opportunity to circumvent the challenges surrounding DNS of turbulence, there are now more unknown variables than equations; this gives rise to the so called "closure problem". Turbulence models are designed to solve the RANS equations by introducing additional equations to account for

these unknown variables. One step in this direction is to invoke the Boussinesq eddy viscosity approximation (not to be confused with Boussinesq’s approximation for stratification, as discussed in Section 2.5.1.1). The eddy viscosity approximation treats the Reynolds stresses as though they were viscous stresses in a laminar flow regime [126], in tensor notation this can be expressed as:

$$-\rho \overline{u'_i u'_j} = \mu_T \left(\frac{\partial U_i}{\partial x_j} + \frac{\partial U_j}{\partial x_i} \right) \quad (2-39) \quad \left| \begin{array}{l} \text{The Boussinesq eddy} \\ \text{viscosity approximation} \end{array} \right.$$

Where μ_T is the turbulent viscosity. In an analogous manner, a turbulent diffusivity can be derived for the heat equation. This approach is taken by classical treatments of turbulence such as the mixing length and $k - \epsilon$ models, in spite of the fact that: “*the physics of turbulence is vastly different than the physics of the molecular processes that lead to the viscous stress law*” according to Pope [127]. At this stage it is useful to discuss some qualitative features of the most well known turbulence models that are currently used:

1. *Mixing length models*

Mixing length models (also known as zero equation models) apply Prandtl’s mixing length hypothesis which relates the turbulent viscosity to the local velocity gradient. The challenge with this approach is finding the appropriate length scale. Prandtl and Von-Karman define relationships between length scale and the element’s proximity to the wall, with separate functions for the laminar sublayer, transition layer and outer layer (discussed by White [128]). Whilst this approach is relatively light on computational requirements, it is not very generalizable and breaks down for flow regimes where the characteristic length scale associated with turbulence varies across the flow field; as happens when there is a significant amount of separation and recirculation.

2. *Two equation models*

To overcome the limitations associated with mixing length models, two equation models have been formulated to solve a wider class of problems. In particular, the $k - \epsilon$ model relates the turbulent viscosity to the turbulent kinetic energy and the rate of turbulence dissipation [127]. For flow close to boundary surfaces, where the no slip condition prevails, attention must be paid to ensure that the influence of the laminar sublayer is taken into account through the application of an appropriate wall-function. In these cases, the centroid of the first finite element must be located outside of the viscous and buffer layers, this can be achieved via reference to the law of the wall and computation of the local Y^+ values as discussed in [129]. Whilst the standard $k - \epsilon$ model performs poorly for complex flows, there are extensions of the model such as the RNG $k - \epsilon$ model and the Realizable $k - \epsilon$ model which can handle moderately complex flows along with jet-impingement [130] – an artefact of flow that is typical of a horizontal cold inlet feeding a hot water tank. Although $k - \epsilon$ models are widely used in comparison

to mixing length models, they are more expensive computationally to implement since two additional PDEs have to be solved at each time step.

3. *Reynolds stress equation models*

The Reynolds stress equation models have been developed to handle complex flows subject to strong body forces. In these applications, $k - \epsilon$ models often break down. Rather than applying the eddy-viscosity approximation, which assumes that the turbulence is equivalent to an isotropic viscosity, a set of equations to directly compute the additional Reynolds stress terms independently are used, these capture the true anisotropy of turbulence [131]. Whilst providing more generality, this approach is more costly to compute than the $k - \epsilon$ models since there are now seven additional PDEs.

4. *Algebraic stress model (ASM)*

The Algebraic Stress Model (ASM) is a compromise between the oversimplification associated with the Boussinesq turbulence approximation and the computational expense associated with simulation of all the Reynolds stress terms. The sum of the convection and diffusion terms of the Reynolds stresses is assumed to be proportional to the turbulent kinetic energy terms allowing the problem to be reduced to a set of simultaneous equations which can be solved algebraically. The Algebraic Stress Model is a low cost way to account for the anisotropy of turbulence however it is not as widely validated as the mixing length and $k - \epsilon$ models.

5. *Large eddy simulation (LES)*

The Large Eddy Simulation (LES) model takes a direct approach to the simulation of the mean flow and largest eddies that form throughout the flow-field. At smaller scales, the eddies are assumed to be isotropic and are modelled separately using the Boussinesq approximation as for the mixing and $k - \epsilon$ models (see Mathie et al [132]). The LES model has the advantage of capturing some of the features associated with eddies above a chosen scale without the computational expense associated with full DNS; however in comparison to the $k - \epsilon$ models and mixing models, the LES model is still comparatively expensive to run.

2.5.1.5 LIMITATIONS ASSOCIATED WITH CFD

The governing equations discussed above, along with whatever turbulence model is applied, forms a coupled system of non-linear PDEs which makes them difficult to solve analytically. A general solution to the Navier Stokes equation is one of the holy grails within the mathematics community, exemplified by a one million dollar prize from the Clay Institute to whoever is successful [133]. For now however, scientists and engineers must make do with numerical approximations to the governing equations to provide answers to real world problems. In addition to the approximate nature of numerical solutions to PDEs, it is important to also consider that there may be many assumptions inherent in a typical CFD model used for the purposes of simulating thermal stratification, these include:

1. Incompressibility, meaning internal viscous dissipation is ignored in the energy equation
2. Thermodynamic equilibrium, which implies that even for large flow velocities, the properties of a finite volume will change rapidly enough such that at each time step it is at equilibrium with its environment
3. The Boussinesq approximation of stratification to account for buoyancy which invokes the assumption of incompressibility
4. Temperature independence of fluid properties such as, specific heat capacity, viscosity and thermal conductivity.
5. The approximations introduced by the RANS equations when turbulent flow regimes are modelled which in turn depends on the specific turbulence model that is used.

Given all of these approximations and assumptions, it is crucial that the results of a CFD simulation are compared with experiment. In this thesis, CFD results are used to provide insights into the flow field which are hard to visualise directly.

2.5.1.6 COMMERCIAL CFD PACKAGES

For the purposes of computation, it is convenient to consider the governing equations in terms of the general transport equation and express them in integral form for generic flow variables ϕ and λ [134]:

$$\begin{array}{ccccccc}
 \text{Rate of increase} & & \text{Net rate of flow} & & \text{Rate of increase} & & \text{Rate of increase} \\
 \text{of } \phi \text{ of fluid} & + & \text{of } \phi \text{ out} & = & \text{of } \phi \text{ due to} & + & \text{of } \phi \text{ due to} \\
 \text{element} & & \text{of fluid element} & & \text{diffusion} & & \text{sources} \\
 & & & & & & (2-40)
 \end{array}
 \left. \begin{array}{l}
 \text{General transport} \\
 \text{equation used for finite} \\
 \text{volume method}
 \end{array} \right\}$$

The finite volume method involves applying the above equation to each control volume, CV, as below:

$$\begin{array}{ccccccc}
 \iiint_{CV} \frac{\partial(\rho\phi)}{\partial t} dV & + & \iiint_{CV} \nabla(\rho \phi \mathbf{V}) dV & = & \iiint_{CV} \nabla^2(\lambda \phi \mathbf{V}) dV & + & \iiint_{CV} S_\phi dV \\
 & & & & & & (2-41)
 \end{array}
 \left. \begin{array}{l}
 \text{Integral treatment of a} \\
 \text{finite control volume in} \\
 \text{CFD}
 \end{array} \right\}$$

In practice, the control volumes are developed using a mesh solver which discretises the geometry associated with the problem at hand. This thesis makes use of CD-Adapco's Star CCM+™ CFD package to create the mesh and apply the appropriate physics and boundary conditions which are then simulated using the software's solver. Star CCM+™ also has a range of tools to visualise the results that are produced. Whilst the meshing, physics and post-processing facilities within Star CCM+™ are very capable, the internal geometry package is limited. For this reason the Solidworks™ Computer Aided Design (CAD) package was used since it has powerful features such as:

1. The ability to define curves using parametric equations
2. Tools to produce complex manifold geometries by subtraction
3. Tools to create elaborate sheet features defined along arbitrary curves

The workflow associated with the CFD work undertaken for this thesis is illustrated by Figure 2-13:

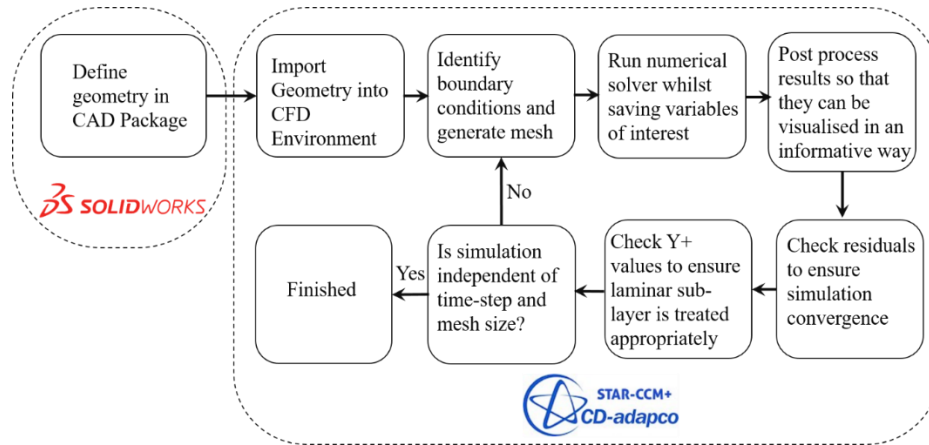


Figure 2-13 Workflow associated with CFD analysis described in this thesis

2.6 EXPERIMENTAL TEST RIG

“No one trusts a model except the man who wrote it; everyone trusts an observation, except the man who made it” – Harlow Shapley

Sections 2.4.2 and 2.5 discussed one dimensional stratification and CFD models respectively. Both approaches suffer from a number of limiting assumptions. In the case of multi-node one dimensional models, dynamic mode mixing is captured in a crude way through the use of numerical diffusion that is tuned by adjusting the node size. Whilst CFD models are more sophisticated, many assumptions are required to make computation feasible such as incompressibility, an isotropic turbulent eddy viscosity and the Boussinesq approximation of thermal stratification. The results produced by these models must therefore be viewed with scepticism until they can be compared with experiment. For this reason, an experimental test rig, illustrated by Figure 2-14, was built.

2.6.1 TEST RIG OVERVIEW

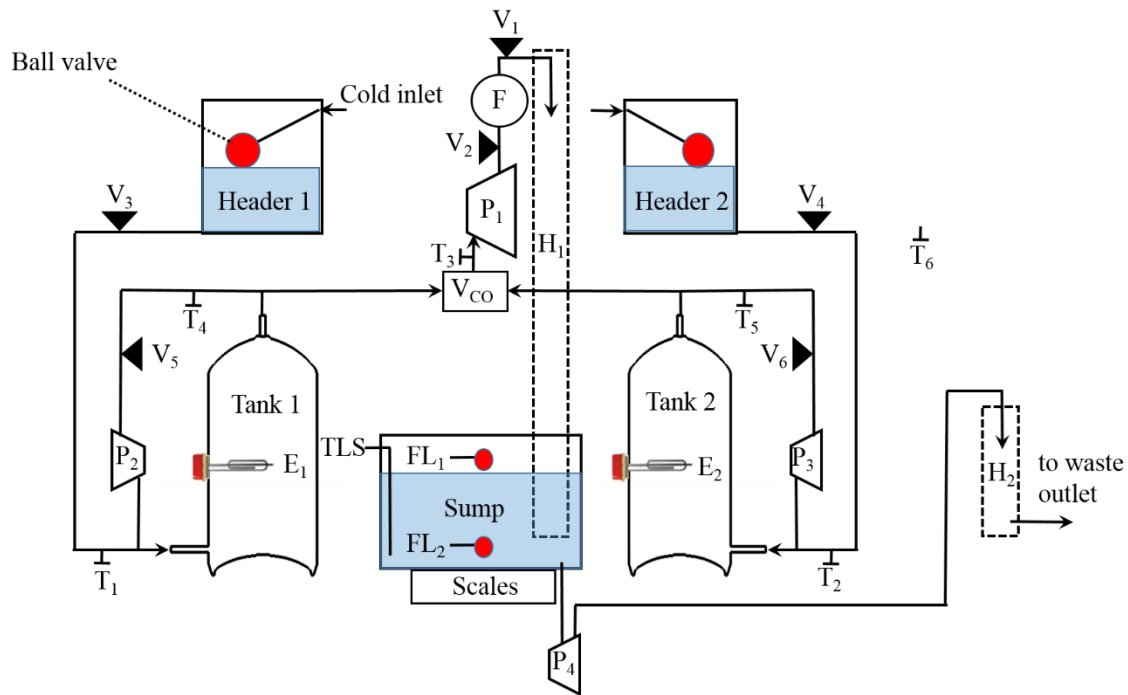


Figure 2-14 Schematic layout of tank test rig

The test rig was designed to undertake controlled draw events from two heated tanks, shown as tank 1 and tank 2 on Figure 2-14. Undertaking parallel tests in this way allows for design modifications to be tested in one tank against a baseline tank under identical environmental conditions. The two test tanks are fed by header tanks 1 and 2 whose level are maintained by a cold mains connected ball valve. Primary pump, P_1 , draws water from either tank via an electronically controlled change-over valve, V_{CO} . Having the primary pump downstream of the test tanks ensures that experiments won't be affected by bubbles released if pump cavitation occurs, a problem encountered by Lavan et al who had to discard results for this reason [88]. In addition to the primary pump, de-

stratification pumps, P_2 and P_3 were installed to mix tanks 1 and 2; this ensures that identical initial states of charge can be attained before undertaking a particular sequence of draw events. The water drawn from the test tanks was discharged, via a hydro-static non-return, H_1 , into a sump which has a level sensor installed and sits on electronic scales. Figure 2-15 is a photograph of the test rig which is annotated to show some of the main features illustrated in Figure 2-14:

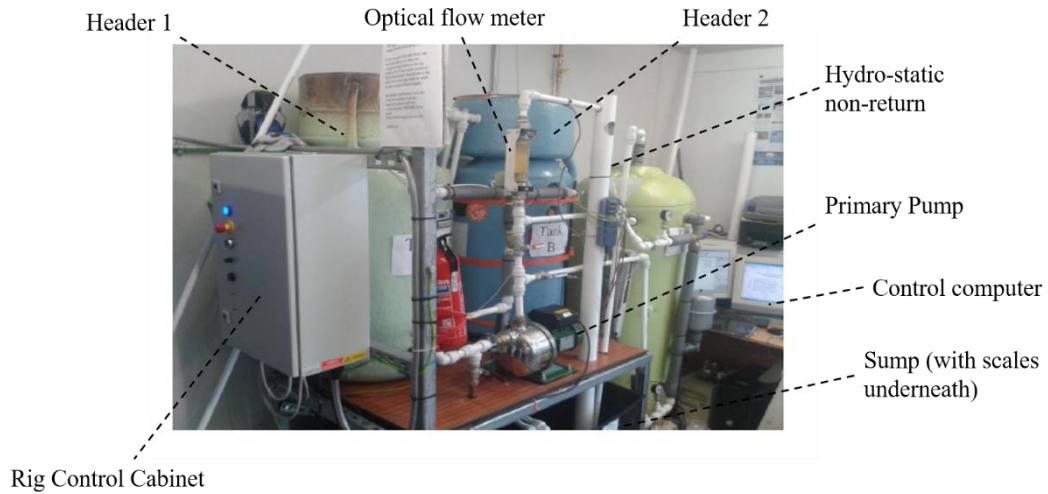


Figure 2-15 Photograph of test rig

Figure 2-16 shows the inside of the rig control cabinet. A 63 Amp mains connection is terminated to a set of fuses which breaks power out to the primary pump control inverter along with pump, valve and heating element control relays via the main safety contactor.

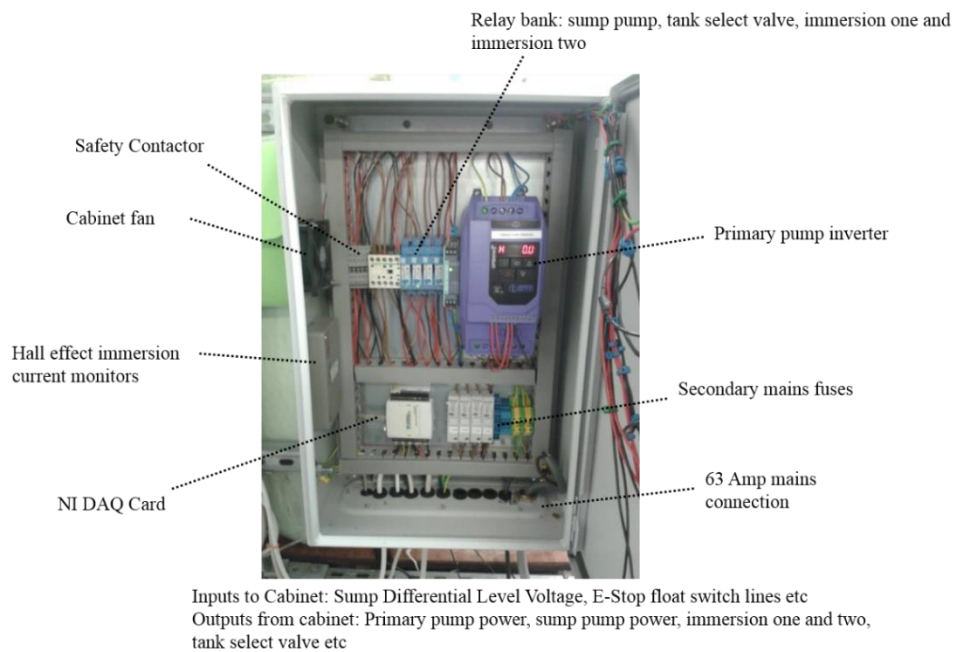


Figure 2-16 Photograph showing inside of rig control cabinet

The wiring scheme is shown in Appendix A.2, Figure A-3. A safety contactor provides an emergency stop circuit which de-activates the test rig by opening the live feeds in the event that: the emergency stop button, E_{stop} , is activated, or if the sump float switches, FL_1 and FL_2 are triggered; or if the cooling fan motor coils burn-out. This level of safety was required to enable the rig to operate autonomously for extended periods of time.

The control relays are operated by the digital control lines from a National Instruments data-acquisition (DAQ) card which is connected to a PC running Matlab Simulink™ in real time. The DAQ's analogue lines are used to control the primary pump inverter frequency and to read the current waveforms feeding the immersion heating elements which are measured by a pair of current transformers (CTs).

The full inventory of components used in the test rig is provided by in Appendix A.2, Table A-1.

2.6.2 FLOWRATE MEASUREMENT AND CONTROL

The changing level and weight of the sump is used to monitor the flow rate. This approach to flow rate measurement was taken because of the shortcomings associated with alternative methods. For instance, orifice plate and Venturi style differential pressure flow meters can be contaminated by particulate in the flow and suffer low accuracy for small flow-rates; calorimetric flow meters, such as hot wire anemometers suffer from limited responsiveness due to their thermal time constant and moreover can become contaminated by scale which precipitates on hot surfaces; rotary flow meters such as turbines and positive displacement units have moving parts and can incur a high pressure drop at large flow rates whilst indirect flow meters, such as ultrasonic Doppler or electromagnetic induction units are very expensive [135].

The sump capacity to the top overflow float switch is 110 litres and so the sump pump, P_4 , was periodically switched on during tests automatically using the level sensor and control algorithm to clear it. The level sensor, which produces an analogue 0-5volt signal across the depth of the tank was calibrated using the sump scales which have an accuracy of $\pm 0.01\text{kg}$. In practice, the minimum depth of the sump was 15 litres, to ensure that the sump pump didn't dry out. The maximum operating level of the sump, 95 litres, corresponded to an output voltage of 4.45 volts implying a volume of 106.7 litres at 5 volts. The ADC on the DAQ card has a 12bit register which translates to a resolution of 1.2mV implying that the mass of water in the sump could be determined to within ± 0.03 litres. The timing accuracy of the DAQ card is within 1ms and consequently the average flow rate of a typical draw event at 15lpm, lasting 30 seconds, could be measured to within $\pm 0.06\text{lpm}$ from the sensor. The sump scales could be used to independently verify the output of the sensor and were timed manually to within an accuracy of ± 1 second. The output of the sensor was calibrated against 120 second draws at different flow rates, given the mass and timing errors, at 15lpm, this translates to an error of $\pm 0.002\text{kg/sec}$ or $\pm 0.13\text{kg/minute}$. The operating temperature of the tank could be between 10°C and 65°C and so, considering that water's density changes by 2% across this range[121], the maximum flow rate measurement error is therefore 0.133lpm.

Control of the flow rate was achieved by varying the frequency applied to the primary pump. The primary pump is driven by a 2 pole induction motor. When an AC waveform is applied to the motor's stator, a rotating magnetic field is established which in turn induces current to flow in the motor's squirrel cage rotor. The resulting magnetic field, produced by the rotor's induced current, interacts with the rotating stator field to produce torque, see Slemon [136]. The rotational speed of the induction motor is determined by the frequency of the applied waveform along with the load torque on the motor's shaft which gives rise to slip. Slip is the ratio of speed difference between the rotating magnetic field on the stator and the physical speed of the rotor shaft. As the slip rises, the induced current on the rotor bars increases due to an increased rate of change of flux on the rotor bars creating a greater voltage potential according to Faraday's law. This mechanism makes an induction motor straightforward to control within its nominal operating range since any additional torque load is stabilised by a corresponding increase in slip and consequent rotor torque. The flow rate associated with each draw event was associated with an applied frequency which was determined experimentally. Sources of error associated with this approach include the changing density of water with temperature which effects the mass flow extracted for each rotation of the pump impellor. Other factors, such as changing mains voltage and bearing temperature would also have an influence. To determine the implication that these factors might have on repeatability, multiple measurements were conducted in succession where the inverter was set to run periodically at a set frequency whilst the resulting flow rate was observed. An example of this is shown in Figure 2-17:

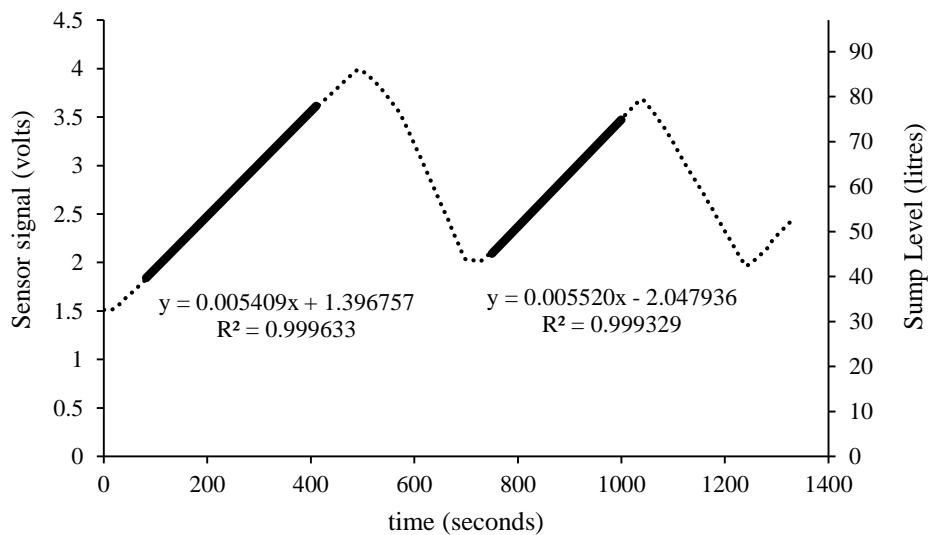


Figure 2-17 Sump draw test showing linearity and repeatability of measurement

In the above example, the primary pump was turned on after 3 seconds with an applied stator frequency of 24Hz delivering a flow rate of 7lpm for 500 seconds. The sump pump was then operated to drain the tank before the test was repeated. Trend lines are added to Figure 2-17 to show both the consistency of the flow rate during each test (linearity), along with the repeatability between tests (gradient). In the above example, the first and second

test were delivered at 6.93lpm and 7.07lpm respectively, a variation of 2%. Tests, conducted at 15lpm with flow temperatures of 15°C to 65°C indicated that the variability of flow rate was less than 4%.

2.6.3 WATER TEMPERATURE MEASUREMENTS

In order to determine the yield of hot water from a tank under a particular draw sequence, inlet and outlet hot water temperature measurements were performed using T-type thermocouples immersed into the fluid stream. The mechanical arrangement is illustrated by Figure 2-18. At each of the measurement points T_1 to T_6 , a 3mm hole was drilled through the side wall of the polyethylene 22mm plumbing pipework. A T-type thermocouple was then inserted before the hole was filled with silicon, wrapped in tape and fitted with a jubilee clip, this method proved to be reliable and quick to implement.

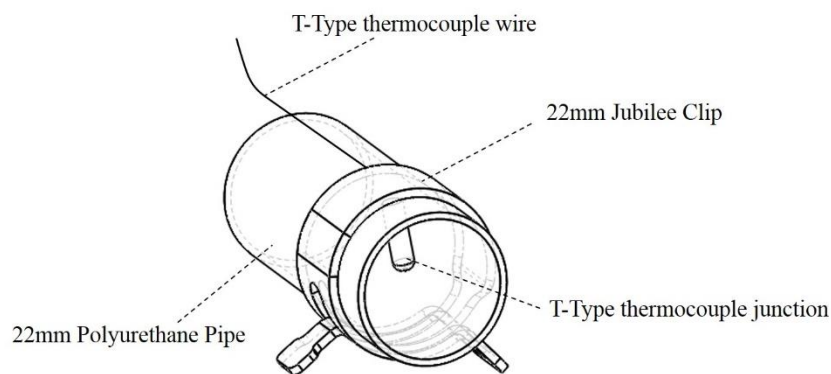


Figure 2-18 Thermocouple immersed into stream within pipe

In addition to fluid stream temperature measurements within the pipework, a vertical array of thermocouples was fitted to each tank to resolve $T(x)$, this was accomplished using the mechanical arrangement shown in Figure 2-19:

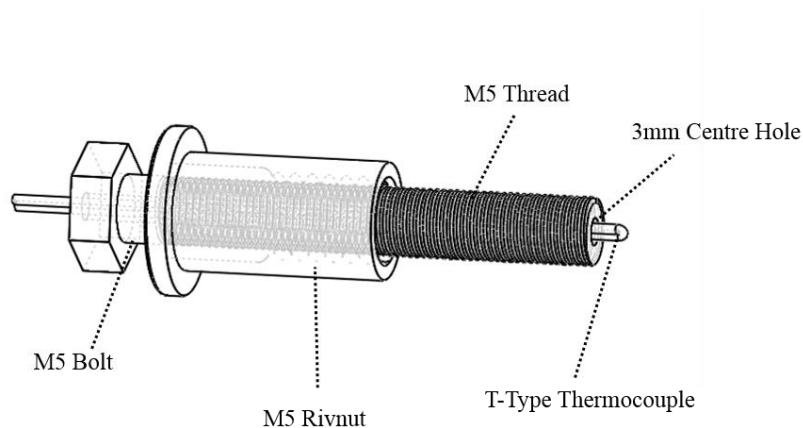


Figure 2-19 Thermocouple arrangement for insertion into tank wall

An M5 bolt was centre drilled to 3mm with a thermocouple inserted through it before being filled with silicon. At each measurement location in the tank wall, a hole to accommodate an M5 Rivnut was drilled before the Rivnut was inserted and secured using a rivet-gun. The bolt and thermocouple assembly could then be screwed into the tank wall with silicon applied to the outer threads to form a waterproof seal. Figure 2-20 illustrates a test tank which has been fitted with 8 thermocouple probes at isochoric intervals:

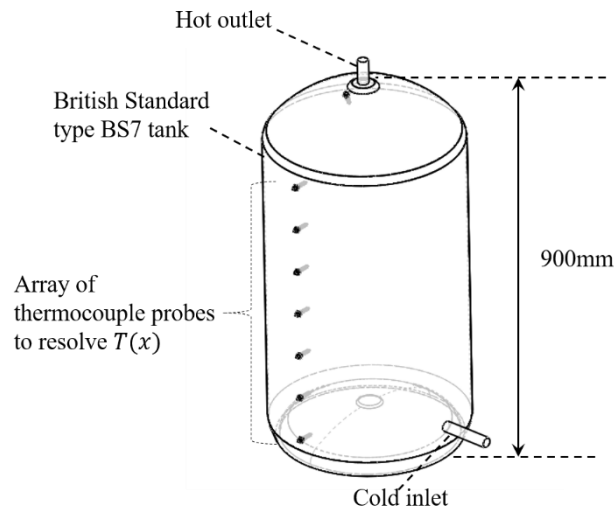


Figure 2-20 British Standard test tank with array of thermocouple probes fitted

The readings from the thermocouples were logged using a Picotech™ TC08 thermocouple data-logger. Thermocouples, which exploit the Seebeck principle whereby a temperature gradient across a conductor gives rise to a voltage potential, can be affected by a variety of sources of error such as: cold junction compensation error; linearity, gain and offset errors associated with the instrumentation amplifier and contamination of the junction itself [137].

To account for all possible sources of error, the complete instrumentation system, comprising thermocouples, logger and host PC, were calibrated against a platinum precision reference thermometer with an accuracy of $\pm 0.05^{\circ}\text{C}$ across a temperature range of -30°C to $+150^{\circ}\text{C}$. The calibration system, shown in Appendix A.2, Figure A-4, comprised of a temperature controlled water bath and a lid that was fabricated to include a mount to secure a motor with a stirring impellor on its shaft. 16 thermocouples could be calibrated simultaneously by immersing them in the water bath along with the precision reference thermometer. The bath was initially filled with wet crushed ice which was stirred to ensure a homogenous temperature across all measurement points. Once the temperatures had all settled to steady state, readings were taken against the reference thermometer at 5 temperature points as shown in Appendix A.2, Table A-2. Across the range of measurements that were taken, the highest discrepancy between any single channel and the precision reference was 0.46°C and the largest standard deviation across all channels was 0.38°C , this is consistent with the quoted accuracy for T-Type thermocouples which is $\pm 0.5^{\circ}\text{C}$.

2.6.4 ERROR ANALYSIS

Errors can be considered in quadrature where measurements are made independently of each other allowing for more precision to be assumed [138]. However, the thermocouple data-logger used on the test rig referenced all of the thermocouple junctions to a single internal cold reference. It is therefore not possible to rule out a common error across all temperature measurements and so a more conservative approach to error analysis is taken throughout this thesis. This approach is illustrated by equations (2-42) to (2-44) where the worst extremes associated with the useable volume, discharged energy and exergy measurements are calculated. These equations are used in chapters 3 and 5 to quantify the error bounds associated with experimental results.

$$\begin{aligned}
 V_u &= \int_0^t \dot{m} \left[1 + \frac{T_h(t) - T_u}{T_u - T_m} \right] dt \\
 +Err(V_u) &= \int_0^{t_s} (\dot{m} + \Delta\dot{m}) \left[1 + \frac{T_h(t) + \Delta T_h - T_u}{T_u - T_m - \Delta T_m} \right] dt \\
 -Err(V_u) &= \int_0^{t_s} (\dot{m} - \Delta\dot{m}) \left[1 + \frac{T_h(t) - \Delta T_h - T_u}{T_u - T_m + \Delta T_m} \right] dt
 \end{aligned} \tag{2-42}$$

Development
of uncertainty
associated
with extracted
useable
volume

$$\begin{aligned}
 Q_d &= \int_0^t \dot{m} C_p [T_h(t) - T_m(t)] dt \\
 +Err(Q_d) &= \int_0^{t_s} (\dot{m} + \Delta\dot{m}) C_p [T_h(t) + \Delta T_h - T_m(t) - \Delta T_m] dt \\
 -Err(Q_d) &= \int_0^{t_s} (\dot{m} - \Delta\dot{m}) C_p [T_h(t) - \Delta T_h - T_m(t) + \Delta T_m] dt
 \end{aligned} \tag{2-43}$$

Development
of uncertainty
associated
with extracted
energy

$$\begin{aligned}
 E_x &= \int_0^{t_s} \dot{m} C_p [T_h(t) - T_m(t)] \left[1 - \frac{T_h}{T_a} \right] dt \\
 +Err(E_x) &= \int_0^{t_s} (\dot{m} + \Delta\dot{m}) C_p [T_h(t) + \Delta T_h - T_m(t) - \Delta T_m] \left[1 - \frac{T_a(t) - \Delta T_a}{T_h(t) + \Delta T_h} \right] dt \\
 -Err(E_x) &= \int_0^{t_s} (\dot{m} - \Delta\dot{m}) C_p [T_h(t) - \Delta T_h + T_m(t) + \Delta T_m] \left[1 - \frac{T_a(t) + \Delta T_a}{T_h(t) - \Delta T_h} \right] dt
 \end{aligned} \tag{2-44}$$

Development
of uncertainty
associated
with extracted
Exergy

In chapter 4, section 4.3.2, a similar approach is applied to resolve errors associated with the measurement of $T(x)$ along with the tank's corresponding state of charge.

2.7 MODEL OVERVIEW

Table 2-1 provides an overview of the modelling approaches that have been discussed in this chapter. Whilst one dimensional models can be used to illustrate the benefits of thermal stratification, they are limited by their inability to accurately resolve dynamic-mode mixing from the cold inlet. Consequently, CFD and experimental models were used more extensively to pursue the research objectives discussed throughout the rest of this thesis.

Table 2-1 Overview of model types along with their associated advantages and disadvantages

<i>Model Type</i>	<i>Advantages</i>	<i>Disadvantages</i>
Dimensionless parameters	Quick to use Provide qualitative physical insights	Overlook important phenomenon (for instance presence or absence of a diffuser) Specific to particular geometries/flow regimes
One dimensional models	Efficient way to capture the behaviour of hot water tanks over long timescales. (Possible to simulate 3 days of operation in approximately 5 minutes for a 50 node model). Able to replicate dynamic mode de-stratification via numerical diffusion (less computationally intense than CFD turbulence models)	Numerical diffusion is a crude way to model inlet mixing which is likely to break down over a wide range of flow rates
CFD models	Can provide a relatively accurate prediction of how an arbitrary system will perform. Provides physical insights through visualisation of internal flow vector fields and temperature scalar fields	Very computationally expensive relative to tank operating timescales. (Takes approximately 1 day for a 250,000 node, 3d simulation of a draw event lasting 1000 seconds).
Experimental models	Provides a ground truth with which to assess models. Real time measurement is significantly faster than a CFD simulation	Expensive and time consuming to build a test rig. Difficult to adjust geometries and materials used within a test tank.

3. BACTERIAL GROWTH WITHIN HOT WATER TANKS²

3.1 INTRODUCTION

Chapter 2 set out the tools used to analyse a hot water tank from a thermodynamic perspective and in particular, the approaches that are required to capture thermal stratification. However, as discussed in section 1.3.3, thermally stratified hot water tanks have been associated with bacterial growth in the base of hot water tanks operating throughout Germany and Canada [55], [139]. This, coupled with uncertainty around the implications that more flexible control strategies might have on sanitary performance[53], led to the desire to understand the real world behaviour of hot water tanks in the UK. This would facilitate an understanding as to whether a conflict exists between thermal performance on the one hand and sanitary performance on the other. A set of microbial and laboratory tests were therefore conducted on hot water tanks operating within a sample of student flats in Summertown, Oxfordshire.

Section 3.2 provides background on the nature of bacterial growth, and in particular *Legionella*, within hot water systems along with instances of contamination that have been reported in the literature. The influence of wall materials such as copper and stainless steel are discussed along with the recommendation that large tanks are periodically de-stratified by a circulating pump.

To determine the extent to which there is a problem with bacterial growth within existing UK hot water tanks, section 3.3 details a small field study which was conducted with a view to determining whether growth can be attributed to thermal stratification. This involved retrofit of temperature sensing arrays along with microbial sampling over a two week period. The results of this study are discussed in section 3.4.

On discovering a significant preference for bacterial growth within the base of the cylinders, alongside temperatures that were chronically beneath the sterilising threshold for *Legionella*, one of the tanks were removed and retrofitted with a de-stratification pump to explore the implications that such a measure would have on dynamic mode performance. This work along with its results are detailed in section 3.5 with a summary of the findings provided in section 3.6.

²This chapter is based on two papers by the author published in *Journal Energy Policy and Applied Energy* ([199]and [200]).

3.2 DISCUSSION OF BACTERIAL GROWTH IN THE LITERATURE

Whilst there are many waterborne pathogens [140], domestic hot water design and inspection guidelines in the UK tend to be focused around the control of *Legionella*. The *Legionella* bacterium colonises biofilms that form on solid surfaces such as tank and pipe walls in plumbing systems [141]. Kooij et al demonstrated how *Legionella* can be cultivated on common plumbing materials such as copper, stainless steel and polyethylene within a domestic hot water system [142] whilst Shoen et al describes the process by which *Legionella* can become detached from the biofilm and infect humans when aerolised during a showering event [143]. Exposure to *Legionella* bacteria can lead to a form of pneumonia called Legionnaires disease, which in 2005 was fatal in 6.5% of reported incidences [144]. It is further estimated that only 10% of cases are correctly identified as *Legionella* with the remaining infections being misdiagnosed as flu or other ailments [144]. *Legionella* multiplies at temperatures between 25°C and 45°C with temperatures beyond 49°C leading to an exponentially increasing rate of bacterial sterilization [66]; this is illustrated by Figure 3-1:

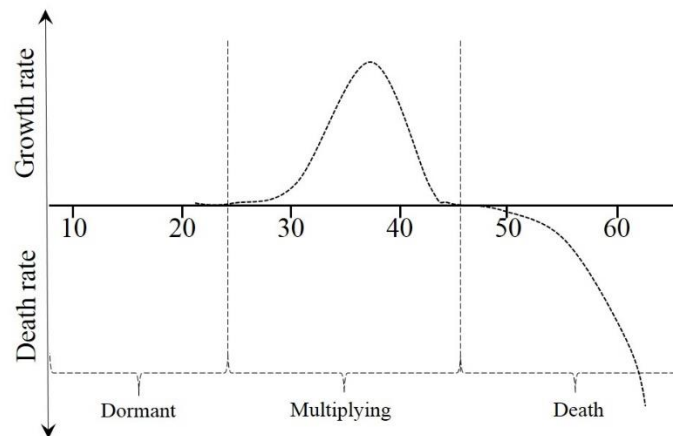


Figure 3-1 Qualitative illustration of *Legionella* growth rate against temperature, adapted from [145]

To avoid bacterial growth, UK guidelines stipulate that water should be stored at 60°C and reach 50°C at tap outlets within one minute of being opened; in addition, they recommend that de-stratification pumps are considered for large hot water stores to allow for periodic sterilisation of the whole system [111]. Hot water tanks, which are charged from renewable sources, such as solar collectors and heat pumps, often operate a back-up heating element to ensure that sanitising temperatures are attained on a weekly basis [146], [147]. This frequency reflects the slow growth rates associated with *Legionella* whose population takes approximately 18 hours to double at 37°C [145] compared to 20 minutes for *Ecoli* [148].

The prevalence of *Legionella* in domestic hot water systems has been reported widely in the literature, however the extent to which thermal stratification can be attributed is not clear. For instance, a large study in Germany, [139], found *Legionella* was present in 12% of homes that use a hot water tank whereas systems using an instantaneous hot water supply were free of contamination. In this study, however, single samples were taken

from the bathroom hot water tap and so it isn't possible to attribute the growth to stratification within the tank. Microbial samples, taken from 178 electrically heated tanks operating in Canada, tested positive for *Legionella* in 39% of the systems [55]. In this case, 500ml water samples were taken from the tank's drain valve, however in many UK hot water tanks, the drain valve is remote from the base of the tank itself and so stagnant water in the intermediary pipework may have an effect on the results. In [149] sample ports were fitted to a single hot water tank servicing 100 apartments in Denmark using a methodology discussed in [150]. The sample ports were located at top, middle and bottom positions on the hot water tank walls. However the temperature at the sample locations only ever ranged between 57°C and 60°C which, the authors conceded, was small in comparison to more typical hot water systems, consequently it is not possible to extrapolate these findings for smaller, more stratified UK domestic tanks. Given the shortcomings in the literature, to determine the extent to which thermal stratification influences bacterial growth within the tanks sampled for the Oxfordshire field study, samples were taken directly from the tank outlet and at the bottom of the tank using a sample probe and endoscope, detailed in section 3.3.2.

In summary, whilst there is evidence of prolific bacterial growth within hot water tanks, it is unclear from the literature whether this can be attributed directly to thermal stratification. As discussed in section 1.3.3, this in turn raises questions about the viability of demand side management control strategies intended to alleviate stress on energy systems since curtailment of heat to a tank may create conditions which are hospitable towards *Legionella*.

3.3 FIELD STUDY OF STUDENT APARTMENTS

120 and 166 litre copper hot water tanks, operating in ten student apartments within a single apartment block, were sampled for bacteria and instrumented with vertical arrays of temperature sensors over a two week period in Summertown Oxfordshire. Each hot water tank was fed from a single cold header tank located in the roof of the building. These apartments are designated as flat *a* to *j* on Table 3-1. On finding significant quantities of bacteria, a further 10 apartments, which had been uninhabited for two weeks, were sampled before and after the immersion heating element had been operated over a full cycle of off-peak heating to determine whether the tanks were capable of being sterilised during periods where there were no draw events. These additional apartments are designated letters *k* to *t*.

3.3.1 RETROFIT OF TEMPERATURE SENSOR ARRAYS

Since the apartments were inhabited throughout the period of the field trial, any interruption in hot water service had to be limited to less than 30 minutes. It was therefore decided that temperature sensors would be fitted to the outer surface of the copper wall behind the polyurethane insulation. Six temperature sensors were fitted from the very top, adjacent to the tank's outlet, down towards the bottom of the tank at isochoric intervals. The isochoric intervals were determined by drawing up solid models of the tanks based on a description of their dimensions provided in the British Standards [151]. Since the cylinders have a varying diameter towards the pressure relief

domes at the top and bottom, incremental volumes were extruded from the solid model to obtain the relationship between the vertical sensor position and the volume beneath as illustrated by Figure 3-2:

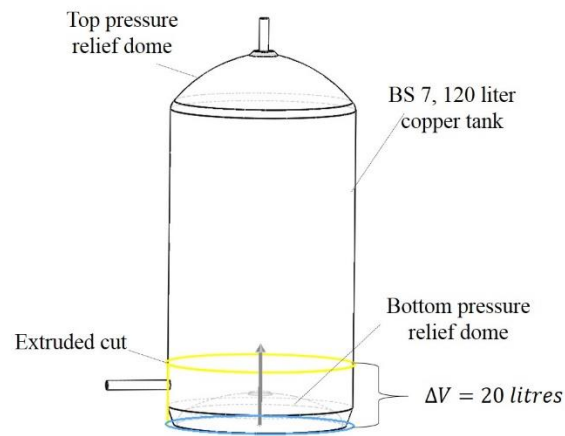


Figure 3-2 Illustration of extruded cut applied to tank solid model to deduce isochoric volume intervals

The sensing arrangement is illustrated by Figure 3-3 whilst Figure 3-4 shows a Raspberry PI which was used to log the data from the temperature sensors. Six Texas Instruments™ LM35 analogue devices with a quoted accuracy of $\pm 0.5^\circ\text{C}$ across a range of -55°C to $+150^\circ\text{C}$ with a linear output of $10\text{mV}/^\circ\text{C}$ were used [152]. The sensors were supplied in a TO-220 case style which provided a large surface area meaning they could be fastened to the tank wall using an adhesive tape. The sensors were wired to an Analogue Digital Converter (ADC) module via a ribbon cable. The ADCs aboard the module were MCP3422 units from Microchip™ and had an 18bit resolution over a scale of 0.3V to 4.7V [153]. Sources of error within the ADC include:

1. Limited resolution imposed by the least significant bit within its memory register. In the case of an 18 bit word length, this source of error is insignificant.
2. The input gain error which, in the case of the MCP3422, is 0.05% of its full scale which equates to $\pm 2.2\text{mV}$.
3. The offset error which, at $55\mu\text{V}$, can be considered negligible

The primary source of error is the ADC's input gain error which, when mapped to the range of the temperature sensor's output, amounts to $\pm 0.22^\circ\text{C}$. The error associated with the temperature sensor is assumed to be independent of the error contribution from the ADC and so taking the errors in quadrature, a total error in the temperature reading at the tank wall surface is estimated to be $\pm 0.55^\circ\text{C}$, see [138].

demonstrating the installation of the sensing arrangements on to the tanks. Once installed, the vertical temperature sensors were logged for two weeks.

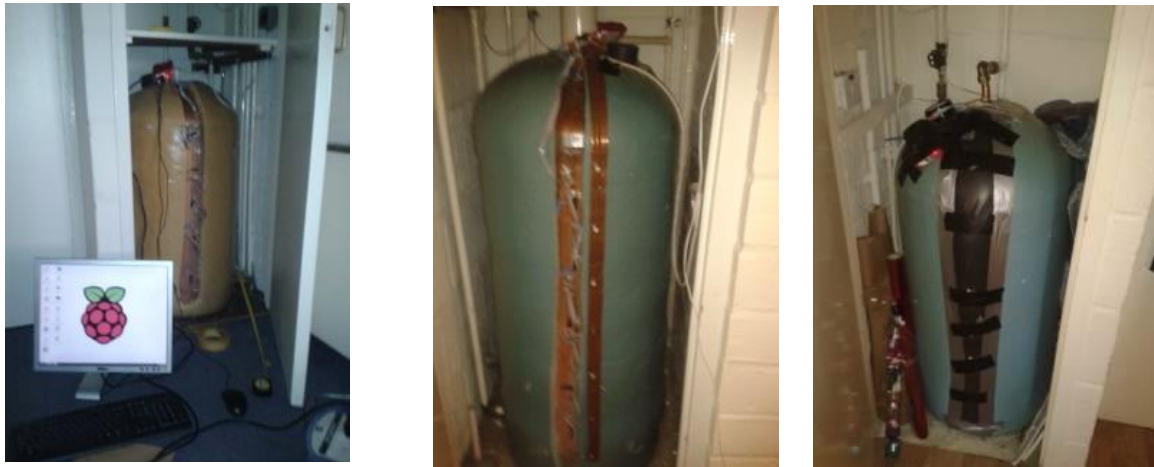


Figure 3-5 Photographs showing (left) hot water tank with sensors fixed to outer surface and raspberry pi powered up to verify operation (middle) close up of sensor arrangement fastened to tank wall outer surface. (Right) tank with sensors in place and insulation replaced with expanding foam held by polythene sheeting

3.3.2 BACTERIAL SAMPLE ANALYSIS

In addition to monitoring the vertical temperature distribution throughout the tank, water samples were taken to establish microbial levels. Section 3.2 discussed the limitations around previous field studies which fail to relate microbial levels to the vertical temperature distribution throughout the tank. To overcome this problem, water samples were taken from the top of the tank using the bathroom tap and from the bottom using a sample probe. The sample probe comprised of a 10mm stainless steel pipe with a machined scoop on the bottom and a 5mm PVC tube running through its centre to a manually operated syringe, see Figure 3-6:

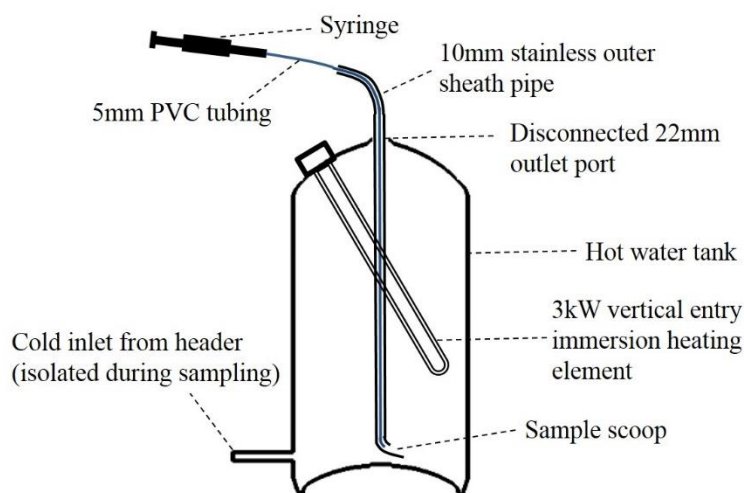


Figure 3-6 Cross section of sample scoop arrangement inserted into hot water tank

Figure 3-7 shows Meg Uapipatanakul, from Oxford's microbiology research group, assisting with the sampling process. The sample probe is being inserted into one of the tanks to retrieve a sample on the left photograph, the right photograph shows an endoscopic camera being used to take images of the bottom of the tank (Figure 3-8).



Figure 3-7 (Left) Meg Uapipatanakul from the Oxford Microbiology Research Group taking samples from bottom of tank using sample probe (right) endoscope camera inserted to take images of bottom of tank

The hot water tap in the bathroom was run for 20 seconds to ensure all intermediary pipework was cleared before taking a 500ml water sample using a sterilised bottle. Before extracting a sample from the bottom of the tank, the tank had to be isolated from the cold supply provided by the header tank. The outlet pipe was then disconnected from the 22mm compression fitting allowing access for the sample probe and endoscope. The sample probe was inserted until it made contact with the bottom of the tank at which point 500ml was drawn using the manual syringe. In each apartment, a control sample was also taken from the cold tap to check that bacterial growth couldn't be attributed to the cold supply. The probe and syringe was disinfected using alcohol between each sample. Once the sample had been taken, the endoscope camera was inserted to get an image of the bottom of the tank as shown for one system in Figure 3-8 which shows a thick deposit of calcium carbonate scale and biofilm which had developed:

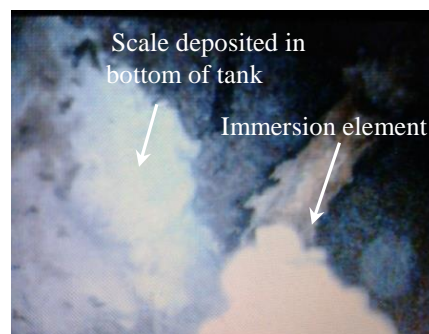


Figure 3-8 (left) image of bottom of tank (right) temperature data logger fitted to record temperature profiles over time

A second set of samples from 10 apartments, *k* to *t*, were taken by scraping the tank bottom with the probe scoop to capture the sediment in the tank for analysis of the bacterial growth within the mixture of biofilm and scale. The apartments had been uninhabited for a period of two weeks whilst renovation work was being undertaken, during this period the power to the hot water tank controllers had been disconnected. A set of samples were taken

before and after the heating elements were reconnected over a period of 18 hours. This was to see whether the tanks were capable of sterilising themselves without any draw events which would otherwise lower the temperature of the bottom of the tank during operation. During the heating period, T-Type thermocouples were fitted to the outer surface of the top and bottom of six of the tanks, apartments *k* to *p*, and recorded at one minute intervals.

Heterotrophic plate counts were taken from all water samples according to the protocol outlined in [154]. 1ml of sample water was added to 9ml of Maximum Recovery Diluent (MRD) for a 1 in 10 dilution, 1ml of the resulting solution was added to a separate container holding 9ml of diluent again for a 1 in 100 dilution and again for a 1 in 1000 dilution. Diluted samples were plated and incubated with sterility control plates at 37°C for 44 hours +/- 4 hours and 22°C for 68hours +/-4hours. After incubation, colonies were counted using a colony counter and magnifying glass. All colonies up to 300cfu/ml were counted, any plates in excess of 300cfu/ml had an estimate made using a Wolffheugel graticule. This procedure yields the total number of cells that can be cultivated at temperatures similar to the human body and is used by the water industry as a proxy for indicating the potential for pathogens such as *Legionella*. Whilst this test alone is insufficient to determine whether there is an immediate health risk, it can be used as a low cost investigative tool to determine whether one location provides more hospitable conditions for bacterial growth than another (see Bartram et al [155]).

The bacterial sampling for flats *a* to *j* were undertaken by water sampling contractor, Lattis Scientific Ltd, whilst samples from flats *k* to *t* were undertaken by Meg Uapipatanakul at Oxford University's microbiology research group.

3.4 FIELD STUDY RESULTS

3.4.1 TEMPERATURE READINGS

After two weeks of operation, the data-loggers, detailed in section 3.3.1, were removed so that the data produced by the temperature sensor arrays could be retrieved. Figure 3-9 shows a time series plot of the temperatures that were produced by the data logger operating within flat c, detailed in Table 3-1.

Over the course of the two week test period, the temperature at the bottom four sensor locations was beneath the 49°C sterilising threshold for *Legionella* bacteria at all times. At the very bottom of the tank, sensor locations T5 and T6, the temperature of the tank was beneath the 25°C threshold below which the bacteria becomes dormant and doesn't multiply. However, at sensor locations T3 and T4, the water temperatures were within the range hospitable for growth, 25°C ↔ 45°C.

The tank in flat c, along with the rest in the field study, was heated on an Economy 7 time of use tariff. One of the heating intervals has been circled on Figure 3-9. Over the course of this heating interval it is evident that the tank reaches the immersion element's thermostat temperature because of the sawtooth temperature variations which

are characteristic of hysteresis within the thermostat's bimetallic strip. At the end of this period, the temperature at locations T3 and T4 appear to be approaching steady state with temperatures at T5 and T6 slowly rising as a result of gradual thermal conduction from the hot water above. This would appear to result from the fact that the vertical entry heating element arrangement, as illustrated in Figure 3-6, doesn't extend all the way to the bottom of the tank. In the region of the tank in which the immersion element is immersed, convection around the heating element will ensure that heat is more evenly distributed whereas beneath the heating element, transfer of heat is via conduction which is much more gradual due to water's relatively low thermal conductivity. Periods where the temperature at the tank's outlet, T1, is beneath the sterilising threshold for *Legionella* due to cooling have been highlighted in orange to show periods during which the tank can be considered to be in a potentially unsanitary state. Instances where the outlet temperature drops rapidly due to a draw event are highlighted in red to show exposures to potentially unsanitary water. In the case of flat c, 7 potentially unsanitary exposures were recorded over two weeks with an average of 9 exposures across the seven tanks for which the data-loggers operated successfully, see Table 3-1.

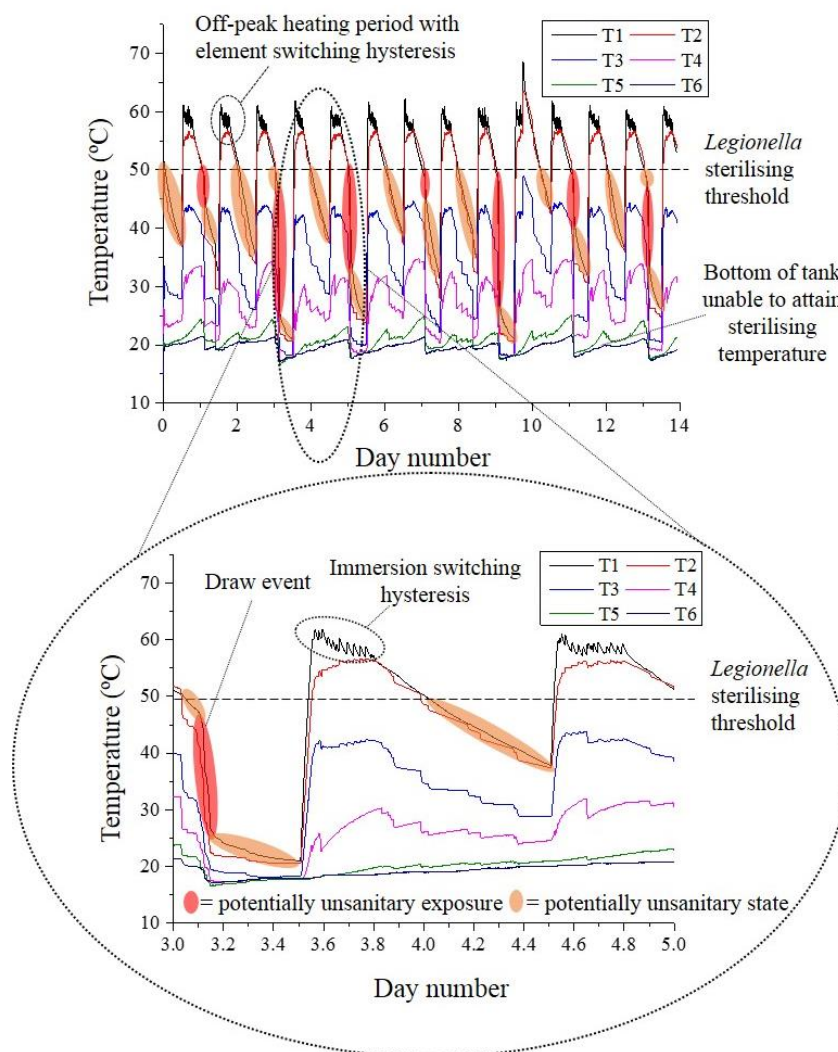


Figure 3-9 Temperature traces over two week period at flat c

Figure 3-10 shows the average mean, minimum and maximum temperatures which were recorded at each sensor location over the course of the two week trial period for all of the seven successfully monitored hot water tanks. For all tanks, maximum temperatures T5 and T6 were beneath the sterilising threshold for *Legionella* indicating that approximately one third of the volume of the tanks would remain chronically unsterilized.

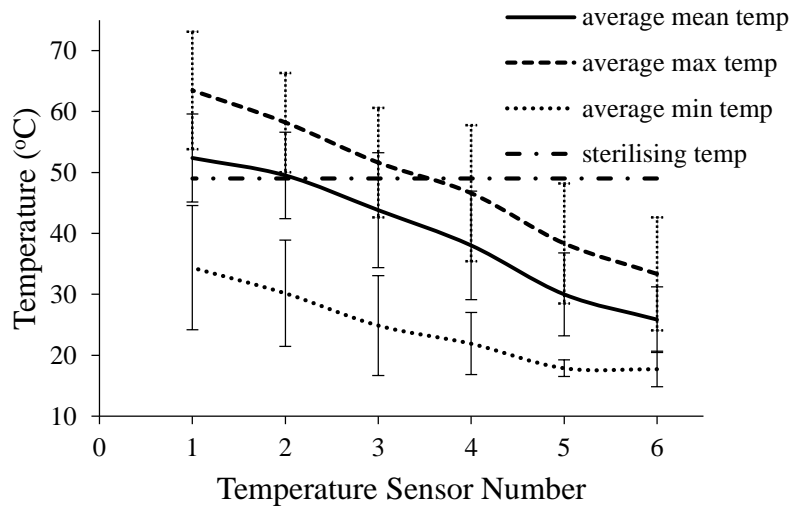


Figure 3-10 Average mean, minimum and maximum temperatures recorded across all successfully logged tanks at each sensor location with bars showing standard deviation across tanks

Figure 3-11 shows temperatures recorded at the top and bottom of tanks *k* to *p* whilst their controllers were reconnected to the mains supply over a period of 18 hours without use. It is evident from this figure that there is a wide range of thermostat temperature settings and that the bottom of the tanks fail to attain the sterilising threshold as was the case for flats *a* to *j*.

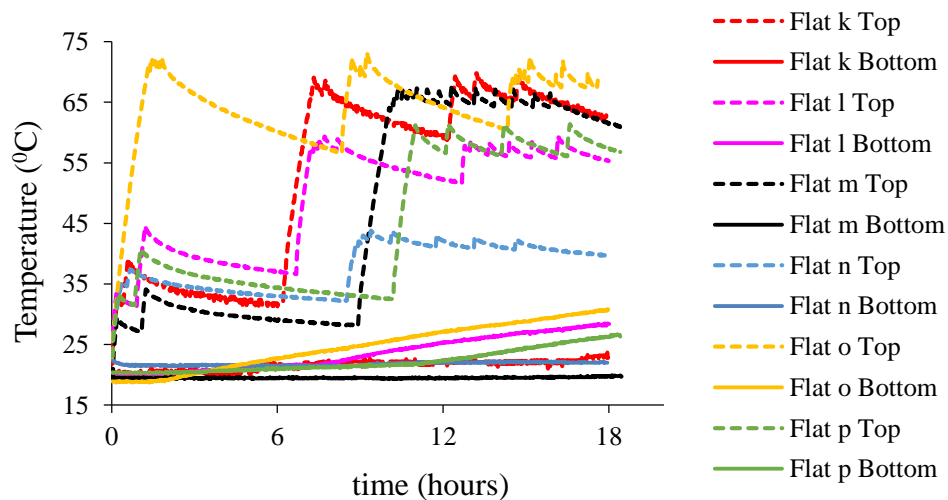


Figure 3-11 Temperatures at the top and bottom of tanks *k* to *p* during reconnection to mains power supply

3.4.2 BACTERIAL SAMPLE RESULTS

The bacterial sample results, associated with each tank within the inhabited apartments, are presented in the last two columns of Table 3-1. Of the ten tanks sampled, the bacterial growth in the bottom of 6 were in excess of 10,000 Colony Forming Units (CFU) per millilitre compared with one of the sampled taps. Given that the sample size was small and that the underlying probability distribution was unknown, the Mann Whitney U test, [156], was conducted to determine the statistical significance of the differing results for the tap and tank samples. The procedure, described by Ware et al [157], involves ranking the results and processing an algorithm to yield a U value which, using a look-up table, is then used to determine the statistical significance against the null hypothesis. In this case, the null hypothesis is that the difference between the tank and tap values are attributable to chance alone. With a U value of 9, the test indicated that the null hypothesis should be rejected with a significance of $P < 0.01$ providing a strong argument that conditions in the bottom of the tank are conducive to bacterial growth.

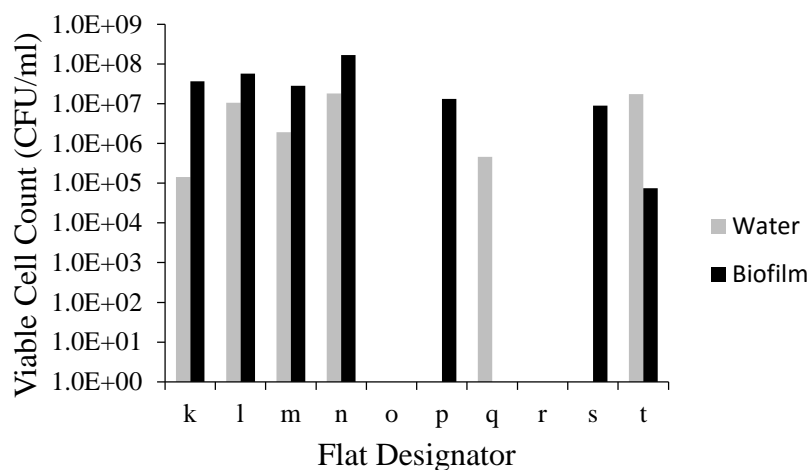


Figure 3-12 Bacterial counts in tank water and sediment samples before heating

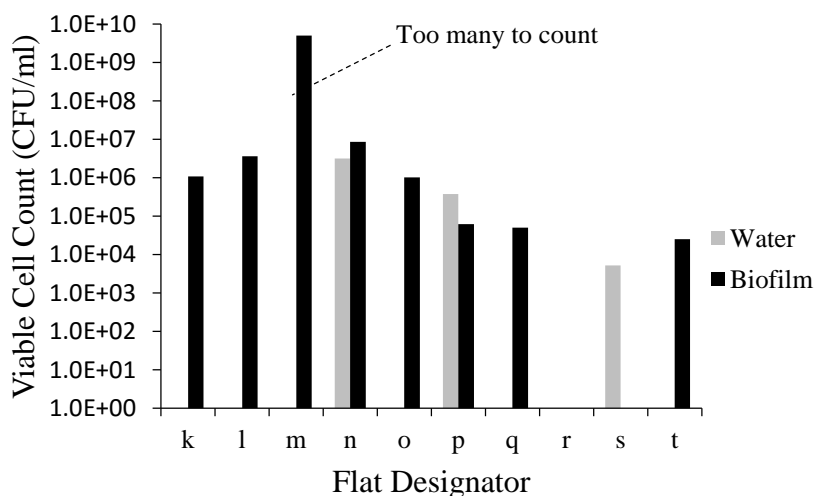


Figure 3-13 Bacterial counts in tank water and sediment samples after heating

Table 3-1 Details of inhabited flats sampled along with bacterial counts for bottom and top tank water samples

Flat Number	Number of Potentially Unsanitary Exposures (notes)	Number of Bedrooms/Tank Size (litres)	Bacterial Count (Bottom) (CFU/ml)	Bacterial Count (Tap) (CFU/ml)
Flat a	3	1/120	>10,000	>10,000
Flat b	10	1/120	>10,000	120
Flat c	7	2/166	4,455	10
Flat d	14	2/166	>10,000	13
Flat e	(Unoccupied)	2/166	>10,000	40
Flat f	14	1/120	715	10
Flat g	1 (Data-logger failure)	1/120	340	224
Flat h	12	2/166	6,930	162
Flat i	3	2/166	>10,000	120
Flat j	0 (Data logger disconnected after 14 hours)	2/166	>10,000	770
Flat k	NA	2/166	NA see figs	10 and 11
Flat l	NA	1/120	NA see figs	10 and 11
Flat m	NA	2/166	NA see figs	10 and 11
Flat n	NA	2/166	NA see figs	10 and 11
Flat o	NA	1/120	NA see figs	10 and 11
Flat p	NA	1/120	NA see figs	10 and 11
Flat q	NA	2/166	NA see figs	10 and 11
Flat r	NA	1/120	NA see figs	10 and 11
Flat s	NA	1/120	NA see figs	10 and 11
Flat t	NA	2/166	NA see figs	10 and 11

Figures 3-12 and 3-13 show the bacterial counts cultivated from the water samples before and after a period of 24 hours reconnection to the mains supply. Prior to heating, the average bacterial count across the triplicate samples in the water and sediment samples was 4.84×10^6 CFU/ml and 3.11×10^7 CFU/ml respectively. This changed to 3.51×10^5 CFU/ml and 1.6×10^6 CFU/ml for water and sediment samples after heating. Whilst the average counts across all samples was higher in the sediment than water, the U-test failed to indicate a statistically significant preference with a U value of 35. However, after heating the tanks, the U-test indicated a statistically significant preference for growth in the sediment ($P < 0.05$) with a U-value of 21. The reduced counts in the water samples after heating may have been due to slight convective mixing caused whilst the heating elements were operational leading to dilution.

3.5 LABORATORY TESTING OF STUDENT TANK

Since the bacterial sampling and temperature measurements indicated that bacterial growth was attributable to thermal stratification, the 120 litre hot water tank from flat *a* was removed and retrofitted with a de-stratification pump within the laboratory test rig detailed in chapter 2, section 2.6. The de-stratification pump would ensure that sanitary temperatures were attained throughout the tank, however the experiment sought to determine the effect that this measure would have on the dynamic losses within the tank during a draw event.

3.5.1 RETROFIT OF DE-STRATIFICATION PUMP

The tank was installed in place of tank A within the test rig shown on Figure 2-14. The schematic is redrawn in Figure 3-14 to reflect the aspects of the rig that were in operation. A photograph of the test rig is provided by Figure 3-15.

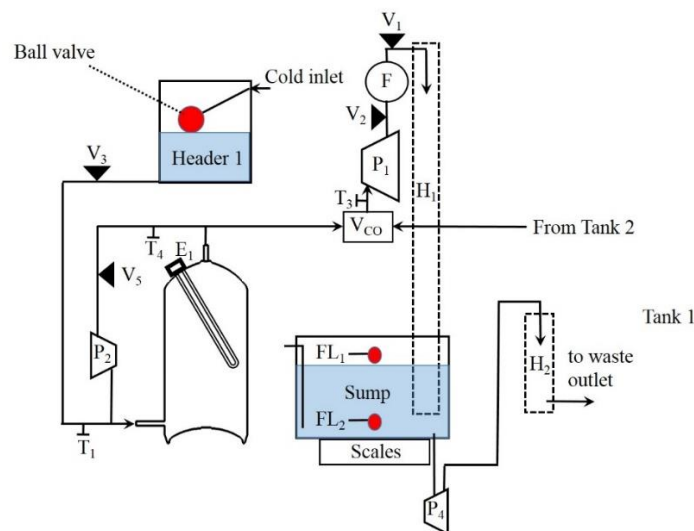


Figure 3-14 Schematic of test rig for testing influence of de-stratification pump on the dynamic performance of a BS 7 tank

Two tests were conducted, a baseline stratified test and a de-stratified test. In each test, the 3.2kW heating element was fired for 5200 seconds, delivering 4.62kWh of thermal energy. The mains voltage was observed to fluctuate by less than 5 volts over the day during which the tests were conducted (see Figure 3-16) and the immersion element's resistance was measured at 18 ohms +/-0.1 ohms giving a figure of 3200 W +/- 4% for each test taking the errors in quadrature. For the baseline stratified test, water was drawn from the tank's outlet at a rate of 15lpm +/-0.12lpm for 500 seconds whilst the inlet and outlet temperatures at T₁ and T₃ were monitored. The de-stratified test was identical in procedure except that whilst heating, valve V₅ was opened and the de-stratification pump was operated to ensure a homogenous temperature throughout the tank. After heating, the de-stratification pump was shut off and V₅ was closed. Prior to undertaking each test, the tank was fully flushed with mains water and the de-stratification pump was operated to ensure the initial temperature of the tank prior to heating was the same.



Figure 3-15 Photograph of tank from flat a retrofitted with destratification pump

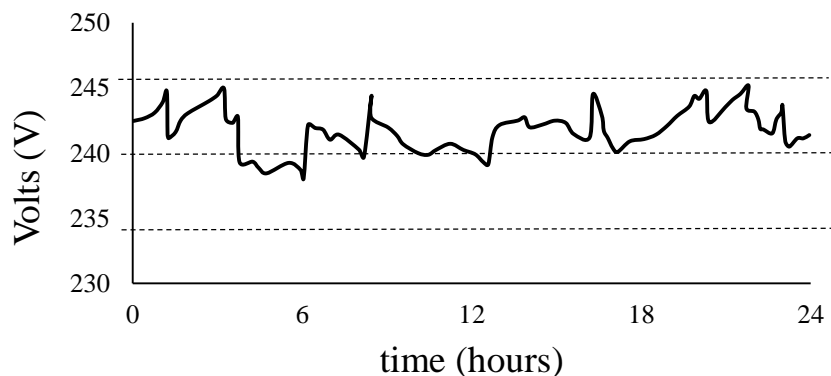


Figure 3-16 Fluctuation of mains voltage within lab over the course of 24 hours

3.5.2 LABORATORY RESULTS

By computing equation 2-10 from chapter 2 over time, t , where the annotations on Figure 3-14 correspond to: $T_h = T_3$, $T_m = T_1$ and $T_u = 43^\circ\text{C}$, the cumulative useable volume of hot water developed by the tank during draw off is plotted in Figure 3-17 for both the stratified (s) and de-stratified (ds) cases. We can compute the initial state of charge of the tank, V_{usoc} using (3-1), where E_{elec} is the energy delivered by the immersion element assuming that heat losses over the course of the experiment are negligible:

$$V_{usoc} = \frac{E_{elec}}{C_p(T_u - T_m)} \quad (3-1) \quad \left. \begin{array}{l} \text{Initial state of charge} \\ \text{of the tank in terms of} \\ \text{useable volume} \end{array} \right\}$$

This allows us to compute the volumetric efficiency, η_{vu} , of the hot water tank described by equation 2-12 in chapter 2 for each test. For both tests, V_{usoc} was 177 ± 11 litres. The stratified test delivered 144 ± 4 litres of useable hot water whereas the de-stratified test delivered 117 ± 3 litres implying volumetric efficiencies of $81 \pm 6\%$ and $66 \pm 5\%$ respectively. The analysis behind these error bounds are detailed in chapter 2, section 2.6.

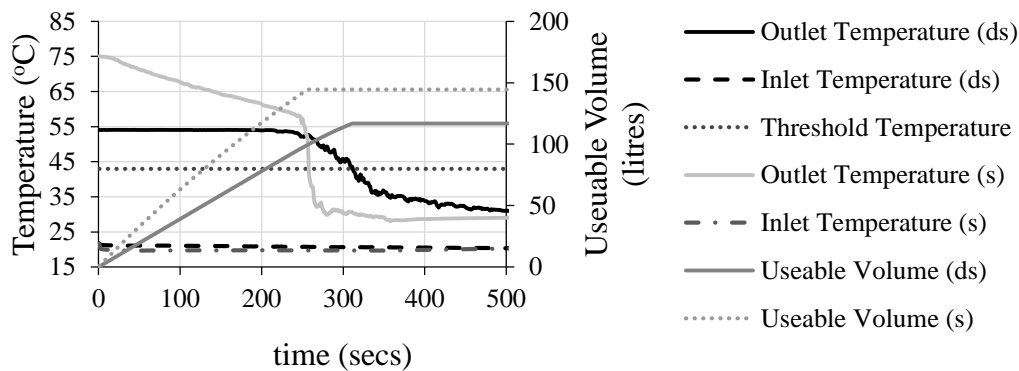


Figure 3-17 experimental comparison of tank output from initial 4.62kWh charge

The discharge efficiency, η_d , for the stratified and de-stratified cases, assuming a threshold temperature of 45°C , the convention advocated by [70], were 82% and 63% respectively; however, if the convention whereby all heat recovered beneath 20% of the initial outlet temperature is used, as favoured by [69], these figures change to 75% and 64% respectively. This reflects the fact that for the stratified case, the angled heating element gave rise to a non-uniform vertical temperature distribution meaning that the outlet temperature dropped continuously before a more sudden thermocline was encountered as is evident from Figure 3-17.

An interesting feature of Figure 3-17 is that the temperature of the outlet for the stratified case starts out at 75°C and drops steadily until the thermocline is approached after approximately 250 seconds. Figure 3-14 shows a cross section through the test tank which had an immersion element entering vertically at an angle through the top of the cylinder. This arrangement is common in small UK hot water cylinders. One hypothesis for this is that since

the element is heating at a constant heat flux over its surface, yet over a changing geometry due to the profile of the cylinder's pressure relief dome, a non-uniform temperature distribution arises. Later chapters focus on systems that are heated using a horizontal immersion element coming in through the sidewall of the tank as these are more common in the UK. It was therefore decided that investigating this phenomena further was beyond the scope of this thesis.

3.6 SUMMARY

The results from the field study clearly show that potentially pathogenic bacteria is prolific within domestic water tanks designed according to British Standards. Furthermore, there is a statistically significant preference for growth at the bottom of the tank ($P < 0.01$). Temperature measurements indicated that the base of the cylinder was chronically unsterilized during operation due to the large stand-off between the lowest part of the heating element and the bottom of the tank. Operating a de-stratification pump, to achieve sterilising temperatures throughout the tank, results in a significant reduction in volumetric efficiency (81% to 61%).

All of the tanks within the field study were copper, in chapter 4 it is demonstrated that copper tank walls lead to increased rates of static mode de-stratification and yet the perceived anti-microbial properties don't seem to be reflected by the results in this chapter. This could be due to a build-up of calcium carbonate scale and formation of copper-oxide over the years in the bottom of the tanks providing hospitable conditions. This would be consistent with findings in Germany which also found no inhibitory effect from copper for tanks that were over two years old [139].

The temperatures at the base of all of the hot water tanks were chronically beneath the sterilising threshold for *Legionella*, this was true even when the tanks were switched on without draw events over a period of 18 hours. It is clear that the position of the heating element, prescribed by the British design standards, gives rise to the problem since heat conducts very slowly beneath the heating element where there is no convective mixing. However, lowering the heating element to address this problem may lead to increased mixing between cold incoming water and stored hot water within the cylinder. To address these problems, a diffuser arrangement was developed which simultaneously reduces mixing whilst providing a thermal path to the base of the cylinder to ensure sanitising temperatures are attained during operation, this work is detailed in chapter 5.

4 THE INFLUENCE OF WALL MATERIAL SPECIFICATION ON STATIC MODE PERFORMANCE³

4.1 INTRODUCTION

The tests, conducted in chapter 3 section 3.5, highlighted the extent to which dynamic mode performance can be influenced by inlet mixing. This chapter examines the role that wall material selection plays on static mode performance. The literature is mainly focused on the role that the tank's aspect ratio plays on static mode performance, see chapter 2, section 2.3. There has been comparatively little emphasis on the role that wall material selection plays, however a hint to its importance was provided by Chauvet et al in [89] where they stated that: “*the heat capacity of the water in the tank should far exceed that of the tank itself*” to ensure that a high degree of stratification is achieved.

Section 4.2 narrows the choice of wall materials considered by examining the selection criteria, such as compatibility with potable water and mechanical strength. Section 4.3 details an experiment conducted to compare the rates of de-stratification within two 74 litre domestic hot water tanks using stainless and copper lining walls. Section 4.4 discusses the shortcomings associated with one-dimensional and analytical approaches, in particular the inability to capture the local heat transfer coefficient as it changes around the thermocline region, justifying the application of an axisymmetric 2d CFD model whose changing vertical temperature distribution was initialised and validated by experimental work discussed in section 4.3. The results of the numerical and experimental work is summarised in section 4.5 where it is found that switching from copper to stainless steel results in a significant reduction in the rate of useable hot water loss. The results of a wider numerical exploration, where the effect of changing the tank's aspect ratio and volume in addition to the wall material, is investigated. The chapter ends with a discussion and conclusions in section 4.6.

³ This chapter has been published in *Journal Energy*, 2014 [201].

4.2 WALL MATERIAL SELECTION CRITERIA

When specifying the tank wall material for a domestic hot water cylinder, a number of criteria including: cost, compatibility with potable water, mechanical properties and thermal performance are considered. We deal with each of these in turn:

4.2.1 MATERIAL COST

Table 4-1 shows the prices associated with the materials considered in this chapter. In recent years the price of copper has fluctuated between \$3000 and \$10,000 USD/ton and is presently worth \$5600USD/ton[158]. Since September 2012, stainless steel has averaged \$2800 USD/ton and peaked at \$4000 USD/ton, or roughly half the price of copper [159]. Polyethylene, a plastic used in potable hot water applications [160], traded for between \$1500 and \$1700 USD/ton since 2013 [161] making it about half the price of stainless steel.

4.2.2 COMPATIBILITY WITH POTABLE WATER

Any wall material in contact with potable water will have to withstand corrosion and should not promote the growth of biofilms which can host human pathogens. Heavy bacterial colonization has been associated with certain rubbers, silicones and aluminium [145], [162], [163], whilst aluminium has been associated with the onset of neurological disorders such as Alzheimer's [164], [165]. There is conflicting evidence around copper's potency against bacteria; one laboratory study found copper to exhibit lower growth rates than other plumbing materials [142] however this is contradicted by [139] where a positive correlation between copper walled tanks and *Legionella* growth was observed.

4.2.3 MECHANICAL PROPERTIES

Copper is malleable and straightforward to work whereas stainless steel is harder to drill and welds at higher temperatures requiring more sophisticated manufacturing processes⁴. Whilst polyethylene can be joined easily at low temperatures, its relatively low tensile strength limits its application without reinforcement from other materials within a composite assembly. Composite pressure vessels have been developed where a pre-tensioned continuous filament winding is wrapped around an inner liner material to achieve high strength and low weight [166]. Given the relatively low pressures that domestic hot water systems operate at, along with time constraints, composite wall structures will not be considered in this chapter.

The maximum operating pressures for unvented UK hot water systems is 6.5 bar [58]. The wall thickness must be specified in order to withstand the associated stresses at this pressure. When the ratio of wall thickness, T , to vessel radius r , within a cylindrical vessel falls beneath $1/20$, membrane stress theory can be applied to resolve

⁴ These insights came from conversations with Mark Smith, managing director at Newark Copper Cylinder limited

the Von Mises stresses, σ_{VM} , that occur by calculating the longitudinal and hoop stresses, σ_l and σ_h , that prevail [167]:

$$\sigma_h = \frac{P \cdot r}{T} \quad (4-1) \quad \left| \begin{array}{l} \text{Hoop stress within} \\ \text{cylinder walls due to} \\ \text{internal pressure} \end{array} \right.$$

$$\sigma_l = \frac{P \cdot r}{2T} \quad (4-2) \quad \left| \begin{array}{l} \text{Longitudinal stress} \\ \text{within cylinder walls} \\ \text{due to internal pressure} \end{array} \right.$$

$$\sigma_{VM} = \sqrt{\sigma_h^2 - \sigma_h \sigma_l + \sigma_l^2} \quad (4-3) \quad \left| \begin{array}{l} \text{Von Mises stress within} \\ \text{main cylinder walls from} \\ \text{superposition of hoop} \\ \text{and longitudinal stresses} \end{array} \right.$$

Where: P is the pressure within the tank.

Whilst the above analysis provides a good approximation of the stresses within the vertical wall sections, stress concentrations arise where the geometry changes towards the top and bottom ends of the tank; this is reflected in the British design standard for vented cylinders which specifies a thicker grade of copper for the top and bottom dome sections [151]. To optimize the thickness of wall material across the entire cylinder, finite element stress analysis would be required [167], this is however beyond the scope of this thesis.

The peak stresses within the tank liner wall will be determined by both the operating pressure and tank diameter. In the UK, the average hot water consumption is 122 litres/day [168]; this can be satisfied by a UK BS8° tank which has a diameter of 450mm [151]. The amount of wall material required can be calculated using equations (4-1) to (4-3) and through reference to gauge requirements specified in BS7206:1990 [58]. Table 4-2 shows these gauge requirements translated into costs against operating pressure for a BS8° tank.

Table 4-1 shows the tensile strength associated with the main wall material options. Cross linked polyethylene has the lowest tensile strength of between 14MPa and 40MPa [169] rendering it unsuitable on its own. However, there may be scope for its use if reinforced by other materials; for instance a glass reinforced fibre plastic tank, designed to capture heat from a solar collector has been tested recently in Nigeria [170]; however, the tank was evaluated on the basis of a single average temperature with no reference to the system's performance with respect to static mode performance, the subject of this chapter.

In addition to the material options discussed so far, some manufacturers produce tanks using a vitreous enamel coating applied to steel, however the enamel is prone to cracking due to thermally induced stresses meaning that sacrificial anodes are required and a shorter lifespan can be expected compared to stainless steel [171].

4.2.4 THERMAL PERFORMANCE

Domestic hot water tank walls range in thickness by between 0.5 and 2.6mm [58], [151]. Being thin and metallic, the inner wall has little influence on heat losses which are determined primarily by the external insulation cladding. Typically, a 50mm thick layer of rigid polyurethane foam is applied to domestic tanks in the UK. However, it has been observed that a significant fraction of the heat flux conducted vertically during de-stratification is through the metal tank inner walls and convection currents adjacent to them [89], [102], [172], this mechanism is explored in section 4.5.2.

4.2.5 SUMMARY TABLE

Table 4-1 summarizes the three wall materials that will be analysed. The insulation foam applied to the experimental test tanks, detailed in section 6, is also included.

Table 4-1 Materials and their associated parameters considered in this chapter

Material	Strength (MPa)	Thermal Conductivity (W/mK)	Manufacturability	Material Cost (\$/ton)	Properties Reference
Copper C106	200 - 300	398	Malleable, welds at low temperatures	5600	[173], [174]
Stainless steel (UNS444000)	415	26.8	More difficult to machine, requires more sophisticated welding processes	3000	[58], [175]
Cross linked polyethylene	14 – 40	0.33	Joins at low temperatures though requires additional materials to withstand operating pressures	1600	[169], [176]
Rigid polyurethane insulating foam	NA	0.028	NA	NA	[112]

Table 4-2 Cost of wall materials against operating pressure for a 144 litre cylindrical tank

Operating Pressure (bar)	Stainless Cost (\$)	Copper Cost (\$)	Polyethylene Liner Cost (\$)
2.5	26.5	90.2	3.4
3.5	26.5	140.3	3.4
4.5	28.4	180.4	3.4
5.5	34.1	220.5	3.4
6.5	39.8	260.6	3.4

4.3 EXPERIMENTAL MODEL

4.3.1 EXPERIMENTAL TEST SET-UP AND PROCEDURE

An experiment with two objectives was conducted. Firstly, the CFD model, described in section 4.5, needed to be initialized and validated so that a wider exploration of alternative material options could be explored. Secondly, a direct comparison of the static mode de-stratification rate for a commercially available domestic tank, made in copper and an equivalently sized stainless steel tank, was to be made. This was to test the hypothesis that de-stratification would be less pronounced for stainless cylinder walls due to the lower thermal conductivity compared to copper walls (see Table 4-1).

Two tanks with a volume of 74 litres and diameter of 350mm were tested, see Figure 4-1 and Figure 4-2. One tank was made from 1mm thick stainless steel (type UNS444000 specified in [58]) whilst the other was a commercially available British Standard BS tank made from 0.7mm thick copper (type C106) as specified in [151]. The stainless tank was 790mm high whilst the copper tank was 900mm tall but with the same volume because of domed top and bottom features which conform to British Standard 699:1984 [151]. Both cylinders had a 57mm immersion port centred half way up the side of the tank wall to accommodate a 3 kW direct 279mm immersion heating element. Prior to being sprayed with 50mm of polyurethane rigid insulating foam, both tanks were fitted with an array of 8 internal temperature probes comprising M5 nylon bolts which were centre drilled to accommodate T-type thermocouple temperature sensors as described in chapter 2 section 2.6.3. Each probe assembly was inserted such that the thermocouple junction was immersed in the water at a distance of 50mm +/- 5mm radially from the tank wall, this was to ensure that the thermocouple was away from convection currents close to the wall, which were shown to be most significant up to a distance of 30mm in [172]. The probe intervals were spaced at isochoric intervals, as discussed in chapter 3 section 3.3.1, so that interpolating between them would yield the temperature distribution $T(x)$.



Figure 4-1 (Left) photograph of the stainless and (centre) copper test tanks prior to insulation (right)

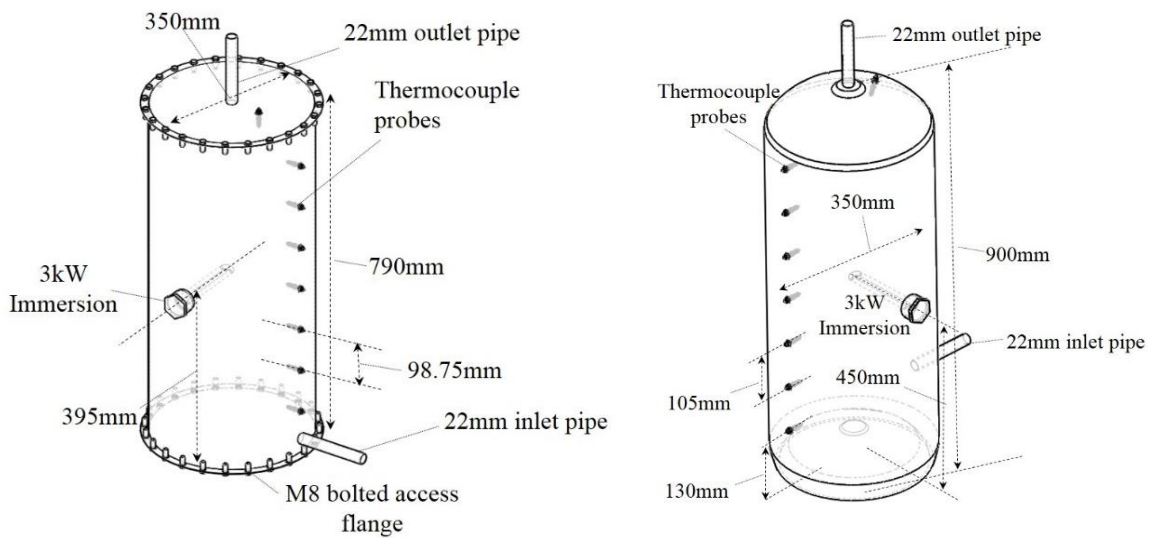


Figure 4-2 Schematic showing (left) stainless test tank assembly and (right) copper BS1 test tank assembly

The experimental procedure involved turning both immersion elements on at the same time until the thermostats reached 60°C at which point they were shut off. The vertical temperature distribution was then measured for a period of 48 hours as the tanks de-stratified and lost heat to their surroundings. The temperature distribution, recorded immediately after the point at which the heating elements were shut off, was used to initialize the CFD simulation detailed in section 4.5.

4.3.2 ERROR ANALYSIS

In order for the experimental work in this section to be interpreted properly, we have to account for the influences of various sources of uncertainty to determine whether any conclusions can be drawn from the results.

As discussed in chapter 2, section 2.6, errors can be considered in quadrature where measurements are made independently of each other, allowing for more precision to be assumed [138]. However, the thermocouples used in this experiment made use of a single cold reference for each tank meaning a potential common source of error and therefore a more conservative approach to the analysis has been taken. The maximum error associated with each parameter has been assumed and applied such that the worst possible band of uncertainty $+Err(param) \leftrightarrow -Err(param)$ can be determined for equations (2-4), (2-7) and (2-11). Equations (4-4) to (4-9) show how this is implemented for errors in temperature, ΔT , and water mass measurements Δm for exergy, energy and useable volume measurements.

$$+Err(E_{xsoc}(x)) = [m + \Delta m]C_p \int_0^H ([T(x) + \Delta T] - [T_c - \Delta T]) \left[1 - \frac{[T_a - \Delta T]}{[T(x) + \Delta T]} \right] dx \quad (4-4) \quad \left| \begin{array}{l} \text{Positive exergy error} \end{array} \right.$$

$$-Err(E_{xsoc}(x)) = [m - \Delta m]C_p \int_0^H ([T(x) - \Delta T] - [T_c + \Delta T]) \left[1 - \frac{[T_a + \Delta T]}{[T(x) - \Delta T]} \right] dx \quad (4-5) \quad \left| \begin{array}{l} \text{Negative exergy error} \end{array} \right.$$

$$+Err(Q_o(x)) = [m + \Delta m]C_p \int_0^H ([T(x) + \Delta T] - [T_c - \Delta T]) dx \quad (4-6) \quad \left| \begin{array}{l} \text{Positive energy error} \end{array} \right.$$

$$-Err(Q_o(x)) = [m - \Delta m]C_p \int_0^H ([T(x) - \Delta T] - [T_c + \Delta T]) dx \quad (4-7) \quad \left| \begin{array}{l} \text{Negative exergy error} \end{array} \right.$$

$$+Err(V_{usoc}(x)) = [m + \Delta m] \int_{x \text{ at } T(x) \geq T_u}^H \left(1 + \frac{[T(x) + \Delta T] - T_u}{T_u - [T_c + \Delta T]} \right) dx \quad (4-8) \quad \left| \begin{array}{l} \text{Positive useable volume} \\ \text{error} \end{array} \right.$$

$$-Err(V_{usoc}(x)) = [m - \Delta m] \int_{x \text{ at } T(x) \geq T_u}^H \left(1 + \frac{[T(x) - \Delta T] - T_u}{T_u - [T_c - \Delta T]} \right) dx \quad (4-9) \quad \left| \begin{array}{l} \text{Negative useable} \\ \text{volume error} \end{array} \right.$$

The errors were added to the measurements before the interpolant function, equation (2-22), was applied to the integral within the above equations.

As discussed in chapter 2, section 2.6.3, the thermocouple readings were accurate to within $\pm 0.5^{\circ}\text{C}$. A set of digital scales recorded the water mass to within ± 0.01 kg.

Estimating the uncertainty associated with V_u is less straightforward due to the lower limit on the integral term in equations (4-8) and (4-9). The upper and lower bounds for V_u are therefore calculated across the entire duration of the experiment and shown alongside the results. This is shown on Figure 4-4, (c), where the changing error has been annotated with a red circle to show the increasing uncertainty in useable volume against time as the hot water in the tank approaches the threshold temperature beneath which there is no more useful energy.

4.4 NUMERICAL MODEL

4.4.1 NUMERICAL APPROACHES TO STATIC MODE DE-STRATIFICATION

Chapter 2, section 2.4.1 discusses the application of a coupled heat equation to describe how the temperatures of the wall and water volumes will change over time, see equation (2-20). The challenge with this approach is that the local film heat transfer coefficient, $h(x)$, which acts as the coupling term, prohibits a closed form solution. The problem could be solved numerically if an appropriate function describing $h(x)$ can be found. An averaged Nusselt number for a heated vertical cylinder is presented in [177], however there are no correlations that relate to a conductive vertical geometry which is immersed in a stratified fluid. One correlation, presented in [178], relates specifically to a cylinder which is cooled at the top and heated from the bottom where the wall is assumed to be either a perfect insulator or conductor of heat meaning that it could not be considered for this application where the conductivity of the wall changes depending on the material selection. One dimensional models, discussed in chapter 2 section 2.4.2, make use of an extra conduction term in the energy balance for each node to account for the influence of convection currents around the wall [102]. However, this conduction term has to be derived empirically and relies on the assumption that the wall and water volumes are isothermal at any vertical location.

Given the challenges around determining an accurate value of $h(x)$, along with the observation in [172] that pronounced convection currents occur within the tank during de-stratification, it was decided that a CFD model would be applied as discussed in chapter 2, section 2.5.

4.4.2 APPLICATION OF A 2 DIMENSIONAL AXISYMMETRIC MODEL

To reduce simulation time, a 2d axisymmetric mesh was applied to the tank geometry, as shown by Figure 4-3 for the stainless test tank. To implement an axisymmetric model, the governing equations associated with each node in the mesh are expressed in cylindrical coordinates [179]; an example of this approach is given in [180] and in this case the software used was Star CCM® courtesy of CD ADAPCO™ [181].

A polyhedral mesh was used to simulate the wall and water volumes associated with the stainless test tank detailed in section 5. A contact interface between the nodes separating the wall and water volumes was specified to facilitate conjugate heat transfer. A 2nd order solver using a simulation time step of 1 second was used. The Boussinesq approximation, where: the density is assumed to be constant along with all other fluid properties, viscous dissipation is assumed to be negligible and an additional buoyancy force term is included in the momentum equation, which takes account of the thermal expansion of water with temperature, was applied [182]. The domain over which the Boussinesq approximation is valid has been provided by Gray et al [118]. The mesh was sized at 0.1mm for the wall volume and was allowed to grow out from the wall at a rate of 40% towards the centre of the tank. This was to ensure that the detail around heat transfer close to the wall/water interface was resolved with minimal computational expense. Figure 4-3 shows the polyhedral mesh as applied to the stainless tank geometry:

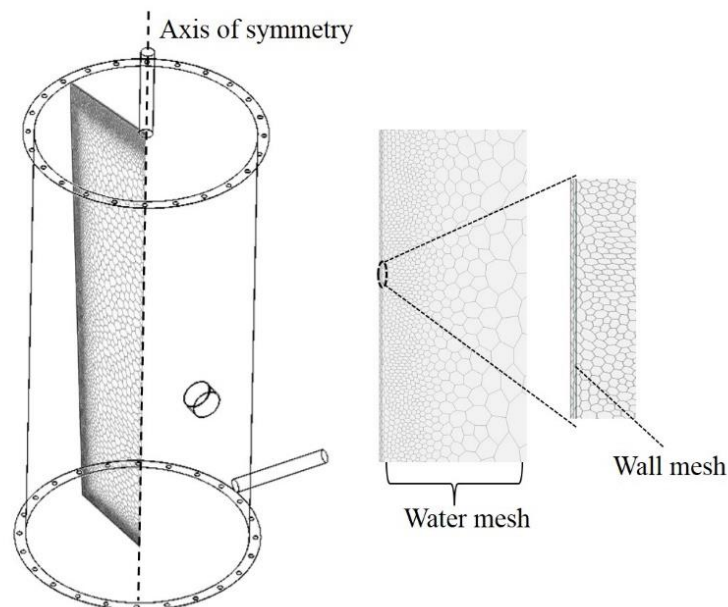


Figure 4-3 Application of 2d axisymmetric CFD model to stainless test tank geometry

The outer wall boundaries were set as a thermal resistance to ambient of $0.6\text{W/m}^2\text{K}$, reflecting the thermal path associated with a 50mm layer of polyurethane insulation. The ambient temperature, used throughout the simulation, was set to that measured during experiment.

Table 4-3 Specifications of CFD platform used to conduct simulations

CFD Model Parameter	Value
Model	Laminar
Solver	2 nd Order
Simulation time step	1 second
Mesh type	Polyhedral
Run time	10.8 seconds simulation time for 1 second real time (4 hours 27 minutes for 48 hour simulation)
Platform details	Processor: Intel i3-2100 3.1GHz 8GB of RAM

4.5 RESULTS

4.5.1 EXPERIMENTAL RESULTS

The measured temperature distribution over time for the copper and stainless tanks are shown by Figure 4-4 (a) and (b). After warm up, the temperature distributions within both tanks were nearly identical with initial exergy and useable volume values being within 0.2% and 0.6% of each other with initial values of 1.077MJ compared to 1.075MJ and 65.4 compared to 65 litres for the stainless and copper units respectively. Comparing (a) and (b) over the 48 hour period, de-stratification is much more rapid in the copper cylinder as can be seen by the more rapid convergence of temperatures. The results of this are evident in (c) which shows the change in useable volume over time; all useable hot water, for a threshold temperature of 43°C, was lost in the copper cylinder by 28 hours (+/- 1 hour) compared to 42 hours (+/- 1½ hours) for the stainless tank. After 24 hours, the copper tank had 24% less exergy than the stainless tank, as the temperatures converge, the disparity between the two tanks reduce such that by 48 hours, measurement error bounds overlap one another as can be seen in (d).

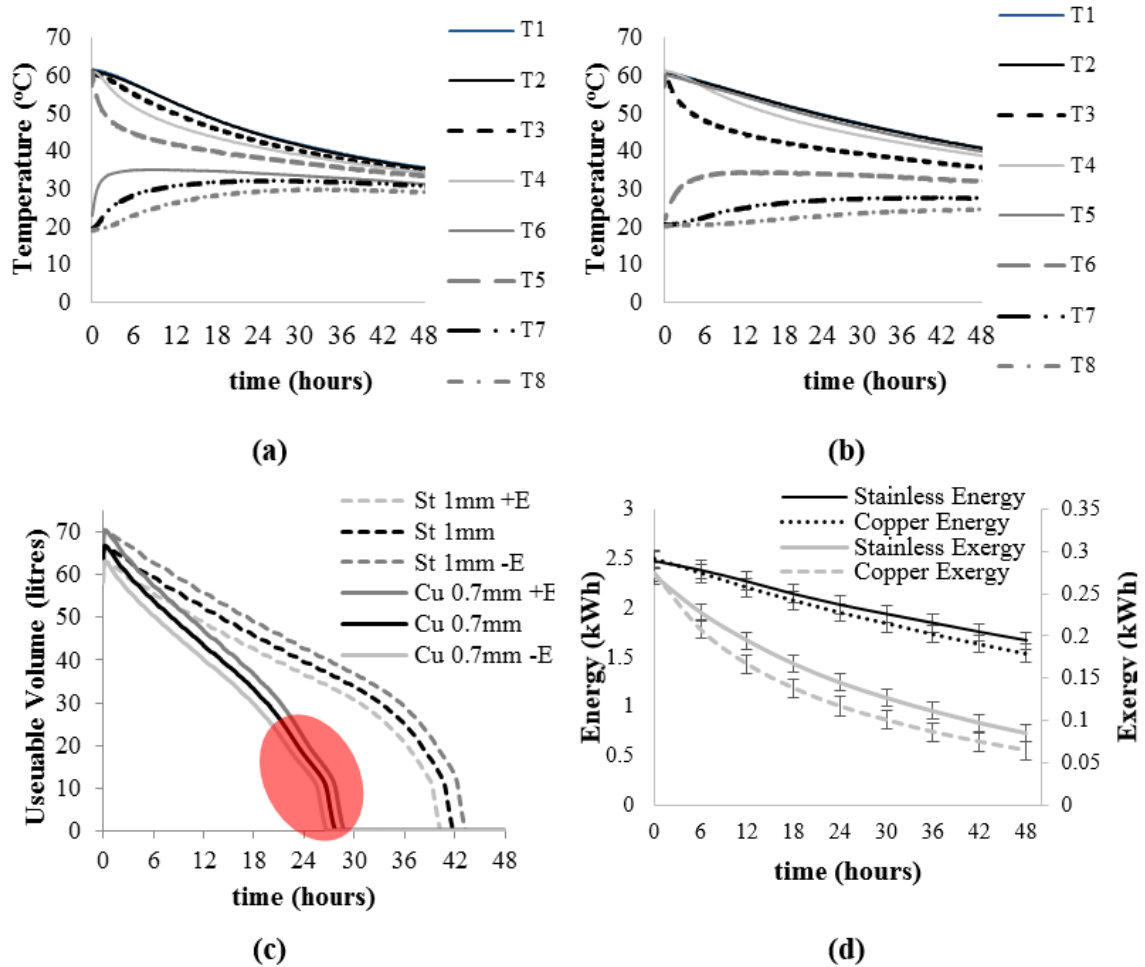


Figure 4-4 Experimental results: (a) vertical temperature distribution over time for the copper tank, (b) vertical temperature distribution over time for the stainless tank, (c), change in useable volume over time for both copper and stainless tanks where +E and -E denote values associated with maximum error (d) changing internal exergy and energy for both the copper and stainless tanks.

For the first 12 hours, the relationship between useable volume loss and time for both the copper and stainless tanks was linear with values of 2.1 litres per hour ($R^2 = 0.95$) and 1.18 litres per hour ($R^2 = 0.98$) respectively (Figure 5(c)). This linearity breaks down in the hours towards total loss of useable volume.

4.5.2 CFD RESULTS

Before examining the velocity vector and temperature scalar fields along with de-stratification rates for different wall material choices, we first verify the output of the model against the stainless and copper test tanks by examining Figure 4-5. Simulated temperatures from reference mesh node centre positions, which were within 1.5% of the vertical position of temperature sensors 1 to 8 and 50mm from the tank wall, were extracted and compared with experimental results. The temperature distribution for both the initial state after warm-up along with the states after 5 hours and 10 hours for the stainless tank and CFD output are shown. The model and experiment agreed within the $\pm 0.5^\circ\text{C}$ measurement error associated with the thermocouples after 5 hours. However, after 10 hours, the measurements and CFD results diverge with a maximum discrepancy of 1°C between the reading from T7 and the associated CFD mesh node. Figure 7 shows the evolving temperature profile for copper against the CFD results where the peak discrepancy rose to 1.1°C after 10 hours.

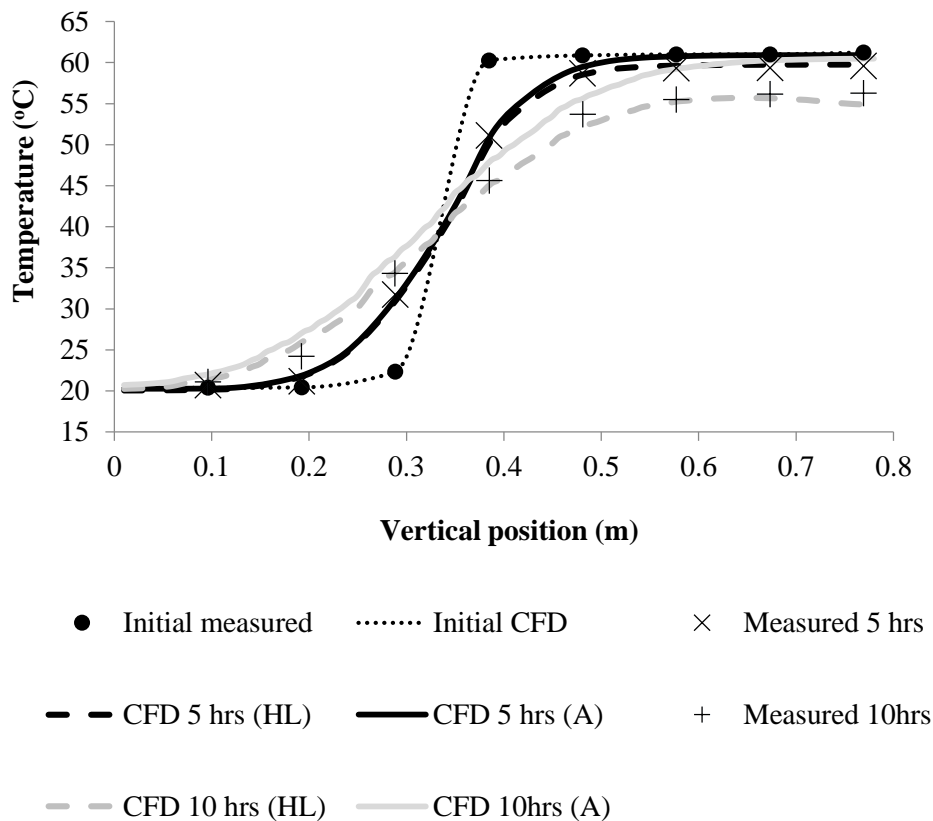


Figure 4-5: Evolution of vertical temperature distribution from initial condition after, 5 and 10 hours against CFD model for the stainless test tank. (HL) = model where heat losses to ambient are included, (A) shows CFD model output for adiabatic system.

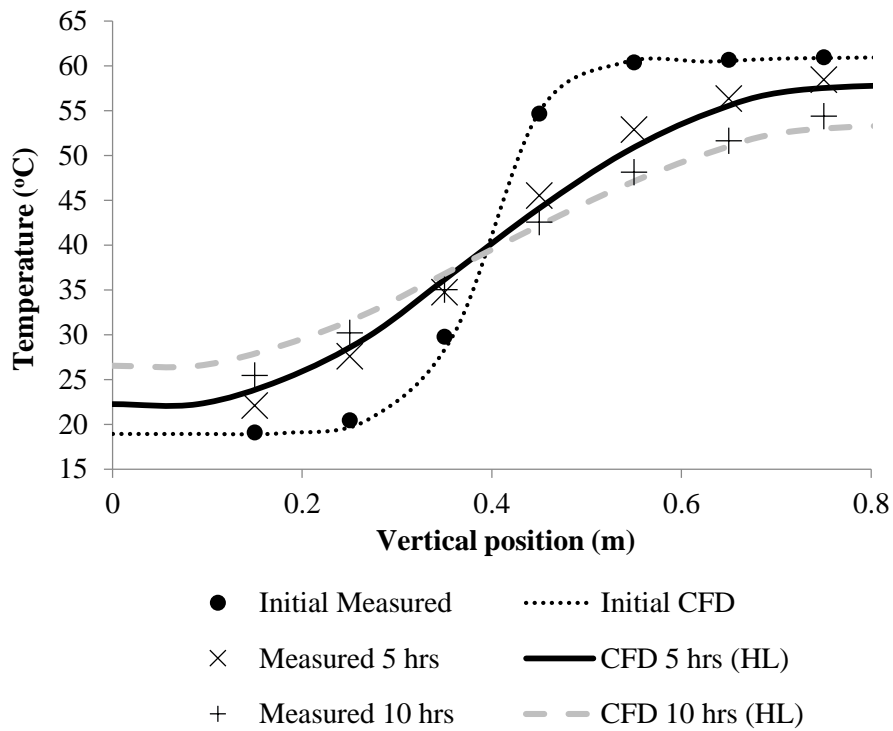


Figure 4-6 Evolving temperature field against CFD simulation for copper tank

Figure 4-7 shows the difference in simulated internal velocity fields for the copper and stainless tanks around the thermocline region. A convection system adjacent to the wall can be observed.

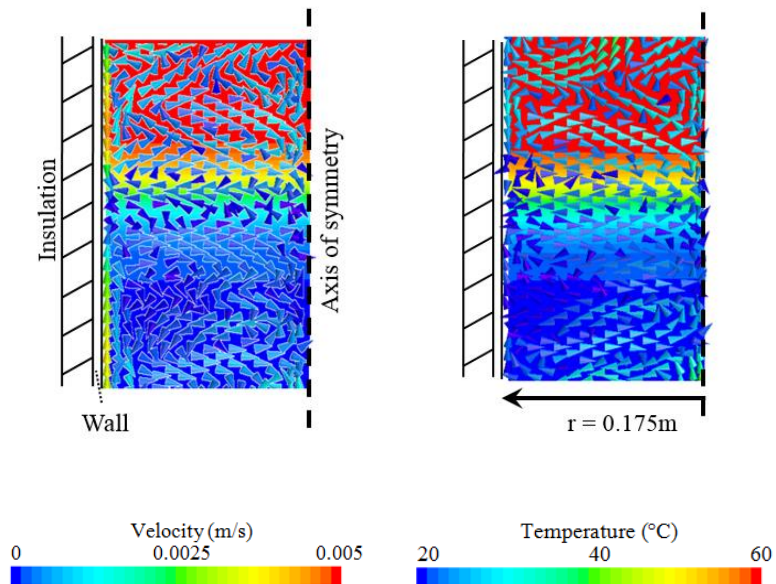


Figure 4-7 Temperature and velocity fields around thermocline for copper (left) and stainless (right) walled 350mm diameter tanks

Two counter rotating currents can be seen above and below the thermocline, the pattern is more pronounced for the copper wall compared to the stainless. Peak velocities of 0.005m/s and 0.003m/s were observed in the copper and stainless tanks respectively; this is consistent with simulated velocities encountered in [172] which were found to be between 0.003 and 0.015m/s. To explain the observation, we draw upon a heat engine analogy which is presented by Bejan [183] to describe the process of natural convection against a vertical heated wall:

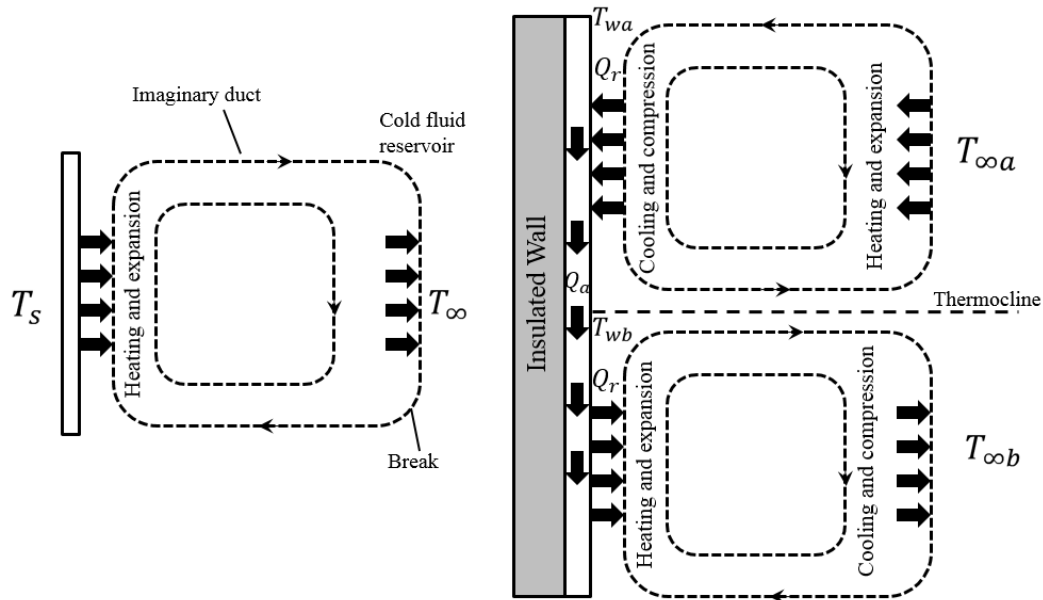


Figure 4-8: (Left) heat engine analogy for natural convection presented in [183] (right) twin heat engine analogy applied to a conductive wall within a stratified fluid

Bejan describes how fluid close to a heated surface, at temperature T_s , expands and rises before cooling and contracting within a cold reservoir adjacent to the wall at temperature T_∞ . The CFD velocity field, shown on Figure 4-7, suggests an extension of this analogy whereby two separate heat engines, below and above the thermocline run clockwise and counter clockwise respectively as heat is transferred from the top of the tank to the bottom via a conductive wall, this is illustrated by the right hand side of Figure 4-8. In this case, we have an adjacent cold reservoir at temperature $T_{\infty b}$ and an adjacent hot reservoir at $T_{\infty a}$.

The simulated radial heat flux exchange between the water and tank wall, Q_r , arising from the system illustrated by Figure 4-8, is plotted on Figure 4-9 against the temperature distribution, $T(x)$. Above the thermocline, the heat flux is negative reflecting the fact that heat is withdrawn from the fluid whilst beneath the thermocline, the heat flux is positive as the water below is heated. The peak value recorded for copper is 1858 W/m² compared to 356 W/m² for stainless and 25 W/m² for polyethylene. If we assume the heat losses from the tank wall to the environment to be negligible compared to the conjugate exchange with the water, then the net radial heat exchange should equal zero, we can therefore estimate the total axial heat transfer, Q_a , from the top of the tank to the bottom during de-stratification via the following equation:

$$Q_a \approx \int_0^H 1/2 |Q_r(x)| dx$$

(4-10)

Approximation of axial heat flux through cylinder wall across thermocline

Q_a values of 181.5W, 11W and 0.8W for 1mm walls made from copper, stainless and polyethylene were calculated respectively for a thermocline gradient of 400K/m.

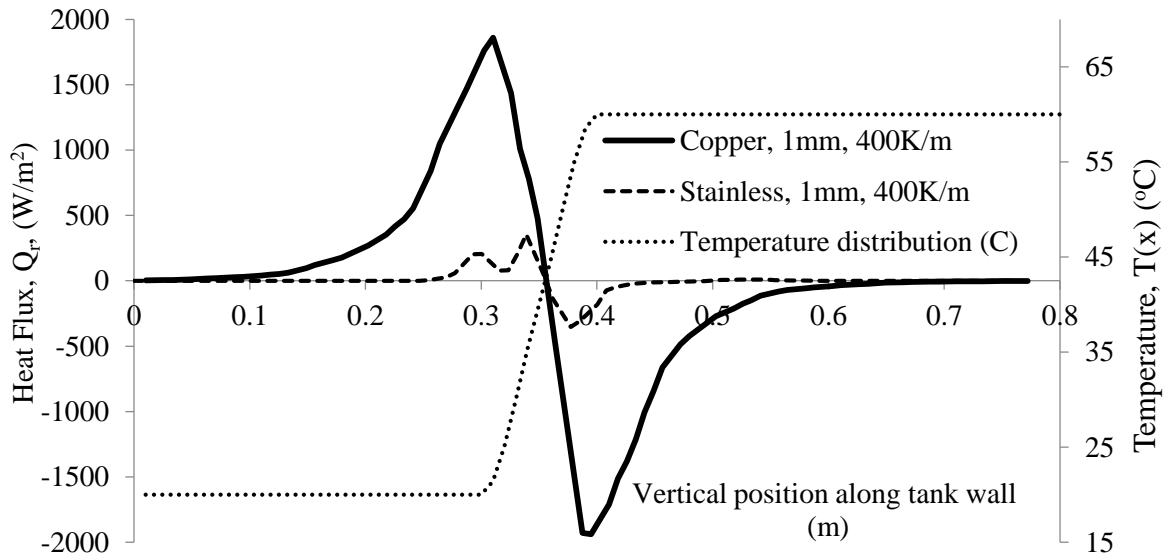


Figure 4-9 Simulated radial heat flux exchange between wall and water for stainless and copper 1mm walls with thermocline gradient of 400K/m.

The thermocline gradient will depend on the geometry and thermal distribution associated with heat transfer surfaces within the tank, along with the passage of time during which the gradient drops. Table 4-4 presents the value of the measured thermocline gradient within the stainless and copper tanks after warm up alongside values found in the literature:

Table 4-4 Thermal gradients measured and sourced from the literature

Experimental Study	Maximum Measured Thermocline Gradient (°C/m)
Initial gradient in stainless tank	407
Initial gradient in copper tank	395
S. Alizadeh et al [184]	297.5
J. Fernandezseara et al [185]	174.7
E. M. Kleinbach et al [104]	105.3
Furbo et al [105]	286

To determine the influence of the thermocline gradient, mesh wall node temperatures and water node temperatures from outside of the thermal boundary layer were taken alongside the wall radial heat flux values, $Q_r(x)$, to calculate the local heat transfer coefficient $h(x)$. The values are shown in Figure 4-10 for the 1mm copper wall with thermocline gradients of 400 and 200 K/m.

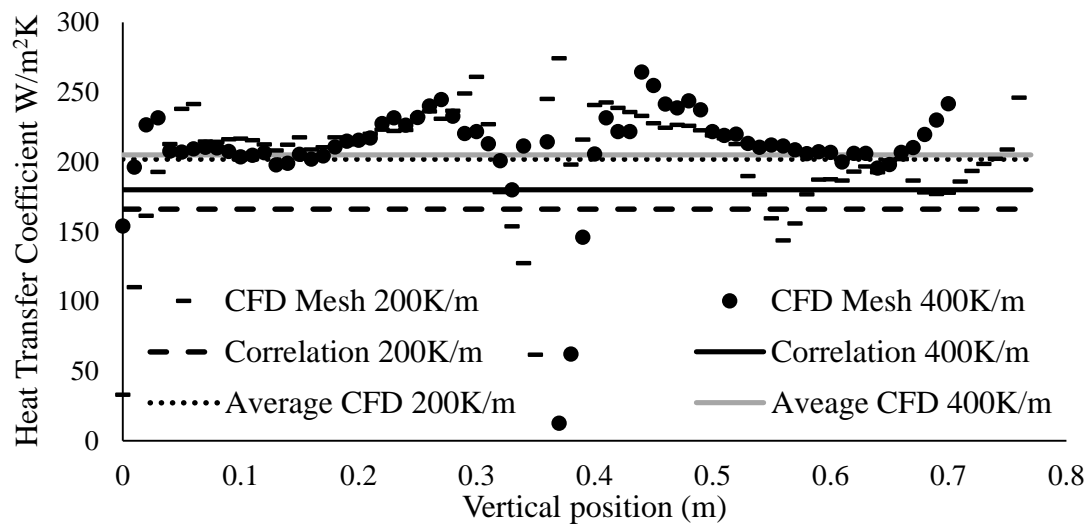


Figure 4-10 Simulated local heat transfer coefficient for 1mm copper wall alongside averaged analytical flat plate correlations based on mean wall water temperature difference.

The average local heat transfer coefficients were 205 W/m^2 and 202 W/m^2 for thermocline gradients of 400K/m and 200K/m respectively. Whilst $h(x)$ was relatively flat across most of the wall, there appeared to be a pronounced dip around the thermocline region, this could be associated with reduced buoyancy driven flow around the centre of the thermocline. The magnitude of these values was checked against the values provided by the averaged Nusselt number, \overline{Nu}_u , for natural convection around a vertically heated plate given in [92]:

$$\overline{N}_u = 0.1R_a^{1/3} \text{ for } 10^9 < R_a < 10^{13} \quad (4-11)$$

Nusselt number for
natural convection
around a vertically
heated plate

Where the Rayleigh number is given as:

$$R_a = \frac{g\beta(\overline{\Delta T})H^3}{\nu^2} Pr = Gr Pr \quad (4-12)$$

Rayleigh number for
vertically heated plate

Where: g is gravitational acceleration, β , is the volumetric expansion coefficient, $\overline{\Delta T}$ is the average temperature difference between the wall and water outside the thermal boundary layer measured from the CFD model, ν is the kinematic viscosity and Gr is the Grashoff number. The average heat transfer coefficient, \overline{h} , can then be given by:

$$\overline{h} = \frac{N_u k}{H} \quad (4-13)$$

Average heat transfer
coefficient across wall
surface

Equation (4-13) yielded values of 180 W/m²K and 166 W/m²K for thermocline gradients of 400K/m and 200K/m respectively.

It has been shown that heat transfer correlations for cylindrical geometries are equivalent to results applied for flat plates providing the diameter to height ratio exceeds the following [186]:

$$\frac{d}{H} \geq \frac{55}{Gr^{1/4}} \quad (4-14)$$

Domain over which flat
plate correlations are
valid for applications to
cylinders

For the stainless tank, tested and simulated in this paper, the RHS of (4-13) is $55/Gr^{1/4} = 0.28$ whereas $d/H = 0.44$ indicating that the heat transfer results discussed in this section would be applicable for both flat plates and cylinders where the above condition is met and where $10^9 < R_a < 10^{13}$.

With the CFD simulation validated by the stainless test tank, along with the check that values seemed reasonable against those produced by the correlation described by (4-11), the CFD model was run for the different material choices involving: copper, stainless and polyethylene. Results for both perfect wall insulation (adiabatic) and tanks insulated with 50mm of polyurethane foam with $T_a = 15^\circ\text{C}$ over a period of 12 hours were produced. These results, alongside measurements from the test tanks, are presented in Figure 4-11 and Table 4-5:

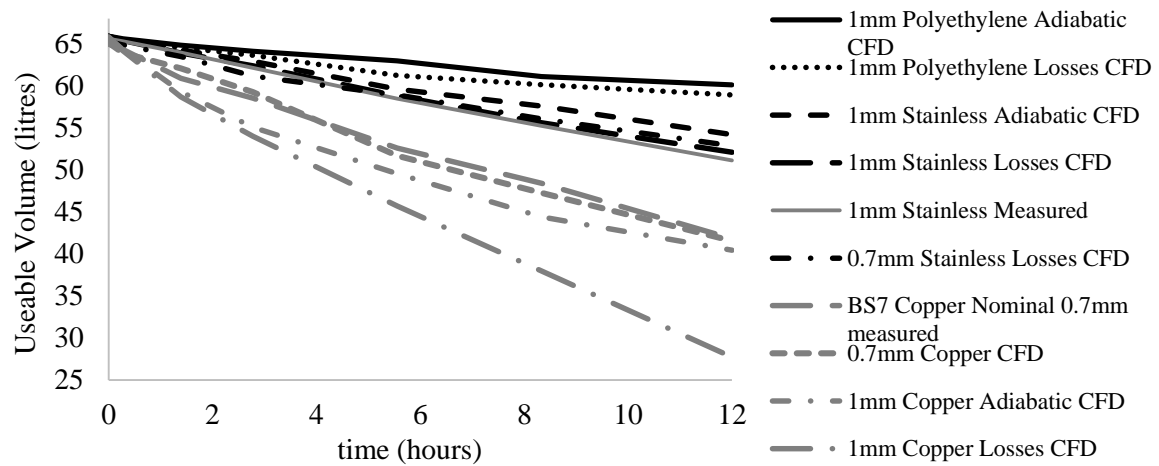


Figure 4-11 Simulated and measured useable volume loss curves for stainless, copper and polyethylene materials.

Table 4-5 Simulated and measured rates of useable volume and exergy loss within test tanks for different wall materials and thicknesses

Material type/thickness	Useable volume loss rate over 12 hours (litres/hour) (R^2)	Exergy loss (%)	Maximum tank wall operating pressure (bar)
1mm Copper with losses (CFD)	3.12 (0.99)	39	4.4 – 6.6
BS7 tank 0.7mm Copper nominal (Measured)	2.10 (0.95)	35	3 – 4.6
0.7mm Copper CFD	2.11 (0.99)	35	3 – 4.6
1mm Copper adiabatic (CFD)	1.91 (0.99)	29	4.4 – 6.6
1mm Stainless (Measured)	1.18 (0.98)	25	9.1
1mm Stainless with losses (CFD)	1.16 (0.99)	24	9.1
0.7mm Stainless with losses (CFD)	1.03 (0.99)	21	6.3
1mm Stainless adiabatic (CFD)	0.97 (0.99)	10.2	9.1
1mm Polyethylene with losses (CFD)	0.60 (0.96)	22	0.3 – 0.8
1mm Polyethylene adiabatic (CFD)	0.49 (0.99)	8.3	0.3 – 0.8

As had been observed during experiment, the CFD results indicated an approximately linear relationship between decreasing useable volume and time over 12 hours with R^2 values provided in Table 4-5. The CFD model was consistent with the stainless test tank to within +/-1.3 litres and +/-1.2 litres for the copper tank over the duration of the 12 hour run.

Table 4-5 shows that the selection of stainless over copper for a 1mm wall decreased useable volume loss by a factor of 2.7 with a switch from copper to polyethylene yielding a 5 fold reduction. Perfect insulation of a 1mm stainless wall resulted in 9.4% reduction in usable volume loss compared to 50mm of Polyurethane with a reduction of 64% for copper.

Equations (4-1) to (4-3) were applied to estimate the pressure rating of the vertical wall section with a factor of safety of 3 using the ultimate tensile strength values specified in table 1. 1mm grade polyethylene could withstand less than 1 bar of pressure making it unsuitable without reinforcement whereas 1mm stainless could withstand more than 9 bar of pressure.

4.5.3 EXPLORATION OF DIFFERENT ASPECT RATIOS AND CYLINDER VOLUMES

So far, all of the experimental and numerical analysis has demonstrated that the influence of wall material selection has a significant bearing on rates of de-stratification for a small 74 litre cylinder with an aspect ratio of 2.3. In practice, hot water cylinders have a wide range of aspect ratios and volumes as is evident in Figure 4-12 which plots 82 common sizes of cylinders manufactured for the UK market by Newark Copper Cylinder limited.

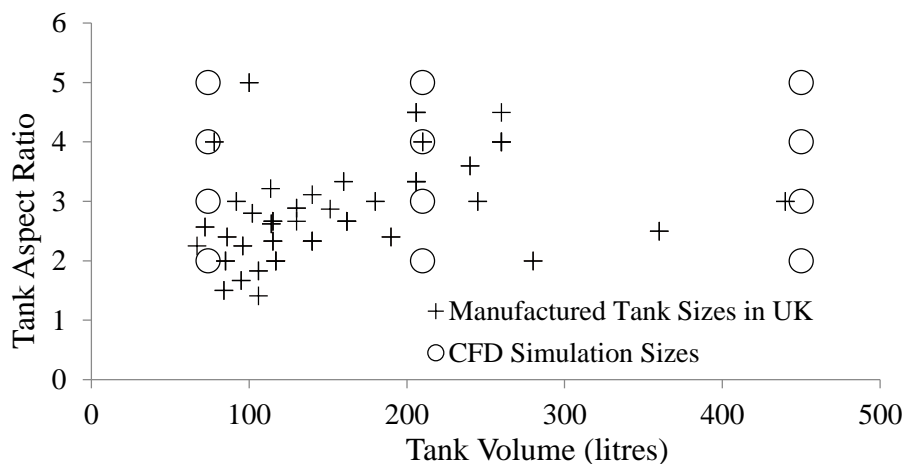


Figure 4-12 Sizes of 83 hot water tanks manufactured in the UK according to volume and aspect ratio against simulation points (data from Newark Copper Cylinder Ltd)

Standard domestic hot water tanks range in volume by between 60 litres to 450 litres with aspect ratios of 1.5 to 5. This begs the question: *to what extent is static mode de-stratification influenced by the combined effect of aspect ratio, tank volume and wall material selection over the range of tank sizes encountered in domestic applications?*

Jabbar et al undertook experimental work to quantify the extent to which thermal stratification occurs within tanks with aspect ratios of 1/2, 1 and 2 [90]. However the cylinders were made from galvanised steel and were uninsulated whereas design standards in the UK mandate the use of insulation in order to meet heat loss standards specified in BS5422:2009 [187]. Furthermore, such low aspect ratios are unusual for tanks in the UK which have to fit within small airing cupboards. A static mode test, undertaken by Fernández et al was conducted with a 30mm layer of polyurethane insulation on a tank with an aspect ratio of 1.81 [185], however a wider exploration of the influence of different aspect ratios and volumes was not pursued. As discussed previously, an optimum aspect ratio of between 3 and 4 has been suggested on the basis that discharge efficiencies improved, during experimental work conducted by [88], but that higher aspect ratios begin to incur significant heat losses. However, relative heat losses will also be determined by the volume of the cylinder since the ratio of surface area to stored water capacity will reduce, a point that seems to be overlooked in the literature. One has to ask: *will a larger volume of tank, experiencing lower relative heat losses, benefit from a higher aspect ratio compared to a smaller tank and how does the wall material selection influence the answer?* This question reflects a gap in the literature in that the combined influence of wall material, aspect ratio and water volume has not been explored thoroughly.

To explore the effect of varying the aspect ratio and volume, the axisymmetric CFD model, discussed in section 4.5.2, was extended to simulate tanks sized according to the circled locations on Figure 4-12. Figure 4-13 illustrates the scale of these simulated tanks relative to a typical adult male to give a sense of their proportions. Each simulation was initialised with a thermocline gradient of 400K/m reflecting the gradient produced during experiment. The simulation was run until 14 hours of real time had elapsed and the change in useable volume and internal energy, was recorded based on the vertical temperature distributions at the end of each run. All simulations assumed that the walls were insulated with 50mm of polyurethane and an ambient temperature of 20°C was imposed on the outer surface of the insulation. Each simulation was run assuming either a copper or a stainless wall material with a thickness of 1mm.

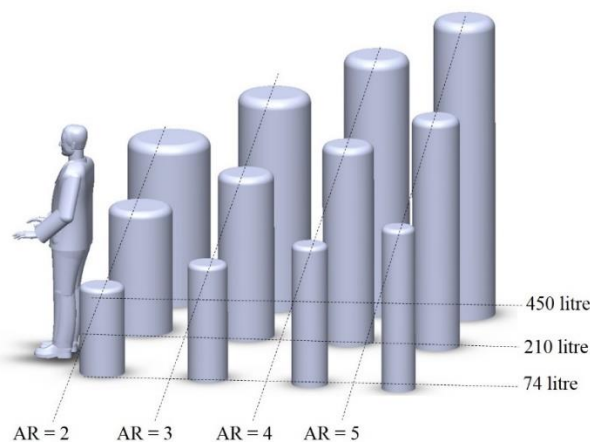


Figure 4-13 Cylinder sizes used for static mode de-stratification simulations against dimensions of a typical adult male for references

The resulting changes in useable volume for each simulation are plotted on Figure 4-14. The changes in state of charge within the tank against aspect ratio is plotted on Figure 4-15. Whilst the retention of useable volume was enhanced under all circumstances as aspect ratio increased, the improvement was most pronounced for the copper walled 74 litre cylinder which saw a jump from 76% to 80% between an aspect ratio of 2 to 5. All cylinders saw a plateauing response to aspect ratio above 4 with the subsequent increase in retained useable volume being less than 1%, probably due to the increasing loss of energy at higher aspect ratios as can be seen on Figure 4-15. The difference between using stainless and copper walls had a greater influence on useable volume retention than the aspect ratio for all of the cylinders simulated. At an aspect ratio of 3, the enhancement derived from switching from copper to stainless walls for the 74, 210 and 450 litre tanks was 7%, 6% and 3% respectively. This result shows that for smaller volumes of tank, the wall's thermal conductivity has a more pronounced influence, this is perhaps due to the fact that the vertical de-stratification for copper cylinders becomes driven largely by the circumference of the cylinder rather than the cross section due to the significant rate of heat transfer through the wall. Since the ratio of circumference over cross sectional area will diminish as the tank diameter increases, we might expect larger cylinders to be less influenced by the contribution of the wall to de-stratification.

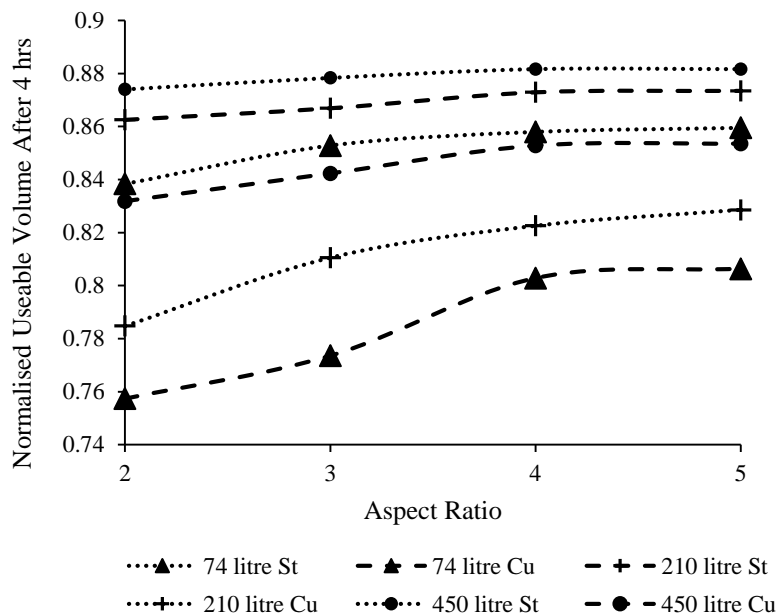


Figure 4-14 Changes in useable volume against aspect ratio for different stainless and copper walled tanks at 74, 210 and 450 litres.

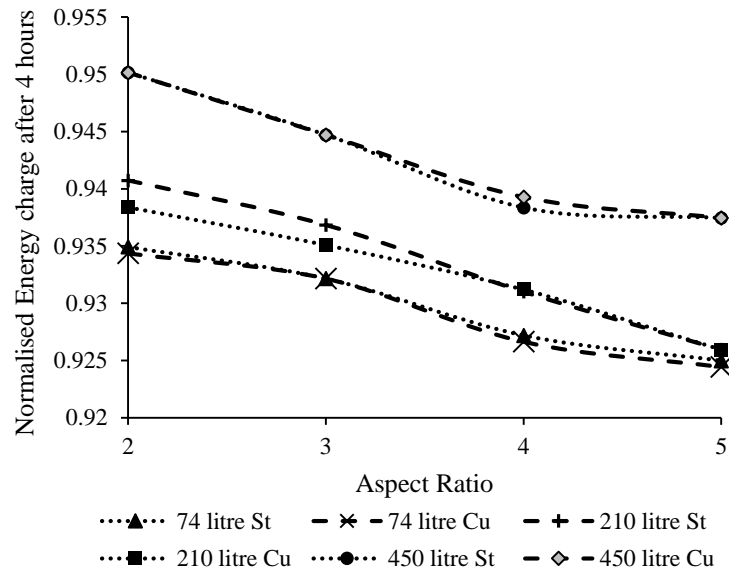


Figure 4-15 Changing state of charge of tank against aspect ratio after 4 hours for 74, 210 and 450 litre volumes in stainless and copper

4.6 DISCUSSION AND CONCLUSIONS

The experimental and numerical findings in this chapter clearly demonstrates that the use of copper as a wall material results in a significant increase in the rate of de-stratification during the tank's static mode of operation. Total loss of useable hot water occurred after 28 hours for the copper tank under test compared to 42 hours for the stainless unit which had the same volume and overall diameter. The consequences of this are that during operation, the copper tank would be less capable as a store of intermittent energy on a renewable or flexible tariff scheme since the heating element would have to fire more frequently to maintain an adequate volume of hot water for the end user. Further work is required to quantify the system costs associated with de-stratification in hot water tanks within energy systems against different draw cycles along with the extent to which improved standing thermal performance can lead to better utilization of renewable energy sources.

A 2d axisymmetric CFD model was validated against the measurements taken from the stainless and copper test tanks. This model overcomes the limitations around multi-node approaches where the effect of convection is neglected along with an assumption that the wall and water volumes are isothermal with respect to vertical location. The axisymmetric model runs much faster than a 3d equivalent allowing for a wider exploration of alternative wall materials, aspect ratios and tank volumes. The numerical results showed that, for a 350mm diameter tank, the selection of stainless over copper, for a 1mm thick wall, decreased useable volume loss by a factor of 2.7 with a switch from copper to polyethylene yielding a 5 fold reduction. In addition to this, the lower cost of stainless, compounded with its higher tensile strength, means that for mains pressurized systems operating up to 6.5 bar, a lighter, thinner, stainless wall within a UK tank would be less than a sixth of the material cost in

comparison to its copper equivalent; further analysis is required to account for the additional manufacturing costs associated with stainless due to its higher melting temperature and stiffness. Whilst a polyethylene wall exhibits very low rates of de-stratification, it would have to be reinforced by additional materials. Further work is required to understand whether alternative low conductivity materials and composites could offer significant improvements in useable volume retention, one option may be stainless coated with vitreous enamel glass, this would lower thermal conductivity and be immune to the corrosion problems that have been encountered in enamelled mild steel tanks. By conducting additional simulations of domestic tanks with aspect ratios and volumes across the range sold in the UK, it was found that switching from copper to stainless had a more pronounced effect in reducing static mode de-stratification than the aspect ratio. Whilst increasing the aspect ratio did reduce the rate of static mode de-stratification by several percent, the improvement at higher aspect ratios declined due to the increasing rate of heat losses to the environment due to the larger surface to volume ratio.

In chapter 3, it was demonstrated that the evidence for copper as a sanitizing agent is inconclusive, whilst it has been shown to inhibit *legionella* under laboratory conditions, field work in the literature has found a positive association between copper tanks and *legionella* along with prolific bacterial growth. On the basis of this, along with the findings in this chapter, it would seem that the superior thermal performance, reduced material cost and high tensile strength associated with stainless steel; makes it a preferable alternative to copper. Whilst the use of polyethylene would result in a lower rate of de-stratification compared to stainless, polyethylene has been associated with higher rates of biofilm growth and would require additional materials to compensate for its low tensile strength.

Reducing the thickness of stainless steel walls from 1mm to 0.7mm decreases useable volume loss by 13%, however the associated pressure rating falls to 6.3 bar for a 350mm diameter tank which is beneath the rating of expansion relief valves in pressurized UK domestic systems [58]. This highlights the trade-off between material thickness, de-stratification, pressure rating and material cost when specifying the wall thickness. It is also crucial to consider the stress concentrations that arise towards the top and bottom ends of a hot water cylinder where the wall thicknesses must be increased. Further work could be undertaken to explore these trade-offs along with fabrication techniques that could optimize the wall grade without incurring unreasonable costs.

The CFD analysis provided further insight into the flow patterns that arise within the tank. Counter rotating convection currents were observed above and below the thermocline. This convection system was more pronounced for a copper wall compared to stainless or polyethylene due to the higher rate of heat flux that travels radially and axially through the wall.

Due to the complex flow phenomena around the thermocline, along with the computational expense associated with multiple simulations, it was decided that formulating dimensionless parameters, capturing all of the variables which influence the rate of static mode de-stratification, such as: wall thermal conductivity, wall thickness, tank aspect ratio, tank volume, fluid viscosity and the thermocline temperature gradient, would be beyond the scope of

this thesis. Further work in this area would be desirable to advance a broader understanding which could be applied to other thermal storage applications. Future work could examine whether the physical insights gleaned through simulation can lead to the formulation of more accurate heat transfer correlations for conductive walls immersed in stratified fluids, this would improve the accuracy of one dimensional stratification models allowing the implications of static mode performance of hot water tanks to be understood over larger time-scales against different draw cycles within different energy systems.

Although there is much more that can be understood through further experiment and simulation, the work discussed in this chapter demonstrates that selecting stainless over copper will significantly enhance the static mode performance of hot water tanks.

5. ADDRESSING DYNAMIC LOSSES AND BACTERIAL GROWTH THROUGH APPLICATION OF A SPIRAL INLET DIFFUSER⁵

5.1 CHAPTER INTRODUCTION AND ROADMAP

The previous chapter focused on the static mode performance of a tank against different wall materials and aspect ratios, this chapter is instead concerned with dynamic mode performance. In chapter 3, it was demonstrated that de-stratifying a tank, to ensure its contents are fully heated and sterilised, results in a drop in volumetric efficiency due to the increased inlet mixing. Furthermore, de-stratifying the tank necessitates the use of a pump which incurs additional cost and introduces another component which consumes energy and has to be maintained. Chapter 3 therefore raise the dilemma that on the one hand we want to minimise dynamic losses whilst on the other we want to ensure that bacterial growth within hot water cylinders is minimised.

This chapter describes a spiral diffuser which has been developed to resolve the above dilemma. The spiralled wall within the diffuser channels flow to a series of holes in such a way as to minimise mixing. At the same time, the same material conducts heat vertically to ensure the base of the cylinder is heated to a sanitary temperature during operation.

An overview of the diffuser design is introduced in section 5.2 along with a bespoke tank that was built to test it. Section 5.3 discusses the thermal model used to determine the number of spiral turns required so that sufficient heat transfer is achieved towards the bottom of the tank, the section also discusses the performance of the model against experiment. A one dimensional flow model, used to determine an initial hole size specification that seeks to balance the flow out of the diffuser, is presented in section 5.4. Section 5.5 presents a CFD model which is used to provide insight into the flow phenomena within the tank both with and without the diffuser. The experimental test rig configuration and procedure is described in section 5.6 the results of which are provided in section 5.7 informing conclusions in section 5.8.

⁵ *The work in this chapter has led to a patent being filed on a novel diffuser arrangement within domestic hot water tanks under filing number P44091GB*

5.2 DIFFUSER DESIGN

The design specification for the diffuser was to reduce inlet mixing within the tank whilst at the same time, ensure that heat from the immersion element is conducted sufficiently to the bottom to ensure that the sterilising threshold temperature for *Legionella* is attained within the heating period associated with an Economy 7 tariff.

Figure 5-1 shows transparent views of the test tank with diffuser assembly on the left alongside a bottom view on the right where a spiral walled profile and inlet configuration is visible. An aluminium wall runs from the tank inlet position to the centre. The wall returns on itself behind the inlet so that all the flow is constrained along the spiralled path. In addition to distributing the flow from the inlet to a series of outlet holes. The centre height of the immersion element from the base of the cylinder was set to 80mm. The manufacturer who produced the cylinder advised setting this centre height so that the weld around the immersion boss wouldn't cause warping around the sheet edge and to allow access for tooling to fit the immersion. To ensure that the diffuser outlet plate was as close as possible to the immersion element, whilst at the same time allowing for a clearance of 15mm for its installation, the height of the spiralled wall was set to 45mm. The inlet diameter of the diffuser pipe is 18mm and terminates on to a 22mm compression fitting. The tank in which the diffuser was tested has a diameter of 350mm and height of 790mm. The entire diffuser assembly could be fitted or removed from the base of the cylinder by unbolting a flanged plate which coupled the base of the cylinder to the walls with a 3mm rubber sealing gasket in between.

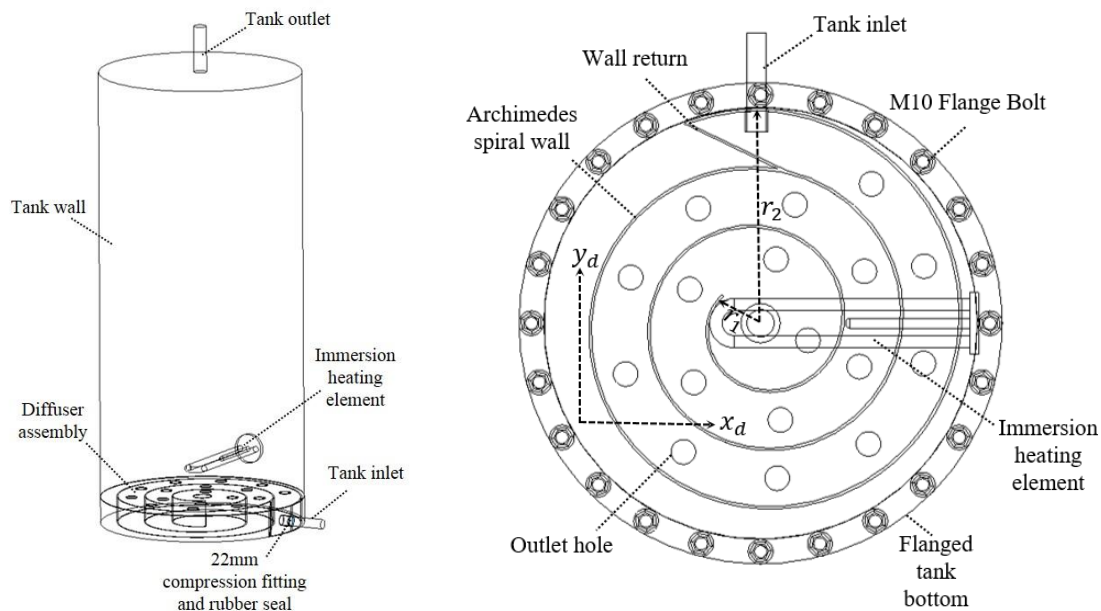


Figure 5-1 (Left) Hot water test tank assembly (shown without flange bolts for clarity), (right) bottom view of hot water test tank showing diffuser assembly

For the purposes of design, it is convenient to define the path of the spiral wall by the parametric equation form of the Archimedes spiral since this enables design constraints such as the minimum and maximum radii, r_1 and r_2

to be applied whilst allowing the number of turns, N_t , to vary. The right hand side of Figure 5-1 shows these parameters against the diffuser's geometry:

$$\begin{aligned} x_d &= x_c + (r_1(1-t) + r_2t)\cos(2\pi N_t\Gamma + \theta) \\ y_d &= x_c + (r_1(1-t) + r_2t)\sin(2\pi N_t\Gamma + \theta) \end{aligned} \quad (5-1)$$

Parametric form of
Archimedes spiral
equation used to specify
wall path

Where: y_d and x_d are the vertical and horizontal coordinates with subscript c denoting the centre position, θ is an offset angle and Γ is a 'time' variable which controls the starting and finishing points of the trajectory of the curve. The outer diameter of the test tank immediately imposes constraint r_2 at 174mm to accommodate the 1mm aluminium sheet that was used for the spiralled wall. Parameters r_1 and Γ were set at 32mm and 0.05 respectively to allow room for a hole in the centre of the spiral. With these constraints imposed, it is now possible to investigate the influence that the number of turns, N, has on the total arc length of the spiral.

The design of the diffuser involves a number of trade-offs and considerations such as:

1. Increasing the number of spiral turns enhances heat transfer to the bottom of the tank but increases the overall amount of material used
2. Increasing the number of turns reduces the channel area through which the incoming water can flow along with the channel length so that the head losses associated with the diffuser increases
3. Increasing the spiral wall thickness increases heat transfer and reduces the required number of turns but the wall becomes more difficult to roll into shape.
4. Hole sizes can be tapered to balance the flow distribution across the outlet plate, however, this restricts the overall diffuser outlet area leading to increased head losses, moreover smaller holes may also be susceptible to blockage from debris and scale build up.

5.3 DIFFUSER THERMAL MODEL

The purpose of the diffuser thermal model is to determine whether the bottom of the tank will attain a sterilising threshold temperature for *Legionella* within a reasonable time frame. Chapter 2 section 2.4.2.4, details a thermal stratification model which is used widely in the literature. In this model the thermal influence of the tank wall is accounted for by including an extra conductivity term, Δk_{sp} . This procedure however assumes that the wall and water volumes are at the same temperature and assumes perfect heat transfer between them. In order to overcome these limitations, a multi-nodal approach was taken which considered the wall and water volumes as a series of distinct nodes, separated by the resistance associated with natural convection, see Figure 5-2:

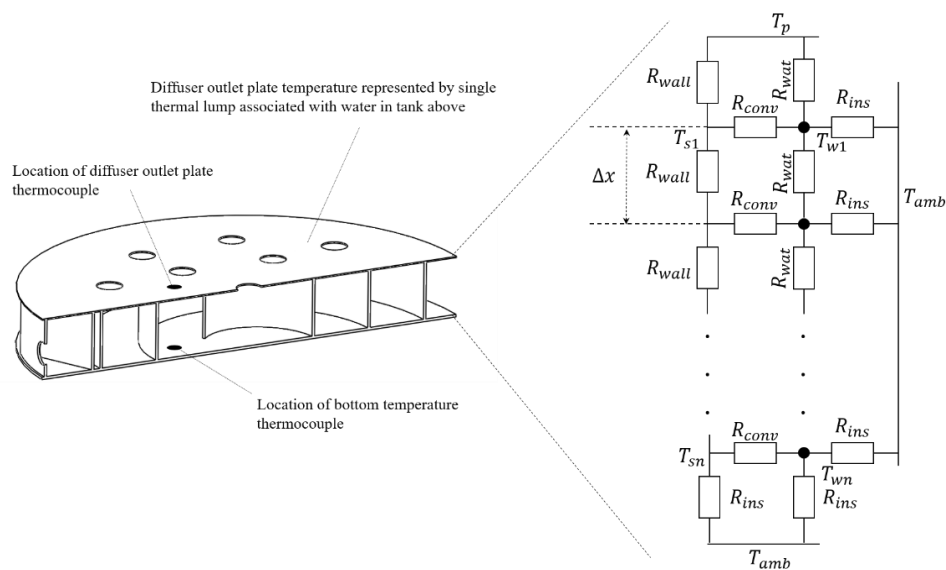


Figure 5-2 Application of multi node model which treats wall and water volumes separately

5.3.1 MODEL DESCRIPTION

The assumptions underlying the diffuser thermal model include:

1. The heat capacity of the spiral wall is negligible in comparison to the surrounding water and can therefore be ignored.
2. The thermal conductivity of the stainless steel test tank wall is low in comparison to the aluminium spiral wall and so can therefore be ignored.
3. Thermal stratification can be ignored since heat is being conducted downwards only and so there is no need to run a mixing algorithm on nodal temperatures as described in chapter 2 section 2.4.2.4.
4. Water above the diffuser plate can be represented by one single thermal lump since convection ensures that the entire volume is mixed to a homogenous temperature.
5. The clearance between the immersion element heating surface and the diffuser outlet plate is so small that it is ignored for the purposes of the thermal model and therefore the temperature of the top boundary, T_p assumes the value associated with the single thermal lump from assumption 4.

In the model schematic depicted on the right hand side of Figure 5-2, R_{wall} denotes the thermal resistance associated with a discretised segment of the wall spiral over its entire length and is given by:

$$R_{wall} = 1 / \left[\frac{k_{alu} t_s L_s}{\Delta x} \right] \quad (5-2) \quad \left. \begin{array}{l} \text{Thermal resistance} \\ \text{associated with spiral} \\ \text{wall} \end{array} \right\}$$

Where: k_{alu} , is the thermal conductivity of the wall, t_s is the spiral wall thickness and L_s is the length of the spiral wall. The nodal height, Δx is the spiral wall height, H_s divided by the number of nodes, N_s .

$$\Delta x = \frac{H_s}{N_s} \quad (5-3) \quad \left. \begin{array}{l} \text{Nodal height associated} \\ \text{with diffuser thermal} \\ \text{model} \end{array} \right\}$$

The thermal resistance between the spiral wall and the surrounding water is given by:

$$R_{conv} = 1 / [h_{ws} \Delta x L_s] \quad (5-4) \quad \left. \begin{array}{l} \text{Thermal resistance} \\ \text{associated with} \\ \text{water/spiral convection} \end{array} \right\}$$

Where h_{ws} is the heat transfer coefficient between the wall and water volumes and is given by (4-13) in chapter 4. The thermal resistance between vertically adjacent water nodes, R_{wat} , is:

$$R_{wat} = 1 / \left[\frac{k_w A_w}{\Delta x} \right] \quad (5-5) \quad \left. \begin{array}{l} \text{Thermal resistance} \\ \text{associated with vertical} \\ \text{conduction between} \end{array} \right\}$$

Where A_w is the tank's cross sectional area. Finally, the thermal resistance associated with the tank wall's insulation is given by:

$$R_{ins} = 1 / \left[\frac{k_{ins} \Delta x \pi D}{t_i} \right] \quad (5-6) \quad \left. \begin{array}{l} \text{Thermal resistance} \\ \text{associated outer tank} \\ \text{wall insulation water} \end{array} \right\}$$

Where, k_{ins} is the thermal conductivity associated with the insulation, t_i is the insulation thickness and D is the tank diameter.

From assumptions 4 and 5 we derive the temperature of the diffuser outlet plate, T_p , to be:

$$T_p = \int_0^t \frac{h_{is} A_s (T_p - T_a) + Q_E}{m_{wu} C_p} dt \quad (5-7)$$

Diffuser outlet plate
temperature as a
function of time

Where, h_{is} is the heat transfer coefficient associated with the 50mm of polyurethane insulation applied to the tank, A_s is the tank's surface area, Q_E is the electrical input from the immersion element, controlled by a thermostat to attain 60°C, m_{wu} is the mass of water above the diffuser plate.

In order to solve for the nodal water temperatures, T_{wi} , we have to perform energy balances for the top and bottom boundary nodes, T_{w1} and T_{wn} along with all intermediary nodes T_{w2} to T_{wn-1} . The energy balance associated with the top boundary is:

$$\frac{dT_{w1}}{dt} = \beta_w [T_p - T_{w1}] + \beta_w [T_{w2} - T_{w1}] + \delta_c [T_{s1} - T_{w1}] + \rho_{ins} [T_a - T_{w1}] \quad (5-8)$$

Energy balance
associated with top
boundary node segments

Where the coefficients associated with the thermal paths between nodes, β_w , δ_c and ρ_{ins} are given by:

$$\beta_w = \frac{1}{R_{wat} m_w C_p} \quad (5-9)$$

Water thermal path
coefficient segments

$$\delta_c = \frac{1}{R_{conv} m_w C_p} \quad (5-10)$$

Spiral wall/water
convection thermal path
coefficient

$$\rho_{ins} = \frac{1}{R_{ins} m_w C_p} \quad (5-11)$$

Insulation thermal path
coefficient

For nodes lying between the top and bottom boundaries, $T_{w2} \rightarrow T_{wn-1}$, the energy balance yields:

$$\frac{dT_{wj}}{dt} = \beta_w [T_{j-1} - T_{wj}] + \beta_w [T_{wj+1} - T_{wj}] + \delta_c [T_{sj} - T_{wj}] + \rho_{ins} [T_a - T_{wj}] \quad (5-12)$$

Energy balance
associated with
intermediate nodes

Finally, for the bottom boundary node, T_{wn} , the energy balance is:

$$\frac{dT_{wn}}{dt} = \beta_w [T_a - T_{wn}] + \beta_w [T_{wn-1} - T_{wn}] + \delta_c [T_{sn} - T_{wn}] + \rho_{ins} [T_a - T_{wn}] \quad (5-13)$$

Energy balance
associated with bottom
boundary node

The above equations can be vectorised so that the solution vector for all water node temperatures, $\overline{T_w}$, can be developed from the derivative vector derived from equations (5-8), (5-12) and (5-13) for $\frac{dT_{w1}}{dt}$ to $\frac{dT_{wn}}{dt}$ by taking the integral over time:

$$\overline{T_w} = \int_0^t \frac{d\overline{T_w}}{dt} dt \quad (5-14)$$

Deriving water node
temperature vector
solution

In order to solve $\overline{T_w}$, we must also simultaneously solve the nodal spiral wall temperatures T_{s1} to T_{sn} . To do this we invoke the network solution matrix $\overline{N_{sm}}$ which is derived by applying nodal analysis around the spiral wall temperatures:

$$\overline{N_{sm}} = \begin{bmatrix} \epsilon_1 & \epsilon_2 & 0 & 0 & \cdot & \cdot & \cdot & 0 \\ \epsilon_2 & \epsilon_1 & \epsilon_2 & 0 & \cdot & \cdot & \cdot & 0 \\ 0 & \epsilon_2 & \epsilon_1 & \epsilon_2 & 0 & \cdot & \cdot & 0 \\ 0 & 0 & \epsilon_2 & \epsilon_1 & \epsilon_2 & 0 & \cdot & \cdot \\ \cdot & \cdot \\ \cdot & \cdot & \cdot & 0 & \epsilon_2 & \epsilon_1 & \epsilon_2 & 0 \\ 0 & 0 & \cdot & \cdot & 0 & \epsilon_2 & \epsilon_1 & \epsilon_2 \\ 0 & 0 & \cdot & \cdot & \cdot & 0 & \epsilon_3 & \epsilon_4 \end{bmatrix} \quad (5-15)$$

The Network Solution
Matrix

Where the network terms ϵ_1 , ϵ_2 , ϵ_3 and ϵ_4 are given as:

$$\epsilon_1 = -R_{wall}^2 - 2R_{conv}R_{wall} \quad (5-16)$$

Network term 1

$$\epsilon_2 = R_{conv}R_{wall} \quad (5-17)$$

Network term 2

$$\epsilon_3 = R_{conv}R_{ins} \quad (5-18)$$

Network term 3

$$\epsilon_4 = -R_{ins}R_{wall} - R_{conv}R_{wall} - R_{ins}R_{conv} \quad (5-19) \quad \left| \begin{array}{l} \text{Network term 4} \end{array} \right.$$

In order for the heat fluxes to balance to zero at each node, equation (5-20) must be satisfied:

$$\overline{N}_{sm} \cdot \overline{T}_s = \overline{S}_b \quad (5-20) \quad \left| \begin{array}{l} \text{Spiral node temperature} \\ \text{equation} \end{array} \right.$$

Where the solution balance vector, \overline{S}_b , is given as:

$$\overline{S}_b = \begin{bmatrix} -\epsilon_2 T_p - R_{wall}^2 T_{w1} \\ -R_{wall}^2 T_{w2} \\ -R_{wall}^2 T_{w3} \\ \vdots \\ \vdots \\ -R_{wall}^2 T_{wn-1} \\ -R_{conv}R_{wall}T_{wn} - \epsilon_2 T_a \end{bmatrix} \quad (5-21) \quad \left| \begin{array}{l} \text{The spiral solution} \\ \text{balance vector} \end{array} \right.$$

Finally, once the matrices have all been developed, we can solve for the spiral wall nodal temperatures:

$$\overline{T}_s = \overline{N}_{sm}^{-1} \cdot \overline{S}_b \quad (5-22) \quad \left| \begin{array}{l} \text{Solving for the spiral} \\ \text{wall node temperatures} \end{array} \right.$$

In practice, (5-14) and (5-22) are solved simultaneously at each time-step.

5.3.2 MODEL AND EXPERIMENTAL RESULTS

The left hand side of Figure 5-2 shows the location of two thermocouples on the diffuser outlet plate and at the very bottom of the tank. The temperature at these two locations were monitored over the course of an experiment during which the tank was heated for 3 hours to test the output of the model described in the previous section.

The model was parameterised according to Table 5-1. It was found that the simulation solution stabilised at nodal numbers of 12 and above and time steps of 5 seconds and below.

Table 5-1 parameters used to run diffuser thermal model

Parameter	Value	Units
Number of simulation nodes	12	NA
Simulation time-step	5	seconds
Water thermal conductivity	0.405	W/mK
Aluminium thermal conductivity	202	W/mK
Polyurethane thermal conductivity	0.03	W/mK
Average ambient temperature measured throughout experiment and used for simulation	16	°C

The original simulation results, shown in Figure 5-3, indicated that the bottom of the tank would heat up to a temperature of 49°C and beyond after 1.6 hours for a diffuser with three spiral turns. This would ensure that the base of the cylinder would subject any *legionella* bacterium to sterilising conditions within the 7 hour off peak period during which a hot water tank would operate at night. The model indicated that fewer than 3 turns would have been insufficient. However, when the diffuser was made and tested, it was found that over 2.5 hours was required as is evident from the annotations below.

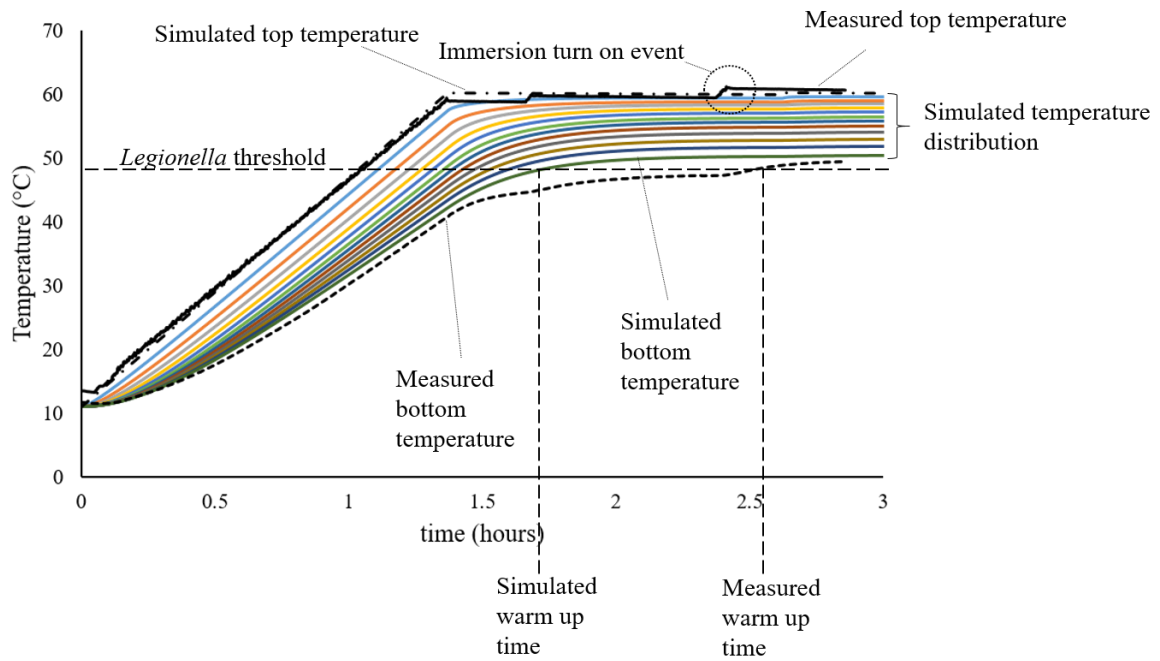


Figure 5-3 Simulation of temperature distribution through diffuser for a 3 turn spiral with 20 nodes applied to represent diffuser geometry assuming initial ambient temperature of 13°C.

There are a number of reasons that might explain the disparity between the simulation and the results. One potential contributing factor is assumption 5 which assumes the element and plate are close enough to one another to be effectively thermally coupled. The 15mm of separation between the immersion element's heating surface and the diffuser outlet plate may have introduced a thermal resistance. Another potential factor is the assumption that equation (4-11) from chapter 4, section 4.5.2 accurately predicts the heat transfer coefficient between the spiral wall and water volumes.

Given that the diffuser prototype had been made and that it did in the end ensure a sterilising temperature at the base of the cylinder. It was decided that refining the diffuser thermal model further was beyond the scope of the thesis in order to allow time to explore the flow dynamics, detailed in the following sections. In practice, using a higher conductivity material such as copper, or a greater thickness of aluminium would have reduced the warm up time further.

5.4 SPECIFYING THE DIFFUSER OUTLET HOLES USING A ONE DIMENSIONAL FLOW MODEL

Once the spiral geometry had been set, the outlet plate hole arrangement could be specified. The objective behind the outlet hole specification is to arrange the flow such that there is minimal mixing during operation. Experimental work undertaken in [188] explored 3 configurations of a horizontal inlet pipe designed to reduce mixing. The pipe was either wedged, slotted or perforated and it was found that the efficiency was highest for the slotted arrangement. The design of these inlet profiles however seems rather arbitrary and so the model described in this section was developed to explore whether tapering the holes, to achieve a constant flow rate across the surface of the outlet plate, would improve performance relative to constant hole sizes.

To formulate a relationship between the hole sizes and their respective flow rates, a simple analytical approach, utilising empirical design tables provided by [189], was taken. Figure 5-4 illustrates the schematic layout of the model used to estimate flow and pressure distribution throughout the spiral. The spiral is split up into a number of curved splines each connecting one hole to the next.

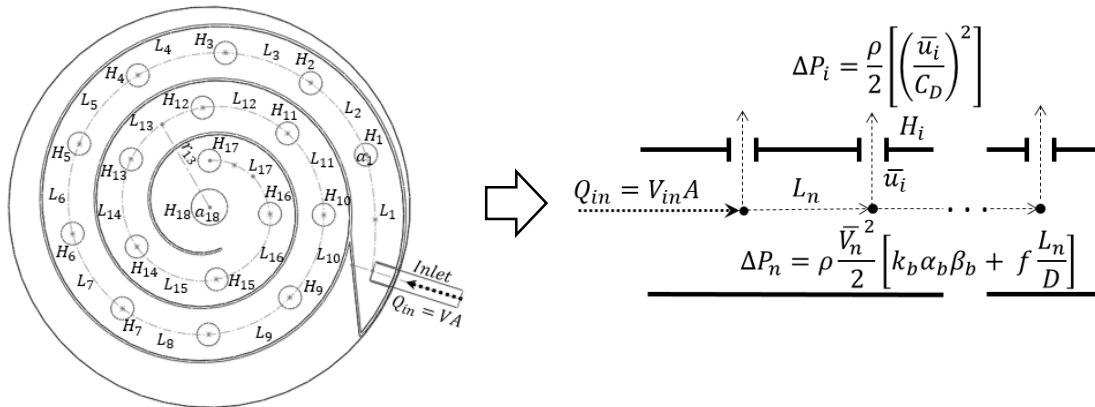


Figure 5-4 Hole locations and numbering scheme (left) related to an analytical flow distribution model (right)

The model accounts for three sources of head loss that occur as water flows through the diffuser: first is the pressure drop associated with the outlet holes, second is the shear stress between the flow and the walls associated with each spline and finally there's the loss associated with the transverse flow across the spiral path due to the centripetal forces associated with the flow path curvature. We can summarise the total pressure drop with the following equation:

$$\Delta P_{Total} = \sum_{n=1}^{n=17} \rho \frac{\bar{V}_n^2}{2} \left[k_b \alpha_b \beta_b + f \frac{L_n}{D_{hyd}} + \sum_{i=1}^{i=18} \frac{\rho}{2} \left[\left(\frac{\bar{u}_i}{C_D} \right)^2 \right] \right] \quad (5-23)$$

Wall shear pressure loss
Total pressure drop

Transverse pressure loss terms
associated with diffuser

Hole pressure loss terms
assembly

Where: subscripts n and i denote the individual splines and holes respectively, ρ is the fluid density, \bar{V} is the average spline flow velocity, k_b , α_b and β_b are spline curve, Reynolds number and interaction correction factors sourced from [189], f is the Darcy friction factor, L is the spline length D_{hyd} is the spline hydraulic diameter, u is the outlet hole flow velocity and C_D is the hole loss coefficient sourced from [190]. Loss coefficients were sourced from Figure 5-5 by computing the radius to the segment arc centre between each of the holes along with the arc outlet tangent angle θ . The Reynolds correction factors were looked up by computing the Reynolds number where the characteristic dimension is the hydraulic diameter:

$$D_{hyd} = \frac{4A_d}{P_r} \quad (5-24) \quad \left. \begin{array}{l} \text{Hydraulic diameter for} \\ \text{Reynolds number} \\ \text{correction factors} \end{array} \right\}$$

Where A_d is the duct area and P_r is the duct perimeter.

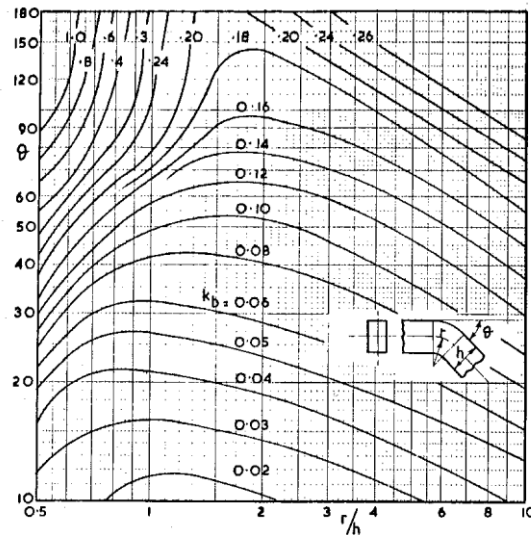


Figure 5-5 Loss coefficients associated with duct bends, image sourced from [190]

Any analytical solution to the flow rate through the holes must respect the principle that mass is conserved, assuming the flow is incompressible, this is stated by (5-25) as:

$$\bar{V}_m A = \sum_{i=1}^{i=18} \bar{u}_i a_i \quad (5-25) \quad \left. \begin{array}{l} \text{Conservation of mass} \\ \text{principle applied to all} \\ \text{holes} \end{array} \right\}$$

Where: \bar{V}_m is the average inlet flow velocity, A is the spline cross sectional area, \bar{u} is the average outlet hole velocity and a is the outlet hole area. To solve for the flow rate throughout the diffuser, an initial guess of the outlet hole velocity, \bar{u}_{18} , is made, the upstream pressure and flow distribution is then solved before the

conservation of mass principle (5-25) is checked. If (5-25) holds to within an acceptable tolerance, then the solution is complete, otherwise a new guess for \bar{u}_{18} is made. The procedure is illustrated by Figure 5-6:

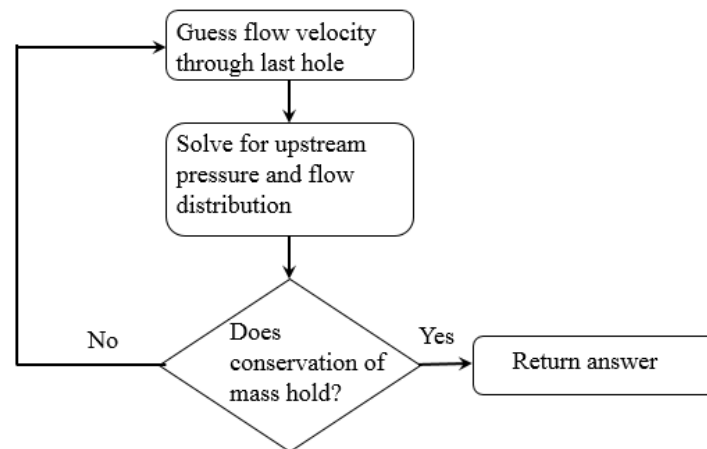


Figure 5-6 Algorithmic procedure to solve for flow rates throughout the diffuser

The procedure was applied to derive the flow rates through constant diameter, 20mm outlet holes to provide a baseline flow distribution. This distribution was then equalised by judicious adjustment of the hole diameters and re-running the solution algorithm until a more balanced distribution of flows, to within $\pm 0.01\text{kg/sec}$, was achieved. Hole diameters were rounded to the nearest integer mm value so that they could be made from available drills and punches. The resulting hole diameters and flow distributions for both the constant and tapered hole arrangements are shown in Figure 5-7. Figure 5-7 indicates that with a constant hole diameter, a substantial fraction of the overall inlet flow will escape from the first few holes whereas the tapered arrangement achieves a more balanced distribution. A bird's eye view of the hole patterns is shown on Figure 5-8 whilst Figure 5-9 shows a photograph of the final assembly on the left before being inserted into the tank on the right.

The results shown in Figure 5-7 must be treated with a high degree of caution given that there are a number of assumptions that the model relies on:

1. The flow is incompressible
2. Viscous dissipation is negligible
3. There are no entrance effects (i.e spiral segment L_1 , on Figure 5-4, is sufficiently long to ensure fully developed turbulent flow before hole H_1)
4. The conditions along any radial section of the spiral path are isobaric and consequently the hole radial position has no bearing on its contribution to the overall pressure drop
5. Empirical loss coefficients associated with spiral segments are additive and not interacting
6. The flow terminates at the last hole

Whilst the model's fidelity may be questionable due to these assumptions, it provided a quick semi-empirical means of creating a design which could be tested against the baseline, constant hole diameter case. An iterative approach using CFD would have been very time consuming and computationally expensive to undertake.

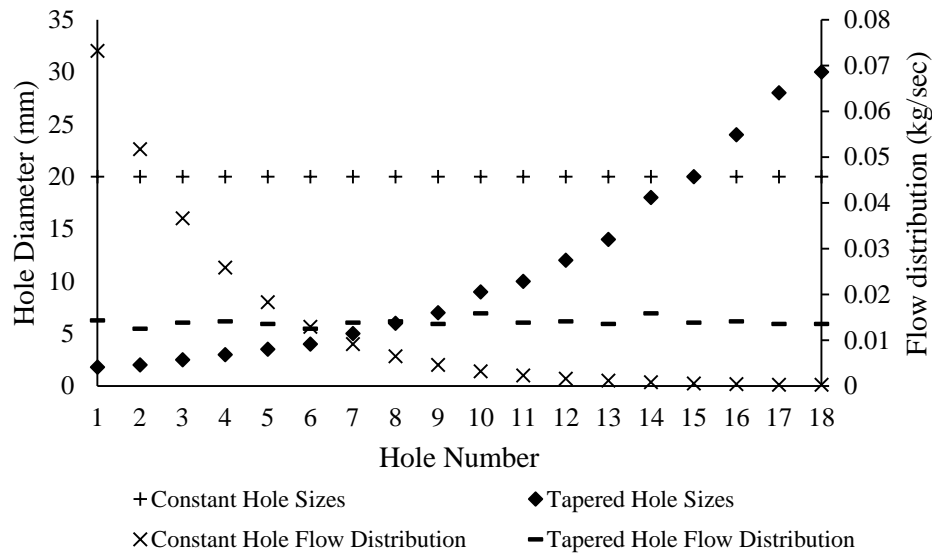


Figure 5-7 Hole sizes and flow distributions for the constant and tapered arrangements

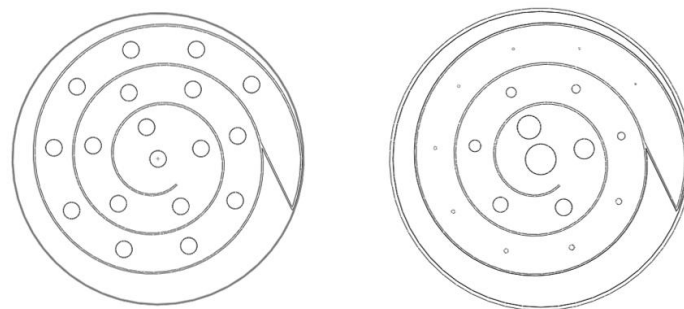


Figure 5-8 (Left) constant hole arrangement (right) tapered hole arrangement

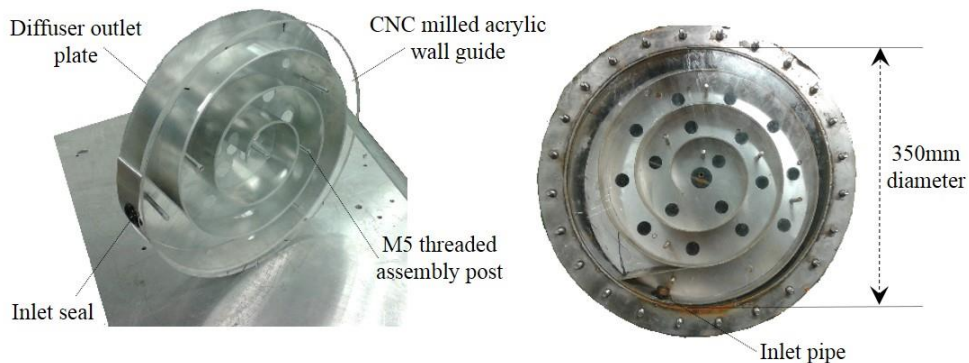


Figure 5-9 (left) photo showing isometric view of diffuser, (right) photo showing underside view of diffuser in tank assembly

5.5 CFD MODEL

To develop further insight into the flow phenomenon within the tank, a 3 dimensional CFD model of the stainless test tank and constant hole spiral diffuser was developed. The primary motivation for this was the work conducted by the authors of [191] who had observed that as a horizontal inlet jet flowed into a rectangular test tank, it impinged on the opposite tank wall which led to increased mixing. The purpose of the CFD simulation discussed in this section was to understand whether this would occur within the 350mm diameter cylindrical test tank and to what extent this would affect the performance of the tank in terms of the recoverable useable volume from the system. The CFD model would also shed light on whether inclusion of the spiral diffuser would reduce the degree of mixing compared to a standard horizontal inlet configuration. Once validated experimentally, the model was used to generalise the results further to explore the influence that a diffuser would have within cylinders over a range of diameters that are encountered in the UK.

A 3 dimensional finite volume model was applied using the Boussinesq approximation for thermal stratification as discussed in chapter 2, section 2.5.1.2, along with the $k - \epsilon$ turbulence model as discussed in chapter 2, section 2.5.1.4. A constant mass flow rate was specified at the inlet along with a turbulent viscosity ratio of 10 and turbulence intensity of 0.01 as recommended by the Star CCM+ user guide [181]. The roughness height of the surface boundaries was set to 0.4 μ m which is specified for stainless steel sheet in BS EN 10088-2 [192]. The inlet was located 10 pipe diameters (220mm) from the diffuser flow entry point to ensure that a turbulent plug flow velocity distribution was achieved. A constant pressure outlet boundary condition of 100kPa was applied and all tank walls were adiabatic meaning the effect of heat losses was ignored.

A polyhedral mesh was applied to the test tank geometry with a base mesh size of 15mm applied after a mesh dependency study was conducted. The study started by simulating draws of water and recording useable volumes at base mesh sizes of 18mm, 15mm and 12mm at a flow rate of 15lpm. The difference in outputs was 8% and 3% respectively indicating that 15mm provided sufficient resolution. A similar approach to the time step size was taken where it was found there was a negligible difference in result beneath 0.5 seconds at 15lpm. Mesh refinement zones, where the mesh nodes were shrunk to 15% of the base size (2.25mm) at a surface growth rate of 1.3, were added to the inlet and outlet pipes along with the diffuser geometry to capture the smaller geometric features in detail as shown in Figure 5-10. In total, there were 221,725 cells within the mesh applied to the tank including the diffuser. Figure 5-12 shows the mesh applied to the empty tank. The same base size and refinement zone parameters were used, however, refinement zones were only applied to the inlet and outlet pipes meaning that the number of cells were 102,734.

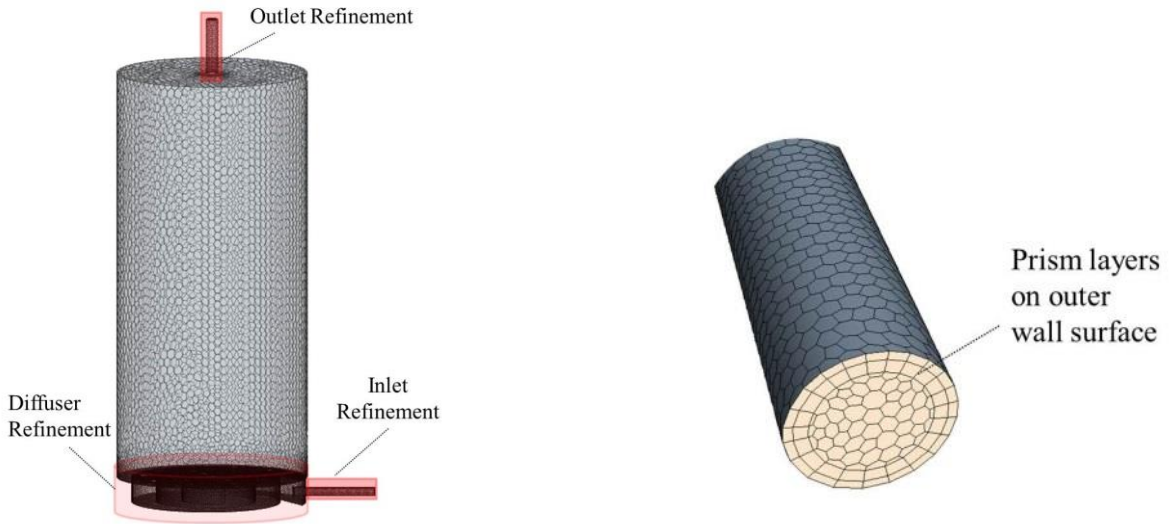


Figure 5-10 (left) side view of tank showing application of mesh refinement zones to capture inlet and outlet pipes along with diffuser geometry (right) close up view of inlet pipe showing application of prism layer meshing to wall boundary

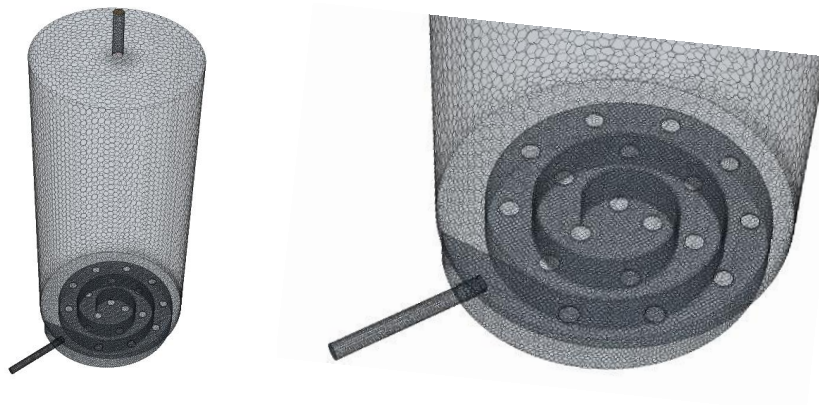


Figure 5-11 Isometric view of tank (left) and close up showing diffuser geometry (right)



Figure 5-12 Mesh applied to empty tank

The governing equations were solved using a 2nd order solver with a time step of 0.5 seconds and 5 solver iterations per time step. Numerical stability was inferred through inspection of the residuals as illustrated by Figure 5-13 where the residual error associated with the continuity equation, Y-momentum equation, turbulent kinetic energy and dissipation rate (T_{ke} and T_{dr}) are shown:

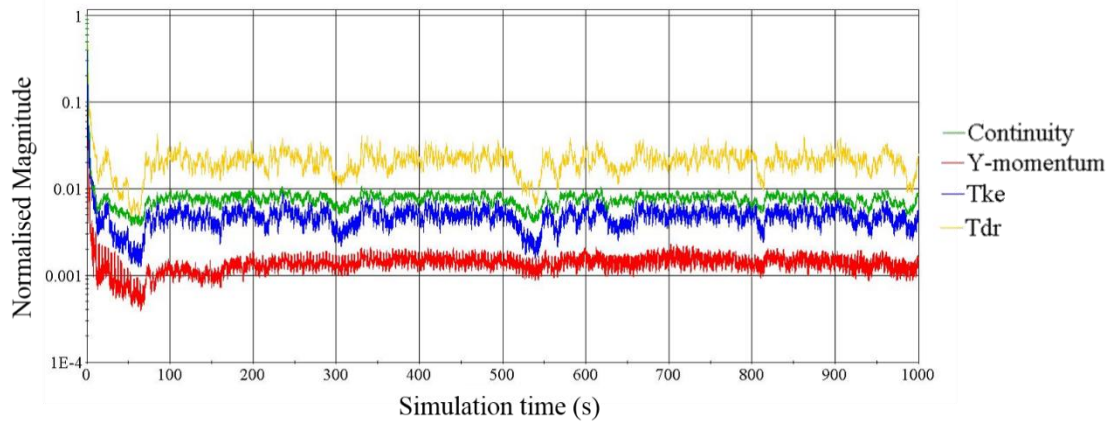


Figure 5-13 Magnitude of a selection of numerical residuals over time

To ensure that the turbulence wall models were applied to the laminar sub-layer over the extent of the pipe inlet, Y^+ values were observed to be between $30 < Y^+ < 300$ (see Chapter 2 Section 2.5.1.4):

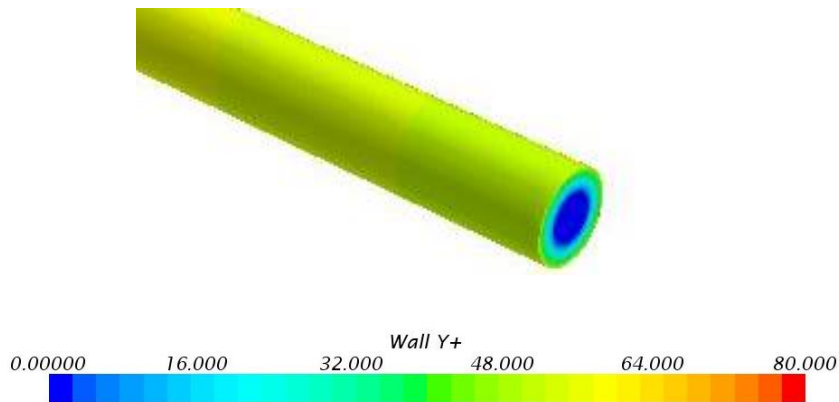


Figure 5-14 Y^+ values plotted for wall boundary surface nodes to ensure that turbulence wall models are applied

The CFD model was run to simulate each experimental test case, with and without the constant hole diffuser. The resulting temperature distributions were used to compute the volumetric, discharge and exergetic efficiencies as discussed throughout chapter 2, section 2.2.

5.6 EXPERIMENTAL TEST

To validate the output of the CFD model described in the previous section, the constant hole and tapered diffuser designs were built and integrated into the base of the stainless steel, 76 litre test tank as illustrated in Figure 5-1 and photographed prior to being insulated in Figure 5-15:



Figure 5-15 Stainless steel test tank before insulation was applied

5.6.1 DESCRIPTION OF TEST PROCEDURE

The test tank was installed into the test rig, described in section 2.61, as tank 1. Three draw events were conducted with and without the diffuser at target flow rates of 5, 10 and 15 litres per minute until. The tank was heated and stirred by the de-stratification pump, P_2 , prior to each test to ensure that the initial state of charge was identical within the accuracy of the thermocouple, T_4 . Once the tank had reached the test temperature, the heating element E_1 and P_2 were shut off and isolation valve V_5 was closed. Pump P_1 was then operated whilst the tank outlet water was routed through the changeover valve V_{CO} to thermocouple T_3 .

5.6.2 EXPERIMENTAL ERRORS AND UNCERTAINTIES

Figure 5-16 shows the cold inlet and changing outlet temperatures associated with three draw tests that were undertaken at a flow rate of 15lpm.

By repeating the draw tests, the degree of consistency between measurements can be assessed as illustrated by Table 5-2. Repeating the draw tests indicated that a high degree of consistency between measurements could be achieved with the maximum discrepancy in useable volume measurements being less than 1% with a figure of 2% for the energy that was discharged from 60°C to 48°C.

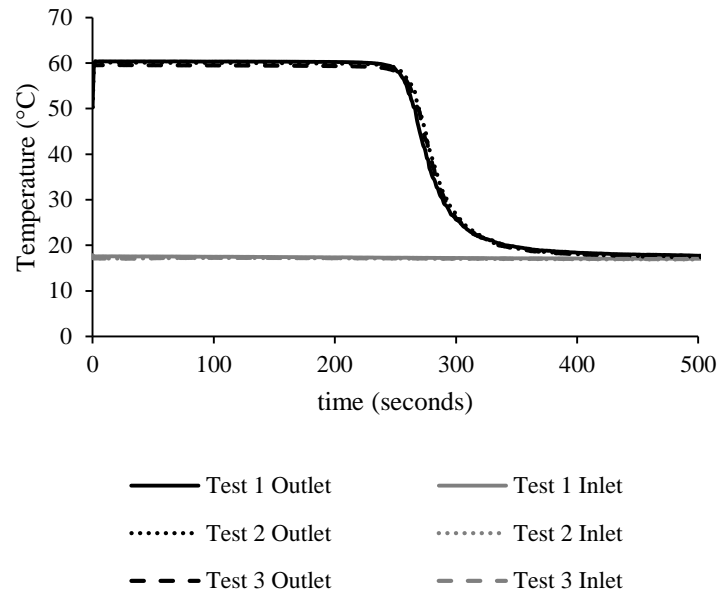


Figure 5-16 Outlet/inlet temperature traces for three draw tests showing consistency of experiments

Table 5-2 Repetition of draw tests to assess consistency of measurements

	Useable Volume (litres)	Energy extracted from 60°C to 48°C (kWh)
Test 1	115.9	3.69
Test 2	116.9	3.73
Test 3	119.5	3.67
Standard Deviation		
(litres/kWh)	1.5	0.026
Maximum		
discrepancy (%)	0.9	1.7

In addition to repeating the tests, we can estimate the uncertainty associated with measurement errors. Chapter 2, section 2.6.4 discusses the approach to error analysis with equations (2-42), (2-43) and (2-44) defining the error bounds for useable volume, extracted energy and extracted exergy respectively.

Table 5-3 shows the measurement parameters and associated errors relating to the measurements that were taken.

Table 5-3 Measurement parameters and associated error estimates

Measurement Parameter	Estimated Error	Units	Comments
Outlet temperature, $T_h(t)$	+/-0.5	°C	Thermocouples calibrated in temperature controlled bath
Inlet mains temperature, $T_m(t)$	+/-0.5	°C	Thermocouples calibrated in temperature controlled bath
Ambient temperature, $T_m(t)$	+/-0.5	°C	Thermocouples calibrated in temperature controlled bath
Flow rate, \dot{m}	+/-0.002	kg/sec	See chapter 2 section 2.6.2

5.7 RESULTS

This section details both the experimental and numerical results together. CFD simulations were conducted on the constant hole diffuser and diffuser-less test tank configurations. The simulations were initialised with the experimental data which included the initial mixed tank temperature, cold inlet temperature over the duration of the test and measured flow rate. Due to the considerable time taken to run each simulation (up to 24 hours per run), simulations were stopped once the outlet temperature dropped to 40°C. Scalar fields from the CFD simulations were used to shed light on the flow dynamics during mixing and once they had been validated by experiment, were extended to explore the influence that the tank's diameter might have on the performance of the diffuser, detailed in section 5.7.3.

5.7.1 EXPERIMENTAL AND NUMERICAL RESULTS

Figure 5-17 shows the inlet and outlet temperatures associated with the experimental and numerical tests conducted on the constant hole diffuser and diffuser-less tank configurations.

The reduction in mixing within the tank, due to the presence of the diffuser, is evident from the steep drop in temperature as the thermocline approaches and passes through the tank outlet. This distinctive difference between the outlet temperature curves is true across all flow rates though most pronounced at high flow rates.

Another notable feature of Figure 5-17 is the discrepancy between the CFD results and the measurements as the temperature changes. It appears that the CFD simulations overestimate the degree of mixing for the tests which included the diffuser particular at low flow rates. Whilst this could be as a result of numerical diffusion within the simulation, a grid and time step dependency study was conducted before choosing the mesh and time step sizes to minimise the influence of numerical errors. The discrepancy is therefore likely to be associated primarily with the turbulence k- ϵ turbulence model. However, as will be seen later in this section, once Equations (2-42) to

(2-44) were computed, the overall discrepancies were within the experimental errors and so it was decided that it was beyond scope to explore the performance of different turbulence models for the purposes of this thesis.

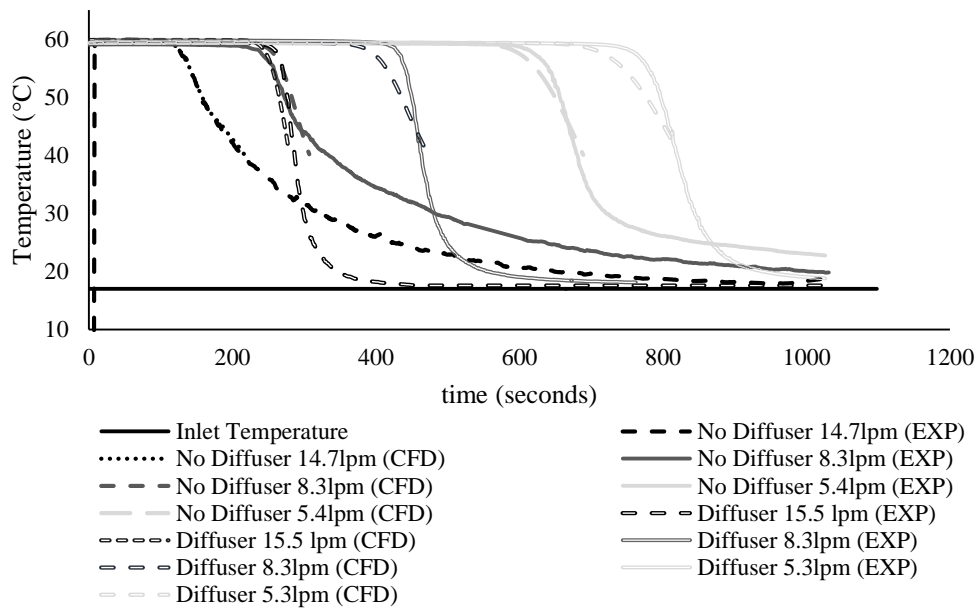


Figure 5-17 Draw event test results against CFD simulations for diffuser with constant holes compared to the no diffuser case

By applying Equation (2-42) to the traces shown in Figure 5-17 we can plot the volumetric efficiencies and corresponding error margins associated with each experiment:

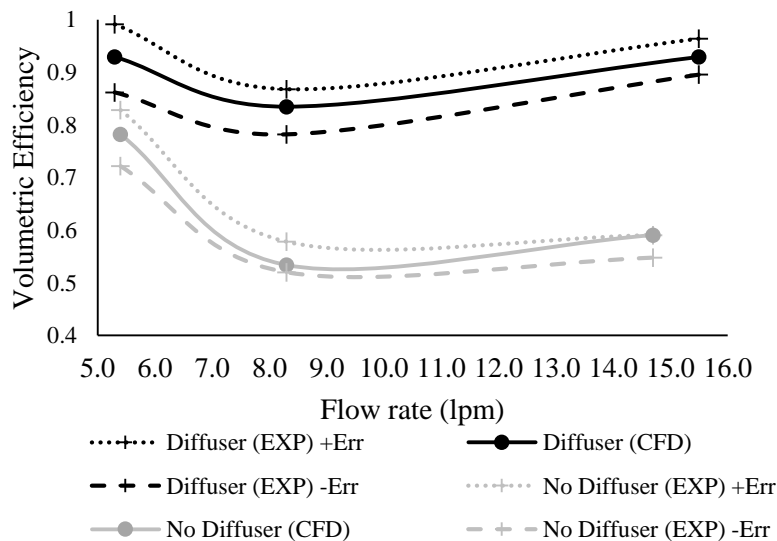


Figure 5-18 Volumetric efficiency as a function of flow rate for the diffuser and no diffuser cases assuming a usable temperature threshold of 43°C

By repeating the above procedure for Equations (2-43) and (2-44) we get similar plots for the discharge and exergetic efficiencies respectively.

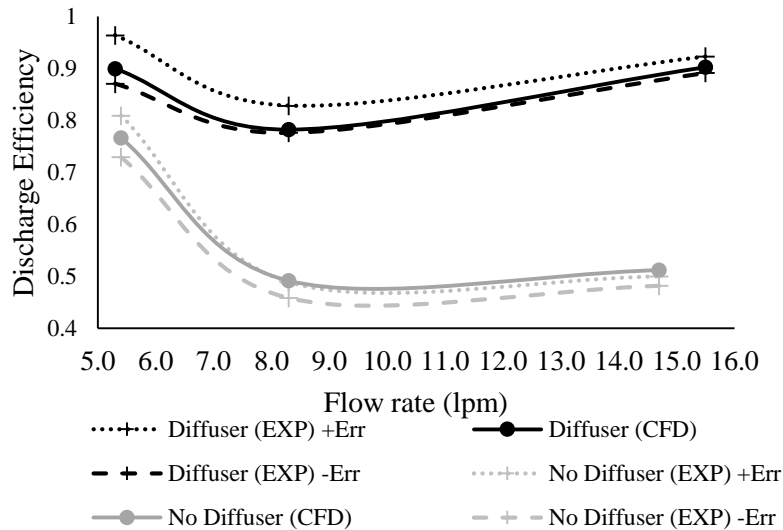


Figure 5-19 Discharge efficiency as a function of flow rate for the diffuser and no diffuser cases assuming a threshold temperature of 48°C (outlet temperature -20%)

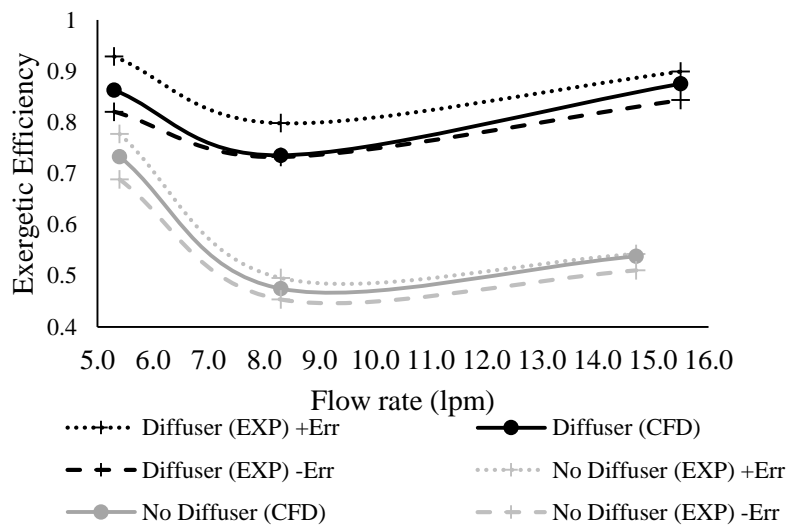


Figure 5-20 Exergetic efficiency as a function of flow rate for the diffuser and no diffuser cases

Tests were also conducted to compare the performance of the optimised diffuser, where the holes were tapered according to the right hand side of Figure 5-8 with the constant hole arrangement. The results of this experiment in terms of volumetric, discharge and exergetic efficiency are presented in Figures (5-20) to (5-22):

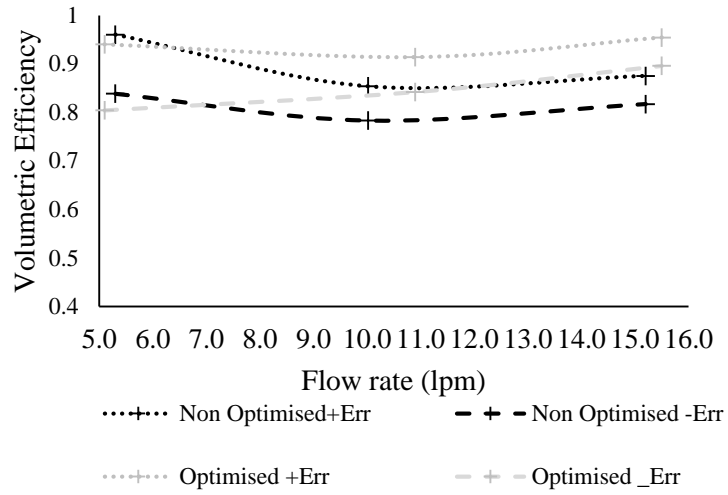


Figure 5-21 Volumetric efficiency of the optimised (tapered hole) versus non-optimised (constant hole) diffuser arrangements against flow rate

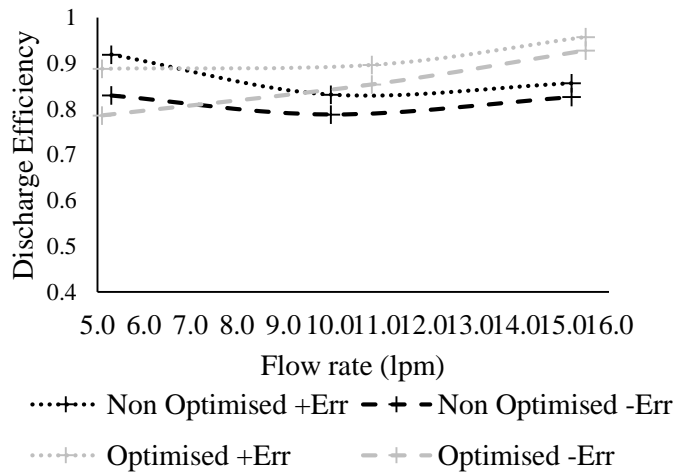


Figure 5-22 Discharge efficiency of the optimised (tapered hole) versus non-optimised (constant hole) diffuser arrangements against flow rate

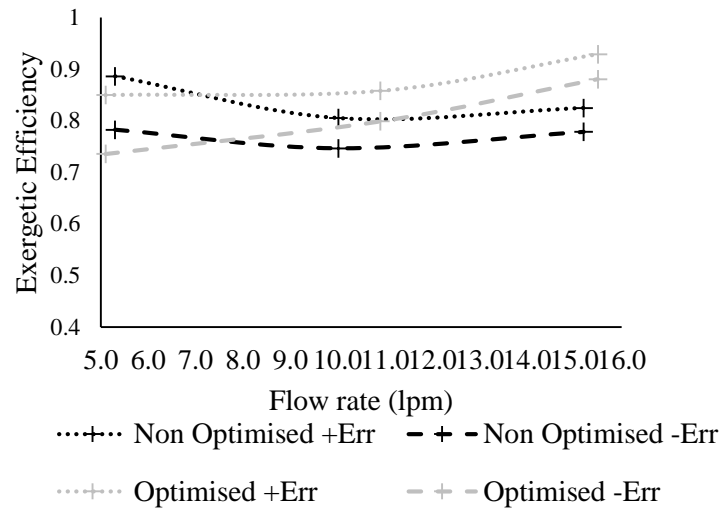


Figure 5-23 Exergetic efficiency of the optimised (tapered hole) versus non-optimised (constant hole) diffuser arrangements against flow rate

Figures (5-17) to (5-19) clearly show an increase in volumetric, discharge and exergetic efficiencies across all flow rates through inclusion of the diffuser in excess of the error margins. The improvements became particularly pronounced as the flow rate increased beyond 5.4 lpm. In the case of volumetric efficiency, including a diffuser enhanced performance by 4, 21 and 30% for flow rates of 5.4, 8.3 and 15.5lpm respectively. Improvements in discharge efficiency and exergetic efficiency were 7, 28 and 41% and 5, 24 and 30% respectively. Interestingly, across all experiments, there appeared to be a slight increase in performance between flow rates of 8lpm and 15lpm, the reasons for this are unknown and because the increase is close to or within the margins of experimental error, it was decided that exploring this phenomena was beyond the scope of this thesis.

The CFD results were within or close to the error margins across all experiments, however this has to be caveated with the fact that the error analysis undertaken was conservative as discussed in section 5.6.2.

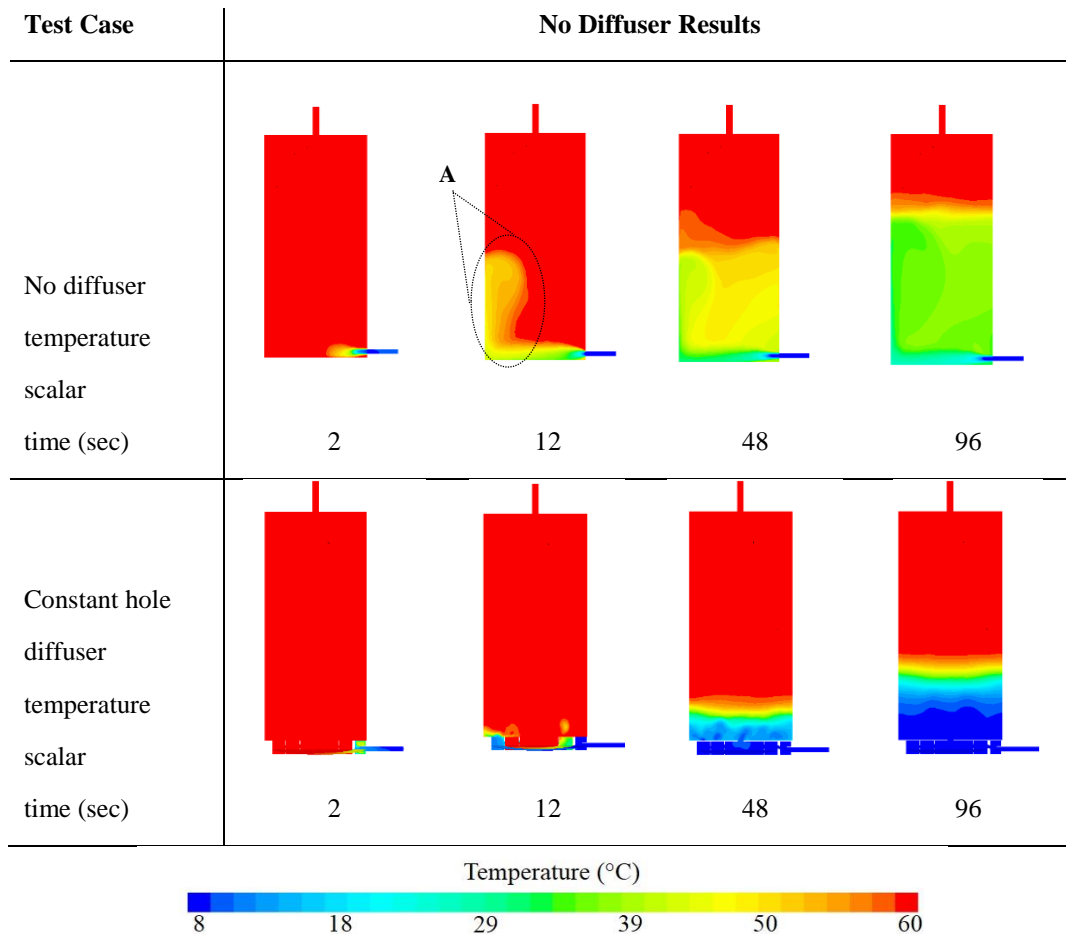
The difference in performance between the constant (non-optimised) and tapered (optimised) hole arrangements was less pronounced and, with the exception of experiments conducted at the highest flow rates where a slight improvement of 2, 6 and 6 % for volumetric, discharge and exergetic efficiencies respectively was recorded, were within the experimental error bounds.

Given the relatively second order influence that the hole sizing seems to have on the diffuser performance, it appears that most of the improvement resulted from the containment of the inlet jet which is achieved by the spiral wall. To explore the difference in dynamics associated with the inlet plume further, the CFD scalar fields associated with draw events conducted on the constant hole and diffuser-less tank configurations are discussed in the next section.

5.7.2 INSIGHTS FROM CFD SCALAR FIELDS

A section view through the centre of the simulated tank, rotated to run through the middle of the cold inlet, provides an interesting insight into the flow dynamics associated with the cold inlet jet as can be seen from Table 5-4:

Table 5-4 Evolution of temperature distribution within tank for no diffuser (top) and constant hole diffuser case for a flow rate of 15lpm drawn over 96 seconds



Four frames, taken at 2, 12, 48 and 96 seconds, show the temperature scalar through the tank for the diffuser-less tank on the top row of the table along with the constant hole diffuser tank configuration on the bottom. It is clear from the temperature scalar fields that inclusion of the diffuser leads to a far more stratified temperature distribution. At 12 seconds, the cold inlet plume associated with the diffuser-less case has collided with the side wall of the tank and has been diverted upwards to approximately half way up the extent of the cylinder before mixing into the surrounding volume of hot water (see annotation **A**). At the same point in time, the tank fitted with the constant hole diffuser exhibits very little mixing with a comparatively stratified temperature distribution emerging from the outlet plate at intervals of 48 and 96 seconds.

By adding another plane orthogonal to the scalar fields in Table 5-5, the progression of the cold inlet plume through the diffuser's spiralled channel can be seen in Figure 5-24:

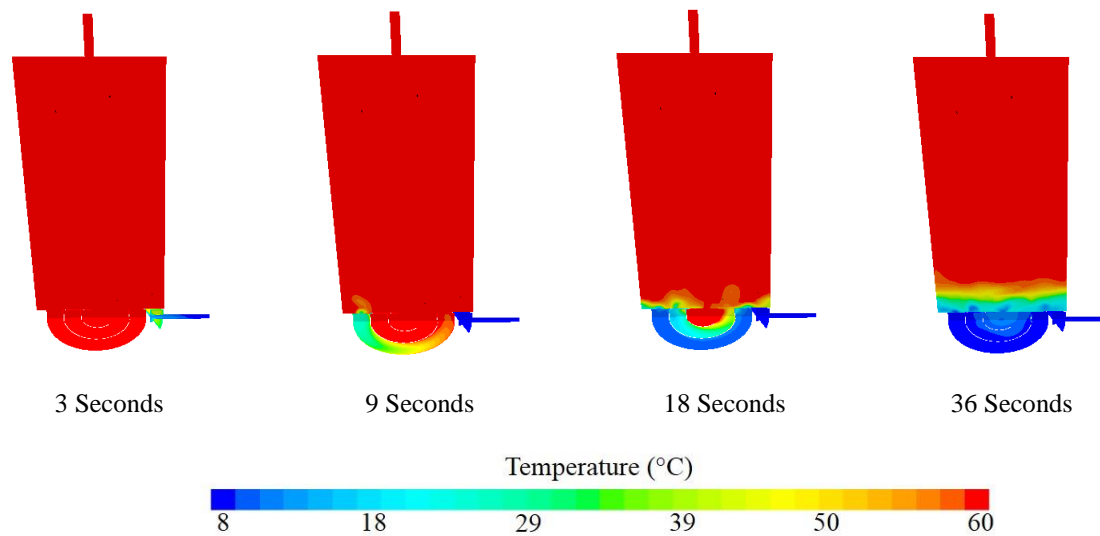


Figure 5-24 Isometric view of scalar field over the course of 36 seconds showing progression of cold inlet through diffuser spiral channel

At 9 seconds, it is evident that the plume is mixing inside the spiral channel as it progresses. The degree of mixing that occurs within the channel appears to determine the thermocline gradient that emerges from the diffuser outlet plate. By reducing the channel volume within the diffuser, it may be possible to further enhance the performance of the diffuser by reducing this initial source of mixing.

5.7.3 EXPLORATION OF LARGER TANK DIAMETERS

The results in the preceding section demonstrated that inclusion of the diffuser assembly within a 350mm diameter tank increased the recovery of useable hot water by up to 30%. In practice however, domestic hot water tanks have a range of sizes and diameters which might influence the degree of mixing that occurs. For instance, whilst Table 5-4 illustrates the collision of the inlet plume with the tank's side wall and the consequent mixing that results, how is this phenomena influenced by the diameter of the tank? At a larger diameter, it may be expected that the momentum associated with the cold inlet plume is dissipated as it approaches the opposite sidewall of the tank, leading to a less dramatic collision and consequent mixing when compared to the test case. This scenario would render diffusers less relevant for larger tanks.

To answer the above question, the CFD model, once validated, was applied to hypothetical tank sections with 3 diameters: 300mm, 450mm and 600mm, these sizes cover the full range of diameters encountered in UK domestic tanks, as detailed in BS 1566-1:2002 [46]. Each tank section was simulated with and without a spiral diffuser which was scaled from the original dimensions as used in the test tank (see Figure 5-25).

To quantify the degree of mixing that would result within each of these tank sections, draw events, at flow rates of 5, 10 and 15 litres per minute were simulated until 25% of the initial volume of each tank section was discharged. The tanks were initialised to be at a homogenous temperature of 60°C throughout with cold inlet water entering the bottom at 20°C. Each tank section had a constant height of 800mm and a constant inlet diameter of 22mm, this was to ensure that the Richardson's number, detailed by Equation (2-19) in chapter 2, would be consistent at each flow rate across all of the simulated section diameters. Ensuring that the Richardson's number was consistent for each test section would allow for the influence of the diffuser to be isolated from other factors that may affect mixing, such as the buoyancy gradient above the cold inlet along with the initial momentum of the incoming cold plume.

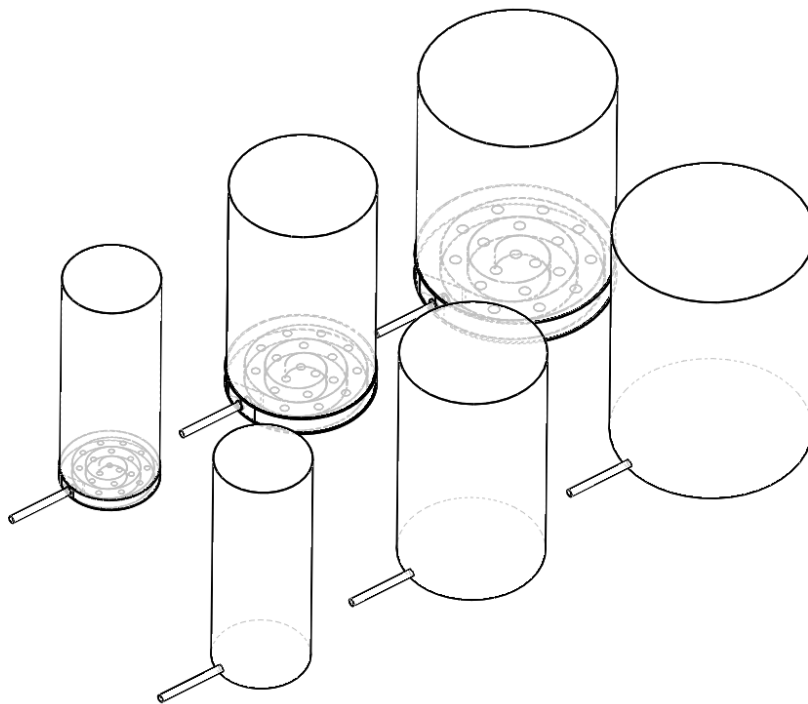


Figure 5-25 Hot water tank sections explored to understand the influence that tank diameter would have on the performance of a diffuser

After each draw event, the vertical temperature distribution throughout the tank was recorded and is shown for each of the tanks in Figures (5-26), (5-27) and (5-28) against an equivalent perfectly stratified temperature distribution representing the same energy content.

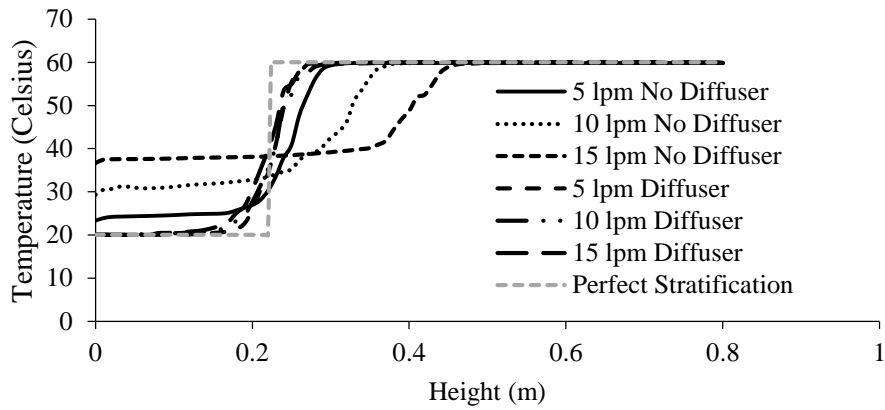


Figure 5-26 Temperature distribution within tank after 15 litre draw events from 300mm diameter tank

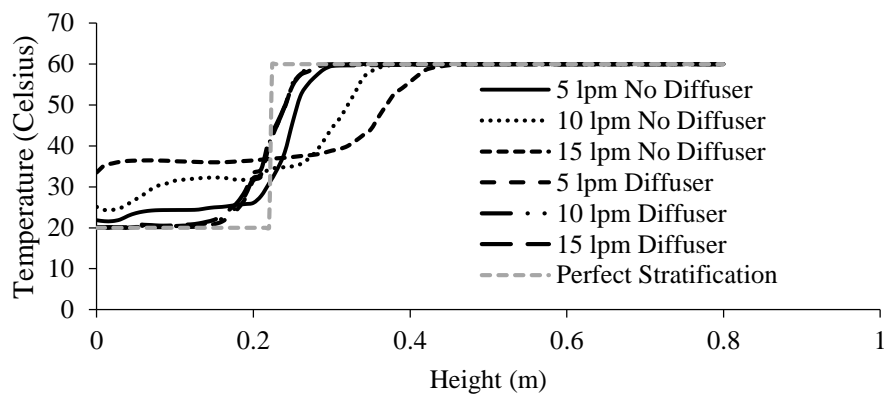


Figure 5-27 Temperature distribution within tank after 15 litre draw events from 450mm diameter tank

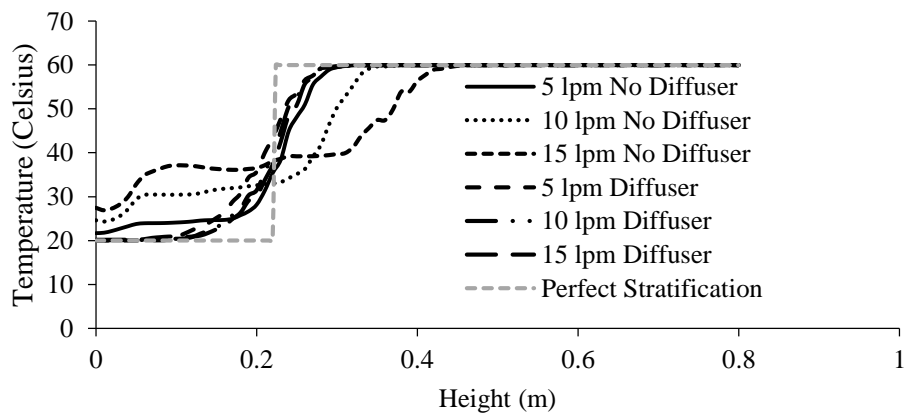


Figure 5-28 Temperature distribution within tank after 15 litre draw events from 600mm diameter tank

By applying equations (2-7) and (2-11) from Chapter 2, we can calculate the percentage loss of useable volume and exergy with respect to the initially charged tank for each simulation run. These results are plotted against the corresponding Richardson number associated with each of the test flow rates in figures (5-28) and (5-29):

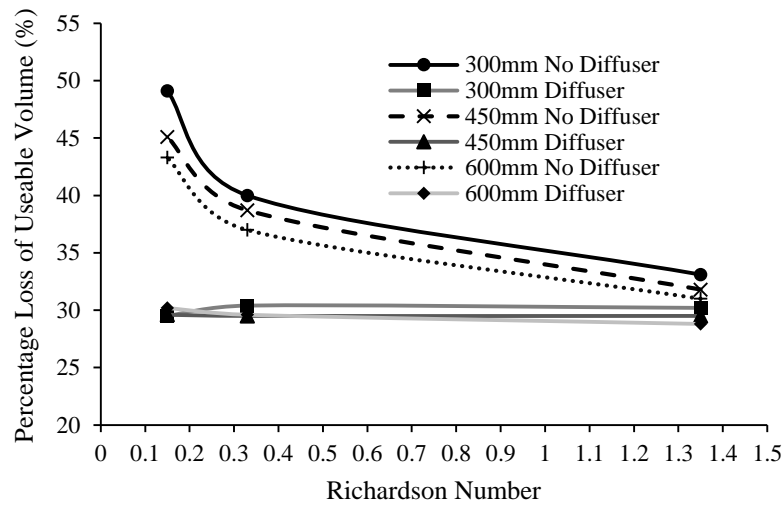


Figure 5-29 Loss of useable volume against the Richardson number for each tank section

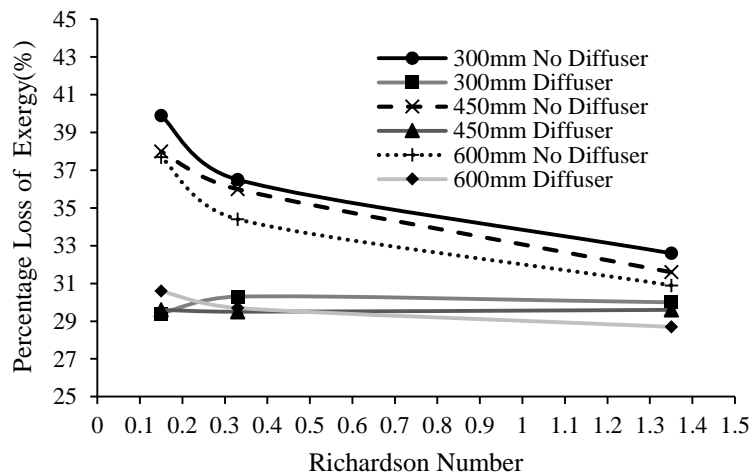


Figure 5-30 Loss of useable volume against the Richardson number for each tank section

Across all test section diameters without diffusers, there was a pronounced increase in losses of both useable volume and exergy as the flow rate increased and Richardson number dropped along with evidence of convergence in performance as the Richardson number increased. This trend is consistent with the literature, in particular [193] where mixing effects within a rectangular test section diminished as the Richardson number increased. Earlier experimental work, discussed in [94], pointed to a critical Richardson value of 0.25 beneath which the onset of mixing was observed, somewhat lower than the results presented here where mixing is clearly prevalent as the Richardson number drops below 1.35. However, where the diffuser was present, there was no discernible correlation between the Richardson number and useable volume or exergy losses.

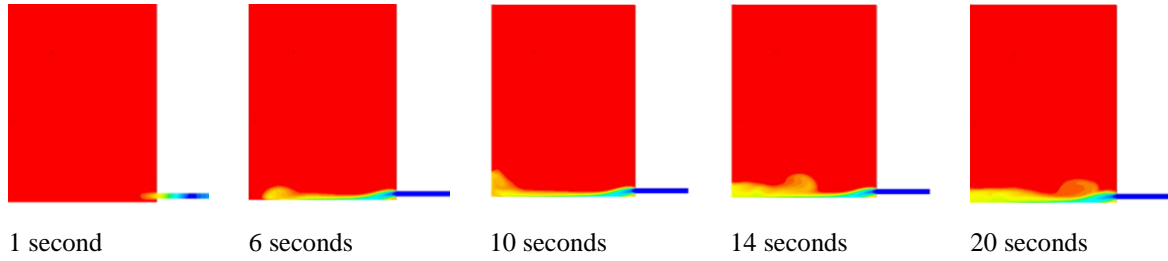
There was a discernible reduction in useable volume and exergy losses within diffuser-less test sections as the diameter increased, this was consistent with the hypothesis discussed earlier that the inlet momentum of the cold jet would be dissipated by the time it reached the opposite side of the tank leading to less mixing. This phenomenon can be observed from the temperature scalar fields taken at intervals of 1, 6, 10, 14 and 20 seconds on Table 5-5 where the extreme test cases associated with diameters of 600mm and 300mm along with flow rates of 5 and 15lpm are shown. The plume collision with the sidewall is visually more pronounced for the 300mm tank compared with the 600mm tank at both flow rates.

Simulated draws through tank sections including the diffuser assembly resulted with mixing substantially reduced to the extent that the correlation between both useable volume and exergy losses and the Richardson number was eliminated.

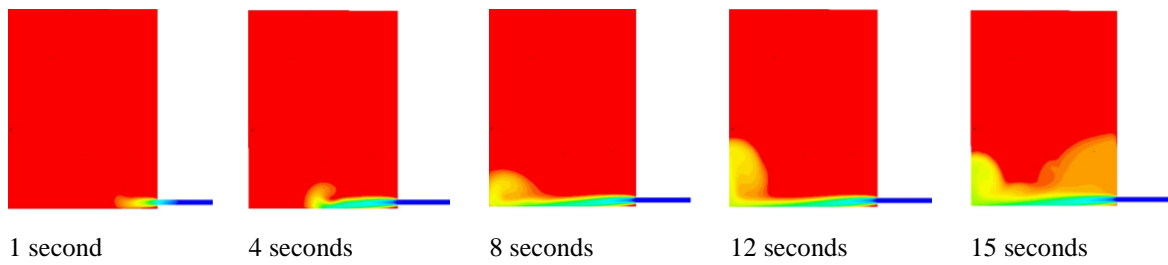
The disparity between the diffuser and no diffuser cases at the extremes of tank diameter size, 300mm and 600mm amounted to a 19% and 13% drop in useable volume and a 10% and 8% drop in exergy respectively at a flow rate of 15lpm (Richardson number of 0.15). So whilst increasing the diameter does reduce the performance difference between tanks with and without diffuser assemblies, there is still a significant reduction in losses at the highest diameters encountered in the UK market.

Table 5-5 Evolution of inlet plume within 300 and 600mm cylinder sections at 5lpm and 15lpm where there was no diffuser

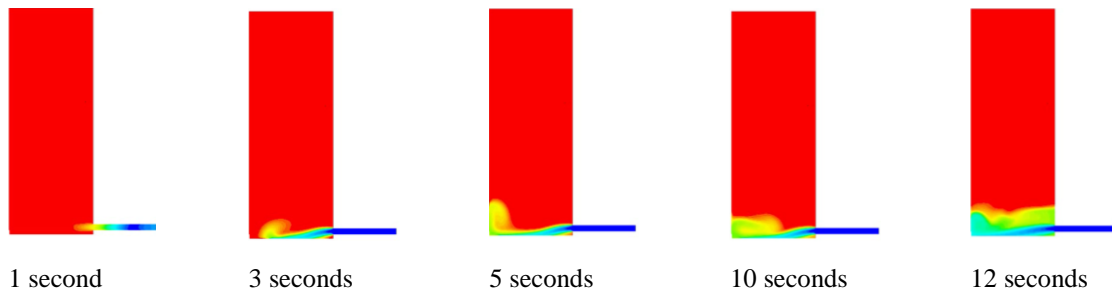
600mm Cylinder, 5lpm



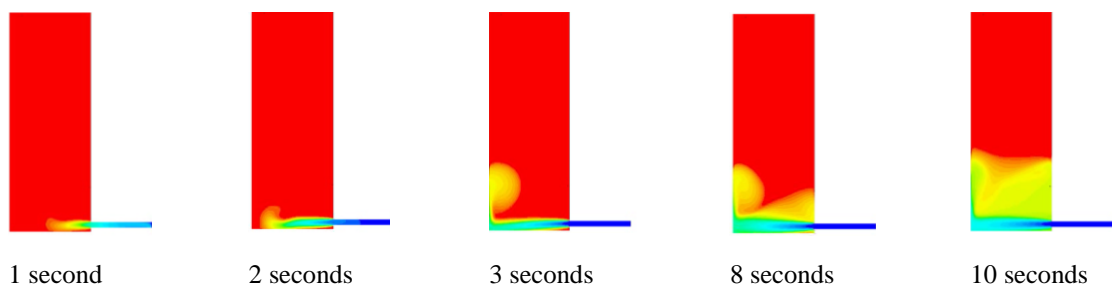
600mm Cylinder, 15lpm



300mm Cylinder, 5lpm



300mm Cylinder, 15lpm



5.8 SUMMARY

The spiral inlet diffuser arrangement, with lowered heating element, ensures that the entire volume of water within the tank is heated beyond the sterilising threshold temperature for *Legionella* within three hours of turning the heating element on. Furthermore, the volumetric efficiency of the test tank was improved by between 4% and 30% across inlet flow rates of 5 to 15 litres per minute with similar improvements in discharge and exergetic efficiencies. By arranging the heating element to be close to the bottom of the tank, so that heat can conduct through the water and diffuser assembly, sterilising temperatures can be attained without using a de-stratification pump. This reduces the cost that would otherwise be incurred along with the reduction in volumetric performance during draw events that was observed in chapter 3.

It was hypothesised that tapering the hole sizes to attain a more balanced flow distribution, would reduce the amount of mixing and enhance the volumetric performance of the tank. However, the performance of the tank with the diffuser was only marginally affected by the hole sizing scheme with an improvement of volumetric efficiency beyond experimental error of only 2%. More research however is required to determine whether the approach to hole sizing taken in this experiment, was the right one. For instance, whilst balancing the mass flow rate across all holes sounds intuitive, balancing outlet hole flow velocities or momentum might be a more appropriate objective.

Whilst the CFD model was consistent with experiment regarding total quantities of recovered useable volume, energy and exergy, there was a disparity between experimental and simulated outlet temperature profiles as the thermocline was encountered which indicated an increased degree of mixing within simulations. This disparity is most likely due to assumptions within the CFD simulation and in particular the $k-\varepsilon$ turbulence model, discussed in chapter 2, section 2.5.1.5.

Temperature scalar fields, produced by the CFD simulations, were used to provide a qualitative understanding of the dynamics of the flow inside the tank during a draw event. Frames taken at successive time intervals indicated that a significant source of mixing within the tank was due to impingement of the horizontal inlet jet on the opposite side wall; this extends the observation, first reported for a rectangular test tank in [191], to a cylindrical tank of a typical size encountered in domestic hot water systems. Given the second order effect that the diffuser hole sizing scheme had on performance, it would seem that the diffuser's primary purpose is to dissipate the momentum of the inlet jet such that impingement on the opposite wall and the consequent mixing that this entails is eliminated.

The CFD model was extended to explore the performance of the diffuser when scaled to fit within tank diameters of 300mm, 450mm and 600mm which represent the full spread of sizes found in the UK market. Whilst increasing the diameter reduced the degree of mixing that occurs when no diffuser is present, the diffuser still reduced the

loss of useable volume by 13% for the 600mm case at a flow rate of 15lpm suggesting that its presence would still be potentially worthwhile even in the largest cylinders.

It was found that introducing a diffuser meant the degree of inlet mixing becomes largely independent of the Richardson number. Without the diffuser, a substantial increase in inlet mixing becomes apparent as the flow rate increases and Richardson number drops, a finding consistent with the literature.

The findings in this chapter motivated a further experimental study, detailed in the next chapter, where the combined enhancements to thermal stratification, associated with both the diffuser and use of stainless tank walls detailed in the previous chapter, is compared to a commercial off the shelf cylinder made of copper with a conventional inlet arrangement.

6 HOW DOES ENHANCED STATIC AND DYNAMIC PERFORMANCE IMPROVE STORAGE OF SERVICE?

6.1 CHAPTER ROADMAP

So far, this thesis has concentrated on addressing static and dynamic modes of de-stratification independently in chapters 4 and 5 respectively. In chapter 4, it was found that the loss of useable hot water could be reduced significantly by switching from copper to stainless steel whilst in the previous chapter, dynamic mode de-stratification was found to be substantially lower by including a spiral inlet diffuser. This chapter details experimental work undertaken to explore how the performance of a hot water tank is affected by the combination of both stainless steel tank walls and a spiral inlet diffuser in comparison to a conventional copper cylinder.

A key question to consider concerns what the interrelationship between static and dynamic modes of de-stratification might be. For example, in the case of a tank fitted with a diffuser, after each draw event a much steeper thermocline will prevail in comparison to the case where no diffuser is present (see table 5-4 in chapter 5). However, a steeper thermocline will result in a greater rate of initial de-stratification during the tank's static mode of operation due to the larger temperature gradient that is established. This begs the question, *'does the improvement in dynamic mode performance, brought about by the inclusion of an inlet diffuser, get offset by static mode de-stratification during operation over time in practice?'* Intuitively, the answer would depend on the amount of time between draw events and the relative difference in thermocline gradients between the diffuser and no-diffuser cases. The experiment, conducted for this chapter, compares the extreme cases of a stainless tank with diffuser on the one hand, designed to minimise both static and dynamic modes of de-stratification, against a copper tank with no diffuser where both modes of de-stratification will in theory be greater. The hypothesis before conducting the experiment was that the stainless tank with diffuser would yield more useable hot water over time for a typical sequence of draw events than its copper counterpart with a conventional horizontal inlet. This is on the basis that a steeper thermocline would be both established by the diffuser and preserved by the lower thermal conductivity associated with the stainless walls.

The test rig configuration and test procedure is discussed in section 6.2 with results and conclusion provided in sections 6.3 and 6.4 respectively.

6.2 EXPERIMENTAL TEST CONFIGURATION AND PROCEDURE

6.2.1 TEST RIG CONFIGURATION

The schematic and details of the test rig are provided in chapter 2, section 2.6.1. Figure 6-1 shows test tanks 1 and 2, detailed dimensions are provided in chapter 4, figure 4-2. Tank 1 is a 74 litre, 350mm diameter stainless test tank fitted with the Archimedes spiral inlet diffuser specified in chapter 5. Tank 2 is a 74 litre, 350mm diameter copper British Standard type 1 cylinder with an open horizontal inlet located 100mm above the base of the tank as specified in [151]. Both tanks were insulated with 50mm of polyurethane insulating foam.

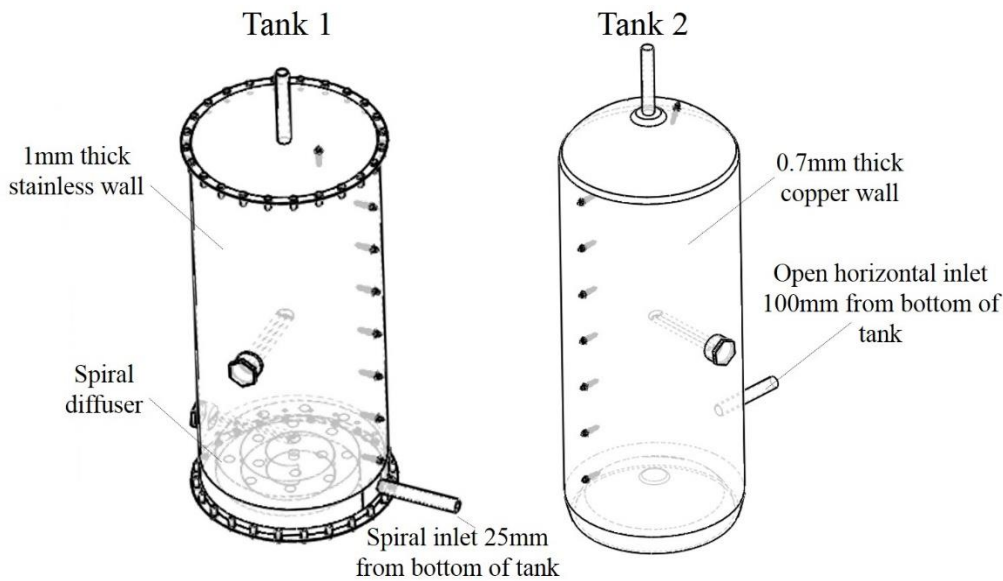


Figure 6-1 Test tanks 1 and 2 without insulation

6.2.2 TEST PROCEDURE

The test was designed to replicate the conditions that a typical system would encounter from 6 am in the morning to midnight. This period reflects the assumption that the tank heating element is fired according to an Economy 7, electric off-peak tariff where the heating element is timed to run from late at night till the early morning before the user has got up. It is assumed that the tank has been unused during the night so that at 6am, it is fully charged. Both tanks 1 and 2 were heated and de-stratified by pumps P_2 and P_3 so that a homogenous temperature of 60°C was achieved throughout each of them prior to the start of the test. At the start of the test, the de-stratification pumps were shut down, valves V_5 and V_6 were shut off before the first draw event of the simulated day was extracted from tank 1 by primary pump P_1 via the changeover valve V_{CO} . Once the draw event from tank 1 was complete, a 30 second delay would ensue whilst V_{CO} automatically switches to tank 2 at which point the same draw event would be repeated. After the second draw event, V_{CO} returned to the tank 1 position as before to await the next draw event at which point the procedure above repeats. During each draw event, inlet temperatures T_1

and T_2 were recorded along with T_3 , the outlet temperature after V_{CO} . The inverter frequency was selected to deliver the desired flow rate which was determined by measuring the changing mass recorded on the scales along with the changing output from the tank level sensor, TLS. This enabled the output of the system to be quantified in terms of the volumetric efficiency, η_{vu} , as described by equation 2-12 from chapter 2.

Each test drew a total of 56 litres of water from tanks 1 and 2 over the course of the draw cycle. This was to reflect the demand that would be typical of a small cylinder servicing one user in the UK as determined by the *Energy Saving Trust* who instrumented the hot water systems within 120 dwellings with flow meters over the course of a year [168].

The test was run twice using two different draw cycles, one of which was the ASHRAE cycle as outlined in Chapter 2, Figure 2-7. One criticism of the ASHRAE cycle is that it is based on averaged data from multiple dwellings which is further averaged over each hourly interval, this filters out the flow intermittency that is encountered when a system is monitored at a sufficiently high resolution as found by [194] where peak flow rates were found to be 40% higher at a 6 second sample interval in comparison to a 60 second interval. The second draw cycle was developed by the National Renewable Energy Laboratory (NREL) [79] who prescribe a more realistic, intermittent draw cycle shown in Figure 6-2.

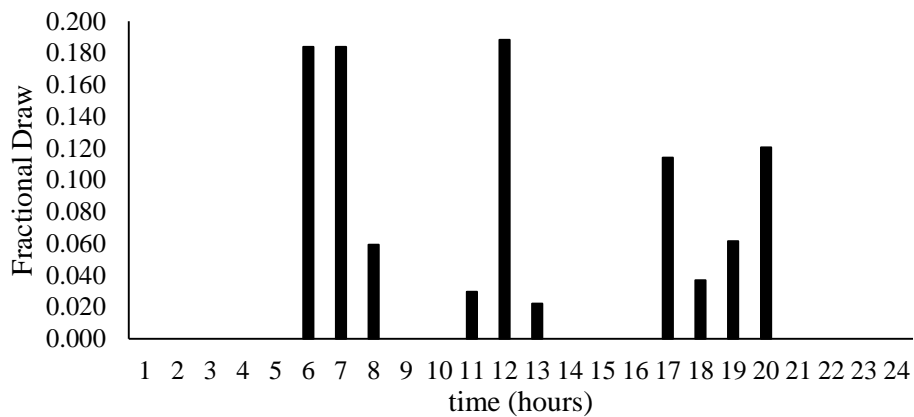


Figure 6-2 Intermittant draw cycle provided by [79]

To include the effect of flow variability, the first draw event is delivered at 15 litres per minute with all subsequent draw events being delivered at 5 litres per minute. This reflects the assumption that the tank’s first usage may be associated with a shower whilst subsequent activities such as, washing the dishes, wash hand basin use etc require only lower flow rates. For the ASHRAE cycle, all draw events were delivered at 10 litres per minute. Draw events up to 6am were ignored since they were negligible in size and on an Economy 7 tariff, the heating element would be energised returning the tank to a fully charged state.

6.3 RESULTS

6.3.1 ASHRAE TEST

Figure 6-3 shows the temperature traces produced by the test rig during the ASHRAE draw cycle. At each hour, two draw events are diverted through the change-over valve, V_{CO} , from tank 1 and 2. This is shown in detail by the breakout graph at 10 am.

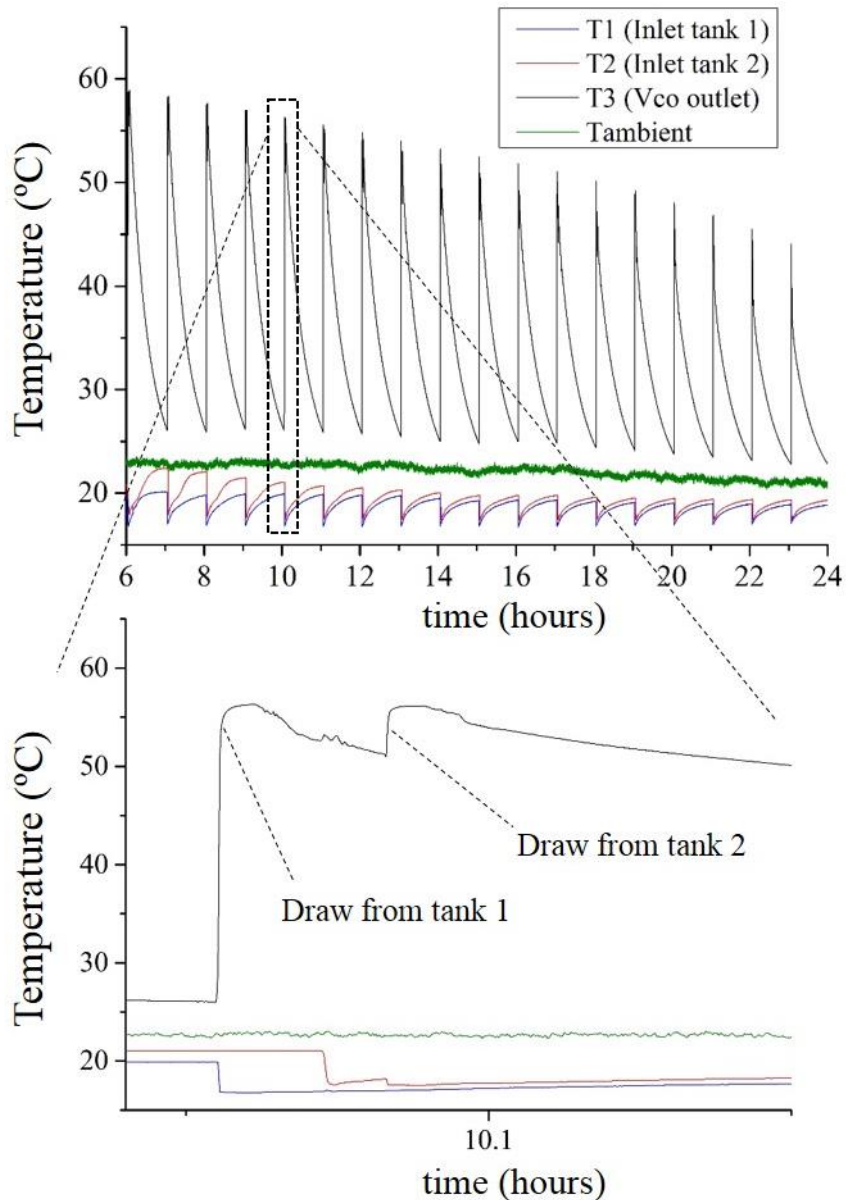


Figure 6-3 Temperature traces produced by test rig during ASHRAE draw test

The temperatures from the internal thermocouple probes, positioned at isochoric intervals as illustrated by Figure 4-2, chapter 4, were recorded and are shown for both tank 1 and tank 2 for the duration of the test in Figure 6-4. The traces are labelled T1 to T8 which correspond to measurement locations from the top to the bottom of the tank respectively.

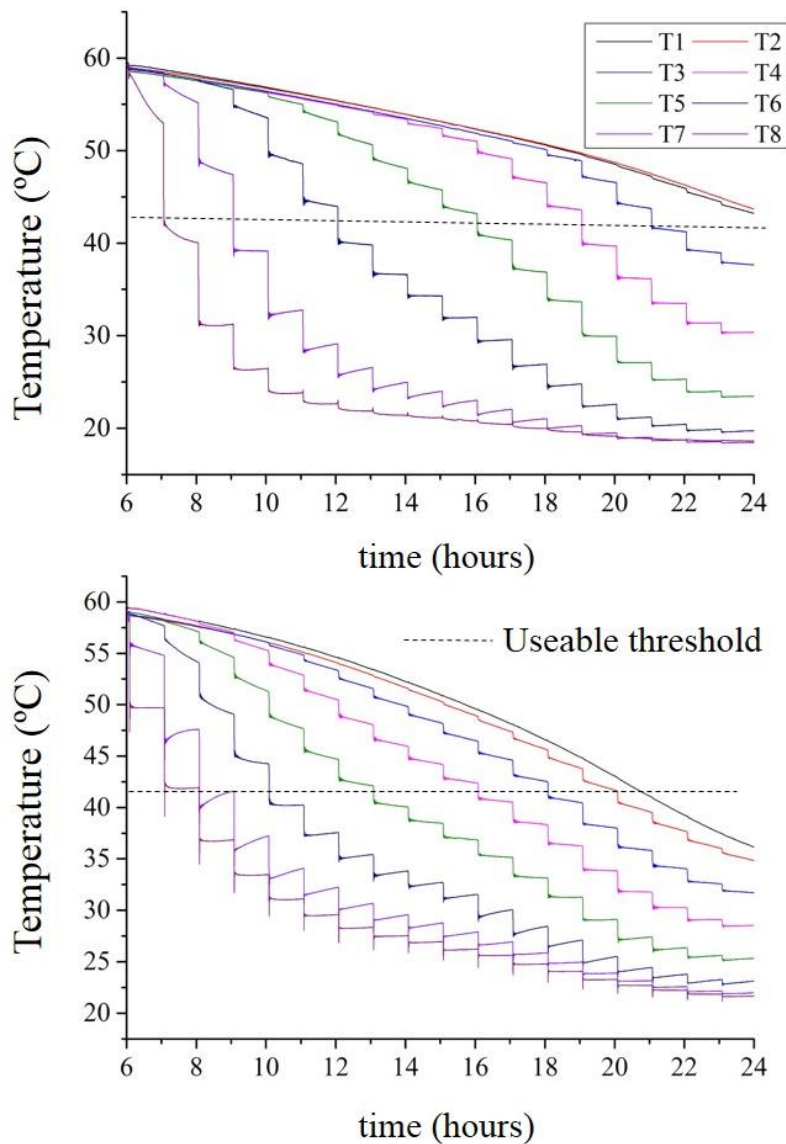


Figure 6-4 Internal temperatures within test tanks (top) tank 1, stainless with diffuser, (bottom) tank 2, copper without diffuser (ASHRAE test)

The increased rate of de-stratification is evident in Figure 6-4 from the more rapid convergence of temperatures across the vertical extent of tank 2 during operation. Assuming a useable threshold temperature of 43°C, it is evident that the temperature at the top of tank 2 goes cold at 8pm, resulting in a complete loss of useable volume whereas tank 1 is able to continue providing useful hot water all the way through to the next off-peak tariff heating time. The performance difference between tanks 1 and 2 is illustrated by Figure 6-5 where the useable volume delivered cumulatively throughout the day is shown as upper and lower error bounds +Err and -Err. The error analysis is detailed in chapter 2 section 2.6.4 with equation (2-42) being applied to determine useable volume error bounds.

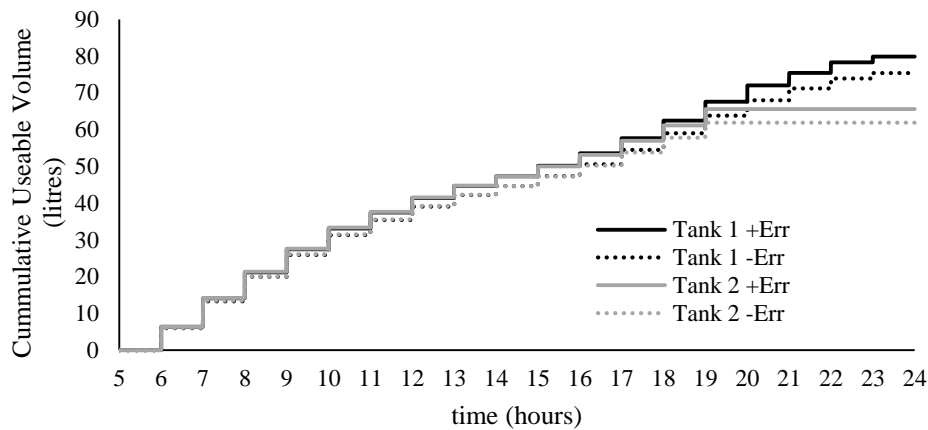


Figure 6-5 Useable volume extracted over time for tank 1 and tank 2 during ASHRAE test

Figure 6-5 shows that the rate of useable volume production from tank 2 begins dropping with respect to tank 1 by 18:00 due to the dropping outlet temperature. At 20:00 and beyond, no more useful hot water was extracted from tank 2 whereas tank 1 went on to deliver a total of 77.7 +/-2.25 litres compared to 63.8 +/-2.55 litres, in other words 22% more useful hot water.

Appendix A.3, table A-3 shows the draw event times, flow rates and average outlet temperatures recorded over the duration of each draw-off during the ASHRAE test.

6.3.2 BURCH & THORNTON TEST

After conducting the ASHRAE test, the Burch & Thornton test, shown on Figure 6-2, was drawn from the tanks once re-charged. Figure 6-6 shows the inlet and V_{co} outlet temperatures over the test period.

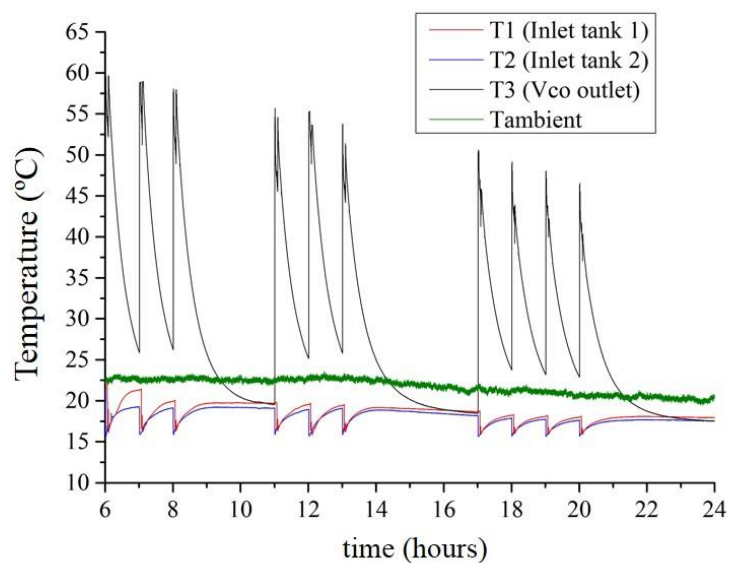


Figure 6-6 Temperature traces produced by test rig during Burch & Thornton test

Figure 6-7 shows the changing internal temperatures for the Burch & Thornton test for both tanks 1 and 2 against the useable threshold temperature. Again, as with the ASHRAE test, the top temperature of tank 2 drops more rapidly as the internal temperatures converge more quickly. This resulted in a complete loss of useable volume delivery by 7pm, as opposed to 8pm for the ASHRAE test. Tank 1 delivered useable hot water at each draw event with a total delivery of useable hot water of 66.7+/-2.4 litres compared to 61+/-2.2 litres.

Appendix A.3, table A-4 shows the draw event times, flow rates and average outlet temperatures recorded over the duration of each draw-off during the Burch & Thornton test.

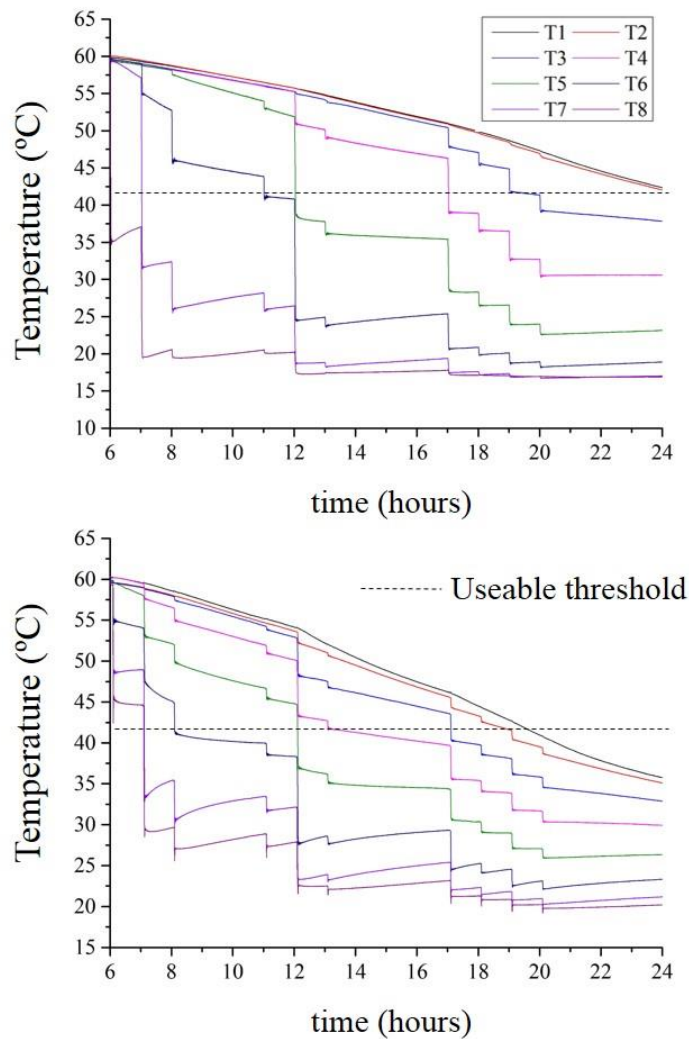


Figure 6-7 Internal temperatures within test tanks (top) tank 1, stainless with diffuser, (bottom) tank 2, copper without diffuser (Burch & Thornton test)

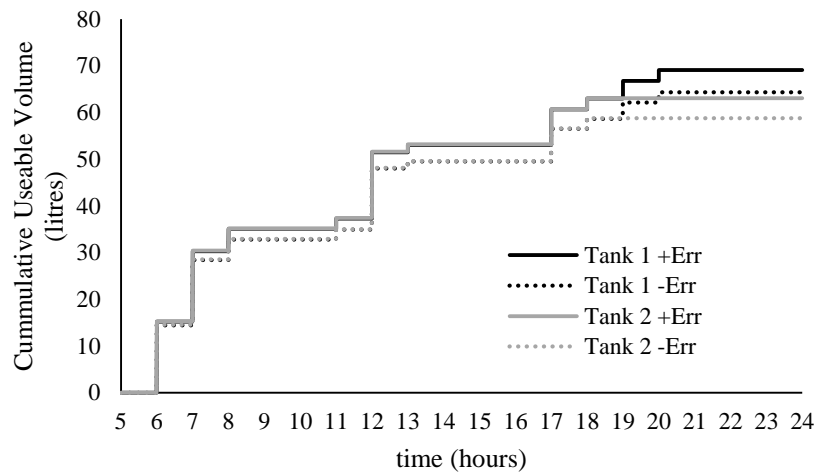


Figure 6-8 Useable volume over time for tank 1 and tank 2 during Burch & Thornton draw test

6.3.3 VOLUMETRIC PERFORMANCE

By computing equation (2-12) from chapter 2, it is possible to quantify the performance of each tank in terms of the volumetric efficiency. These figures are provided in Table 6-1 along with the associated experimental error for each test:

Table 6-1 Performance of tank 1 and tank 2 in terms of volumetric efficiency against ASHRAE and Burch & Thornton draw cycle tests

Test Type	Tank Configuration	Volumetric Efficiency	Experimental Error
ASHRAE	Tank 1	0.85	+/-0.020
	Tank 2	0.70	+/-0.020
Burch & Thornton	Tank 1	0.73	+/-0.026
	Tank 2	0.67	+/-0.024

For both the ASHRAE and Burch & Thornton tests, tank 1 outperformed tank 2 in terms of the volumetric efficiency of the system outside of the error margins. The performance difference was higher for the ASHRAE cycle where tank 1 delivered 21% more useable hot water compared with an increase of 9% for the Burch & Thornton test. It would appear that whilst the Burch & Thornton test subjected the tanks to an initial flow rate of 15lpm, the subsequent draws at 5lpm meant that there was less de-stratification overall compared with the more frequent draws at 10lpm associated with the ASHRAE test. More work is required to understand how flow rates change in practice and the implication on the volumetric efficiency of real world systems.

6.4 SUMMARY

The experimental work discussed in this chapter demonstrates that minimising both static and dynamic modes of de-stratification will increase the overall yield of hot water from a tank. This was true to the extent that a stainless tank with diffuser was able to continue delivering useable hot water until the very end of the day, several hours after an equivalent conventional copper cylinder had run out of useable hot water. Further work is required to determine whether this would reduce the extent to which householders consume energy at peak times. It may be that householders simply accept the tank running cold at certain times of day and change their habits accordingly. In principle however, enhancing the stratifying performance of the cylinder should increase the extent to which flexible tariffs can be exploited using a smaller cylinder.

Tank 1, a stainless cylinder fitted with diffuser, delivered 77.7 ± 2.25 litres compared to 63.8 ± 2.55 litres, from tank 2, a conventional copper unit, on an ASHRAE cycle with volumetric efficiencies at 0.85 ± 0.02 and 0.7 ± 0.02 respectively. This performance enhancement was greater than that encountered during the Burch & Thornton test where useable volumes of 66.7 ± 2.4 litres compared to 61 ± 2.2 litres and volumetric efficiencies of 0.73 ± 0.026 and 0.67 ± 0.024 were measured for tanks 1 and 2 respectively. There is therefore a significant dependency of performance on duty cycle which is non-intuitive to anticipate in advance. Given the computational intensity of CFD models and the inability of one-dimensional models to capture flow rate dependant mixing phenomenon, further research work is required to develop higher fidelity models that can simulate hot water tanks when subjected to different draw cycles over long time scales more effectively.

7. CONCLUSIONS AND FURTHER WORK

In chapter 1, section 1.6, four questions, which framed the objectives underpinning this research, were stated. This section evaluates the work discussed throughout this thesis against those questions before expanding upon further work that should be undertaken in light of the results.

All statements in bold represent claims of novel contributions that have been made as a result of this research. Relevant publications and patents are footnoted where they relate to each research objective.

7.1 THESIS OUTPUT AGAINST RESEARCH OBJECTIVES

7.1.1 TO WHAT EXTENT DOES THERMAL STRATIFICATION AFFECT THE PERFORMANCE OF REAL SYSTEMS AND IS IT RESPONSIBLE FOR BACTERIAL GROWTH? (CHAPTER 3)⁶

Whilst the literature details instances of bacterial contamination within domestic hot water tanks, chapter 3 took a novel approach by monitoring the vertical temperature distribution that prevailed throughout ten hot water tanks during operation. ***This work demonstrated that the temperature at the base of conventional electric hot water tanks, with vertical entry immersion heating elements, is chronically below the sterilising threshold for Legionella as a result of thermal stratification.*** To determine the extent to which temperatures are insufficient within the tanks operating in the 11 million households throughout England and Wales, a larger sample of systems with different topologies and fired by different energy sources would be required.

By taking bacterial samples from the very base of the cylinder, in addition to the tank outlet: ***This work demonstrated a preference for bacterial growth within the bottom of hot water tanks with a probability of this occurring by chance being less than 1%.*** There are a number of caveats to this finding that must be kept in mind. Firstly, the endoscopic camera, which was inserted into each of the tanks prior to being tested, revealed a large build-up of calcium carbonate scale which had precipitated on the heating element and built up in the bottom of the tank. This sediment may have fostered conditions for bacteria beyond what would be expected within a clean tank. However, had the entire volume of the cylinder been heated above 50°C, it is doubtful that any bacteria would have survived. Secondly, the test involved, only showed that bacteria which could be cultivated at temperatures similar to the human body were detected. Whilst this is a standard water quality test, it doesn't demonstrate the presence or absence of pathogens such as *Legionella*. However, as mentioned previously, temperatures were hospitable for *Legionella* during operation due to the positioning of the heating elements. Finally, ten tanks is a small sample, a larger study of systems is required to determine the extent of the problem, however studies of systems in Canada [55] and Germany [139] indicate that *Legionella* contamination is prolific in systems that are similar in design to those operating in the UK.

⁶ Results from this objective published in [199] and [200]

By removing a hot water tank from one of the flats and testing it with and without a de-stratification pump: *this work demonstrated that de-stratifying a hot water tank to improve sanitary performance, reduced the volumetric efficiency from 81+/-6% to 66+/-5% for the same initial charge of energy.* Again, this finding must be put into the context that it was for one topology of system with a vertical entry immersion element. Systems with lower heating elements might exhibit a less pronounced drop in performance since de-stratification would involve mixing a larger ratio of hot to cold water above and below the thermocline respectively.

Given these findings, a direct answer to the question at the heading of this section might be:

Thermal stratification maximises the performance of hot water tanks but allows temperatures to prevail that are conducive for potentially pathogenic bacteria to flourish within UK electric hot water tanks.

7.1.2 TO WHAT EXTENT DOES THE MATERIAL SELECTION ASSOCIATED WITH THE TANK WALL INFLUENCE STATIC MODE DE-STRATIFICATION? (CHAPTER 4)⁷

The tanks used for the experiments detailed in chapter 3 were all made of copper. However, as copper prices have risen, stainless steel systems have become more popular meaning that tanks made from both materials are now available on the market. Whilst the literature had referred qualitatively to the importance of wall material selection on thermal performance, a quantitative analysis was undertaken for chapter 4. An array of sensors, measuring the water temperatures directly, recorded the changing vertical temperature distribution throughout both a copper and stainless tank charged with the same initial thermocline position. *This work demonstrated that static-mode de-stratification is far greater in a copper walled tank in comparison to a tank with a stainless wall.* This was to the extent that all useable hot water was lost within 28 hours of operation for the case of a 0.7mm thick copper wall, compared with 42 hours for a stainless steel tank with a 1mm thick wall.

The experimental findings were corroborated numerically using an axisymmetric 2-dimensional CFD model. *This work suggested that a parasitic counter-rotating vortice system is established by heat flowing from above to below the thermocline through the tank wall.* It would be interesting to validate this finding experimentally, perhaps using particle image velocimetry (PIV) within a semi-transparent tank, whilst this work has been performed on a rectangular vessel [195], undertaking this work for a cylindrical tank would be more challenging.

Further numerical exploration indicated that switching from copper to stainless and copper to polyethylene, yielded a 2.7 fold and 5 fold reduction in the rate of useable hot water loss respectively. However the low tensile strength of polyethylene means that it would have to be reinforced by stronger materials in practice.

The model was also expanded to explore the effect that the tank volume and aspect ratio would have on rates of de-stratification. *This work indicated that the influence of wall material selection is more pronounced for tanks with a smaller volume and smaller aspect ratio.* The static mode performance increases up to an aspect ratio of

⁷ Results from this research objective published in [202]

4 beyond which the effect of heat losses, which rise due to the increasing ratio of surface area to tank volume, begins to take effect. Whilst there was close agreement between the CFD and the experimental data, it would have been useful to experimentally validate some of the simulations at different aspect ratios. Furthermore, undertaking a more detailed stress analysis, to resolve the changing distribution of stress that arises near tank wall connections and sections that transition to pressure relief domes, would have allowed an assessment of whether tapering the wall grade, to minimise static mode de-stratification without risking material failure, is worthwhile.

7.1.3 HOW CAN DYNAMIC MODE DE-STRATIFICATION AND BACTERIAL GROWTH BE INHIBITED BY THE INCLUSION OF A DIFFUSER? (CHAPTER 5)⁸

Chapter 3 demonstrated that de-stratifying a conventional tank had an adverse effect on dynamic performance and so, to ensure sterilising temperatures were attained throughout the tank's entire volume without losing useable hot water through inlet mixing, a test tank was commissioned with a lower heating element and diffuser arrangement. ***This work showed that the dynamic mode performance of a conventional hot water tank could be improved whilst ensuring the entire volume of hot water throughout the tank attains a sanitising temperature within the seven hour off-peak heating period associated with an Economy 7 tariff.***

A simplified, solid conduction network model was used to assess the heat transfer through the diffuser assembly. By ignoring the effects of convection, this led to a disparity between the predicted and simulated warm up time. A CFD model, whilst more computationally expensive, might have provided a more accurate result by capturing the effects that convective heat transfer between the heating element and diffuser outlet plate would have in practice. However, given that sterilising temperatures were attained, along with the fact that the test tank had a flat flanged bottom arrangement to facilitate ease of access, it was decided that further work in this area would be best reserved for real systems where the geometry associated with a pressure relief dome has to be considered.

Experimental work was undertaken to explore the effect that the diffuser assembly would have on the dynamic mode performance associated with a draw event during which the entire useable volume of the tank was discharged. ***This work showed that a diffuser with constant holes could deliver volumetric efficiencies that were between 83% and 95% up to flow rates in excess of 15lpm compared with a range of 52% to 78% for a conventional arrangement with no diffuser for a single continuous draw event.***

An iterative one dimensional flow model, using empirical loss coefficients, was used to develop a tapered hole pattern to achieve a uniform mass flow rate across the diffuser outlet surface. The yields of useable volume delivered from the tapered hole pattern was compared to the constant hole pattern. Whilst a modest performance improvement was observed, it was not outside of experimental error. The error analysis undertaken was however conservative. If higher accuracy platinum resistance thermometers were used, or had the measurements been independent so that errors could be taken in quadrature, it may have been possible to confirm whether a significant

⁸ This work led to patent filing P44091GB

performance advantage is delivered from tapered holes. *This work, combined with insights gleaned from scalar fields produced by a three dimensional CFD simulation, indicated that the primary purpose of the diffuser is to capture the cold inlet plume and prevent it colliding with the opposite wall of the tank.*

The CFD model of the test assembly was scaled to explore the full range of tank diameters that are encountered in the UK market. *This work indicated that a diffuser would significantly reduce the loss of useable volume during a draw event between diameters of 300mm and 600mm and is therefore a worthwhile design feature for all common tank sizes.* Whilst this conclusion is true for the simplified geometry associated with the test tank, where the bottom was a flat flange plate. In practice, the geometry and inlet configurations associated with tanks in the UK market, detailed in the design standards [151] have to be taken into account.

The literature has placed emphasis on the role that the Richardson number plays on dynamic mode de-stratification. *However: this work showed that where a diffuser is used, the correlation between Richardson number and the amount of de-stratification that occurs, breaks down.*

7.1.4 HOW MUCH HOT WATER CAN A TANK DELIVER ON AN OFF-PEAK TARIFF AGAINST TYPICAL DEMAND PROFILES AND CAN THIS BE IMPROVED? (CHAPTER 6)

The test tank, discussed in chapter 5, had both stainless walls and a diffuser to minimise both static and dynamic modes of de-stratification. The performance of this system, against a conventional copper tank with the same volume, was assessed in chapter 6 under a test designed to emulate the conditions associated with an Economy 7 tariff. Both systems were charged to the same temperature, using a de-stratification pump to ensure that the stored water was fully mixed, before being subjected to two standard draw cycles from the literature whilst the volumetric efficiency was monitored. *This work showed that combining both a diffuser and stainless walls enhanced the overall volumetric performance from 70% to 85% and 67% to 73% over the course of an 18 hour ASHRAE and Burch & Thornton draw cycle respectively.*

In practice, there would have been no de-stratification pump to initialise the temperature distribution. This would have meant that less energy would have been stored within the copper tank compared to the stainless system due to the limited heat transfer beneath the immersion element. This would have led to a potentially larger disparity in performance in reality because of the lower position of the heating element. The test tank would have been able to store more thermal energy in a conventional installation implying a greater utilisation of off peak tariffs.

Further work is required to determine whether these performance enhancements would translate into significant reductions of peak energy consumption for real world users. In particular, this thesis has assumed a useable temperature threshold of 43°C throughout on the basis of thermostatic mixing valves that are used for bathing applications, furthermore, the influence of pipe losses downstream from the tank have been neglected. In reality the extent to which de-stratification determines peak energy consumption will depend on the user's actual perception of hot water temperatures which are likely to vary in practice.

7.2 FURTHER WORK

Section 7.1 flagged up some of the areas of further work that could be pursued. This section discusses the items of work which arguably deserve most attention in order of priority.

7.2.1 EXPLORATION OF THE IMPLICATIONS OF RESEARCH FINDINGS WITHIN A REAL WORLD CONTEXT

Whilst it was shown that an overall increase in volumetric efficiency could be delivered by improving static and dynamic modes of performance in the laboratory, determining whether this would translate into a reduction in peak energy consumption in practice demands a real world trial. This would involve installing a fleet of enhanced tanks, including stainless walls and diffusers, in domestic premises and monitoring their operation. These measurements would have to be compared against a baseline comprising conventional copper hot water tanks with open side inlets. The question that such a trial would set out to answer would be:

Does enhanced dynamic and static mode performance translate into a significant shift in energy consumption from peak hours, to off-peak hours under a time of use tariff such as Economy 7 in reality?

In addition to assessing thermal performance, such a trial would provide an opportunity to determine the benefits that lowering the heating element delivers in terms of sanitary performance.

Work has begun in this direction with the development of a diffuser, cold inlet and heating element arrangement which has been integrated within mains pressurised conventional hot water tanks that are manufactured by Newark Copper Cylinder Limited. Figure 7-1 shows a semi-transparent model of the tank on the left, without insulation along with top and underside views of the diffuser assembly to the centre and far right respectively.

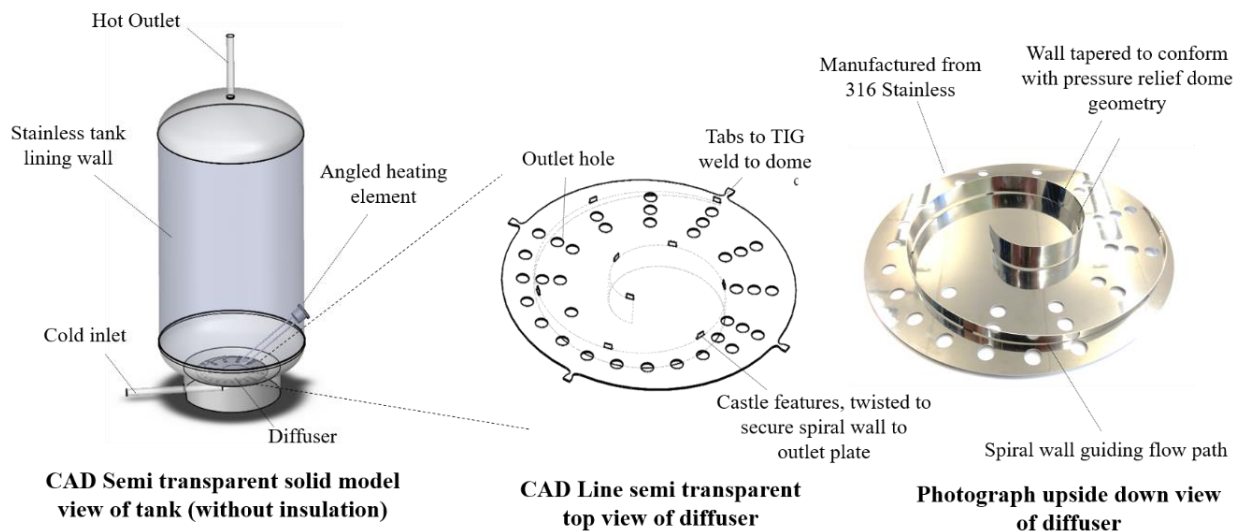


Figure 7-1 Integration of diffuser assembly into manufacturer's hot water tank range. (Left) isometric transparent solid model view of tank without insulation. (Centre) semi transparent line drawing showing castleated wall/plate assembly. (Right) photograph showing underside of manufacturing prototype diffuser assembly

Due to the curvature of the pressure relief dome, it was not possible to lower the heating element as described in chapter 5 for the test tank. Instead, the heating element boss has been angled so that the immersion tip clears the diffuser outlet plate by 20mm. The cold inlet, rather than coming in horizontally, 150mm from the base of the cylinder as before, now enters the tank at the very bottom with the flow path being diffused by a spiral wall which is tapered to conform to the geometry of the pressure relief dome. Figure 7-2 shows cylinders that have been manufactured, prior to insulation, along with the diffuser assemblies on the left, with a finished production tank on the right:

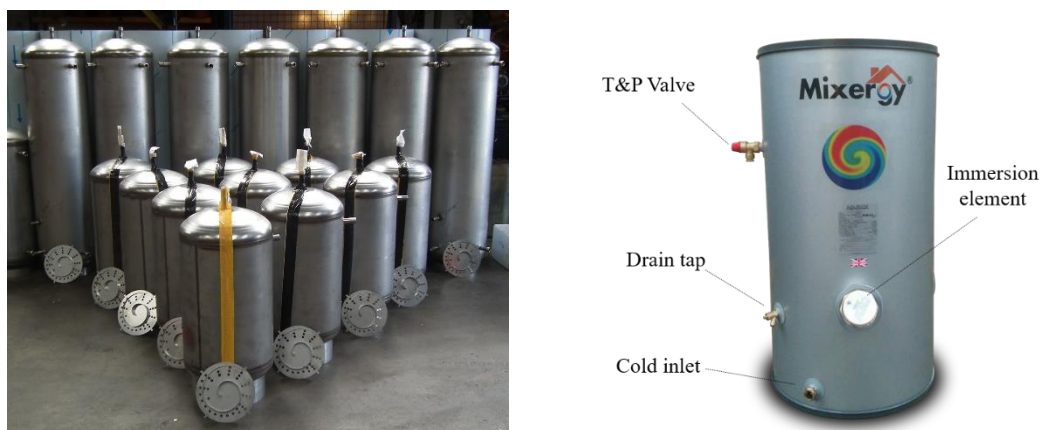


Figure 7-2 (Left) stainless tanks and diffusers prior to insulation, (right) stainless tanks insulated and cased

The improvement in volumetric efficiency resulting from these design changes, is shown in Figure 7-3. Newark Copper Cylinder's original 130 litre tank has a volumetric efficiency of between 79% and 66% between flow rates of 5 lpm to 15lpm. Introducing the new inlet arrangement, diffuser and angled heating element, results in a higher and more consistent performance of 94% to 95%.

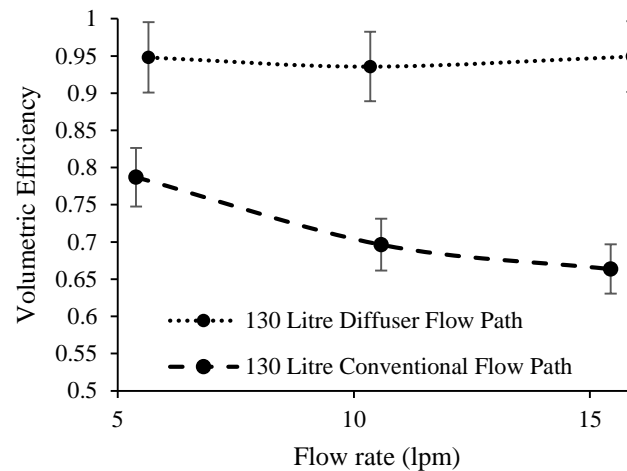


Figure 7-3 Volumetric efficiency of tank with a diffuser and flow path entering in at the bottom of the tank against performance of the same cylinder with conventional inlet and heating element scheme.

The performance enhancements that have been demonstrated in the production prototype exceed those discussed in chapter 5 section 5.7.1. This is due to the additional state of charge that is delivered by angling the heating element in comparison to the horizontal element. Furthermore, by bringing the inlet into the very bottom of the tank for the diffuser path, as opposed to 150mm off the base of the cylinder in the conventional arrangement, inlet mixing is reduced further, an observation first made by Lavan et al [88].

A 130 litre tank, incorporating the new design features, has been trialled in a housing association flat in Blackbird Leys, Oxfordshire, with two elderly occupants using the system. The outlet temperature over a period of 14 days was monitored and is compared to the same results presented in Figure 3-9, where a 166 litre conventional tank servicing two PhD students was monitored.

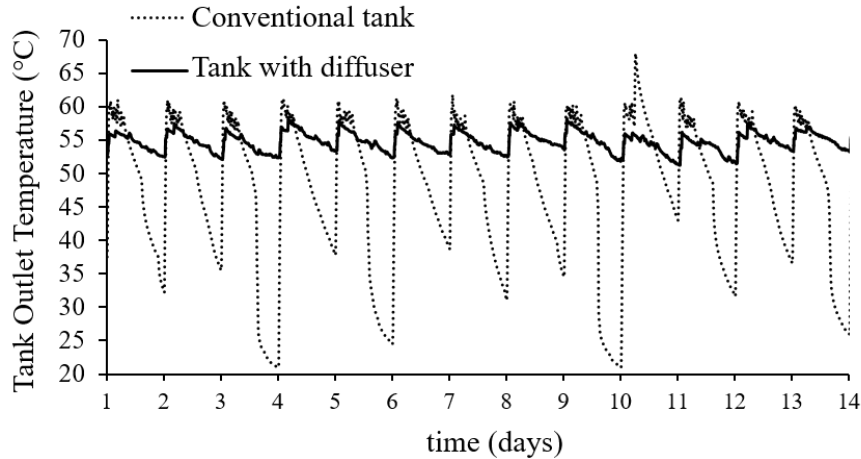


Figure 7-4 Comparison of conventional 166 litre tank to a 130 litre tank with diffuser in two different dwellings with two occupants both operating on an Economy 7 tariff

The outlet temperature of the tank with diffuser was consistently above 50°C in comparison to the conventional cylinder where there were 7 instances during which the temperature dropped below 50°C.

Whilst this preliminary evidence is encouraging, it is not sufficient to answer the above question since there are only two samples which represent different demographics. As more systems are trialled, it is hoped that a fuller understanding as to whether there is a significant benefit will emerge.

7.2.2 EXPLORATION OF THE BENEFITS THAT HIGHER PERFORMING TANKS MIGHT BRING UNDER FLEXIBLE CONTROL STRATEGIES

The focus of this thesis has been to enhance the extent to which a conventional tank can deliver useable hot water under an Economy 7 tariff. Further work, exploring the implications of this research for other existing tariffs, such as Economy 10, where there are ten off-peak heating hours split between the evening and afternoon, along with more flexible tariffs that seek to respond dynamically to the changing supply-demand balance resulting from intermittent renewable energy sources, would assist in answering the question:

How important a role does dynamic and static mode performance play in ensuring that flexible tariff schemes are utilised most effectively?

A hot water tank that remains well stratified during operation might be expected to demand energy less frequently during periods where energy is at its highest cost in terms of price/kWh, carbon intensity and stress on the power infrastructure. However, the extent to which a benefit is derived would depend on the mix of energy sources and their characteristics, a topic with a great deal of uncertainty associated with it, as discussed in section 1.3.

7.2.3 EXPLORATION OF THE BENEFITS THAT ENHANCED STRATIFICATION BRINGS TO OTHER TANK TOPOLOGIES

This thesis has focused on the performance of a conventional electric only hot water tank so that the role of thermal stratification could be isolated without the complicating factors introduced by internal heat exchangers. However, by improving thermal stratification within the cylinder, the performance of indirect thermal inputs, where a heat exchanger is used, could be enhanced. To illustrate this potential, Figure 7-5 shows the vertical temperature distribution from Figure 6-4 for both the stainless and copper test tanks during the ASHRAE draw cycle just before the draw event which was scheduled at 12pm.

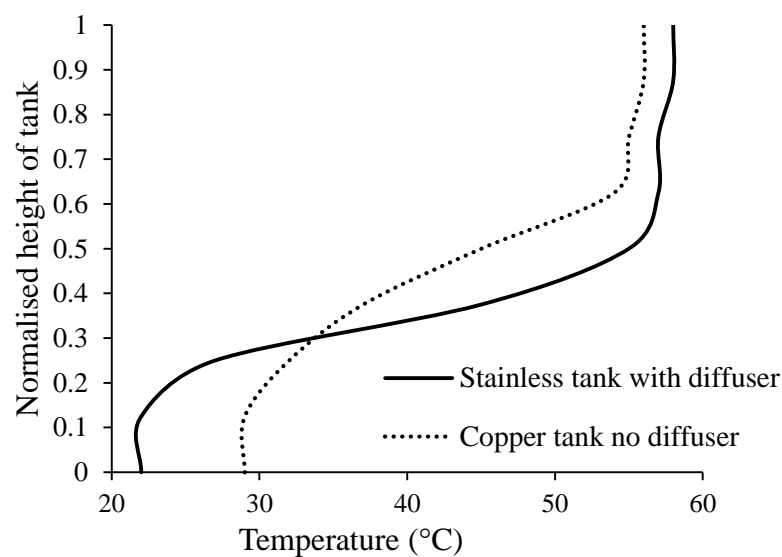


Figure 7-5 Temperature distribution within test cylinders during ASHRAE draw cycle at 10lpm

It is evident that the temperature distribution, associated with the stainless tank, is more stratified than the copper tank's distribution. Over the bottom third of the two tanks, the average temperatures were 23.7°C and 30°C respectively. If we consider the theoretical coefficient of performance of a heat pump [196], we can estimate that energy being sourced from a temperature of 0°C to the lower third of the cylinder, would be delivered with a coefficient of performance of 12.5 and 10.1 for the stainless and copper tanks respectively. Whilst this analysis assumes an ideal system with no irreversibilities, it does hint at the potential tandem benefits of increased volumetric performance alongside enhanced efficiency of indirect thermal inputs. Testing alternative system topologies would be useful in answering the question:

To what extent does thermal stratification improve the performance of indirect thermal sources? In particular, how does the operating COP of a heat pump change over a typical draw cycle when dynamic and static modes of de-stratification are minimised?

7.2.4 UNDERTAKE MORE RESEARCH INTO WAYS IN WHICH THE DIFFUSER DESIGN COULD BE FURTHER OPTIMISED

Whilst tapering the diffuser holes achieved no significant improvement in performance, it is likely that the hole sizing and design becomes more critical if the diffuser is made smaller since it will be more challenging to dissipate the momentum associated with the plume.

One of the challenges with pursuing this work is corroborating any numerical model's estimation of flow distribution with experimental results. Whilst Palacios et al attributed mixing due to a cold plume impinging on the wall of an experimental rectangular tank [191]; recent work, undertaken by Swiatek et al, showed that the plume dynamics associated with the inlet to a solar thermal rectangular tank could be resolved using Particle Image Velocimetry (PIV) [195]. However, as discussed earlier, domestic hot water tanks are typically cylindrical in order to withstand the required operating pressure, and so it is less likely that PIV could be used to capture the flow field as effectively. Another approach might be to use arrays of hot wire anemometers to capture local variations in velocity at fixed points, an approach applied to analyse the performance of a diffuser within a centrifugal compressor [197]. Undertaking more detailed simulations and experiments might deliver an answer to the question:

What is the optimal design of a diffuser? Should outlet holes be sized to achieve a uniform velocity, mass flow rate or momentum across the outlet surface?

7.2.5 THE IMPLICATIONS OF REDUCED DYNAMIC MODE DE-STRATIFICATION ON THE ACCURACY OF ONE DIMENSIONAL MULTI-NODE MODELS

As discussed in chapter 5, section 5.7.1, dynamic mode de-stratification is largely eliminated by the diffuser assembly. The correlation between the Richardson number and volumetric efficiency breaks down and consequently the output of the tank becomes less dependent on the inlet flow rate. This phenomenon presents an opportunity since a limiting feature of multi-node stratification models, discussed in section 2.4.2.4, is their inability to capture the effect of inlet mixing over a range of flow rates. Further work might therefore answer the question:

To what extent can multi-node stratification models accurately predict the performance of tanks fitted with a diffuser over a wide range of operating flow rates?

If by introducing a diffuser tanks become more deterministic during operation, simulating large fleets of systems could become less computationally expensive. This would allow for a thorough numerical study of how the distributed demand resource, associated with a fleet of highly stratified tanks, might help alleviate imbalances between supply and demand whilst ensuring continuity of service to householders.

REFERENCES

- [1] S. L. Lewis and M. a. Maslin, “Defining the Anthropocene,” *Nature*, vol. 519, no. 7542, pp. 171–180, Mar. 2015.
- [2] N. Bostrom, “Existential Risks, Analyzing Human Extinction Scenarios and Related Hazards,” *J. Evol. Technol.*, vol. 9, no. 1, 2001.
- [3] W. Lutz, “Global Human Capital Projections form the Human Core of new IPCC SSP Scenarios,” no. 44, pp. 1–12, 2013.
- [4] “Climate Change 2014 Synthesis Report Summary Chapter for Policymakers,” 2014.
- [5] B. Studies, *Trends in global co 2 emissions 2014*. 2014.
- [6] J. Latham, K. Bower, T. Choularton, H. Coe, P. Connolly, G. Cooper, T. Craft, J. Foster, A. Gadian, L. Galbraith, H. Iacovides, D. Johnston, B. Launder, B. Leslie, J. Meyer, A. Neukermans, B. Ormond, B. Parkes, P. Rasch, J. Rush, S. Salter, T. Stevenson, H. Wang, Q. Wang, and R. Wood, “Marine cloud brightening,,” *Philos. Trans. A. Math. Phys. Eng. Sci.*, vol. 370, no. 1974, pp. 4217–62, Sep. 2012.
- [7] O. Bahn, M. Chesney, J. Gheysens, R. Knutti, and A. C. Pana, “Is there room for geoengineering in the optimal climate policy mix?,” *Environ. Sci. Policy*, vol. 48, no. i, pp. 67–76, Apr. 2015.
- [8] F. Pearce, “What the UN ban on geoengineering really means,” *New Scientist*, Nov-2010.
- [9] C. D. Harvell, P. F. Sale, A. J. Edwards, K. Caldeira, N. Knowlton, and C. M. Eakin, “Coral Reefs Under Rapid Climate Change and Ocean Acidification,” *J. Sci.*, vol. 318, no. December 2007, pp. 1737–1743, 2007.
- [10] R. M. Cuéllar-Franca and A. Azapagic, “Carbon capture, storage and utilisation technologies: A critical analysis and comparison of their life cycle environmental impacts,” *J. CO2 Util.*, vol. 9, pp. 82–102, Dec. 2015.
- [11] Q. Schiermeier, “Iron seeding creates fleeting carbon sink in Southern Ocean,” *Nature*, vol. 428, no. 788, 2004.
- [12] M. E. Kragt, D. J. Pannell, and E. Al, “Assessing costs of soil carbon sequestration by crop-livestock farmers in Western Australia,” *Agric. Syst.*, vol. 112, pp. 27–37, 2012.
- [13] T. Herzog, “World Greenhouse Gas Emissions in 2005,” *World Resour. Inst.*, pp. 1–5, 2009.
- [14] J. Palmer and I. Cooper, “Great Britain’s housing energy fact file,” *Dep. Energy Clim. Chang.*, p. 28, 2011.
- [15] K. C. van Blommestein and T. U. Daim, “Residential energy efficient device adoption in South Africa,” *Sustain. Energy Technol. Assessments*, vol. 1, pp. 13–27, Mar. 2013.
- [16] “Discussion Paper 03 : Aviation and Climate Change April 2013,” London, 2013.
- [17] P. J. Boait, D. Dixon, D. Fan, and A. Stafford, “Production Efficiency of Hot Water for Domestic Use,” *Energy Build.*, vol. 54, pp. 160–168Boait, P. J., Dixon, D., Fan, D., & Staffor.
- [18] M. Chaudry, M. Abeysekera, S. H. R. Hosseini, N. Jenkins, and J. Wu, “Uncertainties in decarbonising heat in the UK,” *Energy Policy*, vol. 87, pp. 623–640, 2015.

- [19] “OVO Energy domestic gas tariff UK,” *OVO Energy*, 2015. [Online]. Available: www.ovoenergy.com. [Accessed: 02-Nov-2015].
- [20] EIA, “Energy Information Administration,” *eia.gov*. [Online]. Available: http://www.eia.gov/environment/emissions/co2_vol_mass.cfm. [Accessed: 02-Nov-2015].
- [21] E. A. Reitan, *The Thatcher Revolution - Margaret Thatcher, John Major, Tony Blair, and the Transformation of Modern Britain, 1979 - 2001*. Lanham: Rowan & Littlefield Publishers Inc, 2003.
- [22] P. E. Dodds and W. McDowall, “The future of the UK gas network,” *Energy Policy*, vol. 60, pp. 305–316, 2013.
- [23] DEFRA, “Energy use in homes - a series of reports on domestic energy use in England,” London, 2005.
- [24] “Year 1947,” in *Electricity Supply in the United Kingdom, A Chronology*, 4th ed., Chatham: The Electricity Council, 1987, p. 60.
- [25] R. Cochrane, *The CEBG Story*. London: CEBG, 1990.
- [26] C. Hering, “The Two or Three Phase Current Alternating System,” *Sci. Am.*, vol. 32, 1891.
- [27] M. Ceraolo and P. Davide, “Large Power Systems: Structure and Operation,” in *Fundamentals of Electric Power Engineering*, Wiley, 2014, p. 478.
- [28] P. Breeze, “Pumped Storage Hydropower,” in *Power Generation Technologies*, Oxford: Elsevier, 2005, pp. 137 – 138.
- [29] “Year 1978,” in *Electricity Supply in the United Kingdom, A Chronology*, 4th ed., Chatham: The Electricity Council, 1987, p. 127.
- [30] EDF (Électricité de France), “Off Peak and Electrical Heating Tariffs,” Electricite de France, 2015.
- [31] “Natioal Grid Data Explorer,” *National Grid*, 2015. [Online]. Available: <http://www2.nationalgrid.com/uk/Industry-information/Electricity-transmission-operational-data/Data-Explorer/>. [Accessed: 02-Nov-2015].
- [32] P. Fairey and D. Parker, “A Review of Hot Water Draw Profiles Used in Performance Analysis of Residential Domestic Hot Water Systems.” Florida Energy Centre, 1679 Clearlake Road, Cocoa, Florida, 32922-5703 (www.fsec.ucf.edu), 2004.
- [33] “Elexon Balancing Market Data,” *Elexon - UK electricity market mechanism who tender for generation or curtailment depending on the system balance*, 2015. [Online]. Available: <https://www.elexonportal.co.uk>.
- [34] “Economy 7 Electricity Prices,” *EDF (Électricité de France)*, 2015. [Online]. Available: <https://my.edfenergy.com/>.
- [35] “Electricity Act 1989,” *The National Archives*, 1989. [Online]. Available: <http://www.legislation.gov.uk/ukpga/1989/29>. [Accessed: 02-Nov-2015].
- [36] “The Impact of Distributed Generation on European Power Utilities,” in *Distributed Generation and its Implications for the Utility Industry*, Kidlington: Elsevier, 2014, p. 124 to 137.
- [37] L. Stamford and A. Azapagic, “Life cycle environmental impacts of UK shale gas,” *Appl. Energy*, vol. 134, pp. 506–518, 2014.

- [38] S. Farrell and T. Macalister, "Work to begin on Hinkley Point reactor within weeks after China deal signed," *The Guardian*, Oct-2015.
- [39] W. Bayley, "National Grid cannot take any more power from renewable schemes in the Westcountry," *Western Morning News*, 01-Apr-2015.
- [40] S. Dierkes, F. Bennewitz, M. Maercks, L. Verheggen, and A. Moser, "Impact of distributed reactive power control of renewable energy sources in smart grids on voltage stability of the power system," *2014 Electr. Power Qual. Supply Reliab. Conf.*, pp. 119–126, Jun. 2014.
- [41] P. Balcombe, D. Rigby, and A. Azapagic, "Energy self-sufficiency, grid demand variability and consumer costs: Integrating solar PV, Stirling engine CHP and battery storage," *Appl. Energy*, vol. 155, pp. 393–408, 2015.
- [42] S. Anuphapparadorn, S. Sukchai, C. Sirisamphanwong, and N. Ketjoy, "Comparison the Economic Analysis of the Battery between Lithium-ion and Lead-acid in PV Stand-alone Application," *Energy Procedia*, vol. 56, pp. 352–358, 2014.
- [43] "Tesla's New Battery: The Future Is on the Wall," *Electr. J.*, vol. 28, no. 6, pp. 1–4, 2015.
- [44] D. P. Finegan, M. Scheel, J. B. Robinson, B. Tjaden, I. Hunt, T. J. Mason, J. Millichamp, M. Di Michiel, G. J. Offer, G. Hinds, D. J. L. Brett, and P. R. Shearing, "In-operando high-speed tomography of lithium-ion batteries during thermal runaway.," *Nat. Commun.*, vol. 6, p. 6924, 2015.
- [45] H. James, "Power showers use twice as much water and electricity as baths," *The Telegraph*, 2011.
- [46] "British Standard BS 1566-1:2002 +A1:2011: 'Copper indirect cylinders for domestic purposes, Part 1: Open vented copper cylinders Requirements and test methods,'" *Br. Stand. Inst.*, 2011.
- [47] T. Ross, "Wind farms paid £30m to shut down during high winds," *The Telegraph*. [Online]. Available: <http://www.telegraph.co.uk/news/politics/10655742/Wind-farms-paid-30m-to-shut-down-during-high-winds.html>.
- [48] BBC, "Scots windfarms paid cash to stop producing energy," *BBC News Online*, 2011. [Online]. Available: <http://www.bbc.co.uk/news/uk-scotland-13253876>.
- [49] U. Atikol, "A simple peak shifting DSM (demand-side management) strategy for residential water heaters," *Energy*, vol. 62, pp. 435–440, Dec. 2013.
- [50] L. Paull, H. Li, and L. Chang, "A novel domestic electric water heater model for a multi-objective demand side management program," *Electr. Power Syst. Res.*, vol. 80, no. 12, pp. 1446–1451, Dec. 2010.
- [51] M. . Nehrir, B. LaMeres, and V. Gerez, "A Customer-Interactive Electric Water Heater Demand Side Management Strategy Using Fuzzy Logic," in *IEEE*, 1998, pp. 433–435.
- [52] Y. M. Atwa and M. M. Salama, "DSM Approach for Water Heater Control Strategy Utilizing Elman Neural Network," in *IEEE Canada Electrical Power Conference*, 2007, pp. 1–5.
- [53] M. Lacroix, "Electric water heater designs for load shifting and control of bacterial contamination," *Energy Convers. Manag.*, vol. 40, no. 12, pp. 1313–1340, Aug. 1999.
- [54] A. Moreau, "Control Strategy for Domestic Water Heaters during Peak Periods and its Impact on the Demand for Electricity," *Energy Procedia*, vol. 12, pp. 1074–1082, Jan. 2011.

- [55] M. Alary and J. R. Joly, "Risk factors for contamination of domestic hot water systems by legionellae.," *Appl. Environ. Microbiol.*, vol. 57, no. 8, pp. 2360–7, Aug. 1991.
- [56] "Central Solar Hot Water Systems Design Guide," Department of Energy, US Army Corps of Engineers, Washington, 2011.
- [57] "The Assessment of Unvented Hot Water Systems and the Approval and Surveillance of Installers.," *Br. Board Agrément*, 1986.
- [58] "Unvented hot water storage units and packages," in *British Standard BS 7206:1990*., no. 1, British Standards Institute, 1990.
- [59] "Fined Tube Heat Exchangers," Wieland Thermal Solutions, 2015, pp. 3–6.
- [60] P. Verkempynck, "How does a thermal store work?," *Daikin*, vol. 1, no. 16, p. 11, Jan. 2013.
- [61] A. . Mills, *Heat Transfer*, 1st ed. Boston: IRWIN, 1992.
- [62] "Metal Prices Online: Stainless steel price time series - Date Accessed: January 2014 [www.metalprices.com]," *Arg. Media ltd*, 2015.
- [63] "Recommended minimum standards for circulation (Table 20)," in *Domestic Building Services Compliance Guide*, HM Government, 2011, p. 69.
- [64] "Minimum provision for new systems in new and existing dwellings," in *Domestic Building Services Compliance Guide*, HM Government, 2008, p. 26.
- [65] J. . Turner, *Buoyancy effects in fluids*, 1st ed. Cambridge: Cambridge University Press, 1979.
- [66] J. V Lee, J. Bartram, Y. Chartier, K. Pond, and S. Surmann-Lee, "Legionella and the prevention of legionellosis," *World Heal. Organ.*, 2008.
- [67] C. Angel, "Guidance Controlling Scalding Risks from Bathing and Showering," *United Kingdom Home Care Assoc.*, no. 3083104, pp. 1–12, 2012.
- [68] Y. A. Cengel and M. A. Boles, *Thermodynamics an Engineering Approach*, 5th ed. Singapore: McGraw Hill, 2006.
- [69] M. A. Abdolyt and D. Rapp, "Theoretical and Experimental Studies of Stratified Thermocline Storage of Hot Water," *Energy Convers. Manag.*, vol. 22, no. Iii, p. 275 to 285, 1982.
- [70] A. Castell, M. Medrano, C. Solé, and L. F. Cabeza, "Dimensionless numbers used to characterize stratification in water tanks for discharging at low flow rates," *Renew. Energy*, vol. 35, no. 10, pp. 2192–2199, Oct. 2010.
- [71] I. Dincer and M. A. Rosen, *Thermal Energy Storage Systems and Applications*, 2nd ed. Wiley, 2002.
- [72] Y. A. Cengel and M. A. Boles, *Thermodynamics: An Engineering Approach*, Fifth Edit. McGraw Hill, 2006.
- [73] T. K. Ray, A. Datta, A. Gupta, and R. Ganguly, "Exergy-based performance analysis for proper O&M decisions in a steam power plant," *Energy Convers. Manag.*, vol. 51, no. 6, pp. 1333–1344, Jun. 2010.
- [74] A. Tiwari, S. Dubey, G. S. Sandhu, M. S. Sodha, and S. I. Anwar, "Exergy analysis of integrated photovoltaic thermal solar water heater under constant flow rate and constant collection temperature modes," *Appl. Energy*, vol. 86, no. 12, pp. 2592–2597, Dec. 2009.

- [75] H. Gunerhan and A. Hepbasli, "Exergetic modeling and performance evaluation of solar water heating systems for building applications," *Energy Build.*, vol. 39, no. 5, pp. 509–516, May 2007.
- [76] A. Hepbasli, "Exergetic modeling and assessment of solar assisted domestic hot water tank integrated ground-source heat pump systems for residences," *Energy Build.*, vol. 39, no. 12, pp. 1211–1217, Dec. 2007.
- [77] M. a Rosen, "The exergy of stratified thermal energy storages," *Sol. Energy*, vol. 71, no. 3, pp. 173–185, Jan. 2001.
- [78] P. M. Armstrong, D. Ager, I. Thompson, and M. D. McCulloch, "Domestic Hot Water Storage: Balancing Thermal and Sanitary Performance," *Energy Policy*, 2014.
- [79] J. Burch and J. Thornton, *A Realistic Hot Water Draw Specification for Rating Solar Water Heaters by the National Renewable Energy Laboratory*, no. June. Denver: National Renewable Energy Laboratory, 2012.
- [80] S. Lonsdale, "Green Property: Hot Fill Washing Machines," *The Telegraph*, Aug-2010.
- [81] A. Trigg, "Connect a cold fill washing machine to the hot water tap," <http://www.whitegoodshelp.co.uk/>, 2007. [Online]. Available: <http://www.whitegoodshelp.co.uk/connect-cold-fill-washing-machine-to-hot-tap/>. [Accessed: 13-Dec-2014].
- [82] Bristan, "Datasheet on: Deck Mounted Bath Filler With Thermostatic Shower Control Fitting Instructions & Contents List." Tamworth, p. 4, 2015.
- [83] A. . Mills, *Heat Transfer*, 1st ed. Boston: IRWIN, 1992.
- [84] O. Reynolds, "An Experimental Investigation of the Circumstances Which Determine Whether the Motion of Water Shall Be Direct or Sinuous, and of the Law of Resistance in Parallel Channels," *Philos. Trans. R. Soc. London*, vol. 174, pp. 935–982, Jan. 1883.
- [85] O. Reynolds, "On the Dynamical Theory of Incompressible Viscous Fluids and the Determination of the Criterion," *Philosophical Trans. R. Soc. London*, vol. 186, no. 1895, pp. 123–164, 1894.
- [86] T. von Karmen, *Aerodynamics*. McGraw Hill, 1963.
- [87] R. L. Street, G. Z. Watters, and J. K. Vennard, *Elementary Fluid Mechanics*, 7th ed. California: John Wiley & Sons, inc, 1996.
- [88] Z. Lavan and J. Thompson, "Experimental Study of Thermally Stratified Hot Water Storage Tanks," *Sol. Energy*, vol. 19, pp. 519–524, 1976.
- [89] L. Chauvet, S. Probert, and D. Nevrala, "Thermal-energy Stores for Supplying Domestic Hot-water and Space-heating," *Appl. Energy*, vol. 48, no. ii, pp. 163–190, 1994.
- [90] A. J. N. Khalifa, A. T. Mustafa, and F. A. Khammas, "Experimental Study of Temperature Stratification in a Thermal Storage Tank in the Static Mode for Different Aspect Ratios," *ARPJ. Eng. an Appl. Sci.*, vol. 6, no. 2, pp. 53–60, 2011.
- [91] A. . Mills, *Heat Transfer*, 1st ed. Boston: IRWIN, 1992.
- [92] M. Bahrami, "Natural Convection, Heat Transfer Course Notes, Simon Fraser University," 2014. [Online]. Available: <http://www.sfu.ca/~mbahrami/ENSC 388/Notes/Natural Convection.pdf>.
- [93] S. Kakac and Y. Yener, *Convective Heat Transfer*, 2nd ed. Florida: CRC Press, 1995.

- [94] R. L. Cole and F. O. Bellinger, "Natural Thermal Stratification in Tanks: Final Report," *Argonne Natl. Lab.*, 1982.
- [95] E. Hahne and Y. Chen, "Numerical Study of Flow and Heat Transfer Characteristics in Hot Water Stores," *Sol. Energy*, vol. 64, no. 1–3, pp. 9–18, 1998.
- [96] R. Cohen, "PhD Thesis: Thermal Energy Accumulation in Stratified Hot Water Stores," Cranfield Institute of Technology, 1986.
- [97] P. Armstrong and M. McCulloch, "Distributed energy storage using domestic hot water tanks and a novel thermocline sensor," in *IEEE ISGT*, 2014.
- [98] A. Ng, "Stanford Machine Learning Course: Linear Regression with Multiple Variables (week 2)," *Coursera*, 2013. [Online]. Available: <https://class.coursera.org/ml-003/lecture/preview>.
- [99] "Least-Squares (Model Fitting) Algorithms," *Matlab Documentation Centre*. [Online]. Available: <http://www.mathworks.co.uk/help/optim/ug/least-squares-model-fitting-algorithms.html>.
- [100] F. . Fritsch and R. . Carlson, "Monotone Piecewise Cubic Interpolation," *SIAM Soc. Ind. Appl. Math.*, vol. 17, no. 2, p. 238 to 246, Feb. 1980.
- [101] S. A. Klein and W. A. Beckman, "TRNSYS 16: A Transient System Simulation program: Mathematical Reference - Volume 5," *TRNSYS*, vol. 5, p. 389 to 396, 2007.
- [102] B. J. Newton, "Master's Thesis: Modelling of Solar Storage Tanks," University of Wisconsin-Madison, 1995.
- [103] B. Gebhart, Y. Jaluria, R. . Mahajan, and B. Sammakia, *Buoyancy-Induced Flows and Transport*. New York: Hemisphere Publishing, 1988.
- [104] E. M. Kleinbach, W. A. Beckman, and S. A. Klein, "Performance study of one-dimensional models for stratified thermal storage tanks," *Sol. Energy*, vol. 50, no. 2, pp. 155–166, Feb. 1993.
- [105] U. Jordan and S. Furbo, "Thermal stratification in small solar domestic storage tanks caused by draw-offs," *Sol. Energy*, vol. 78, no. 2, pp. 291–300, Feb. 2005.
- [106] J. Kiusalaas, *Numerical Methods in Engineering with Python*, 1st ed. New York: Cambridge University Press, 2005.
- [107] J. A. Strain, "Convergence of Euler Method." University of Berkley, Department of Mathematics, pp. 2–11, 2015.
- [108] R. Spur, D. Fiala, D. Nevrala, and D. Probert, "Influence of the domestic hot-water daily draw-off profile on the performance of a hot-water store," *Appl. Energy*, vol. 83, no. 7, pp. 749–773, Jul. 2006.
- [109] A. Buonomano, F. Calise, and G. Ferruzzi, "Thermoeconomic analysis of storage systems for solar heating and cooling systems: A comparison between variable-volume and fixed-volume tanks," *Energy*, vol. 59, pp. 600–616, Sep. 2013.
- [110] "Economy 10 Electricity Tariff," in *Scottish Hydro Energy Pricing (www.hydro.co.uk)*, Scottish Hydro, 2015, p. 3.
- [111] A. Adams, "Legionnaires' disease: The control of legionella bacteria in water systems Approved Code of Practice and Guidance," Crown, UK Health and Safety Executive, 2012.

- [112] *British Standard BS EN 14318-1:2013: "In-situ formed dispensed rigid polyurethane and polyisocyanurate foam products."* British Standards Institute, 2013.
- [113] W. M. H K Versteeg, *An Introduction to Computational Fluid Dynamics The Finite Volume Method, 2nd Edition*, 2nd ed. New York: Longman Scientific and Technical.
- [114] N. Altuntop, M. Arslan, V. Ozceyhan, and M. Kanoglu, "Effect of obstacles on thermal stratification in hot water storage tanks," *Appl. Therm. Eng.*, vol. 25, no. 14–15, pp. 2285–2298, Oct. 2005.
- [115] S. Ievers and W. Lin, "Numerical simulation of three-dimensional flow dynamics in a hot water storage tank," *Appl. Energy*, vol. 86, no. 12, pp. 2604–2614, Dec. 2009.
- [116] J. . Anderson, *Computational Fluid Dynamics the basics with applications*, 1st ed. Singapore: McGraw Hill, 1995.
- [117] J. . Anderson, "The Governing Equations of Fluid Dynamics," in *Computational Fluid Dynamics, the basics with applications*, Singapore: McGraw Hill, 1995, pp. 41–52.
- [118] D. D. Gray and A. Giorcini, "The validity of the Boussinesq approximation for liquids and gases," *Heat Mass Transf.*, vol. 19, pp. 545–551, 1976.
- [119] J. F. Douglas, G. M. Janusz, J. A. Swaffield, and L. B. Jack, "Fluids and their properties," in *Fluid Mechanics*, 5th ed., Gosport: Prentice Hall, 2005, p. 11.
- [120] H. K. Versteeg and W. Malalasekera, "Conservation laws of fluid motion and boundary conditions," in *An Introduction to Computational Fluid Dynamics, The Finite Volume Method*, London: Longman Scientific and Technical, 1995, p. 16.
- [121] J. F. Douglas, G. M. Janusz, J. A. Swaffield, and L. B. Jack, "Appendix 1: Some Properties of Common Fluids," in *Fluid Mechanics*, 5th ed., Gosport: Prentice Hall, 2005, pp. 938–939.
- [122] J. Gleick, "Chaos," in *Chaos*, 1st ed., London: Heinemann, 1988, p. 119.
- [123] P. . Davidson, *Turbulence, an introduction for scientists and engineers*. New York: Oxford University Press, 2004.
- [124] H. K. Versteeg and W. Malalasekera, "Turbulence and its modelling," in *An Introduction to Computational Fluid Dynamics, The Finite Volume Method*, New York: Longman Scientific and Technical, 1995, p. 41 to 83.
- [125] P. Buchave and W. K. George, "The measurement of turbulence with the laser doppler anemometer," *Annu. Rev. Fluid Mech.*, vol. 11, pp. 443–503, 1979.
- [126] J. Boussinesq, "Theorie de l'ecoulement Turbillonnant et Tumultueux des Liquides Dans les lits Rectilignes a Grande Section," *Gauthier Villars*, 1897.
- [127] S. B. Pope, *Turbulent Flows*. Cambridge: Cambridge University Press, 2000.
- [128] F. M. White, *Viscous Fluid Flow*, Third. Singapore: McGraw Hill, 2006.
- [129] H. K. Versteeg and Mala, "Implementation of Boundary Conditions," in *An Introduction to Computational Fluid Dynamics, The Finite Volume Method*, New York: Longman Scientific and Technical, 1995, p. 200 to 203.
- [130] F. Durst, "Turbulence Models and their Applications - Lecture Series." Indian Institute of Technology, 2011.

- [131] B. E. Launder, G. J. Reece, and W. Rodi, "Progress in the Development of a Reynolds Stress Turbulent Closure," *J. Fluid Mech.*, vol. 68, no. 3, pp. 537–566, 1975.
- [132] J. Mathieu and J. Scott, "Large-Eddy Simulation (LES)," in *An Introduction to Turbulent Flow*, Madrid: Cambridge University Press, 2000, pp. 340–352.
- [133] "Clay millenium problems: The Navier Stokes Equations," *CMI (Clay Mathematics Institute)*, 2015. [Online]. Available: <http://www.claymath.org/millenium-problems/navier-stokes-equation>. [Accessed: 10-Jan-2015].
- [134] H. K. Versteeg and W. Malalasekera, "Differential and integral forms of the general transport equations," in *An Introduction to Computational Fluid Dynamics, The Finite Volume Method*, Longman Scientific and Technical, 1995, p. 25.
- [135] N. B.E., "Instrumentation Reference Book," in *Instrumentation Reference Book*, London: Butterworths, 1990, pp. 4–40.
- [136] G. R. Slemon, "Induction Motors," in *Electric Machines and Drives*, Toronto: Addison Wesley, 1992, pp. 171–212.
- [137] Acromag, "How to prevent temperature measurement errors when installing thermocouple sensors and transmitters: White Paper," 2015.
- [138] J. R. Taylor, "Independent versus dependent measurements," in *An Introduction to Error Analysis*, Second., Colorado: University Science Books, 1997, pp. 45–79.
- [139] W. Mathys, J. Stanke, M. Harmuth, and E. Junge-Mathys, "Occurrence of Legionella in hot water systems of single-family residences in suburbs of two German cities with special reference to solar and district heating," *Int. J. Hyg. Environ. Health*, vol. 211, no. 1–2, pp. 179–85, Mar. 2008.
- [140] "Waterborne pathogens and their significance in water supplies," *World Health Organisation*, 2012. [Online]. Available: http://www.who.int/water_sanitation_health/gdwqrevision/watborpath/en/index.html. [Accessed: 24-Aug-2012].
- [141] M. Jörg, S. Thomas, W. S. S, A. J. H. Janus, M. Søren, and H. Hubert, "Biofilm formation of Legionella Pneumophila in complex medium under static and dynamic flow conditions," in *Legionella: State of the art 30 years after its recognition*, 1st ed., P. Cianciotto, Nicholas, Ed. Washington, D.C: ASM Press, 2006, p. 398 to 401.
- [142] D. van der Kooij, H. R. Veenendaal, and W. J. H. Scheffer, "Biofilm formation and multiplication of Legionella in a model warm water system with pipes of copper, stainless steel and cross-linked polyethylene.," *Water Res.*, vol. 39, no. 13, pp. 2789–98, Aug. 2005.
- [143] M. E. Schoen and N. J. Ashbolt, "An in-premise model for Legionella exposure during showering events.," *Water Res.*, vol. 45, no. 18, pp. 5826–36, Nov. 2011.
- [144] C. J. and K. Ricketts, "The Epidemiology of Legionnaires' Disease," in *Legionella Molecular Microbiology*, 1st ed., K. and M. S. Heuner, Ed. 2008, p. 35 to 54.
- [145] G. . Brundett, "Legionnaires' Disease Building Services - Healthy Buildings," *Buiding Res. Pract. J. CIB*, no. 2, pp. 96–107, 1989.
- [146] "Yougen: guidance on solar thermal hot water systems," *Yougen*, 2015. [Online]. Available: <http://www.yougen.co.uk/blog-entry/1772/Five+key+ways+to+get+the+best+from+your+solar+hot+water+system/>. [Accessed: 29-Nov-2015].

- [147] Y. Evans, "Modern Building Services: Controlling Legionella in solar thermal systems," *Modern Building Services*, 2015. [Online]. Available: http://www.modbs.co.uk/news/archivestory.php/aid/5638/Controlling_legionella_in_solar-thermal_systems.html. [Accessed: 29-Nov-2015].
- [148] G. Sezonov, D. Joseleau-Petit, and R. D'Ari, "Escherichia coli Physiology in Luria-Bertani Broth," *J. Bacteriol.*, vol. 189, no. 23, pp. 8746–8749, 2007.
- [149] L. K. Bagh, H. J. Albrechtsen, E. Arvin, and K. Ovesen, "Distribution of bacteria in a domestic hot water system in a Danish apartment building.," *Water Res.*, vol. 38, no. 1, pp. 225–35, Jan. 2004.
- [150] P. Taylor, L. K. Bagh, H. J. Albrechtsen, and E. Arvin, "Biofouling : The Journal of Bioadhesion and Biofilm Development of equipment for in situ studies of biofilm in hot water systems Development of Equipment for in situ Studies of Biofilm in Hot Water Systems," *Building*, no. March, pp. 37–41, 1998.
- [151] *British Standard 699:1984: Copper direct cylinders for domestic purposes*. The British Standards Institute, 1990.
- [152] "LM35 Precision Temperature Sensor Datasheet." Texas Instruments, pp. 1–16, 2013.
- [153] "ADC Parameters," in *MCP3422 Analog to Digital Converter Datasheet*, Microchip Technology, 2009, pp. 1–58.
- [154] P. Boyd, J. Bryant, and S. Bullock, "Methods for the enumeration of heterotrophic bacteria Methods for the Examination of Waters and Associated Materials," *UK Environ. Agency*, 2012.
- [155] J. Bartram, J. Cotruvo, M. Exner, C. Fricker, and A. Glasmacher, *Heterotrophic Plate Counts and Drinking-water Safety - The Significance of HPCs for Water Quality and Human Health*. Padstow: World Health Organisation, 2003.
- [156] H. B. Mann and D. R. Whitney, "On a test of whether one of two random variables is stochastically larger than the other," *Ann. Math. Stat.*, vol. 18, no. 1, pp. 50–60, 1947.
- [157] W. B. Ware, J. M. Ferron, and B. M. Miller, *Introductory Statistics a Conceptual Approach Using R*. Abingdon: Routledge, 2013.
- [158] "Copper price time series," in <http://www.lme.com/>, The London Metal Exchange, 2015.
- [159] "Stainless steel price time series," in www.metalprices.com, Argus Media Ltd, 2015.
- [160] P. Taylor, P. L. Waines, R. Moate, A. J. Moody, M. Allen, and G. Bradley, "Biofouling : The Journal of Bioadhesion and Biofilm The effect of material choice on biofilm formation in a model warm water distribution system," *Biofouling*, no. March, pp. 37–41, 2012.
- [161] "Platts McGraw Hill Financial: Global Petrochemical Index -." [Online]. Available: <http://www.platts.com/news-feature/2013/petrochemicals/pgpi/ldpe>. [Accessed: 19-Nov-2015].
- [162] J. S. Colbourne, R. Avenue, and L. Ecr, "Water fittings as sources of Legionella Pneumophila in a Hospital Plumbing System," *Lancet*, vol. 323, no. 8370, pp. 210–213, 1984.
- [163] G. M. Schofield and R. Locci, "Colonization of components of a model hot water system by Legionella pneumophila.," *J. Appl. Bacteriol.*, vol. 58, no. 2, pp. 151–62, Feb. 1985.
- [164] S. Brenner, "Aluminium, hot water tanks and neurobiology," *Lancet*, vol. 1, no. 8641, p. 781, 1989.

- [165] V. Rondeau, D. Commenges, H. Jacqmin-gadda, and J. Dartigues, "Relation between Aluminum Concentrations in Drinking Water and Alzheimer's Disease : An 8-year Follow-up Study," *J. Epidemiol.*, vol. 152, no. 1, pp. 59–66, 2000.
- [166] V. V. Vasiliev, a. a. Krikanov, and a. F. Razin, "New generation of filament-wound composite pressure vessels for commercial applications," *Compos. Struct.*, vol. 62, no. 3–4, pp. 449–459, Jan. 2003.
- [167] M. . Williams and J. . Todd, "Membrane stress theory," in *Structures, theory and analysis*, Wiltshire: Macmillan Press Ltd, 2000, pp. 286 – 314.
- [168] "Measurement of Domestic Hot Water Consumption in Dwellings." Energy Saving Trust, 21 Dartmouth Street, London, SW1H 9BP (<http://www.energysavingtrust.org.uk>), 2008.
- [169] "Polyethylene entry (<http://www.matweb.com/search/DataSheet.aspx?MatGUID=f9470672aa5549cb9c7b157677d02062>)," in *Mat-Web, materials database*, Mat-Web, 2015.
- [170] P. N. Nwosu and D. Agbiogwu, "Thermal analysis of a novel fibre-reinforced plastic solar hot water storage tank," *Energy*, vol. 60, pp. 109–115, Oct. 2013.
- [171] Endless-Solar, "Stainless Steel Tanks," in *Endless Solar Guide*, Sydney: Endless Solar, 2014, p. 1 to 2.
- [172] J. Fan and S. Furbo, "Buoyancy driven flow in a hot water tank due to standby heat loss," *Sol. Energy*, vol. 86, no. 11, pp. 3438–3449, Nov. 2012.
- [173] "Copper entry (<http://www.matweb.com/search/DataSheet.aspx?MatGUID=9aeb83845c04c1db5126fada6f76f7e>)," in *Mat-Web, materials database*, Mat-Web, 2015.
- [174] "British Standard EN 1172:1996: 'Copper and copper alloys - sheet and strip for building purposes' The British Standards Institute," 1997.
- [175] "Stainless steel entry (<http://www.matweb.com/search/DataSheet.aspx?MatGUID=ace15139b9e846a493dc630db9dac567&cck=1>)," in *Mat-Web, materials database*, Mat-Web, 2015.
- [176] "British Standard BS 7291-3:2006: 'Thermoplastic pipes and associated fittings for hot and cold water for domestic purposes and heating installations in buildings' The British Standards Institute," 2006.
- [177] A. Bejan, "Convection Heat Transfer," in *Convection Heat Transfer*, 4th ed., New Jersey: Wiley, 2013, p. 210 to 211.
- [178] D. K. Edwards and I. Catton, "Prediction of Heat Transfer by Natural Convection in closed Cylinders Heated from below," *J. Heat Mass Transf.*, vol. 12, pp. 22–30, 1968.
- [179] T. . Chung, *Computational Fluid Dynamics*, 1st ed. Cambridge: Cambridge University Press, 2002.
- [180] R. D. C. Oliveski, M. H. Macagnan, J. B. Copetti, and A. D. L. M. Petroll, "Natural convection in a tank of oil: experimental validation of a numerical code with prescribed boundary condition," *Exp. Therm. Fluid Sci.*, vol. 29, no. 6, pp. 671–680, Jul. 2005.
- [181] "Star CCM+ Multiphysics Software," *CD Adapco*, 2014. [Online]. Available: <http://www.cd-adapco.com/products/star-ccm>.
- [182] W. Pieter, *Principles of Computational Fluid Dynamics*, 1st ed. Berlin: Springer, 1991.

- [183] A. Bejan, "Convection Heat Transfer," in *Convection Heat Transfer*, 4th ed., New Jersey, 2013, p. 168 to 169.
- [184] S. Alizadeh, "An experimental and numerical study of thermal stratification in a horizontal cylindrical solar storage tank," *Sol. Energy*, vol. 66, no. 6, pp. 409–421, Sep. 1999.
- [185] J. Fernandezseara, F. Uhia, and J. Sieres, "Experimental analysis of a domestic electric hot water storage tank. Part I: Static mode of operation," *Appl. Therm. Eng.*, vol. 27, no. 1, pp. 129–136, Jan. 2007.
- [186] J. Fernández-Seara, F. J. Uhía, and J. Alberto Dopazo, "Experimental transient natural convection heat transfer from a vertical cylindrical tank," *Appl. Therm. Eng.*, vol. 31, no. 11–12, pp. 1915–1922, Aug. 2011.
- [187] "Method for specifying thermal insulating materials for pipes, tanks, vessels, ductwork and equipment operating within the temperature range -40°C to +700°C," in *BS 5422:2009*, no. 1, British Standards Institution, 2009.
- [188] A. a. Hegazy, "Effect of inlet design on the performance of storage-type domestic electrical water heaters," *Appl. Energy*, vol. 84, no. 12, pp. 1338–1355, Dec. 2007.
- [189] D. Miller, *Internal Flow: A guide to losses in pipe and duct systems*, 1st ed. Cranfield: The British Hydromechanics Research Association, 1971.
- [190] D. Miller, "Loss Coefficients for Bends," in *Internal Flow: A guide to losses in pipe and duct systems*, Cranfield: The British Hydromechanics Research Association, 1971, pp. 14–17.
- [191] E. Palacios, D. M. Admiraal, J. D. Marcos, and M. Izquierdo, "Experimental analysis of solar thermal storage in a water tank with open side inlets," *Appl. Energy*, vol. 89, no. 1, pp. 401–412, Jan. 2012.
- [192] "British Stainless Steel Association: Specifying finishes for stainless steel flat products (sheet and plate)," BSSA, 2015. [Online]. Available: <http://www.bssa.org.uk/topics.php?article=47>. [Accessed: 29-Nov-2015].
- [193] J. van Berkel, C. C. M. Rindt, and A. a van Steenhoven, "Modelling of two-layer stratified stores," *Sol. Energy*, vol. 67, no. 1–3, pp. 65–78, 1999.
- [194] H. Bagge and D. Johansson, "Measurements of household electricity and domestic hot water use in dwellings and the effect of different monitoring time resolution," *Energy*, vol. 36, no. 5, pp. 2943–2951, May 2011.
- [195] M. Swiatek, G. Fraisse, and M. Pailha, "Stratification enhancement for an integrated collector storage solar water heater (ICSSWH)," *Energy Build.*, vol. 106, pp. 35–43, 2015.
- [196] Y. A. Cengel and M. A. Boles, *Thermodynamics: An Engineering Approach*, Fifth. Singapore: McGraw Hill, 2006.
- [197] A. Pinarbasi, "Experimental hot-wire measurements in a centrifugal compressor with vaned diffuser," *Int. J. Heat Fluid Flow*, vol. 29, no. 5, pp. 1512–1526, 2008.
- [198] V. Gnielinski, "Helically coiled tubes of circular cross sections," in *Heat Exchanger Design Handbook*, G. Hewitt, Ed. New York: Begell House, 1998, pp. 2.5.14–1 to 2.5.14–3.
- [199] P. Armstrong, D. Ager, I. Thompson, and M. McCulloch, "Domestic hot water storage : Balancing thermal and sanitary performance," *Energy Policy*, vol. 68, pp. 334–339, 2014.

- [200] P. M. Armstrong, M. Uapipatanakul, I. Thompson, D. Ager, and M. McCulloch, "Thermal and sanitary performance of domestic hot water cylinders: Conflicting requirements," *Appl. Energy*, vol. 131, pp. 171–179, Oct. 2014.
- [201] P. Armstrong, D. Ager, I. Thompson, and M. McCulloch, "Improving the energy storage capability of hot water tanks through wall material specification," *Energy*, pp. 1–13, Nov. 2014.
- [202] P. Armstrong, D. Ager, I. Thompson, and M. McCulloch, "Improving the Energy Storage Capability of Hot Water Tanks through Wall Material Selection," *Energy*, vol. accepted, 2014.

A. APPENDIX

A.1 THERMAL STORES VERSUS CONVENTIONAL HOT WATER TANKS

We can illustrate the penalty associated with a heat exchanger within a thermal store by computing the logarithmic mean temperature difference, T_{LMTD} , between the water-glycol in the store, held at temperature T_s , and the potable supply through the heat exchanger which is incoming at temperature T_m . An iterative procedure, outlined in [91], starts with a guess at the outlet temperature, T_h , to produce T_{LMTD} , using equation (A-1), for a given mass flow rate, \dot{m}_s of water with a heat capacity of C_p . The heat transfer coefficient, h_{ex} determines the energy transferred to the potable water, Q_s which is proportional to the surface area of the heat exchanger A_s . Using these parameters, T_h is re-calculated using equation (A-4) and compared to the guess. This process is iterated until the result produced by (A-1) converges to within an acceptable tolerance.

$$T_{LMTD} = \frac{[(T_s - T_m) - (T_s - T_h)]}{\ln\left(\frac{T_s - T_m}{T_s - T_h}\right)} \quad (A-1) \quad \left| \begin{array}{l} \text{Calculation of mean} \\ \text{logarithmic temperature} \\ \text{difference} \end{array} \right.$$

$$h_{ex} = 14.9T_{LMTD} - 4.1 \quad (A-2) \quad \left| \begin{array}{l} \text{Calculation of mean} \\ \text{logarithmic temperature} \\ \text{difference} \end{array} \right.$$

$$Q_s = h_{ex}A_sT_{LMTD} \quad (A-3) \quad \left| \begin{array}{l} \text{Calculation of heat flux} \\ \text{from thermal store} \end{array} \right.$$

$$T_h = \frac{Q_s}{\dot{m}_s C_p} + T_m \quad (A-4) \quad \left| \begin{array}{l} \text{Calculation of outlet} \\ \text{temperature based on} \\ \text{computed store heat} \\ \text{flux} \end{array} \right.$$

This procedure makes quite a few limiting assumptions, including:

1. The potable water is incompressible and has constant heat capacity
2. The water-glycol throughout the thermal store is homogeneously mixed at one temperature. This may initially be true, but breaks down as energy is drawn out of the system
3. The heat transfer coefficient h_{ex} , is uniform across the exchangers surface whereas in practice flow induced vortices within the coil lead to local variations in heat transfer across its length [198]

In spite of the above simplifications, the method is used in industry and is recommended by the technical datasheet describing a common finned copper heat exchanger, the Wieland WR18W series, that is used by Newark Copper Cylinder [59]. By applying the procedure, illustrated above, it is possible to estimate the required store operating temperature, T_s , needed to deliver 15lpm of water at 60°C from a fully charged thermal store for a given length of helical coil. Figure 1-8 shows the relationship between the coil length, store temperature and resulting heat losses assuming a 200 litre, cylindrical tank with a diameter of 450mm and 50mm of polyurethane insulation with a thermal conductivity of 0.03W/mK where the mains inlet temperature, T_m , and ambient temperature is at 20°C. The figure is also annotated to show the cost of the coil, assuming a market price of 5\$/kg of copper [62] along with the losses that would result from a conventional cylinder where the temperature of the stored water is equal to T_h .

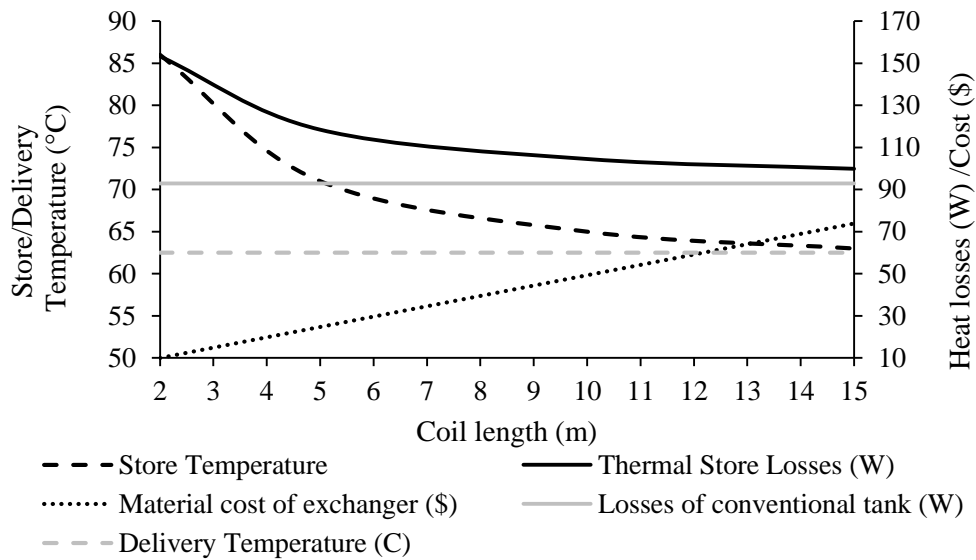


Figure A-1 Relationship between exchanger coil length, associated cost and thermal store operating temperature compared to conventional hot water tank

A.2 TEST RIG DETAILS

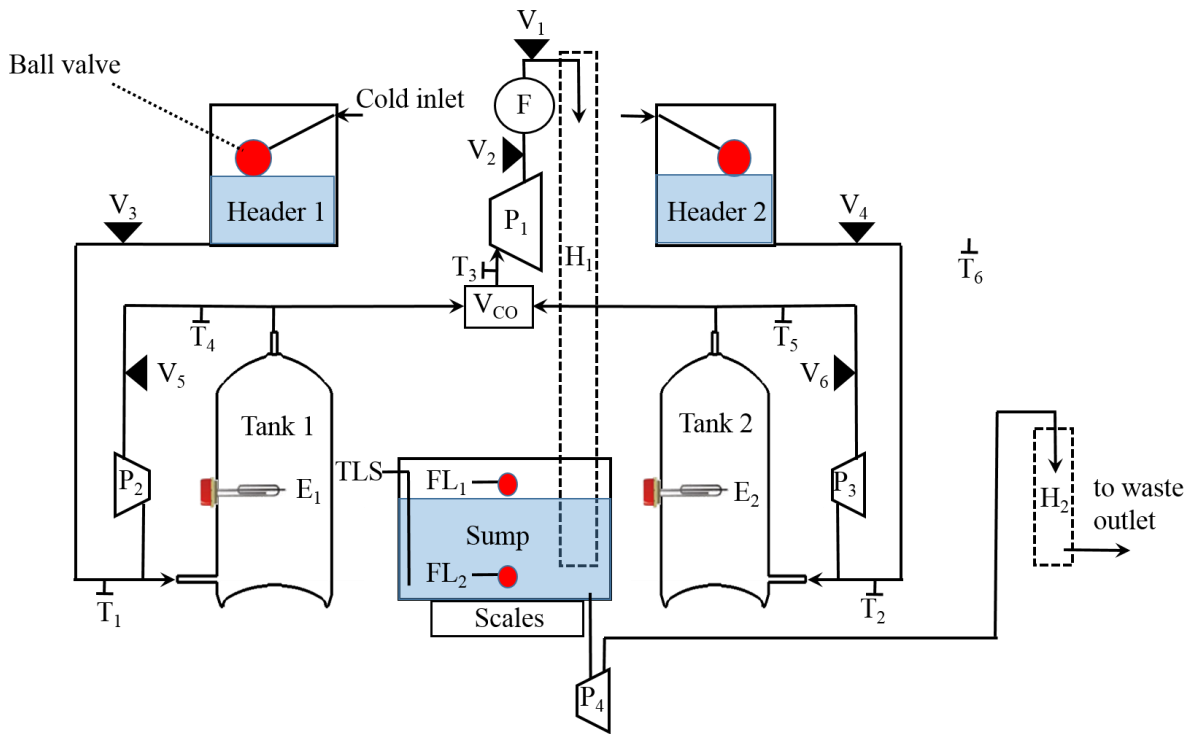


Figure A-2 Schematic layout of test rig used for reference with Table A.1

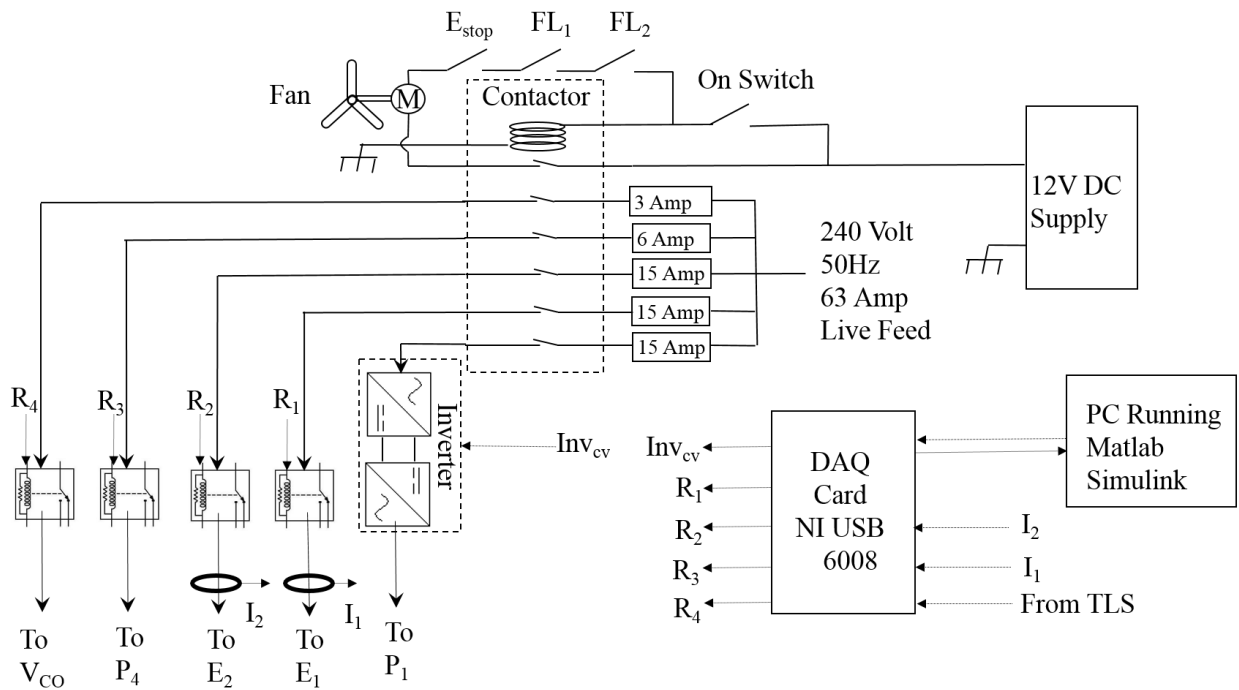


Figure A-3 High level electrical layout of rig control cabinet

Table A-1 Inventory of electrical and mechanical components used on test rig

Mechanical Components

<i>Designator</i>	<i>Item name</i>	<i>Notes</i>
F	Optical flow meter	This is a vertical flow meter with weighted float, used for rough check of flow rates.
P ₁	Primary pump	The primary pump is an induction motor fed by an inverter for variable speed control, the primary pump draws water out of test Tanks 1 and 2.
P ₂	De-stratification pump	The de-stratification pumps mix the contents of the test tank so that an accurate initial state of charge can be achieved
P ₃	De-stratification pump	(as above)
P ₄	Sump pump	The sump pump periodically empties the sump tank when full
V ₁	Test isolation valve	The test isolation valve prevents flow occurring during operation of de-stratification pumps
<i>Designator</i>	<i>Item name</i>	<i>Notes</i>
V ₂	Test throttling valve	The test throttling valve controls the range of flow rates achievable over the primary pump's allowable speed range
V ₃	Inlet isolation valve	Inlet isolation valves inlet supplies from the header tanks to allow test tanks to be fitted to the test rig
V ₄	Inlet isolation valve	(as above)
V ₅	De-stratification valve	The de-stratification valve isolates the de-stratification loop to prevent draw tests being contaminated by water from the header tanks
V ₆	De-stratification valve	(as above)
V _{CO}	Tank change-over valve	Diverts flow from either Tank 1 or Tank 2 depending on whichever is under test
E ₁	Immersion element	Provides 3kW of heat to test tank
E ₂	Immersion element	(as above)
H ₁	Hydro-static non-return	Breaks flow so that a continuous syphon is prevented
H ₂	Hydro-static non-return	(as above)
FL ₁	Upper sump level switch	Switch is wired into emergency stop loop to prevent sump overflowing
FL ₂	Lower sump level switch	Switch is wired into emergency stop loop to prevent sump pump from drying out
T ₁	T-Type thermocouple	Tank 1 inlet flow temperature sensor
T ₂	T-Type thermocouple	Tank 2 inlet flow temperature sensor
T ₃	T-Type thermocouple	This thermocouple reads the outlet flow temperature for whichever tank is under test. The tank change over valve diverts flow to T ₃ depending on which tank is under test
T ₄	T-Type thermocouple	Monitors the temperature of the de-stratification loop on Tank 1 so that the initial state of charge of the tank can be monitored prior to a test
T ₅	T-Type thermocouple	Monitors the temperature of the de-stratification loop on Tank 2 so that the initial state of charge of the tank can be monitored prior to a test
T ₆	T-Type thermocouple	Provides an ambient temperature reading

TLS	Tank level sensor	Provides sump level to control cabinet so that periodic draining of sump is implemented during testing
Header 1	Header tank	Provides cold supply to Tank 1
<i>Designator</i>	<i>Item name</i>	<i>Notes</i>
Header 2	Header tank	Provides cold supply to Tank 2
Tank 1	Test tank 1	Tank under test to evaluate thermal performance under different flow conditions
Tank 2	Test tank 2	(As above)
Scales	Electronic scales	Facilitates accurate flow rate/tank volume measurements

Electrical Components

Designator	Item Name	Notes
E _{Stop}	Emergency stop latch	Disables rig by disconnecting contactor coil when pressed
R ₁	Relay	Relay controlling immersion heating element on Tank 1
R ₂	Relay	Relay controlling immersion heating element on Tank 2
R ₃	Relay	Relay controlling sump pump motor
R ₄	Relay	Relay controlling tank changeover valve so that draw cycles can be run alternately on test tanks in parallel
In _{CV}	Inverter Control Signal	0-5VDC signal controlling frequency of Inverter output
I ₁	Current Measurement	Current feedback from immersion heating element on Tank 1
I ₂	Current Measurement	Current feedback from immersion heating element on Tank 2
Contactor	Safety Contactor	Provides electrical isolation to all systems in the event of sump over-flow/under-fill or activation of emergency stop latch
12V DC Supply	Cabinet Control Line Power Supply	DC to provide power for contactor, cabinet switch panel and Cabinet Fan
Fan	Cabinet Fan	Cabinet fan operates when safety contactor is energised to ensure that inverter module is kept cool
Inverter	Single Phase 3kW Inverter	Single phase inverter provides variable frequency supply to P ₁ so that flow rate associated with draw events can be controlled.
DAQ Card	Data Acquisition Card	National Instruments USB 6008 card to control test rig, connected via USB to Rig Control PC
PC Running Matlab	Rig Control PC	Dell PC outside of control cabinet hosting Matlab Simulink rig control algorithm

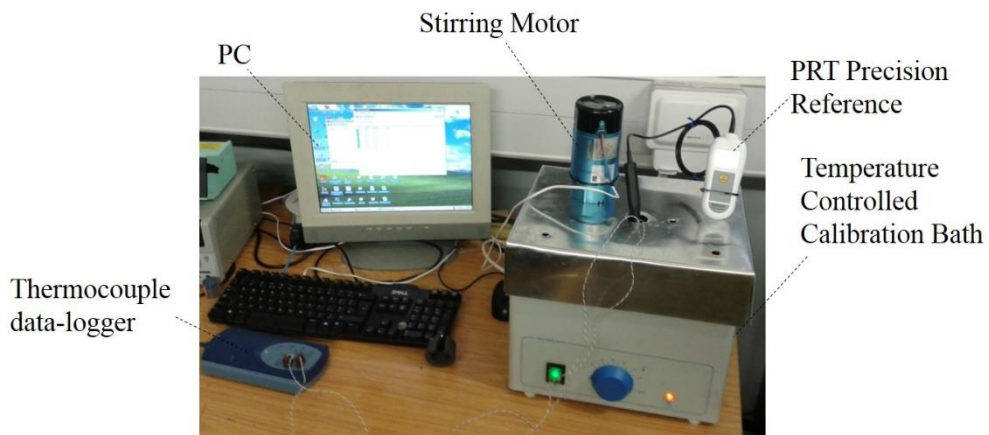


Figure A-4 Thermocouple calibration system

Table A-2 Calibration results for 16 thermocouples

PRT reference Temperature (°C) (Error +/-0.05°C)	Average temperature reading across 16 Thermocouples (°C)	Standard deviation across all channels (°C)	Maximum single channel Error (°C)
0.01	-0.08	0.15	0.14
25.07	24.97	0.38	0.4
43.5	43.60	0.25	0.46
63.36	63.38	0.24	0.4
73.8	73.78	0.23	0.38

A.3 FLOW DRAW CYCLES

Table A-3 ASHRAE draw cycle events

Draw event start time	Flow rate (lpm)	Fractions of total volume drawn from the tank	Tank1 T1 (°C)	Tank2 T1 (°C)
06:00	10	0.011	58.6	58.8
07:00	10	0.080	57.9	58.3
08:00	10	0.079	57.2	57.6
09:00	10	0.069	56.7	56.9
10:00	10	0.068	56	56.1
11:00	10	0.069	55.2	55.1
12:00	10	0.048	54.5	54.1
13:00	10	0.049	53.7	52.9
14:00	10	0.039	52.9	51.6
15:00	10	0.039	52.2	50.4
16:00	10	0.039	51.6	49.1
17:00	10	0.039	50.9	47.7
18:00	10	0.066	49.7	46.0
19:00	10	0.066	49	44.4
20:00	10	0.066	47.9	42.4
21:00	10	0.066	46.6	40.5
22:00	10	0.053	45.3	38.7
23:00	10	0.054	43.8	37.0

Table A-4 Burch & Thornton draw cycle events

Draw start time	Flow rate (lpm)	Fraction of total volume drawn from the tank	Tank1 T1 (°C)	Tank2 T1 (°C)
06:00	15	0.184	59.3	59.6
07:00	5	0.184	58.6	58.9
08:00	5	0.059	57.5	57.7
11:00	5	0.030	54.9	54.3
12:00	5	0.188	55	53.6
13:00	5	0.022	53.1	51.2
17:00	5	0.114	50.4	45.7
18:00	5	0.037	48.7	43.1
19:00	5	0.061	47.8	42.2
20:00	5	0.120	46.3	40.3